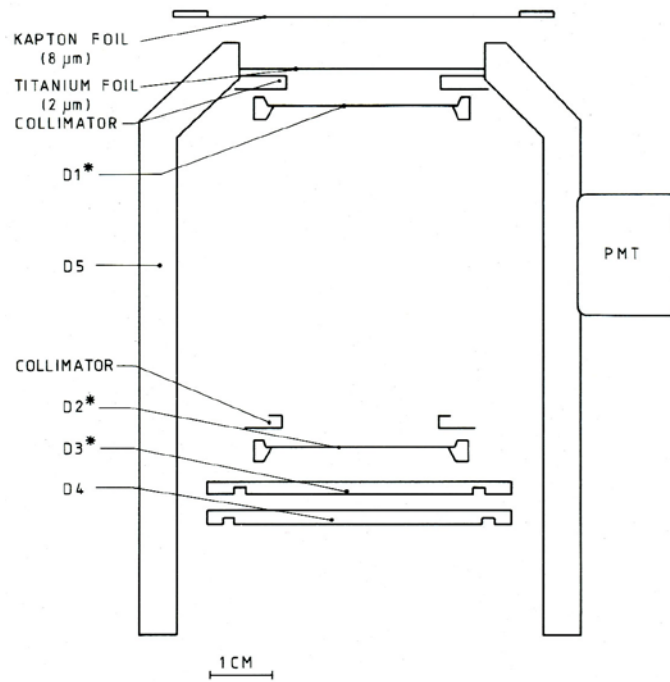
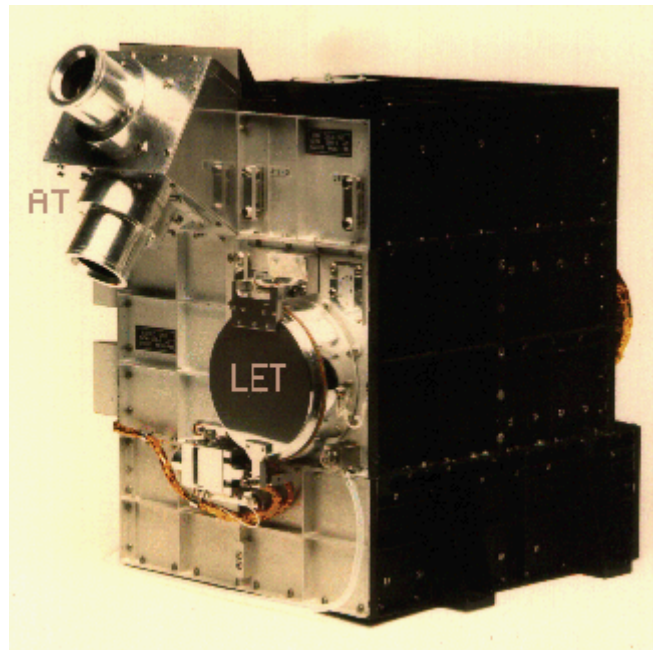


# ULYSSES/COSPIN

## LOW ENERGY TELESCOPE HANDBOOK

REV.1





## Table of Contents

1. Introduction.....	4
2. Functional description.....	5
2.1 Analogue electronics: functional data.....	5
2.1.1 Dynamic ranges, resolution, sensitivity.....	5
2.1.2 Threshold discriminators.....	5
2.1.3 Particle Identifier system.....	5
2.2 Priority system.....	6
2.2.1 Priority look-up table.....	6
3. Mechanical construction.....	7
3.1 Telescope.....	7
3.2 SIM-1.....	7
4. Telemetry.....	7
4.1 Digital data channels.....	7
4.1.1 Counting rate decompression.....	7
4.1.2 PHA word structure.....	8
4.1.3 Status word structure (L45/L46).....	8
4.1.4 Telemetry format and timing.....	8
Accumulation Period.....	9
Channel.....	9
4.2 Analogue data, monitoring.....	9
4.2.1 LET analogue data.....	9
4.2.2 Monitoring.....	9
4.3 Telecommands.....	10
5. LET Calibrations.....	10
5.1 Accelerator calibrations.....	10
5.2 Electronic calibrations.....	11
6. LET PHA data reduction.....	11
6.1 Charge histograms.....	11
6.2 Charge interpolation algorithm.....	12
6.3 Energy-loss in aperture foils.....	13
7. LET LP1 and LP5 count rate correction factors.....	14
7.1 Background from high-energy protons.....	14
7.2 Corrections due to counting limitations (“roll-over”).....	14
8. User Notes for LET Data Products.....	14
8.1 LET counting rate data.....	14
8.2 PHA-derived H and He fluxes.....	16
8.3 PHA-derived O, N and Ne fluxes.....	17
8.4 Yearly PHA plots.....	17
LET Publications.....	18
Appendices.....	22
List of Tables.....	23
List of Figures.....	24

# 1. Introduction

The COSPIN Low Energy Telescope (LET) is part of the collaborative Cosmic Ray and Solar Particle Investigation (COSPIN) experiment designed to investigate the charged particle environment encountered during all phases of the Ulysses mission. The LET measures the flux, energy spectra and elemental composition of solar and heliospheric energetic particles and low energy cosmic ray nuclei from hydrogen up to iron, covering an energy range from  $\sim 1$  to  $\sim 75$  MeV/n. Isotope separation for light nuclei such as He is also achieved. The LET sensor comprises a solid-state detector telescope surrounded by a plastic scintillator anti-coincidence shield, together with associated analogue and digital electronics. The LET utilises the standard  $dE/dX$  vs.  $E$  technique in order to identify the nuclear charge, and in some cases the mass, of the incident particles. For particles stopping in the detector stack, the energy lost in one or both of the thin detectors D1 and D2, together with the residual energy deposited in the remaining detector(s), is measured. Comprehensive on-board particle identifier electronics and an event priority system enable rare nuclei to be analyzed in preference to the more common species.

A simplified block diagram of the LET system is shown in Fig. 1.1. The detecting elements of the telescope are shown in cross-section in Fig. 1.2, together with photographs of the hardware. Detectors D1 and D2 are surface-barrier devices with equal active area ( $6.0 \text{ cm}^2$ ), while D3 and D4 are 2 mm-thick lithium-drifted devices of  $10.0$  and  $12.5 \text{ cm}^2$  active area, respectively. The detailed characteristics of the detectors mounted in the flight instrument are given in Table 1.1. D5, comprising a cylindrical plastic scintillator element viewed by a single photomultiplier tube, forms (together with D4) an anti-coincidence counter. The anti-coincidence shield is needed to reject particles that enter the telescope outside the nominal acceptance cone, or that penetrate part of the internal structure of the telescope, giving rise to spurious signals in one or more detectors. The telescope aperture is covered by two thin foils, an inner Ti foil ( $\sim 2 \mu\text{m}$ ,  $0.9 \text{ mg/cm}^2$ ) for electrical shielding, and an outer aluminised Kapton foil ( $\sim 8 \mu\text{m}$ ,  $1.0 \text{ mg/cm}^2$ ) for thermal protection.

Two main categories of scientific data are obtained from the LET system. Firstly, counting rates for 22 different particle species/energy-range combinations, 2 of which are further sub-divided into 8 angular viewing sectors in the spacecraft spin plane. At the highest available spacecraft bit-rate (1024 bps real-time telemetry), counts are accumulated over 32- or 128-sec intervals (telemetry-format synchronised) for the non-sectored channels, and over an integral number of spins for the 16 spin-synchronised, sectored channels. An overview of all 38 rate channels is given in Table 1.2, and the logic equations used to define these channels are summarised in Table 1.3.

The second type of data obtained consists of the event-by-event pulse-height values from detectors D1, D2 and D3. Owing to telemetry limitations, a maximum of one PHA event per second can be transmitted, the selected event being chosen by a priority scheme (described in section 2.2). In addition to pulse height data and proton, alpha and heavy ion rates, the LET data frame contains digital status information and analogue housekeeping values, as well as counting rate data for the individual detectors. Housekeeping information includes instrument voltages, the detector leakage currents and temperature values for the detector telescope and electronics.

A detailed functional description of the instrument is given in section 2, and information concerning the mechanical construction is provided in section 3. Details of the telemetry word structures, analogue channels, engineering data, etc. are given in section 4.2.

## **2. Functional description**

The detailed operation of the instrument is best understood with reference to the LET functional block diagram (Fig. 1.1). The main elements of the LET system are described in the following sections and in the document “The prototype low-energy telescope system for the international solar polar COSPIN experiment”, R.G. Marsden, J. Henrion, Report ESA STR-202, 1979 (included as an appendix to this Handbook).

### **2.1 Analogue electronics: functional data**

In the following sections, the main functional characteristics of the analogue electronics are presented.

#### **2.1.1 Dynamic ranges, resolution, sensitivity**

The output of each of the three solid state detectors D1, D2 and D3 is fed into an individual amplifier chain consisting of a charge-sensitive preamplifier (CSA) followed by 3 parallel pulse-shaping voltage amplifiers (PSA). In order to accommodate the large dynamic range required (~ 10,000), one low- and one high-gain PSA has been used, selected via an analogue switch controlled by a third (fast) PSA in conjunction with a discriminator. Detectors D4 and D5 utilise simpler CSA-single (fast) PSA amplifier chains.

Table 2.1 shows the appropriate nominal values for dynamic range and sensitivity for each of the amplifier chains. Also shown in this table are the actual PHA system resolution values in keV per channel for the common 10-bit (1024 channel) Analogue-to-Digital Converter (ADC).

#### **2.1.2 Threshold discriminators**

The fast PSAs (PSAF) are followed by a number of threshold discriminators, the outputs of which are used in the coincidence logic to define the various rate channels in accordance with the logic equations presented in Table 1.3. Figure 2.1 shows the nominal threshold levels in relation to the pulse signatures for protons and  $4\text{He}$  in detectors D1, D2 and D3. In this diagram, the energy in MeV deposited in each of the three detectors is plotted as a function of the initial energy for particles entering the telescope system at an angle of  $12.5^\circ$  (the mean incidence angle for an isotropic flux). Table 2.2 gives the nominal values assigned to the discriminators. Discriminators denoted by DDnS are the high-level thresholds used to select the appropriate PSA gain.

#### **2.1.3 Particle Identifier system**

The LET Particle Identifier (PI) system employs a set of analogue function generators and discriminators to divide the multi-detector response into regions corresponding to different incoming particle charge, mass and energy, making it possible to obtain the

counting rates corresponding to groups of nuclear species. The actual analogue functions used are of two types, namely

$$E_1 + b_i E_2 = a_i \quad (1)$$

and

$$E_2(b_i + E_3) = a_i \quad (2)$$

where  $E_1$ ,  $E_2$  and  $E_3$  are the energies deposited in detectors  $D_1$ ,  $D_2$  and  $D_3$ , respectively, and  $a_i$ ,  $b_i$  are constants. For particles stopping in  $D_2$ , the loci of points satisfying equation (1) for given pairs of  $(a_i, b_i)$  values define boundaries on the  $\Delta E$  ( $\equiv E_1$ ) vs. residual  $E$  ( $\equiv E_2$ ) diagram that separate the tracks corresponding to different elements or groups of elements into so-called "charge groups". The charge groups defined for the  $D_1 - D_2$  range are: protons; (He-3, He-4); (Li, Be, B); (C, N, O);  $Z \geq 10$  nuclei. In a similar way, charge group boundaries for particles stopping in  $D_3$  are defined by equation (2) with suitable pairs of  $(a_i, b_i)$  values. A different functional form is required in this case because of the pronounced curvature of the  $\Delta E$  vs. residual  $E$  tracks resulting from the large thickness of  $D_3$  relative to  $D_2$ . The same charge groups as before are defined for the  $D_1 - D_2 - D_3$  range, with the addition of a high- $Z$  group corresponding to  $Z \geq 20$ . In this latter case, the discriminator boundary takes the simpler form of equation (1). Examples of the implementation of this technique are illustrated schematically in Figs. 2.2 and 2.3. The nominal values of the parameters used in the PI system are summarised in Table 2.3.

Each of the charge groups has an associated counting rate register which is incremented each time a valid event within the group is observed. In addition to providing counting rate information, the PI output is used to generate a 4-bit event code that controls the Event Priority System, described in section 2.2.

## 2.2 Priority system

In order to maximise the PHA data collection efficiency for the less common nuclear species in the incident cosmic ray flux, an Event Priority System has been incorporated in the LET. The Priority weighting assigned to a given charge group at any one time determines whether or not an event corresponding to that group will be pulse height analysed. Since the PHA data rate is limited for telemetry reasons to one per second, the Priority System only retains the pulse height information from the event with the highest priority weighting occurring in a given sampling period. Each valid event will, however, increment the appropriate charge group counting rate register regardless of whether it is pulse-height analysed or not.

### 2.2.1 Priority look-up table

Each of the charge groups defined in Table 1.2 is given a unique EVENT CODE number in the range 0 to 15. The priority weighting values are contained in a look-up table (stored in a ROM) which consists of a number (nominally 16) of PRIORITY SEQUENCES which are stepped through sequentially in an 8192 second cycle (512 seconds per sequence). The location containing the weighting value for a given event is specified by the event code number (column) and current sequence number (row), and weighting is defined such that 1 corresponds to lowest priority. The contents of

the ROM are shown in Table 2.4. Measured cosmic ray abundances have been used to determine the rate at which different event types are expected to be seen by the instrument. These rates are a function of both the relative abundances and the energy range corresponding to each event. From these expected event rates, priority sequences with varying degrees of categorisation have been defined in such a way that, when taken over a complete cycle, the sampling of all event types is as well balanced as possible. This means that most of the rare events will be processed, whilst at the same time obtaining good statistics for the more abundant species.

A consequence of including highly categorised weighting is that background occurring in a channel corresponding to a rare event type could monopolize the PHA data. An example would be possible spill-over of carbon events in to the adjacent Li-Be-B region. For this reason the high-priority status of such rare events has been suppressed in certain parts of the priority cycle.

## **3. Mechanical construction**

### **3.1 Telescope**

The LET sensor is shown in Fig. 1.2 (bottom left). Cross-sectional engineering drawings of the LET telescope are reproduced as Figs. 3.1 and 3.2, while details of the scintillator shield and the inner structure (including key dimensions in mm) are shown in Figs. 3.3 and 3.4, respectively.

### **3.2 SIM-1**

The LET telescope is mounted together with the associated analogue and digital electronics in the central section of the SIM-1 package, with the Data Processing Unit below and the Anisotropy Telescopes above (see Figs. 3.5, 3.6a and 3.6b). The LET aperture is protected by a hinged cover that was deployed (opened) after launch, as indicated in Fig. 3.6b. The resource breakdown (mass, power and telemetry) for the units that make up SIM-1 is given in Table 3.1.

## **4. Telemetry**

### **4.1 Digital data channels**

The LET digital channels are defined in Table 1.2. Data from the counting rate channels are compressed from 27 to 12 bits (L1, L2, L3, L12 and L21) or from 19 to 8 bits. Decompression algorithms for these data, given in section 4.1.1, are extracted from ISPM Project document number ISPM-PH-0407, chapter 4.1. Channels L1 to L25 are accumulated over 32 seconds; channels L26 to L38 are accumulated over 128 seconds. The structure of the PHA and status words is described in sections 4.1.2 and 4.1.3, respectively.

#### **4.1.1 Counting rate decompression**

The data conversion algorithms described below are used to convert the counting rate channel readouts (which have been compressed from 19 to 8 bits or from 27 to 12 bits in the COSPIN data system) to the original counts registered in the accumulator. These algorithms are used to recover the binary count,  $C$ , from the telemetered values

of X and Y. In the serial data stream, the value of Y is shifted out first, followed by X. The MSB of each is transmitted first. Different algorithms are used for 27-bit and 19-bit modes. In each case, the telemetered Y value must be converted to an N value using the appropriate look-up tables (Table 4.1a and 4.1b). In the 19-bit mode, the algorithm is as follows (X and Y both 4 bits long):

$$\begin{aligned} &\text{If } X = 15 \text{ and } Y = 6, C = 0 \\ &\text{If } Y = 5, C = X + 1 \\ &\text{Otherwise, } C = 1 + (X + 16) \cdot 2^N \end{aligned}$$

In the 27- to 12-bit mode (X contains 7 bits, Y contains 5 bits):

$$\begin{aligned} &\text{If } Y = 22 \text{ and } X = 127, C = 0 \\ &\text{Otherwise, } C = 1 + (X + 128) \cdot 2^{(N-8)} \end{aligned}$$

In the 27-bit mode, certain values of Y should never occur. These are denoted by "XX" in Table 4.1b. Fractional parts of a result are discarded.

The information given by the algorithm represents the lowest value of input count that would result in the given X and Y values. For example, in the 19-bit mode, a read-out with value (octal) 143 represents an X value of 3 and a Y value of 6 (N=14). Using the algorithm above, the minimum input count is 311297. However, any input count between 311297 and 327680 would result in a code of 143 (octal). The mean value of all such input counts is therefore 319489, and so the user may wish to substitute 16.5 for 16 (or 128.5 for 128) in the algorithms.

#### **4.1.2 PHA word structure**

Table 4.2 shows the structure of the 44-bit PHA word, which is sampled in the experiment once per second and read out at a rate of 32 per format. The bit assignment for bits 30 to 35 is dependent on the value of the LSB of status word L46, which indicates whether the Priority System is in operational or test mode.

#### **4.1.3 Status word structure (L45/L46)**

The 8-bit status words L45 and L46 are read out every 32 seconds. The bit assignment for these words is given in Tables 4.3 and 4.4. Priority Table Address (PTA, L45, bits 4, 5, 6 and 7) refers to the current row number in the Priority Look-up Table (see section 2.3.1 and Table 2.4).

#### **4.1.4 Telemetry format and timing**

The LET digital data words are incorporated in the COSPIN Experiment Telemetry Format, which is read out once every 32 seconds. The complete COSPIN data set is read out in 8 so-called Experiment Subformats (i.e. once every 256 secs.). Data from a given sensor read out in any one subformat do not normally correspond to one and the same accumulation period. The timing reconstruction scheme for the LET is given in Tables 4.5, 4.6 and 4.7. Data that were accumulated during the period corresponding to a given block of 8 subformats (termed "accumulation period" in the Tables) are read out in the subformat numbers tabulated for each channel. Normally, a practical reconstruction method would involve storage of all data read out in a given block of 8

subformats plus a number of temporarily stored words. The following is an example of how to interpret the tables:

Example:

<u>Channel</u>	<u>Accumulation Period</u> (Subformat number)							
	0	1	2	3	4	5	6	7
<u>L<sub>x</sub></u>			m (13/11/B)				mI (13/11/B)	
<u>L<sub>y</sub></u>			n (12/4/A)					

In this example, data from channel L<sub>x</sub> accumulated during the 32 s corresponding to subformat # 2 were read out in subformat # m. (frame 13, s/c word 11, CPU B), m > 2, and must be retrieved from that location. Data from channel L<sub>y</sub> accumulated during the same 32 s as L<sub>x</sub> were read out in subformat # n (n > 2, n ≠ m a priori), and must be retrieved from that location. (Note that subformat number mI corresponds to subformat number m in the next group of 8, i.e. mI = m + 8).

In Tables 4.5, 4.6 and 4.7 only the subformat numbers are given, and not the frame, s/c word and CPU locations. Note that the format is divided into two parts corresponding to read-out from CPU A or CPU B in the COSPIN DPU. Spacecraft words 2 up to and including 11 are read from CPU A; words 12 to 21 are read from CPU B. In the case of the PHA words, Table 4.7 shows the read-out subformats corresponding to the accumulation periods shown. In the Experiment Format the PHA words are labelled as follows:

- LET PHA 2 is the event collected during S/C FRAME 0
- LET PHA 3 is the event collected during S/C FRAME 1
- LET PHA 4 is the event collected during S/C FRAME 2
- Etc.

And LET PHA 1 is the event collected during S/C FRAME 31

## **4.2 Analogue data, monitoring**

### **4.2.1 LET analogue data**

The LET analogue data comprise 12 channels that are multiplexed, each channel having a 4-bit MUX address. The address to be read out is changed by the spacecraft every format (nom. 32 secs), which leads to an updating of a given parameter every 16 formats (= 512 seconds). A list of the analogue parameters, together with their conversion formulae, is given in Table 4.8. Note that the full-scale voltage of 5.1 volts is equivalent to 256 S/C telemetry counts (8-bit S/C ADC).

### **4.2.2 Monitoring**

In addition to the analogue data described above, a number of (digital) channels were monitored by the S/C OCOE during system-level testing. A complete description of

all parameters monitored, together with associated high, low and delta limits, is given in the Project document ISPM-PH-0407-1L "ISPM System Level Check-out Software Requirements for Experiment SIM-LET", chapter D1. A summary list of these parameters is given in Table 4.9.

### **4.3 Telecommands**

Memory load commands are given in the form of a 16-bit word, containing the 4-bit LET address (bits 0 - 3) and a 1-bit internal LET identifier (bit 4, specifying word A or word B). The bit assignments given in Tables 4.10 and 4.11 for the two cases bit 4 = 0 (LET command word A) or bit 4 = 1 (LET command word B).

## **5. LET Calibrations**

LET calibrations (and related instrumental characteristics) are discussed in detail in the following documents that are included as Appendices to this document:

- Kamermans, R., J. Henrion, R.G. Marsden, T.R. Sanderson, K.-P. Wenzel, Element and Isotope Separation for a Heavy Ion Cosmic Ray Telescope with Large Geometrical Factor, Nucl. Instr. and Meth., 171, 87, 1980.
- LeBorgne, J.F., J. Henrion, R.G. Marsden, T.R. Sanderson, K.-P. Wenzel, Accelerator calibration of the Low Energy Telescope of the International Solar Polar Mission COSPIN Experiment, Report ESA STM-224, 1981.
- Marsden, R.G., J. Henrion, T.R. Sanderson, K.-P. Wenzel, N. de Bray, H.P. Blok, Calibration of a Space-Borne Charged Particle Telescope Using Protons in the Energy Range 0.4 To 20 MeV, Nucl. Instr. and Meth., 221, 619, 1984.
- Marsden, R.G. et al., The Phobos Low Energy Telescope Charged Particle Experiment, Nucl. Instr. and Meth., 290, 211, 1990.
- Marsden, R.G., LET Calibration Document, 1990.
- Henrion, J., LET Response to high fluxes, Technical Report, 1992.

### **5.1 Accelerator calibrations**

The LET flight hardware was calibrated at a number of accelerator facilities, as shown in Table 5.1. Reports and/or papers describing the results of these calibrations are also listed in Table 5.1. The main objective of the heavy ion calibrations was to trim the different discriminator levels in the Particle Identifier electronic circuitry against the measured response of the instrument ( $dE/dX$  vs. E tracks). Ideally, beams covering the full response in energy and nuclear species would have been used. In practice, this coverage was approximated using high-mass primary beams that were fragmented on a target, together with a variable-thickness absorber to achieve the required spread in energy. Examples of charge histograms (see 6.1) obtained from runs at the GANIL accelerator are shown in Figs. 5.1 and 5.2.

In addition, so-called "spot" measurements, using unfragmented beams of well-defined energy with minimum spread were used in an attempt to derive first-order

energy calibrations and to study the energy-loss characteristics of the Ti and Kapton aperture foils.

Finally, the response of the proton channels was mapped using proton beams of known energy.

## **5.2 Electronic calibrations**

In addition to accelerator calibrations, the electronic characteristics of the various LET amplifier chains and ADC circuitry have been accurately determined. Measurements included the overall linearity of the combined CSA (charge-sensitive amplifier) => PSA (pulse-shaping amplifier) => ADC chains, as well as the relative gains of the high- and low-gain amplifiers associated with each of the pulse-height analysed detectors. The results are shown in Figs. 5.3, 5.4 and 5.5. Pulse-height vs. energy conversion factors have been determined using high-precision programmable pulse generators (PPG) to stimulate the different amplifier chains, in combination with the known sensitivity of the CSAs (i.e., mV per MeV).

The ADC channel number-to-MeV conversion factors are listed in Table 2.1. The function used for the conversion is of the form

$$E(\text{MeV}) = \alpha n^\beta$$

where  $n$  is the channel number and  $\alpha$  and  $\beta$  are constants. The fact that  $\beta \neq 1.0$  reflects a slight non-linearity in the system. High- and Low-gain factors are given for each of the pulse-height analysed detectors D1, D2 and D3, to be applied depending on the value of the appropriate gain flags in the PHA word (bits 33-35). High-gain mode is indicated by a gain flag = 0; Low-gain is indicated by gain flag = 1.

## **6. LET PHA data reduction**

A three-step procedure has been developed for the reduction of LET PHA data:

1. Creation of charge histogram (charge spectrum) using a charge interpolation algorithm (see 6.2).
2. Application of a correction factor to take into account the energy lost in the aperture foils.
3. Calculation of the incident energy per nucleon using the corrected incident energy and a mass number based on the calculated charge, allowing relative abundances and energy spectra to be computed.

### **6.1 Charge histograms**

The channel number-to-MeV conversion factors have been applied to pulse-height data from the accelerator calibration runs and flight data to define a set of reference “tracks” on the  $\Delta E$  vs. residual  $E$  plots (D1 vs. D2, D2 vs. D3) for the key elements He, O, Si and Fe. These reference tracks are used as input to the charge interpolation algorithm described in section 6.2 to produce charge histograms, examples of which are shown in Figs. 6.1a,b, 6.2a,b, 6.3a,b and 6.4a,b for Helium (showing the clear separation of the isotopes  $\text{He}^3$  and  $\text{He}^4$ ), Oxygen, Silicon and Iron, respectively. (Similar plots using PHA data from different periods throughout the mission show no evidence of shifts in the track positions, indicating negligible instrumental drifts.)

Events falling within pre-set upper and lower limits of the charge value derived using the interpolation routine are then summed to give the total number of events corresponding to a given integer charge (and in the case of He<sup>3</sup> and He<sup>4</sup>, mass) value. These limits are typically set at  $\pm 0.5$  charge units of the nominal value, i.e.  $7.5 \leq Z < 8.5$  charge units corresponds to Oxygen, etc.

## 6.2 Charge interpolation algorithm

The charge interpolation algorithm used to process LET PHA data is based on a generalised range-energy relation for projectiles of charge  $Z$  and mass  $M$  of the form

$$R (\mu\text{m Si}) = \frac{11.9E (\text{MeV})^{1.77}}{Z^2 M^{0.77}}$$

So that

$$E (\text{MeV}) = (A.R)^\beta$$

where

$$A = [Z^2 M^{(1/\beta - 1)}]/11.9$$

and

$$\beta = 1/1.77 = 0.565$$

Consider a 2-detector dE/dX vs. E telescope having detector thicknesses  $t$  and  $T$ , respectively. For projectiles of initial energy  $E_0$  stopping in the second detector with residual energy  $E_{\text{res}}$  and corresponding range  $R_{\text{res}}$ , the following relations apply:

$$E_0 = A^\beta (t + R_{\text{res}})^\beta$$

and

$$E_{\text{res}} = A^\beta R_{\text{res}}^\beta$$

so that

$$\Delta E = E_0 - E_{\text{res}} = E_{\text{res}} R_{\text{res}}^{-\beta} [(t + R_{\text{res}})^\beta - R_{\text{res}}^\beta]$$

This last equation defines the locus of so-called “track end-points” in the  $\Delta E$  vs.  $E_{\text{res}}$  diagram, and (within the constraints of the assumed range-energy relation) represents a straight line (referred to here as the *constant range line*, illustrated in Fig. 6.5).

The separation  $s$  along a given constant range line of the endpoints corresponding to two different nuclear species ( $Z_1, M_1$ ) and ( $Z_2, M_2$ ) is given by

$$s = \sqrt{[(\Delta E_2 - \Delta E_1)^2 + (E_2 - E_1)^2]} = C (A_2^\beta - A_1^\beta)$$

where

$$C = \sqrt{(B^2 + R_{\text{res}}^{2\beta})}$$

and

$$B = (t + R_{\text{res}})^\beta - R_{\text{res}}^\beta$$

Assuming that  $M \approx 2Z$ , and substituting this in the expression for  $A$  gives

$$s = \alpha R_{\text{res}}^{0.565} (Z_2^{1.565} - Z_1^{1.565})$$

where  $\alpha$  is a constant  $\sim 0.33$ . Strictly speaking, this relation will only be valid over the same energy range as the power-law approximation to the generalised range-energy relation (i.e., for incident energies  $\geq \sim 5$  MeV). For the constant range interpolation

charge determination method to work optimally, the *relative* spacing of individual species tracks along given constant range lines must remain constant. For residual ranges  $< \sim 20 \mu\text{m}$ , the approximation becomes less good, and slight broadening of the charge peaks can occur. The contribution of this effect to the overall width of the charge peaks is, however, small.

Assuming now that  $(Z_1, M_1)$  and  $(Z_2, M_2)$  are *reference species* for which the track positions are known, the charge corresponding to each event can be computed from the relative spacing along the appropriate constant range line as follows:

$$[s_Z(\text{MeV})]/[s_{Z_2}(\text{MeV})] = (Z^{1.565} - Z_1^{1.565}) / (Z_2^{1.565} - Z_1^{1.565})$$

but

$$s_Z / s_{Z_2} = (E_{res} - E_{1,res}) / (E_{2,res} - E_{1,res}) = r$$

so that

$$Z = {}^{1.565}\sqrt{[Z_1^{1.565}(1 - r) + rZ_2^{1.565}]}$$

This is shown graphically in Fig. 6.6.

### 6.3 Energy-loss in aperture foils

In order to determine the incident energy of protons and heavy ions stopping in the LET, a correction factor has to be applied to take into account the energy loss occurring in the two aperture foils. Range-energy data for the two materials concerned, Ti ( $0.9 \text{ mg/cm}^2$ ) and Kapton ( $\sim 1.0 \text{ mg/cm}^2$ ), have been used to construct a look-up table for all species and covering all energies detected by the LET. In the case of Kapton, for which no specific range-energy data exist, the polyethelene tabulations of Northcliffe and Schilling (1970), hereafter NS70, were used. These were found to be in reasonable agreement with experimental data acquired for carbon ions during accelerator runs. NS70 data were also used for Ti. In both cases, extrapolations were made beyond the maximum energy of 12 MeV/n in the NS70 tables. The resulting look-up table is reproduced here as Table 6.1.

The following sources have been used in developing the LET PHA analysis software:

- Butler, G.W., A.M. Poskanzer, D.A. Landis, Nuc. Instr. and Meth., **89**, 189 (1970).
- Goulding, F.S., Nuc. Instr. and Meth., **162**, 609 (1979).
- Greiner, D.E., Nuc. Instr. and Meth., **103**, 291 (1972).
- Janni, J.F., Techn. Rep. AFWL-TR-65-150, USAF (1966).
- Littmark, U. and J.F. Ziegler, Stopping and ranges of ions in matter, **6**, Pergamon Press, New York (1979).
- Northcliffe, L.C., R.F. Schilling, Nuc. Data Tables, **7** (1970).

## 7. LET LP1 and LP5 count rate correction factors

### 7.1 Background from high-energy protons

Under specific conditions, the LET rate channels L1 (LP1) and L12 (LP5) are affected by background from high-energy particles that interact with, i.e. lose energy in, the (passive) internal structure of the telescope. The degree to which this occurs depends on the slope of the differential energy spectrum: the harder the spectrum, the higher the background. A correction procedure has been developed using the results of Monte Carlo simulations of the LET response. Channels L3 and L4, which are coincidence channels and as such effectively unaffected by background events, are used to determine the true spectral slope ( $\gamma_0$ ). A correction factor  $F_c$  is then applied according to the following equations:

<u>L1 (LP1)</u>				
	$\gamma_0 <$	-3.5	$F_c =$	1.0
-3.5	$\leq$	$\gamma_0 \leq$	-0.5	$-0.3 \gamma_0 - 0.05$
		$\gamma_0 >$	-0.5	0.0
<u>L12 (LP5)</u>				True rate =
	$\gamma_0 <$	-2.0	$F_c =$	1.0
-2.0	$\leq$	$\gamma_0 \leq$	+1.25	$-0.275 \gamma_0 + 0.45$
		$\gamma_0 >$	+1.25	0.0
				$F_c * \text{measured rate}$

### 7.2 Corrections due to counting limitations (“roll-over”)

Channels L1 (LP1), L2 (LP2) and L22 (LA1) show a non-linearity in input rate vs. output rate at high counting rates (see Fig. 7.1). This so-called “roll-over” becomes significant above the following MEASURED intensities:

L1:  $I > 5.0 \text{ E}+03$  particles/cm<sup>2</sup>.s.sr.MeV/n  
 L2:  $I > 7.5 \text{ E}+02$   
 L22:  $I > 3.0 \text{ E}+02$

At somewhat higher intensities, the response curves turn over, so that ambiguities occur.

## 8. User Notes for LET Data Products

The following is extracted from the User Notes that appear on the Ulysses Data System web page for the COSPIN/Low Energy Telescope.

### 8.1 LET counting rate data

Record Format:

```
IMPLICIT REAL(L)
DIMENSION L4_11(8),L13_20(8),L34_38(5)
```

```

C FREE FORMAT
  READ(1,*)IYEAR,IDOY,IHOUR,IMIN,ISEC,
  .      L1,L2,L3,L4_11,L12,L13_20,L21,
  .      L22,L23,L24,L25,
  .      L26,L27,L28,L29,L30,L31,L32,L33,L34_38
C FIXED FORMAT
  READ(1,100)IYEAR,IDOY,IHOUR,IMIN,ISEC,
  .      L1,L2,L3,L4_11,L12,L13_20,L21,
  .      L22,L23,L24,L25,
  .      L26,L27,L28,L29,L30,L31,L32,L33,L34_38
100  FORMAT(I5,X,I3,3(X,I2),38(X,G9.3))

```

### Parameter List:

```

IYEAR:  year
IDOY:   day of year
IHOUR:  hour
IMIN:   minute
ISEC:   second
L1:     protons      (0.9-1.2 MeV)
L2:     "            (1.2-3.0 MeV)
L3:     "            (1.8-3.8 MeV)
L4_11:  "            "            sectors 1 to 8
L12:    "            (3.8-8.0 MeV)
L13_20: "            "            sectors 1 to 8
L21:    "            (8.0-19.0 MeV)
L22:    alphas      (1.0-5.0 MeV/n)
L23:    "            (1.9-3.7 MeV/n)
L24:    "            (3.7-8.4 MeV/n)
L25:    "            (8.4-19.0 MeV/n)
L26:    Li,Be,B     (1.9-4.9 MeV/n)
L27:    "            (4.9-26 MeV/n)
L28:    C,N,O       (2.6-7.1 MeV/n)
L29:    "            (7.1-39.0 MeV/n)
L30:    Z>=10       (3.0-9.0 MeV/n)
L31:    10<=Z<=20  (9.0-50 MeV/n)
L32:    Z>=20       (12.0-75.0 MeV/n)
L33:    electrons   (0.3-1.0 MeV)
L34_38  single detector counting rates

```

Units: (/cm<sup>2</sup>/s/sr/MeV/nucleon)

Time Resolution: 10 minutes

### Notes:

1. Rate channel L1 (which nominally responds to protons in the energy range 0.9-1.2 MeV) is derived from a single-detector measurement, and as such is sensitive to penetrating particles which lose part of their energy in the detector. The background contribution depends on the energy spectrum of the incident particle population, being negligible for (differential) energy spectral slopes of -3.5 or steeper, increasing to 80% of the total counts for a slope of -1.0 or harder.
2. Rate channel L2 is derived from a single detector measurement, and the nominal energy response to protons (1.2-3.0 MeV) is approximate.

3. Rate channel L21 (which nominally responds to protons in the energy range 9-19 MeV) is also sensitive to higher-energy particles which lose part of their energy in the telescope structure. As in the case of L1, the background contribution depends on the energy spectrum of the incident particle population, being negligible for (differential) energy spectral slopes of -2.0 or steeper, increasing to 80% of the total counts for a slope of +0.75 or harder.
4. Rate channel L22 is derived from a single detector measurement, and the nominal energy response to alpha particles (1.0-5.0 MeV/n) is approximate.
5. Rate channel L25 (which nominally responds to alpha particles in the energy range 8.4-19.0 MeV/n) is also sensitive to higher energy particles that lose part of their energy in the telescope structure. As in the case of L21, the background contribution depends on the energy spectrum of the incident particle population (negligible for differential energy spectral slopes of -2.0 or steeper).
6. Rate channel L26 (L27) suffers from background due to pulse pile-up for proton fluxes in L2 greater than 10 (30) protons/cm<sup>2</sup>/s/sr/MeV.
7. The energy ranges for rate channels L28 – L32 are approximate (species dependent).
8. The energy range for the electron rate channel L33 is approximate (L33 suffers from background from the RTG and GCR).
9. Rate channel L34 includes all particles depositing energy greater than the minimum discriminator level (D1).  
Rate channel L35 includes all particles depositing energy greater than the minimum discriminator level (D2).  
Rate channel L36 includes all particles depositing energy greater than the minimum discriminator level (D3).  
Rate channel L37 includes all particles depositing energy greater than the minimum discriminator level (D4).  
Rate channel L38 includes all particles depositing energy greater than the minimum discriminator level (D5).

## **8.2 PHA-derived H and He fluxes**

### Parameter List:

IYEAR: year

IDOY: day of year

IHOURL: hour of day

E1: 2-4 MeV Protons (/cm<sup>2</sup>/s/sr/MeV)

EE1: Error in E1 "

E2: 4-6 MeV Protons (/cm<sup>2</sup>/s/sr/MeV)

EE2: Error in E2 "

E3: 6-8 MeV Protons (/cm<sup>2</sup>/s/sr/MeV)

EE3: Error in E3 "

E4: 8-16 MeV Protons (/cm<sup>2</sup>/s/sr/MeV)

EE4: Error in E4 "

E5: 16-20 MeV Protons (/cm<sup>2</sup>/s/sr/MeV)

EE5: Error in E5 "

H1: 4-6 MeV/n Helium (/cm<sup>2</sup>/s/sr/MeV)

EH1: Error in H1 "

H2: 6-9 MeV/n Helium (/cm<sup>2</sup>/s/sr/MeV)  
EH2: Error in H2 "  
H3: 11-20 MeV/n Helium (/cm<sup>2</sup>/s/sr/MeV)  
EH3: Error in H3 "

Time Resolution: daily

### **8.3 PHA-derived O, N and Ne fluxes**

IYEAR: year  
IDOY: day of year  
IHOUR: hour of day  
O1: 4-8 MeV/n Oxygen (/cm<sup>2</sup>/s/sr/MeV/n)  
EO1: Error in O1 "  
O2: 8-12 MeV/n Oxygen (/cm<sup>2</sup>/s/sr/MeV/n)  
EO2: Error in O2 "  
O3: 12-16 MeV/n Oxygen (/cm<sup>2</sup>/s/sr/MeV/n)  
EO3: Error in O3 "  
O4: 16-20 MeV/n Oxygen (/cm<sup>2</sup>/s/sr/MeV/n)  
EO4: Error in O4 "  
N1: 4-7 MeV/n Nitrogen (/cm<sup>2</sup>/s/sr/MeV/n)  
EN1: Error in N1 "  
N2: 8-20 MeV/n Nitrogen (/cm<sup>2</sup>/s/sr/MeV/n)  
EN2: Error in N2 "  
Ne1: 4-8 MeV/n Neon (/cm<sup>2</sup>/s/sr/MeV/n)  
ENe1: Error in Ne1 "  
Ne2: 9-30 MeV/n Neon (/cm<sup>2</sup>/s/sr/MeV/n)  
ENe2: Error in Ne2 "

Time Resolution: 20 days

### **8.4 Yearly PHA plots**

Each plot provides a qualitative representation of pulse height measurements made by the COSPIN/LET instrument over a complete year, indicating periods of significant heavy ion fluxes. The plots are constructed using the charge histograms derived from the PHA analysis of the D1 and D2 detectors of the LET instrument. The number of PHA events in a charge bin (having a width of 0.01 of a unit of atomic number) is accumulated over a period of a day, colour coded and plotted as a filled box.

During periods of enhanced particle fluxes, well defined peaks can be seen for typical solar energetic nuclei. Persistent horizontal banding for certain ions (for example O, N and Ne) indicates the presence of anomalous cosmic ray (ACR) populations.

Note that the number of PHA events for a given species shown in the plot does not necessarily reflect its true abundance. This is due to the priority system used by the instrument that maximizes the collecting efficiency of rarer ions. Further normalization is required to produce accurate composition ratios (for example, p/He and He/O). Note also that the majority of events that appear in the region between He and C (i.e., Li, Be, B) are due to background effects in the instrument.

## **LET Publications**

The following is a chronological list of publications describing the Low Energy Telescope, the various calibrations, and key scientific results.

- Marsden, R.G., J. Henrion, The prototype low-energy telescope system for the international solar polar COSPIN experiment, Report ESA STR-202, 1979.
- Kamermans, R., J. Henrion, R.G. Marsden, T.R. Sanderson, K.-P. Wenzel, Element and Isotope Separation for a Heavy Ion Cosmic Ray Telescope with Large Geometrical Factor, Nucl. Instr. and Meth., 171, 87, 1980.
- LeBorgne, J.F., J. Henrion, R.G. Marsden, T.R. Sanderson, K.-P. Wenzel, Accelerator calibration of the Low Energy Telescope of the International Solar Polar Mission COSPIN Experiment, Report ESA STM-224, 1981.
- Marsden, R.G., J. Henrion, T.R. Sanderson, K.-P. Wenzel, N. de Bray, H.P. Blok, Calibration of a Space-Borne Charged Particle Telescope Using Protons in the Energy Range 0.4 To 20 MeV, Nucl. Instr. and Meth., 221, 619, 1984.
- Marsden, R.G. et al., The Phobos Low Energy Telescope Charged Particle Experiment, Nucl. Instr. and Meth., 290, 211, 1990.
- Marsden, R.G., T. R. Sanderson, A. M. Heras, K.-P. Wenzel, Composition Signatures in SEP events: Initial Results from the COSPIN LET Experiment on Ulysses, Solar Wind Seven, Proc. 3rd COSPAR Colloq., Goslar, Germany, E. Marsch, R. Schwenn, eds., 375, 1992.
- Sanderson, T.R., R.G. Marsden, A.M. Heras, K.-P. Wenzel, J.D. Anglin, A. Balogh, R. Forsyth, Ulysses Particle Observations of the March 1991 Solar Flare Events, Geophys. Res. Lett., 19, 1263, 1992.
- Marsden, R.G., T.R. Sanderson, K.-P. Wenzel, S.J. Bame, COSPIN LET Observations of Recurrent Energetic Particle Events During the In-Ecliptic Phase of the Ulysses Mission, Adv. Space Res., 13, (6)95, 1993.
- Sanderson, T. R., R.G. Marsden, K.-P. Wenzel, A. Balogh, R.J. Forsyth, B.E. Goldstein, Ulysses High-Latitude Observations of Ions Accelerated by Co-rotating Interaction Regions, Geophys. Res. Lett., 21, 1113, 1994.
- Bothmer, V., R.G. Marsden, T.R. Sanderson, K.J. Trattner, K.-P. Wenzel, A. Balogh, R.J. Forsyth, B.E. Goldstein, The Ulysses South Polar Pass: Transient Fluxes of Energetic Ions, Geophys. Res. Lett., 22, 3369, 1995.
- Sanderson, T.R., R.G. Marsden, K.-P. Wenzel, A. Balogh, R.J. Forsyth, B.E. Goldstein, High-Latitude Observations of Energetic Ions During the First Ulysses Polar Pass, Space Sci. Rev., 72, 291, 1995.
- Sanderson, T.R., V. Bothmer, R.G. Marsden, K.J. Trattner, K.-P. Wenzel, A. Balogh, R.J. Forsyth, B.E. Goldstein, The Ulysses South Polar Pass: Energetic Ion Observations, Geophys. Res. Lett., 22, 3357, 1995.
- Trattner, K.J., R.G. Marsden, T.R. Sanderson, K.-P. Wenzel, The Evolution of the Anomalous Component of Cosmic Rays During the Ulysses Mission: COSPIN/LET Observations, Space Sci. Rev., 72, 431, 1995.

- Trattner, K.J., R.G. Marsden, T.R. Sanderson, K.-P. Wenzel, B. Klecker, D. Hovestadt, The Anomalous Component of Cosmic Rays: Oxygen Latitudinal Gradient, *Geophys. Res. Lett.*, 22, 337, 1995.
- Trattner, K.J., R.G. Marsden, T.R. Sanderson, K.-P. Wenzel, The Ulysses South Polar Pass: The Anomalous Component of Cosmic Rays, *Geophys. Res. Lett.*, 22, 3349, 1995.
- Trattner, K.J., R.G. Marsden, T.R. Sanderson, K.-P. Wenzel, B. Klecker, D. Hovestadt, The Latitudinal Gradient of Anomalous Cosmic Rays: Ulysses Observations, *Proc. 24th ICRC, Rome*, 4, 760, 1995.
- Bothmer, V., R.G. Marsden, T.R. Sanderson, K.J. Trattner, K.-P. Wenzel, A. Balogh, R.J. Forsyth, B.E. Goldstein, Y. Uchida, H. Hudson, Energetic Particles and Coronal Mass Ejections in the High Latitude Heliosphere: Ulysses-LET Observations, in *Proc. of Solar Wind Eight*, D. Winterhalter, J. Gosling, S. Habbal, W. Kurth, M. Neugebauer (Eds.), *AIP Conf. Proc.* 382, 445, 1996.
- Bothmer V., Desai M.I., Marsden R.G., Sanderson T.R., Trattner K.J., Wenzel K.-P., Gosling J.T., Balogh A., Forsyth R.J., Goldstein B.E., Ulysses Observations of Open and Closed Magnetic Field Lines within a Coronal Mass Ejection, *Astron. Astrophys.*, 316, 493, 1996.
- Sanderson, T.R., R.G. Marsden, V. Bothmer, K.J. Trattner, K.-P. Wenzel, A. Balogh, R.J. Forsyth, B.E. Goldstein, Ulysses Observations of Energetic Ions Over the South Pole of the Sun, in *Proc. of Solar Wind Eight*, D. Winterhalter, J. Gosling, S. Habbal, W. Kurth, M. Neugebauer (Eds.), *AIP Conf. Proc.* 382, 411, 1996.
- Trattner K.J., Marsden R.G., Bothmer V., Sanderson T.R., Wenzel K.-P., Klecker B., Hovestadt D., Ulysses COSPIN/LET: Latitudinal Gradients of Anomalous Cosmic Ray O, N and Ne, *Astron. Astrophys.*, 316, 519, 1996.
- Desai, M.I., R.G. Marsden, T.R. Sanderson, A. Balogh, R.J. Forsyth, J.T. Gosling, Particle Acceleration at Corotating Reverse Shocks in the Southern Heliosphere: Ulysses Results, *Geophys. Res. Lett.*, 24, 1155, 1997.
- Marsden, R.G., M.I. Desai, T.R. Sanderson, R.J. Forsyth, J.T. Gosling, Effects of the 5 October 1996 CME at 4.4 AU: Ulysses Observations, *Proc. 25th ICRC, Durban*, 1, 337, 1997.
- Trattner, K.J., R.G. Marsden, T.R. Sanderson, The Ulysses North Polar Pass: Latitudinal gradients of anomalous cosmic ray O, N and Ne, *Geophys. Res. Lett.*, 24, 1719, 1997.
- Desai, M.I., V. Bothmer, R.G. Marsden, T.R. Sanderson, A. Balogh, R.J. Forsyth, B.E. Goldstein, Acceleration of energetic ions ( $\sim 1$  MeV) in corotating interaction regions, *Adv. Space Res.*, 21, 555, 1998.
- Desai, M.I., R.G. Marsden, T.R. Sanderson, A. Balogh, R.J. Forsyth, J.T. Gosling, Particle acceleration at corotating interaction regions in the three-dimensional heliosphere, *J. Geophys. Res.*, 103, 2003, 1998.
- Lario, D., R.G. Marsden, T.R. Sanderson, M. Maksimovic, A. Balogh, R.J. Forsyth, N. Lin, R.P. Lepping, J.T. Gosling, Ulysses and WIND particle observations of the November 1997 solar events, *Geophys. Res. Lett.*, 25, 3469, 1998.

- Desai, M.I., R.G. Marsden, T.R. Sanderson, D. Lario, E.C. Roelof, G.M. Simnett, J.T. Gosling, A. Balogh, R. Forsyth, Energy spectra of 50-keV to 20-MeV protons accelerated at corotating interaction regions at Ulysses, *J. Geophys. Res.*, 104, 6705, 1999.
- Lario, D., R.G. Marsden, T.R. Sanderson, M. Maksimovic, A. Balogh, R.J. Forsyth, S. Dalla, R.P. Lin, Solar Energetic Particle Events in the Rising Phase of Solar Cycle 23: Observations at 1 and 5 AU, *Proc. 26th Int'l Cosmic Ray Conf. (Salt Lake City, Utah)*, 6, 540, 1999.
- Marsden, R.G., D. Lario, T.R. Sanderson, M. Maksimovic, A. Balogh, S. Dalla, R.J. Forsyth, On the energetic particle fluxes at 5AU associated with the April/May 1998 solar activity: Ulysses observations, in *Solar Wind Nine*, S.R. Habbal, R. Esser, J.V. Hollweg, P.A. Isenberg (Eds.), *AIP Conf. Proc.* 471, 609, 1999.
- Marsden, R.G., T.R. Sanderson, C. Tranquille, K.J. Trattner, A. Anttila, J. Torsti, On the gradients of ACR oxygen at intermediate heliocentric distances: Ulysses/SOHO results, *Adv. Space Res.*, 23(3), 531, 1999.
- Sanderson, T.R., D. Lario, M. Maksimovic, R.G. Marsden, C. Tranquille, A. Balogh, R.J. Forsyth, B.E. Goldstein, Current sheet control of recurrent particle increases at 4-5 AU, *Geophys. Res. Lett.*, 26, 1785, 1999.
- Lario, D., R.G. Marsden, T.R. Sanderson, M. Maksimovic, B. Sanahuja, A. Balogh, R.J. Forsyth, R.P. Lin, J.T. Gosling, Energetic proton observations at 1 and 5 AU 1. January-September 1997, *J. Geophys. Res.*, 105, 18235, 2000.
- Lario, D., R.G. Marsden, T.R. Sanderson, M. Maksimovic, B. Sanahuja, S.P. Plunkett, A. Balogh, R.J. Forsyth, R.P. Lin, J.T. Gosling, Energetic proton observations at 1 and 5 AU 2. Rising phase of the solar cycle 23, *J. Geophys. Res.*, 105, 18251, 2000.
- Sanderson, T.R., G. Erdos, A. Balogh, R.J. Forsyth, R.G. Marsden, J.T. Gosling, J.L. Phillips, C. Tranquille, The effect of magnetic discontinuities on the propagation of energetic particles: Ulysses observations of the onset of the march 1991 solar particle event, *J. Geophys. Res.*, 105, 18275, 2000.
- Heber, B., Keppler, E., Marsden, R.G., Tranquille, C., Blake, B., Fränz, M., The Evolution of the Anomalous Cosmic Ray Oxygen Spectra From 1995 to 1998: Ulysses Observations, *Space Sci. Rev.*, 97, 363, 2001.
- Hofer, M.Y., Marsden, R.G., Sanderson, T.R., Tranquille, C., Moullard, O., Cosmic ray and solar particle composition measurements in the southern solar polar region, *Proc. of ICRC 2001*, 8, 3116, 2001.
- Marsden, R.G., Sanderson, T.R., Tranquille, C., Hofer, M.Y., Moullard, O., Forsyth, R.J., The Ulysses Fast Latitude Scan at Solar Maximum: COSPIN/LET energetic particle observations, *Proc. of ICRC 2001*, 8, 3310, 2001.
- Moullard, O., Marsden, R.G., Sanderson, T.R., Tranquille, C., Forsyth, R.J., Goldstein, B.E., Energetic Ions Observed at Low to High Latitudes in the Southern Heliosphere during Declining and Rising Solar Activity, *Space Sci. Rev.*, 97, 289, 2001.
- Sanderson, T.R., Marsden, R.G., Tranquille, C., Balogh, A., Forsyth, R.J., Goldstein, B.E., Gosling, J.T., Harvey, K.L., The influence of the Sun's magnetic field on energetic particles at high heliospheric latitudes, *Geophys. Res. Lett.*, 28, 4525, 2001.

- Hofer, M.Y., R.G. Marsden, T.R. Sanderson, C. Tranquille, Composition measurements above the southern solar polar region around the solar activity maximum by the Ulysses COSPIN/LET instrument, *Geophys. Res. Lett.*, 29(16), 1793, 10.1029/2002GL014944, 2002.
- Hofer, M.Y., R.G. Marsden, T.R. Sanderson, C. Tranquille, Composition measurements over the solar poles close to solar maximum – Ulysses COSPIN/LET observations, 10th International Conference on Solar Wind, M. Velli, R. Bruno, F. Malara (Eds.), *AIP Conf. Proc.* 679, 183, 2003.
- Hofer, M.Y., R.G. Marsden, T.R. Sanderson, C. Tranquille, From the South to the North Pole and towards the ecliptic –Ulysses COSPIN/LET composition measurements, *Ann. Geophysicae*, 21, 1383, 2003.
- Hofer, M.Y., R.G. Marsden, T.R. Sanderson, C. Tranquille, R.J. Forsyth, Transition to solar minimum at high solar latitudes: Energetic particles from corotating interaction regions, *Geophys. Res. Lett.*, 30(19), 8034, 10.1029/2003GL1017138, 2003.
- Sanderson, T.R., R.G. Marsden, C. Tranquille, S. Dalla, R.J. Forsyth, J.T. Gosling, R.B. McKibben, Propagation of energetic particles in the high-latitude high-speed solar wind, *Geophys. Res. Lett.*, 30(19), 8036, 10.1029/2003GL017306, 2003.
- Tranquille, C., R.G. Marsden, T.R. Sanderson, M.Y. Hofer, A survey of 3He enhancements at 2-20 MeV/nucleon: Ulysses COSPIN/LET observations, *Ann. Geophysicae*, 21, 1245, 2003.
- Malandraki, O.E., R. G. Marsden, C. Tranquille, R. J. Forsyth, H. A. Elliott, L. J. Lanzerotti, Energetic particle observations by Ulysses during the declining phase of solar cycle 23, *J. Geophys. Res.*, 112, A06111, 10.1029/2006JA011876, 2007.
- Malandraki, O.E., R.G. Marsden, C. Tranquille, R.J. Forsyth, H.A. Elliott, L.J. Lanzerotti, Energetic particle measurements from the Ulysses/COSPIN/LET instrument obtained during the August/September 2005 events, *Ann. Geophysicae*, 26, 1029, 2008.
- Cummings, A.C., C. Tranquille, R.G. Marsden, R.A. Mewaldt, E.C. Stone, Radial and latitudinal gradients of anomalous cosmic ray oxygen in the inner heliosphere, *Geophys. Res. Lett.*, 36, L18103, 10.1029/2009GL039851, 2009.
- Malandraki, O.E., R.G. Marsden, D. Lario, C. Tranquille et al., Energetic particle observations and propagation in the three-dimensional heliosphere during the December 2006 events, *ApJ*, 704, 469, 2009.
- Tylka, A.J., O.E. Malandraki, G. Dorrian, Y-K. Ko, R.G. Marsden, C.K. Ng, C. Tranquille, Initial Fe/O Enhancements in Large, Gradual, Solar Energetic Particle Events: Observations from *Wind* and *Ulysses*, *Solar Phys.*, in press, 2012.

## Appendices

The following documents are included as appendices to this Handbook:

- Marsden, R.G., J. Henrion, The prototype low-energy telescope system for the international solar polar COSPIN experiment, Report ESA STR-202, 1979.
- Kamermans, R., J. Henrion, R.G. Marsden, T.R. Sanderson, K.-P. Wenzel, Element and Isotope Separation for a Heavy Ion Cosmic Ray Telescope with Large Geometrical Factor, Nucl. Instr. and Meth., 171, 87, 1980.
- LeBorgne, J.F., J. Henrion, R.G. Marsden, T.R. Sanderson, K.-P. Wenzel, Accelerator calibration of the Low Energy Telescope of the International Solar Polar Mission COSPIN Experiment, Report ESA STM-224, 1981.
- Marsden, R.G., J. Henrion, T.R. Sanderson, K.-P. Wenzel, N. de Bray, H.P. Blok, Calibration of a Space-Borne Charged Particle Telescope Using Protons in the Energy Range 0.4 To 20 MeV, Nucl. Instr. and Meth., 221, 619, 1984.
- Marsden, R.G. et al., The Phobos Low Energy Telescope Charged Particle Experiment, Nucl. Instr. and Meth., 290, 211, 1990.
- Marsden, R.G., LET Calibration Document, 1990.
- Henrion, J., LET Response to high fluxes, Technical Report, 1992.

## ***List of Tables***

Table 1.1	Characteristics of the detectors and aperture foils installed in the flight model LET.
Table 1.2	COSPIN Low Energy Telescope Data Channel Summary.
Table 1.3	Discriminator logic equations for LET counting rate channels.
Table 2.1	Sensitivities and dynamic ranges for LET amplifier chains.
Table 2.2	Nominal discriminator thresholds.
Table 2.3	LET Particle Identifier nominal parameters*.
Table 2.4	Priority System look-up table.
Table 3.1	Resource breakdown for SIM-1 (ATs, LET, DPU).
Table 4.1a	Y to N look-up table for 19-bit mode.
Table 4.1b	Y to N lookup table for 27-bit mode.
Table 4.2	LET PHA word structure.
Table 4.3	Bit assignment for status word L45.
Table 4.4	Bit assignment for status word L46.
Table 4.5	Timing reconstruction for channels having 32 s time resolution.
Table 4.6	Timing reconstruction for channels having 128 s time resolution.
Table 4.7	Timing reconstruction for PHA words. PHA events are read out once.
Table 4.8	LET Analogue data channels.
Table 4.9	LET Monitor Parameters.
Table 4.10	LET Memory Load Command bit assignment (LET command word A).
Table 4.11	LET Memory Load Command bit assignment (LET command word B).
Table 5.1	LET Accelerator calibration history.
Table 6.1	Energy-loss look-up table for the LET aperture foils (0.9 mg/cm <sup>2</sup> Ti + 1.0 mg/cm <sup>2</sup> Kapton).

## **List of Figures**

- Fig. 1.1 Block diagram of the Low Energy Telescope (LET).
- Fig. 1.2 (top) Cross-section of the LET sensor, showing the detectors and aperture foils; (bottom left) LET sensor assembly; (bottom right) Key elements of the LET sensor (PMT, detectors, tube structure).
- Fig. 2.1 Nominal discriminator threshold levels for detectors D1, D2 and D3, together with the energy loss characteristics for protons and alpha particles.
- Fig. 2.2 Particle Identifier discriminator boundaries defining the charge groups in the D1-D2 range (particles stopping in detector D2).
- Fig. 2.3 Particle Identifier discriminator boundaries defining charge groups in the D2-D3 range (particles stopping in detector D3).
- Fig. 3.1 LET telescope: mechanical configuration, showing the internal structure and the photomultiplier tube mounting.
- Fig. 3.2 LET telescope: internal structure in detail.
- Fig. 3.3 Let telescope: cross-section of the plastic scintillator anti-coincidence shield, including key dimensions in mm.
- Fig. 3.4 LET telescope: internal tube structure, with key dimensions in mm.
- Fig. 3.5 SIM-1 package, with the Anisotropy Telescopes (top), Low Energy Telescope (middle) and Data Processing Unit (bottom).
- Fig. 3.6a Front view of SIM-1 package with LET in the centre (dimensions in mm).
- Fig. 3.6b Side view of SIM-1 package with LET in the centre (dimensions in mm).
- Fig. 5.1 D1-D2 response measured at the GANIL accelerator in Nov 1988.
- Fig. 5.2 D1-D2-D3 response measured at the GANIL accelerator in Nov 1988.
- Fig. 5.3 LET detector D1 linearity check.
- Fig. 5.4 LET detector D2 linearity check.
- Fig. 5.5 LET detector D3 linearity check.
- Fig. 6.1a Event “tracks” for Helium ions derived from flight data in the D1-D2 range, together with the reference track used in the PHA analysis routines (upper panel), and the corresponding charge histogram (lower panel).
- Fig. 6.1b As for Fig. 6.1a, but for the D2-D3 range.
- Fig. 6.2a Event “tracks” for Oxygen ions derived from flight data in the D1-D2 range, together with the reference track used in the PHA analysis routines (upper panel), and the corresponding charge histogram (lower panel).
- Fig. 6.2b As for Fig. 6.2a, but for the D2-D3 range.

- Fig. 6.3a Event “tracks” for Silicon ions derived from flight data in the D1-D2 range, together with the reference track used in the PHA analysis routines (upper panel), and the corresponding charge histogram (lower panel).
- Fig. 6.3b As for Fig. 6.3a, but for the D2-D3 range.
- Fig. 6.4a Event “tracks” for Iron ions derived from flight data in the D1-D2 range, together with the reference track used in the PHA analysis routines (upper panel), and the corresponding charge histogram (lower panel).
- Fig. 6.4b As for Fig. 6.4a, but for the D2-D3 range.
- Fig. 6.5 Constant range lines plotted on a typical dE vs. residual E diagram.
- Fig. 6.6 Illustration of the LET charge interpolation algorithm using the reference tracks for Z1 and Z2 and the constant range approximation.
- Fig. 7.1 LET counting rate linearity curves for channels L1, L2 and L22.

Table 1.1 Characteristics of the detectors and aperture foils installed in the flight model LET. (Note that there is some uncertainty in precise thicknesses of the two foils.)

Detector	Type		Thickness		Area (cm <sup>2</sup> )
			( $\mu\text{m}$ )	(mg/cm <sup>2</sup> )	
D1	Si surface barrier	Ortec 600-30 S/N 22-235B	32.2	7.503	6.0
D2	Si surface barrier	Ortec 600-100 S/N 20-663C	95.9	22.345	6.0
D3	Li-drifted	LBL 1000-2000 S/N 4469	2054	478.6	10.0
D4	Li-drifted	LBL 1250-2000 S/N 4506	2000	466.0	12.5
D5	Plastic scintillator / PMT	RCA C70102E 4F4	-	-	-
Outer foil	Aluminised Kapton		~8	~1.0	
Inner foil	Titanium		~2	~0.9	

Table 1.2 COSPIN Low Energy Telescope Data Channel Summary.

<i>Channel</i>	<i>Event Code</i>		<i>Measurement</i>		<i>GF</i> ( $cm^2 sr$ )	<i>Time Res.</i> ( <i>sec</i> )	<i>Synch.</i>	<i>Comp. Mode</i> <sup>2</sup>
L1/P1	0	proton	0.9 – 1.2	MeV	9.1	32	Format	2
L2/P2	1		1.2 – 3.0		9.1	32	Format	2
L3/P3	3		1.8 – 3.8		0.58	32	Format	2
L4-L11 /P3S <sup>1</sup>	-		1.8 – 3.8		0.58	24/36	Spin	1
L12/P4	4		3.8 – 8.0		0.58	32	Format	2
L13-L20 /P4S <sup>1</sup>	-		3.8 – 8.0		0.58	24/36	Spin	1
L21/P5	5		9.0 – 19.0		0.58	32	Format	2
L22/A1	2	alpha	1.0 – 5.0	MeV/n	9.1	32	Format	1
L23/A2	6		1.9 – 4.0		0.58	32	Format	1
L24/A3	7		4.0 – 9.0		0.58	32	Format	1
L25/A4	8		9.0 – 19.0		0.58	32	Format	1
L26/H1	9	Li,Be,B	2.3 – 5.2		0.58	128	Format	1
L27/H2	10		5.2 – 26.0		0.58	128	Format	1
L28/H3	11	C,N,O	3.2 – 7.5		0.58	128	Format	1
L29/H4	12		7.5 – 39.0		0.58	128	Format	1
L30/H5	13	Z ≥ 10	3.9 – 9.5		0.58	128	Format	1
L31/H6	14		9.5 – 50		0.58	128	Format	1
L32/H7	15	Z ≥ 20	12 – 75		0.58	128	Format	1
L33/E1	-	electron	0.35 – 1.5	MeV	-	128	Format	1
L34/S1			D1 singles			128	Format	1
L35/S2			D2 singles			128	Format	1
L36/S3			D3 singles			128	Format	1
L37/S4			D4 singles			128	Format	1
L38/S5			D5 singles			128	Format	1
PHA			Pulse heights/flags			1	Format	-
			LET status			32	Format	-

<sup>1</sup> 8-sector rates

<sup>2</sup> Data compression modes: 1 = 19-to-8 bits; 2 = 27-to-12 bits

Table 1.3 Discriminator logic equations for LET counting rate channels.

<i>Channel</i>		<i>Logic equation</i>	<i>Channel</i>		<i>Logic equation</i>
L1	LP1	D1A. <u>D1B</u> . <u>D2A</u> . <u>D4</u> . <u>D5</u>	L26	LH1	M2. <u>I2</u> . <u>I3</u>
L2	LP2	D1B. <u>D1C</u> . <u>D2A</u> . <u>D4</u> . <u>D5</u>	L27	LH2	M3. <u>I6</u> . <u>I7</u>
L3	LP3	M2. <u>I1</u>	L28	LH3	M2. <u>I3</u> . <u>I4</u>
L4-L11		M2. <u>I1</u>	L29	LH4	M3. <u>I7</u> . <u>I8</u>
L12	LP4	M3. <u>D2B</u> . <u>D3B</u> . <u>I5</u>	L30	LH5	M2. <u>I4</u>
L13-L20		M3. <u>D2B</u> . <u>D3B</u> . <u>I5</u>	L31	LH6	M3. <u>I8</u> . <u>I9</u>
L21	<u>LP5</u>	<u>D1A</u> . <u>D2A</u> . <u>D3B</u> . <u>D4</u> . <u>D5</u>	L32	LH7	M3. <u>I9</u>
L22	LA1	D1C. <u>D2A</u> . <u>D4</u> . <u>D5</u>	L33	LE1	<u>D1A</u> . <u>D3A</u> . <u>D4</u> . <u>D5</u>
L23	LA2	D1A. <u>D2B</u> . <u>D3A</u> . <u>D4</u> . <u>D5</u> . <u>I1</u> . <u>I2</u>	L34	D1 singles	<u>D1A</u> . <u>D4</u> . <u>D5</u>
L24	LA3	M3. <u>D3C</u> . <u>I5</u> . <u>I6</u>	L35	D2 singles	<u>D2A</u> . <u>D4</u> . <u>D5</u>
L25	LA4	D1A. <u>D2A</u> . <u>D3C</u> . <u>D4</u> . <u>D5</u> . <u>I5</u> . <u>I6</u>	L36	D3 singles	<u>D3A</u> . <u>D4</u> . <u>D5</u>
			L37	D4 singles	D4
			L38	D5 singles	D5

D1A.D1B  $\equiv$  D1A ANDNOT D1B etc. M2  $\equiv$  D1A.D2A.D3A.D4.D5 M3  $\equiv$  D1A.D2A.D3A.D4.D5  
 See Table 2.\* for definitions of discriminator functions I1 – I9

Table 2.1 Sensitivities and dynamic ranges for LET amplifier chains.

<i>Detector</i>	<i>Nominal CSA output sensitivity</i>	<i>Dynamic ranges</i>	<i>PHA conversion factors<sup>1)</sup></i> $E(\text{MeV}) = \alpha n^\beta$	
			$\alpha$	$\beta$
D1 (32.2 $\mu\text{m}$ )	20 mV/MeV	0 – 32 MeV 0 – 205	0.0318 MeV/ch 0.2331	0.98 0.98
D2 (95.9 $\mu\text{m}$ )	6.25	0 – 32 0 – 640	0.0381 0.7403	0.98 0.98
D3 (2054 $\mu\text{m}$ )	1.0	0 – 128 0 – 4096	0.1437 4.150	0.98 0.99
D4 (2000 $\mu\text{m}$ )	20	-	-	-

1) Based on flight data evaluation, where n is the PHA channel number

Table 2.2 Nominal discriminator thresholds.

<i>Discriminator</i>	<i>Threshold</i>	<i>Discriminator</i>	<i>Threshold</i>
DD1A	300 keV	DD3A	300 keV
DD1B	900	DD3B	6500
DD1C	2100	DD3C	28 MeV
DD1S	32 MeV	DD3S	128
DD2A	300 keV	DD4	300 keV
DD2B	3400		
DD2S	32 MeV		

Table 2.3 LET Particle Identifier nominal parameters\*.

<i>D1 – D2 Events</i>	<i>Charge range</i>	<i>D2 – D3 Events</i>	<i>Charge range</i>
I1: $E1 + 0.27 \cdot E2 > 3.3 \text{ MeV}$	$Z \geq 2$	I5: $E2 \cdot (E3 + 7) > 53 \text{ MeV}^2$	$Z \geq 2$
I2: $E1 + 0.27 \cdot E2 > 8.5$	$Z \geq 3$	I6: $E2 \cdot (E3 + 18) > 355$	$Z \geq 3$
I3: $E1 + 0.27 \cdot E2 > 24$	$Z \geq 6$	I7: $E2 \cdot (E3 + 67) > 3900$	$Z \geq 6$
I4: $E1 + 0.27 \cdot E2 > 52$	$Z \geq 10$	I8: $E2 \cdot (E3 + 161) > 20342$	$Z \geq 10$
		I9: $E2 + 0.15 \cdot E3 > 375 \text{ MeV}$	$Z > 20$

\* Actual values used in the flight instrument may differ slightly.



Table 3.1 Resource breakdown for SIM-1 (ATs, LET, DPU).

<i>SIM-1 Unit</i>	<i>Mass (kg)</i>	<i>Power (W)</i>	<i>Telemetry fraction<sup>1)</sup></i>
ATs	1.23	5.1 (combined)	0.162
LET	2.10		0.325
DPU	1.69		0.030 <sup>2)</sup>

1) COSPIN telemetry total = 5176 8-bit words per instrument cycle (256 S/C frames).

2) Contains spin counters, CPU status and synch words.

Table 4.1a Y to N look-up table for 19-bit mode.

<b>Y</b>	<b>N</b>	<b>Y</b>	<b>N</b>	<b>Y</b>	<b>N</b>
0	0	6	14	11	9
1	11	7	13	12	4
2	10	8	8	13	7
3	1	9	3	14	6
4	12	10	2	15	5
5	0				

Table 4.1b Y to N lookup table for 27-bit mode.

<b>Y</b>	<b>N</b>	<b>Y</b>	<b>N</b>	<b>Y</b>	<b>N</b>	<b>Y</b>	<b>N</b>
0	13	8	21	16	XX	24	5
1	24	9	16	17	8	25	0
2	23	10	15	18	7	26	XX
3	14	11	22	19	XX	27	6
4	25	12	17	20	9	28	1
5	12	13	20	21	XX	29	4
6	11	14	19	22	27	30	3
7	26	15	18	23	10	31	2

Table 4.2 LET PHA word structure.

Bit																				Bit assignment			
MSB																LSB							
43	42	-	40	39	-	36	35	34	33	32	31	30	29	-	20	19	-	10	9	-	0		
0																							CAL-OFF
1																							CAL-ON
	0																						SECTOR 0-7 (3 bits)
	1	\																					
			0																				
			1																				EVENT CODE 0-15 (4 bits)
				0																			
				1	\																		
						0																	PRIORITY OPERATE (L46, LSB=0)
						1																	
							0																
							1																GAIN3 LO
								0															GAIN2 HI
								1															GAIN2 LO
									0														GAIN1 HI
									1														GAIN1 LO
										0													D4 NOT TRIGGERED
										1													D4 TRIGGERED
											0												D5 NOT TRIGGERED
											1												D5 TRIGGERED
												0											EVENT INHIBITED D4+D5
												1											EVENT NOT IHIBITED D4+D5
																							PRIORITY TEST (L46, LSB=1)
							0																
							1																
								0															ROM bit 3
								1															
									0														ROM bit 2
									1														
										0													ROM bit 1
										1													
											0												PHA NOT START
											1												PHA START
												0											EVENT INHIBITED D4+D5
												1											EVENT NOT IHIBITED D4+D5
													0										PHA D3 MSB
													1	\									
															0								PHA D3 LSB
															1								
																0							PHA D2 MSB
																1	\						
																	0						PHA D2 LSB
																	1						
																		0					PHA D1 MSB
																		1	\				
																				0			PHA D1 LSB
																				1			

Table 4.3 Bit assignment for status word L45.

7	6	5	4	3	2	1	0	Status
0								PTA MSB = 0
1								PTA MSB = 1
	0							PTA bit 2 = 0
	1							PTA bit 2 = 1
		0						PTA bit 1 = 0
		1						PTA bit 1 = 1
			0					PTA LSB = 0
			1					PTA LSB = 1
				0				Mode 1
				1				Mode 2
					0			D1A on
					1			D1A off
						0		D2A on
						1		D2A off
							0	D3A on
							1	D3A off

Table 4.4 Bit assignment for status word L46.

7	6	5	4	3	2	1	0	Status
0								D1 on
1								D1 off
	0							D2 on
	1							D2 off
		0						D3 on
		1						D3 off
			0					D4 on
			1					D4 off
				0				D5 on
				1				D5 off
					0			PHA priority events
					1			PHA M2+M3+P5
						0		Priority table rotated
						1		Priority table fixed
							0	Priority operate
							1	Priority test

Table 4.5 Timing reconstruction for channels having 32 s time resolution.

Channel	Accumulation period (subformat no.)							
	0	1	2	3	4	5	6	7
L1, L45, L46	2	2	4	4	6	6	0I	0I
L2, L3, L12, L21	1	3	3	5	5	7	7	1I
L4-L11	2	3	4	5	6	7	0I	1I
L13-L20	1	2	3	4	5	6	7	0I
L22-L25	3	3	5	5	7	7	1I	1I

Table 4.6 Timing reconstruction for channels having 128 s time resolution.

Channel	Accumulation period (subformat no.)	
	0 - 3	4 - 7
L26-L29	6I	6I
L30-L32	4I	4I
L33-L35	2I	2I
L36-L38	0I	0I

Table 4.7 Timing reconstruction for PHA words. PHA events are read out once per S/C FRAME (i.e. nominally once per sec.)

FRAME	Accumulation period (subformat no.)							
	0	1	2	3	4	5	6	7
0 - 30	1	2	3	4	5	6	7	0I
31	2	3	4	5	6	7	0I	1I

Table 4.8 LET Analogue data channels.

MUX ADDR.	No.	CHANNEL FUNCTION	CONVERSION FORMULAE ( $V_{out}$ F.S. = 5.1 volts)			
0000	1	D1 current	$ID1 (\mu A) \approx 2 \times V_{out} \text{ (volts)}$			
0001	2	D2 current	$ID2 (\mu A) \approx 4 \times V_{out} \text{ (volts)}$			
0010	3	D3 current	$ID3 (\mu A) \approx 8 \times V_{out} \text{ (volts)}$			
0011	4	D4 current	$ID4 (\mu A) \approx 8 \times V_{out} \text{ (volts)}$			
0100	5	HV monitor	$HV \text{ (volts)} \approx 250 \times V_{out} \text{ (volts)}$			
0101	6	+15 V monitor	$V15 \text{ (volts)} \approx 4 \times V_{out} \text{ (volts)}$			
0110	7	+8.5 V monitor	$V8.5 \text{ (volts)} \approx 2 \times V_{out} \text{ (volts)}$			
0111	8	-6 V monitor	$V-6 \text{ (volts)} = +[1.833V_{out} - 12.5] \text{ (volts)}$			
1000	9	-15 V monitor	$V-15 \text{ (volts)} = +[2.667V_{out} - 1.667] \text{ (volts)}$			
1001	10	Temp. (LET)	$T(^{\circ}C)$	$V_{out} \text{ (volts)}$	$T(^{\circ}C)$	$V_{out} \text{ (volts)}$
			-40	4.70	+10	2.35
			-30	4.42	+20	1.80
			-20	4.08	+30	1.34
			-10	3.57	+40	0.97
			0	2.98	+50	0.70
1010	11	Temp. conv. 1	TBD			
1011	12	Temp. conv. 2	TBD			
1100 - 1111	13 - 16	Not used				

Table 4.9 LET Monitor Parameters.

CHANNEL No.	CHANNEL INFORMATION	CHANNEL No.	CHANNEL INFORMATION
H016	LET PHA 1-01	H043	LET CAL 32
H017	LET PHA 2-01	H044	LET L01 (LP1)
H018	LET PHA 3-01	H045	LET L03 (LP3)
H019	LET STATE -01	H046	LET L12 (LP4)
H020	LET EVENT-01	H047	LET L34 (LS1)
H021	LET SECTOR-01	H048	LET L35 (LS2)
H022	LET CAL 01	H049	LET L36 (LS3)
H023	LET PHA 1-02	H050	LET L37 (LS4)
H024	LET PHA 2-02	H051	LET L38 (LS5)
H025	LET PHA 3-02	H052	LET D1 CURRENT
H026	LET STATE -02	H053	LET D2 CURRENT
H027	LET EVENT-02	H054	LET D3 CURRENT
H028	LET SECTOR-02	H055	LET D4 CURRENT
H029	LET CAL 02	H056	LET HV
H030	LET PHA 1-31	H057	LET 15 V
H031	LET PHA 2-31	H058	LET 8.5 V
H032	LET PHA 3-31	H059	LET -6 V
H033	LET STATE -31	H060	LET -15 V
H034	LET EVENT-31	H061	LET TEMP EXP
H035	LET SECTOR-31	H062	LET TEMP S/C
H036	LET CAL 31	H063	LET S D123
H037	LET PHA 1-32	H064	LET S D45
H038	LET PHA 2-32	H065	LET S D123A
H039	LET PHA 3-32	H066	LET S PTA
H040	LET STATE -32	H067	LET S MODE
H041	LET EVENT-32	H068	LET S PRIORITY
H042	LET SECTOR-32	H069	LET S OP/ROT

Table 4.10 LET Memory Load Command bit assignment (LET command word A).

Bit assignment	MSB	Bit 2 <sup>n</sup>														LSB
	15	14	13	12	11	10	9	8	7	6	5	4	3	2	1	0
CAL OFF											0	0	1	1	0	1
CAL ON											1	0	1	1	0	1
MODE 1										0		0	1	1	0	1
MODE 2										1		0	1	1	0	1
HV ON									0			0	1	1	0	1
HV OFF									1			0	1	1	0	1
D1A ON								0				0	1	1	0	1
D1A OFF								1				0	1	1	0	1
D2A ON							0					0	1	1	0	1
D2A OFF							1					0	1	1	0	1
D3A ON						0						0	1	1	0	1
D3A OFF						1						0	1	1	0	1
D1 ON					0							0	1	1	0	1
D1 OFF					1							0	1	1	0	1
D2 ON				0								0	1	1	0	1
D2 OFF				1								0	1	1	0	1
D3 ON			0									0	1	1	0	1
D3 OFF			1									0	1	1	0	1
D4 ON		0										0	1	1	0	1
D4 OFF		1										0	1	1	0	1
D5 ON	0											0	1	1	0	1
D5 OFF	1											0	1	1	0	1
	WORD A											A	D=LET			

Table 4.11 LET Memory Load Command bit assignment (LET command word B).

Bit assignment	MSB	Bit 2 <sup>n</sup>														LSB					
	15	14	13	12	11	10	9	8	7	6	5	4	3	2	1	0					
Event inhib. by D4+D5											0	1	1	1	0	1					
Event not inhib. by D4+D5											1	1	1	1	0	1					
PHA prior.										0		1	1	1	0	1					
PHA M2M3P5										1		1	1	1	0	1					
PT rotated									0			1	1	1	0	1					
PT fixed									1			1	1	1	0	1					
PTA LSB								0				1	1	1	0	1					
								1				1	1	1	0	1					
PTA bit 2							0					1	1	1	0	1					
							1					1	1	1	0	1					
PTA bit 3						0						1	1	1	0	1					
						1						1	1	1	0	1					
PTA MSB					0							1	1	1	0	1					
					1							1	1	1	0	1					
Priority operate				0								1	1	1	0	1					
Priority test				1								1	1	1	0	1					
	NOT USED																1	1	1	0	1
	WORD B											B	D=LET								

Table 5.1 LET Accelerator calibration history.

<i>Date</i>	<i>Facility</i> <sup>1)</sup>	<i>Beam</i> <sup>2)</sup>	<i>Report/Paper</i>
1979 <sup>3)</sup>	VICKSI-HMI	Ne <sup>20</sup>	Kamermans et al., 1980
14-23 Apr 1981 <sup>4)</sup>	LBL Bevatron	Ne <sup>20</sup> Ar <sup>40</sup>	LeBorgne et al., 1981
28 Jul 1982 – 02 Aug 1982	LBL Bevatron	Si <sup>28</sup> Fe <sup>56</sup>	
17-20 May 1983 1-4 Apr 1984	VU Cyclotron MPK MP Tandem	p, H <sup>2</sup> , He <sup>4</sup> C <sup>12</sup>	Marsden et al., 1984
12-20 May 1984	LBL Bevatron	Ni <sup>58</sup> Si <sup>28</sup> Fe <sup>56</sup>	
25-26 Oct 1984 20-24 Nov 1988	VU Cyclotron GANIL	p, H <sup>2</sup> , He <sup>4</sup> Ar <sup>40</sup>	

Notes:

- 1) HMI: Hahn-Meitner Institut, Berlin; LBL: Lawrence Berkeley Lab; VU: Amsterdam Free University; MPK: Max-Planck-Institut fuer Kernphysik, Heidelberg; GANIL: Grand Accelérateur National d'Ions Lourds, Caen.
- 2) Primary beam types (LBL and MPK: separate runs; VU all species simultaneously).
- 3) LET prototype.
- 4) LET Engineering Model.

Table 6.1 Energy-loss look-up table for the LET aperture foils (Ti + Kapton).

ENERGY LOSS CALCULATIONS IN LET FOILS

Z = 1 A= 1									
Einstr(MeV/n):	1.00	1.50	2.00	2.50	3.00	3.50	4.00	4.50	
Ext(MeV/n):	1.44	1.84	2.27	2.73	3.22	3.69	4.16	4.66	
Z = 2 A= 4									
Einstr(MeV/n):	1.00	1.50	2.00	2.50	3.00	3.50	4.00	4.50	
Ext(MeV/n):	1.43	1.84	2.27	2.73	3.22	3.69	4.16	4.66	
Z = 3 A= 7									
Einstr(MeV/n):	1.00	1.50	2.00	2.50	3.00	3.50	4.00	4.50	
Ext(MeV/n):	1.52	1.92	2.35	2.79	3.27	3.74	4.20	4.70	
Z = 4 A= 9									
Einstr(MeV/n):	1.00	1.50	2.00	2.50	3.00	3.50	4.00	4.50	
Ext(MeV/n):	1.65	2.05	2.47	2.90	3.36	3.83	4.28	4.78	
Z = 5 A= 11									
Einstr(MeV/n):	1.00	1.50	2.00	2.50	3.00	3.50	4.00	4.50	
Ext(MeV/n):	1.76	2.15	2.57	3.00	3.45	3.92	4.36	4.86	
Z = 6 A= 12									
Einstr(MeV/n):	1.00	1.50	2.00	2.50	3.00	3.50	4.00	4.50	
Ext(MeV/n):	1.92	2.30	2.70	3.14	3.57	4.04	4.47	4.97	
Z = 7 A= 14									
Einstr(MeV/n):	1.00	1.50	2.00	2.50	3.00	3.50	4.00	4.50	
Ext(MeV/n):	2.01	2.39	2.78	3.22	3.64	4.10	4.53	5.03	
Z = 8 A= 16									
Einstr(MeV/n):	1.00	1.50	2.00	2.50	3.00	3.50	4.00	4.50	
Ext(MeV/n):	2.07	2.45	2.85	3.28	3.70	4.16	4.59	5.08	
Z = 9 A= 18									
Einstr(MeV/n):	1.00	1.50	2.00	2.50	3.00	3.50	4.00	4.50	
Ext(MeV/n):	2.12	2.50	2.90	3.34	3.76	4.22	4.65	5.14	
Z = 10 A= 20									
Einstr(MeV/n):	1.00	1.50	2.00	2.50	3.00	3.50	4.00	4.50	
Ext(MeV/n):	2.17	2.55	2.95	3.39	3.81	4.27	4.70	5.19	
Z = 11 A= 22									
Einstr(MeV/n):	1.00	1.50	2.00	2.50	3.00	3.50	4.00	4.50	
Ext(MeV/n):	2.21	2.59	2.99	3.43	3.85	4.31	4.74	5.23	
Z = 12 A= 24									
Einstr(MeV/n):	1.00	1.50	2.00	2.50	3.00	3.50	4.00	4.50	
Ext(MeV/n):	2.25	2.63	3.03	3.47	3.89	4.35	4.78	5.27	
Z = 13 A= 26									
Einstr(MeV/n):	1.00	1.50	2.00	2.50	3.00	3.50	4.00	4.50	
Ext(MeV/n):	2.29	2.67	3.07	3.51	3.93	4.39	4.82	5.31	
Z = 14 A= 28									
Einstr(MeV/n):	1.00	1.50	2.00	2.50	3.00	3.50	4.00	4.50	
Ext(MeV/n):	2.33	2.71	3.11	3.55	3.97	4.43	4.86	5.35	
Z = 15 A= 30									
Einstr(MeV/n):	1.00	1.50	2.00	2.50	3.00	3.50	4.00	4.50	
Ext(MeV/n):	2.37	2.75	3.15	3.59	4.01	4.47	4.90	5.39	
Z = 16 A= 32									
Einstr(MeV/n):	1.00	1.50	2.00	2.50	3.00	3.50	4.00	4.50	
Ext(MeV/n):	2.41	2.79	3.19	3.63	4.05	4.51	4.94	5.43	
Z = 17 A= 34									
Einstr(MeV/n):	1.00	1.50	2.00	2.50	3.00	3.50	4.00	4.50	
Ext(MeV/n):	2.45	2.83	3.23	3.67	4.09	4.55	4.98	5.47	
Z = 18 A= 36									
Einstr(MeV/n):	1.00	1.50	2.00	2.50	3.00	3.50	4.00	4.50	
Ext(MeV/n):	2.49	2.87	3.27	3.71	4.13	4.59	5.02	5.51	
Z = 19 A= 38									
Einstr(MeV/n):	1.00	1.50	2.00	2.50	3.00	3.50	4.00	4.50	
Ext(MeV/n):	2.53	2.91	3.31	3.75	4.17	4.63	5.06	5.55	
Z = 20 A= 40									
Einstr(MeV/n):	1.00	1.50	2.00	2.50	3.00	3.50	4.00	4.50	
Ext(MeV/n):	2.57	2.95	3.35	3.79	4.21	4.67	5.10	5.59	
Z = 21 A= 42									
Einstr(MeV/n):	1.00	1.50	2.00	2.50	3.00	3.50	4.00	4.50	
Ext(MeV/n):	2.61	2.99	3.39	3.83	4.25	4.71	5.14	5.63	
Z = 22 A= 44									
Einstr(MeV/n):	1.00	1.50	2.00	2.50	3.00	3.50	4.00	4.50	
Ext(MeV/n):	2.65	3.03	3.43	3.87	4.29	4.75	5.18	5.67	
Z = 23 A= 46									
Einstr(MeV/n):	1.00	1.50	2.00	2.50	3.00	3.50	4.00	4.50	
Ext(MeV/n):	2.69	3.07	3.47	3.91	4.33	4.79	5.22	5.71	
Z = 24 A= 48									
Einstr(MeV/n):	1.00	1.50	2.00	2.50	3.00	3.50	4.00	4.50	
Ext(MeV/n):	2.73	3.11	3.51	3.95	4.37	4.83	5.26	5.75	
Z = 25 A= 50									
Einstr(MeV/n):	1.00	1.50	2.00	2.50	3.00	3.50	4.00	4.50	
Ext(MeV/n):	2.77	3.15	3.55	3.99	4.41	4.87	5.30	5.79	
Z = 26 A= 52									
Einstr(MeV/n):	1.00	1.50	2.00	2.50	3.00	3.50	4.00	4.50	
Ext(MeV/n):	2.81	3.19	3.59	4.03	4.45	4.91	5.34	5.83	
Z = 27 A= 54									
Einstr(MeV/n):	1.00	1.50	2.00	2.50	3.00	3.50	4.00	4.50	
Ext(MeV/n):	2.85	3.23	3.63	4.07	4.49	4.95	5.38	5.87	
Z = 28 A= 56									
Einstr(MeV/n):	1.00	1.50	2.00	2.50	3.00	3.50	4.00	4.50	
Ext(MeV/n):	2.89	3.27	3.67	4.11	4.53	4.99	5.42	5.91	
Z = 29 A= 58									
Einstr(MeV/n):	1.00	1.50	2.00	2.50	3.00	3.50	4.00	4.50	
Ext(MeV/n):	2.93	3.31	3.71	4.15	4.57	5.03	5.46	5.95	
Z = 30 A= 60									
Einstr(MeV/n):	1.00	1.50	2.00	2.50	3.00	3.50	4.00	4.50	
Ext(MeV/n):	2.97	3.35	3.75	4.19	4.61	5.07	5.50	5.99	
Z = 31 A= 62									
Einstr(MeV/n):	1.00	1.50	2.00	2.50	3.00	3.50	4.00	4.50	
Ext(MeV/n):	3.01	3.39	3.79	4.23	4.65	5.11	5.54	6.03	
Z = 32 A= 64									
Einstr(MeV/n):	1.00	1.50	2.00	2.50	3.00	3.50	4.00	4.50	
Ext(MeV/n):	3.05	3.43	3.83	4.27	4.69	5.15	5.58	6.07	
Z = 33 A= 66									
Einstr(MeV/n):	1.00	1.50	2.00	2.50	3.00	3.50	4.00	4.50	
Ext(MeV/n):	3.09	3.47	3.87	4.31	4.73	5.19	5.62	6.11	
Z = 34 A= 68									
Einstr(MeV/n):	1.00	1.50	2.00	2.50	3.00	3.50	4.00	4.50	
Ext(MeV/n):	3.13	3.51	3.91	4.35	4.77	5.23	5.66	6.15	
Z = 35 A= 70									
Einstr(MeV/n):	1.00	1.50	2.00	2.50	3.00	3.50	4.00	4.50	
Ext(MeV/n):	3.17	3.55	3.95	4.39	4.81	5.27	5.70	6.19	
Z = 36 A= 72									
Einstr(MeV/n):	1.00	1.50	2.00	2.50	3.00	3.50	4.00	4.50	
Ext(MeV/n):	3.21	3.59	3.99	4.43	4.85	5.31	5.74	6.23	
Z = 37 A= 74									
Einstr(MeV/n):	1.00	1.50	2.00	2.50	3.00	3.50	4.00	4.50	
Ext(MeV/n):	3.25	3.63	4.03	4.47	4.89	5.35	5.78	6.27	
Z = 38 A= 76									
Einstr(MeV/n):	1.00	1.50	2.00	2.50	3.00	3.50	4.00	4.50	
Ext(MeV/n):	3.29	3.67	4.07	4.51	4.93	5.39	5.82	6.31	
Z = 39 A= 78									
Einstr(MeV/n):	1.00	1.50	2.00	2.50	3.00	3.50	4.00	4.50	
Ext(MeV/n):	3.33	3.71	4.11	4.55	4.97	5.43	5.86	6.35	
Z = 40 A= 80									
Einstr(MeV/n):	1.00	1.50	2.00	2.50	3.00	3.50	4.00	4.50	
Ext(MeV/n):	3.37	3.75	4.15	4.59	5.01	5.47	5.90	6.39	
Z = 41 A= 82									
Einstr(MeV/n):	1.00	1.50	2.00	2.50	3.00	3.50	4.00	4.50	
Ext(MeV/n):	3.41	3.79	4.19	4.63	5.05	5.51	5.94	6.43	
Z = 42 A= 84									
Einstr(MeV/n):	1.00	1.50	2.00	2.50	3.00	3.50	4.00	4.50	
Ext(MeV/n):	3.45	3.83	4.23	4.67	5.09	5.55	5.98	6.47	
Z = 43 A= 86									
Einstr(MeV/n):	1.00	1.50	2.00	2.50	3.00	3.50	4.00	4.50	
Ext(MeV/n):	3.49	3.87	4.27	4.71	5.13	5.59	6.02	6.51	
Z = 44 A= 88									
Einstr(MeV/n):	1.00	1.50	2.00	2.50	3.00	3.50	4.00	4.50	
Ext(MeV/n):	3.53	3.91	4.31	4.75	5.17	5.63	6.06	6.55	
Z = 45 A= 90									
Einstr(MeV/n):	1.00	1.50	2.00	2.50	3.00	3.50	4.00	4.50	
Ext(MeV/n):	3.57	3.95	4.35	4.79	5.21	5.67	6.10	6.59	
Z = 46 A= 92									
Einstr(MeV/n):	1.00	1.50	2.00	2.50	3.00	3.50	4.00	4.50	
Ext(MeV/n):	3.61	3.99	4.39	4.83	5.25	5.71	6.14	6.63	
Z = 47 A= 94									
Einstr(MeV/n):	1.00	1.50	2.00	2.50	3.00	3.50	4.00	4.50	
Ext(MeV/n):	3.65	4.03	4.43	4.87	5.29	5.75	6.18	6.67	
Z = 48 A= 96									
Einstr(MeV/n):	1.00	1.50	2.00	2.50	3.00	3.50	4.00	4.50	
Ext(MeV/n):	3.69	4.07	4.47	4.91	5.33	5.79	6.22	6.71	
Z = 49 A= 98									
Einstr(MeV/n):	1.00	1.50	2.00	2.50	3.00	3.50	4.00	4.50	
Ext(MeV/n):	3.73	4.11	4.51	4.95	5.37	5.83	6.26	6.75	
Z = 50 A= 100									
Einstr(MeV/n):	1.00	1.50	2.00	2.50	3.00	3.50	4.00	4.50	
Ext(MeV/n):	3.77	4.15	4.55	4.99	5.41	5.87	6.30	6.79	
Z = 51 A= 102									
Einstr(MeV/n):	1.00	1.50	2.00	2.50	3.00	3.50	4.00	4.50	
Ext(MeV/n):	3.81	4.19	4.59	5.03	5.45	5.91	6.34	6.83	
Z = 52 A= 104									
Einstr(MeV/n):	1.00	1.50	2.00	2.50	3.00	3.50	4.00	4.50	
Ext(MeV/n):	3.85	4.23	4.63	5.07	5.49	5.95	6.38	6.87	
Z = 53 A= 106									
Einstr(MeV/n):	1.00	1.50	2.00	2.50	3.00	3.50	4.00	4.50	
Ext(MeV/n):	3.89	4.27	4.67	5.11	5.53	5.99	6.42	6.91	
Z = 54 A= 108									
Einstr(MeV/n):	1.00	1.50	2.00	2.50	3.00	3.50	4.00	4.50	
Ext(MeV/n):	3.93	4.31	4.71	5.15	5.57	6.03	6.46	6.95	
Z = 55 A= 110									
Einstr(MeV/n):	1.00	1.50	2.00	2.50	3.00	3.50	4.00	4.50	
Ext(MeV/n):	3.97	4.35	4.75	5.19	5.61	6.07	6.50	6.99	

Table 6.1 (contd.)

Z = 9 A= 19			Z = 13 A= 27					
Einstr(MeV/n):	1.00	1.50	2.00	2.50	3.00	3.50	4.00	4.50
Ext(MeV/n):	2.07	2.46	2.84	3.28	3.74	4.18	4.61	5.10
Einstr(MeV/n):	5.00	5.50	6.00	6.50	7.00	7.50	8.00	8.50
Ext(MeV/n):	5.54	6.04	6.48	6.98	7.44	7.94	8.40	8.90
Einstr(MeV/n):	9.00	9.50	10.00	10.50	11.00	11.50	12.00	30.00
Ext(MeV/n):	9.37	9.87	10.34	10.84	11.32	11.82	12.32	30.15
Einstr(MeV/n):	50.00	80.00						
Ext(MeV/n):	50.10	80.07						
Z = 10 A= 20			Z = 14 A= 28					
Einstr(MeV/n):	1.00	1.50	2.00	2.50	3.00	3.50	4.00	4.50
Ext(MeV/n):	2.15	2.54	2.94	3.37	3.81	4.25	4.69	5.17
Einstr(MeV/n):	5.00	5.50	6.00	6.50	7.00	7.50	8.00	8.50
Ext(MeV/n):	5.61	6.10	6.55	7.05	7.50	8.00	8.46	8.96
Einstr(MeV/n):	9.00	9.50	10.00	10.50	11.00	11.50	12.00	30.00
Ext(MeV/n):	9.42	9.92	10.39	10.89	11.37	11.87	12.37	30.16
Einstr(MeV/n):	50.00	80.00						
Ext(MeV/n):	50.12	80.08						
Z = 11 A= 23			Z = 15 A= 31					
Einstr(MeV/n):	1.00	1.50	2.00	2.50	3.00	3.50	4.00	4.50
Ext(MeV/n):	2.14	2.53	2.93	3.36	3.80	4.25	4.69	5.17
Einstr(MeV/n):	5.00	5.50	6.00	6.50	7.00	7.50	8.00	8.50
Ext(MeV/n):	5.61	6.10	6.55	7.05	7.50	8.00	8.46	8.96
Einstr(MeV/n):	9.00	9.50	10.00	10.50	11.00	11.50	12.00	30.00
Ext(MeV/n):	9.43	9.93	10.40	10.90	11.37	11.87	12.37	30.16
Einstr(MeV/n):	50.00	80.00						
Ext(MeV/n):	50.13	80.09						
Z = 12 A= 24			Z = 16 A= 32					
Einstr(MeV/n):	1.00	1.50	2.00	2.50	3.00	3.50	4.00	4.50
Ext(MeV/n):	2.21	2.61	3.01	3.43	3.88	4.31	4.76	5.23
Einstr(MeV/n):	5.00	5.50	6.00	6.50	7.00	7.50	8.00	8.50
Ext(MeV/n):	5.68	6.16	6.61	7.10	7.56	8.05	8.51	9.01
Einstr(MeV/n):	9.00	9.50	10.00	10.50	11.00	11.50	12.00	30.00
Ext(MeV/n):	9.48	9.98	10.44	10.94	11.42	11.92	12.42	30.22
Einstr(MeV/n):	50.00	80.00						
Ext(MeV/n):	50.14	80.10						
Einstr(MeV/n):	1.00	1.50	2.00	2.50	3.00	3.50	4.00	4.50
Ext(MeV/n):	2.20	2.60	3.01	3.44	3.88	4.32	4.76	5.23
Einstr(MeV/n):	5.00	5.50	6.00	6.50	7.00	7.50	8.00	8.50
Ext(MeV/n):	5.68	6.16	6.62	7.11	7.57	8.06	8.52	9.02
Einstr(MeV/n):	9.00	9.50	10.00	10.50	11.00	11.50	12.00	30.00
Ext(MeV/n):	9.48	9.98	10.45	10.95	11.43	11.93	12.43	30.22
Einstr(MeV/n):	50.00	80.00						
Ext(MeV/n):	50.14	80.10						
Einstr(MeV/n):	1.00	1.50	2.00	2.50	3.00	3.50	4.00	4.50
Ext(MeV/n):	2.27	2.67	3.08	3.50	3.94	4.38	4.82	5.29
Einstr(MeV/n):	5.00	5.50	6.00	6.50	7.00	7.50	8.00	8.50
Ext(MeV/n):	5.74	6.21	6.67	7.16	7.61	8.10	8.57	9.06
Einstr(MeV/n):	9.00	9.50	10.00	10.50	11.00	11.50	12.00	30.00
Ext(MeV/n):	9.53	10.03	10.50	11.00	11.47	11.97	12.47	30.25
Einstr(MeV/n):	50.00	80.00						
Ext(MeV/n):	50.17	80.12						
Einstr(MeV/n):	1.00	1.50	2.00	2.50	3.00	3.50	4.00	4.50
Ext(MeV/n):	2.25	2.66	3.08	3.50	3.94	4.38	4.83	5.29
Einstr(MeV/n):	5.00	5.50	6.00	6.50	7.00	7.50	8.00	8.50
Ext(MeV/n):	5.74	6.22	6.67	7.16	7.62	8.11	8.57	9.07
Einstr(MeV/n):	9.00	9.50	10.00	10.50	11.00	11.50	12.00	30.00
Ext(MeV/n):	9.53	10.03	10.50	11.00	11.47	11.97	12.47	30.25
Einstr(MeV/n):	50.00	80.00						
Ext(MeV/n):	50.17	80.12						
Einstr(MeV/n):	1.00	1.50	2.00	2.50	3.00	3.50	4.00	4.50
Ext(MeV/n):	2.31	2.71	3.13	3.55	4.00	4.43	4.88	5.34
Einstr(MeV/n):	5.00	5.50	6.00	6.50	7.00	7.50	8.00	8.50
Ext(MeV/n):	5.79	6.26	6.72	7.20	7.66	8.15	8.62	9.11
Einstr(MeV/n):	9.00	9.50	10.00	10.50	11.00	11.50	12.00	30.00
Ext(MeV/n):	9.58	10.07	10.54	11.04	11.51	12.01	12.51	30.28
Einstr(MeV/n):	50.00	80.00						
Ext(MeV/n):	50.19	80.14						

Table 6.1 (contd.)

Z = 17 A= 35		Z = 21 A= 45	
Einstr(MeV/n):	1.00 1.50 2.00 2.50 3.00 3.50 4.00 4.50	Einstr(MeV/n):	1.00 1.50 2.00 2.50 3.00 3.50 4.00 4.50
Eext(MeV/n):	2.31 2.71 3.13 3.55 4.00 4.43 4.88 5.34	Eext(MeV/n):	2.30 2.74 3.19 3.63 4.08 4.52 4.99 5.44
Einstr(MeV/n):	5.00 5.50 6.00 6.50 7.00 7.50 8.00 8.50	Einstr(MeV/n):	5.00 5.50 6.00 6.50 7.00 7.50 8.00 8.50
Eext(MeV/n):	5.79 6.26 6.72 7.20 7.66 8.15 8.62 9.11	Eext(MeV/n):	5.90 6.37 6.84 7.32 7.78 8.27 8.74 9.22
Einstr(MeV/n):	9.00 9.50 10.00 10.50 11.00 11.50 12.00 30.00	Einstr(MeV/n):	9.00 9.50 10.00 10.50 11.00 11.50 12.00 30.00
Eext(MeV/n):	9.58 10.07 10.54 11.04 11.51 12.01 12.51 30.28	Eext(MeV/n):	9.70 10.19 10.66 11.15 11.63 12.13 12.63 30.35
Einstr(MeV/n):	50.00 80.00	Einstr(MeV/n):	50.00 80.00
Eext(MeV/n):	50.19 80.14	Eext(MeV/n):	50.24 80.17
Z = 18 A= 40		Z = 22 A= 48	
Einstr(MeV/n):	1.00 1.50 2.00 2.50 3.00 3.50 4.00 4.50	Einstr(MeV/n):	1.00 1.50 2.00 2.50 3.00 3.50 4.00 4.50
Eext(MeV/n):	2.31 2.71 3.13 3.55 4.00 4.43 4.88 5.34	Eext(MeV/n):	2.30 2.74 3.19 3.63 4.08 4.52 4.99 5.44
Einstr(MeV/n):	5.00 5.50 6.00 6.50 7.00 7.50 8.00 8.50	Einstr(MeV/n):	5.00 5.50 6.00 6.50 7.00 7.50 8.00 8.50
Eext(MeV/n):	5.79 6.26 6.72 7.20 7.66 8.15 8.62 9.11	Eext(MeV/n):	5.90 6.37 6.84 7.32 7.78 8.27 8.74 9.22
Einstr(MeV/n):	9.00 9.50 10.00 10.50 11.00 11.50 12.00 30.00	Einstr(MeV/n):	9.00 9.50 10.00 10.50 11.00 11.50 12.00 30.00
Eext(MeV/n):	9.58 10.07 10.54 11.04 11.51 12.01 12.51 30.28	Eext(MeV/n):	9.70 10.19 10.66 11.15 11.63 12.13 12.63 30.35
Einstr(MeV/n):	50.00 80.00	Einstr(MeV/n):	50.00 80.00
Eext(MeV/n):	50.19 80.14	Eext(MeV/n):	50.24 80.17
Z = 19 A= 39		Z = 23 A= 51	
Einstr(MeV/n):	1.00 1.50 2.00 2.50 3.00 3.50 4.00 4.50	Einstr(MeV/n):	1.00 1.50 2.00 2.50 3.00 3.50 4.00 4.50
Eext(MeV/n):	2.31 2.71 3.13 3.55 4.00 4.43 4.88 5.34	Eext(MeV/n):	2.30 2.74 3.19 3.63 4.08 4.52 4.99 5.44
Einstr(MeV/n):	5.00 5.50 6.00 6.50 7.00 7.50 8.00 8.50	Einstr(MeV/n):	5.00 5.50 6.00 6.50 7.00 7.50 8.00 8.50
Eext(MeV/n):	5.79 6.26 6.72 7.20 7.66 8.15 8.62 9.11	Eext(MeV/n):	5.90 6.37 6.84 7.32 7.78 8.27 8.74 9.22
Einstr(MeV/n):	9.00 9.50 10.00 10.50 11.00 11.50 12.00 30.00	Einstr(MeV/n):	9.00 9.50 10.00 10.50 11.00 11.50 12.00 30.00
Eext(MeV/n):	9.58 10.07 10.54 11.04 11.51 12.01 12.51 30.28	Eext(MeV/n):	9.70 10.19 10.66 11.15 11.63 12.13 12.63 30.35
Einstr(MeV/n):	50.00 80.00	Einstr(MeV/n):	50.00 80.00
Eext(MeV/n):	50.19 80.14	Eext(MeV/n):	50.24 80.17
Z = 20 A= 40		Z = 24 A= 52	
Einstr(MeV/n):	1.00 1.50 2.00 2.50 3.00 3.50 4.00 4.50	Einstr(MeV/n):	1.00 1.50 2.00 2.50 3.00 3.50 4.00 4.50
Eext(MeV/n):	2.31 2.71 3.13 3.55 4.00 4.43 4.88 5.34	Eext(MeV/n):	2.30 2.74 3.19 3.63 4.08 4.52 4.99 5.44
Einstr(MeV/n):	5.00 5.50 6.00 6.50 7.00 7.50 8.00 8.50	Einstr(MeV/n):	5.00 5.50 6.00 6.50 7.00 7.50 8.00 8.50
Eext(MeV/n):	5.79 6.26 6.72 7.20 7.66 8.15 8.62 9.11	Eext(MeV/n):	5.90 6.37 6.84 7.32 7.78 8.27 8.74 9.22
Einstr(MeV/n):	9.00 9.50 10.00 10.50 11.00 11.50 12.00 30.00	Einstr(MeV/n):	9.00 9.50 10.00 10.50 11.00 11.50 12.00 30.00
Eext(MeV/n):	9.58 10.07 10.54 11.04 11.51 12.01 12.51 30.28	Eext(MeV/n):	9.70 10.19 10.66 11.15 11.63 12.13 12.63 30.35
Einstr(MeV/n):	50.00 80.00	Einstr(MeV/n):	50.00 80.00
Eext(MeV/n):	50.19 80.14	Eext(MeV/n):	50.24 80.17

Z = 25 A= 55

Einstr(MeV/n):	1.00	1.50	2.00	2.50	3.00	3.50	4.00	4.50
Eext(MeV/n):	2.30	2.74	3.19	3.63	4.08	4.52	4.99	5.44
Einstr(MeV/n):	5.00	5.50	6.00	6.50	7.00	7.50	8.00	8.50
Eext(MeV/n):	5.90	6.37	6.84	7.32	7.78	8.27	8.74	9.22
Einstr(MeV/n):	9.00	9.50	10.00	10.50	11.00	11.50	12.00	30.00
Eext(MeV/n):	9.70	10.19	10.66	11.15	11.63	12.13	12.63	30.35
Einstr(MeV/n):	50.00	80.00						
Eext(MeV/n):	50.24	80.17						

Z = 26 A= 56

Einstr(MeV/n):	1.00	1.50	2.00	2.50	3.00	3.50	4.00	4.50
Eext(MeV/n):	2.30	2.74	3.19	3.63	4.08	4.52	4.99	5.44
Einstr(MeV/n):	5.00	5.50	6.00	6.50	7.00	7.50	8.00	8.50
Eext(MeV/n):	5.90	6.37	6.84	7.32	7.78	8.27	8.74	9.22
Einstr(MeV/n):	9.00	9.50	10.00	10.50	11.00	11.50	12.00	30.00
Eext(MeV/n):	9.70	10.19	10.66	11.15	11.63	12.13	12.63	30.40
Einstr(MeV/n):	50.00	80.00						
Eext(MeV/n):	50.28	80.20						

Table 6.1 (contd.)

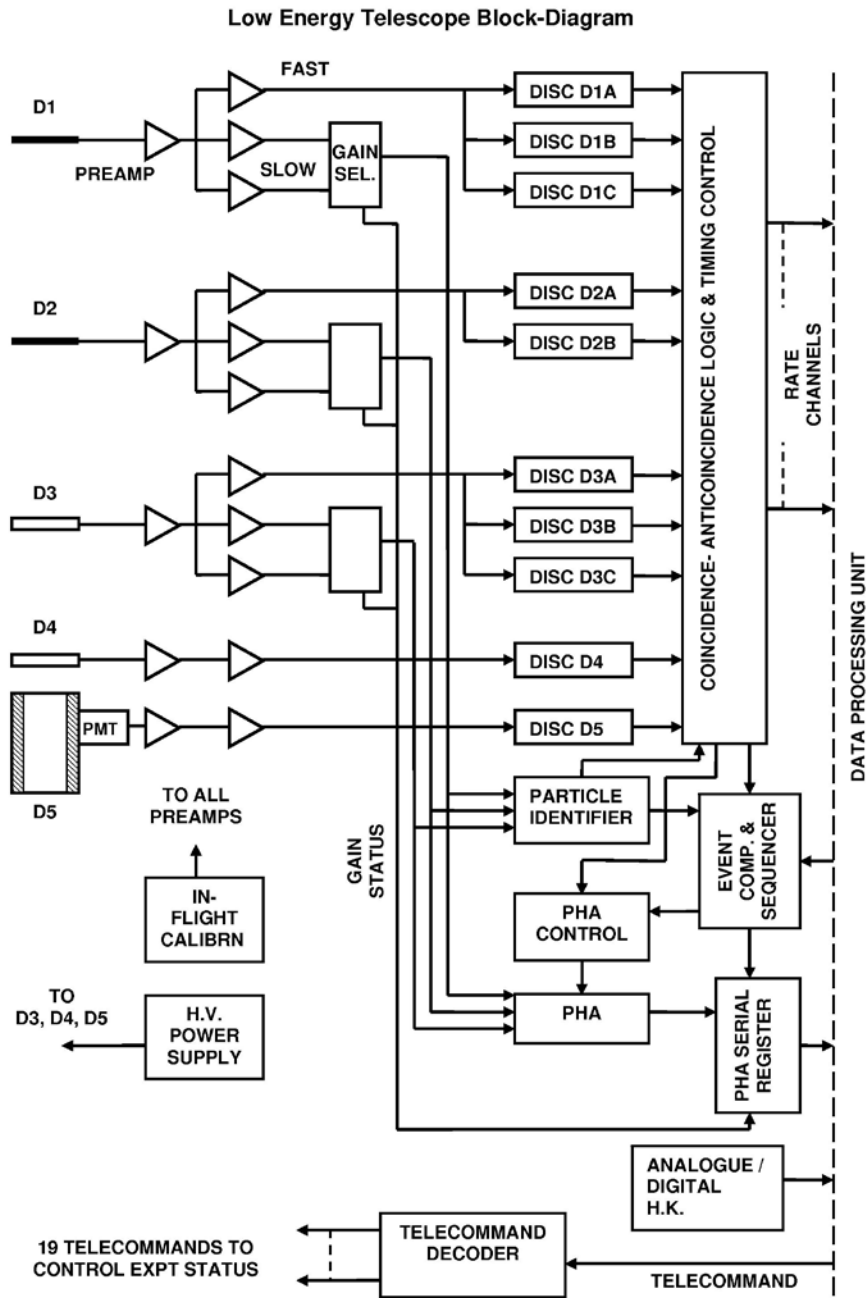


Fig. 1.1 Block diagram of the Low Energy Telescope (LET).

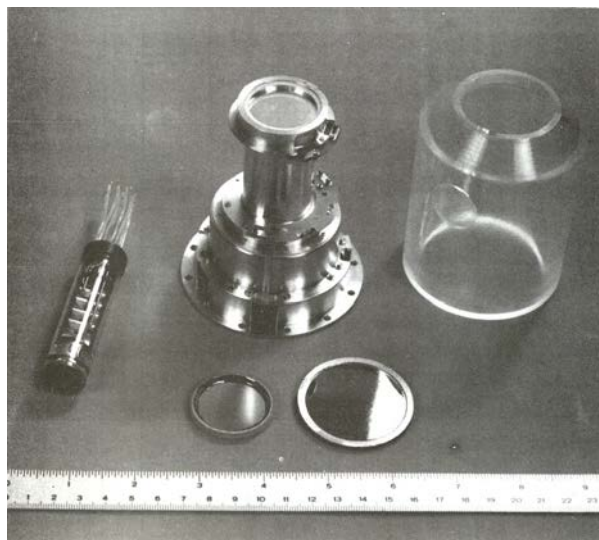
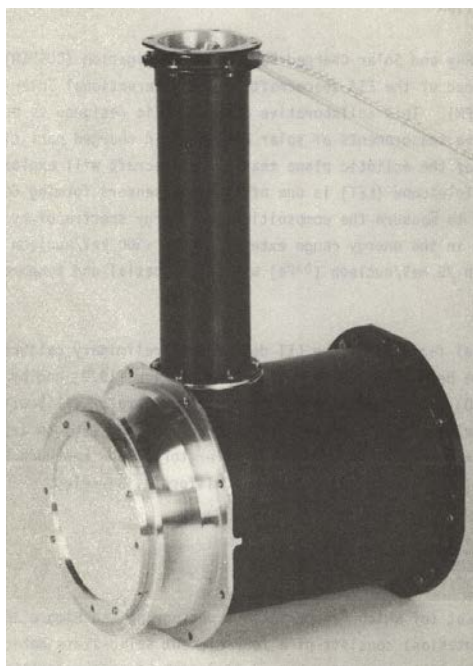
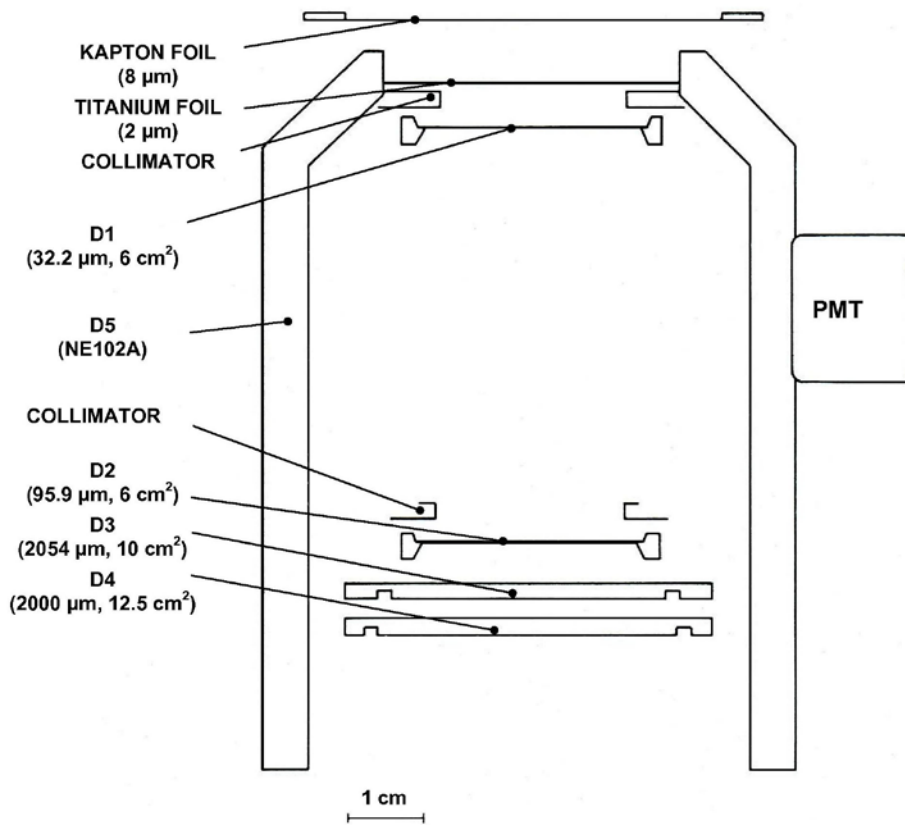


Fig. 1.2 (top) Cross-section of the LET sensor, showing the detectors and aperture foils; (bottom left) LET sensor assembly; (bottom right) Key elements of the LET sensor (PMT, detectors, tube structure).

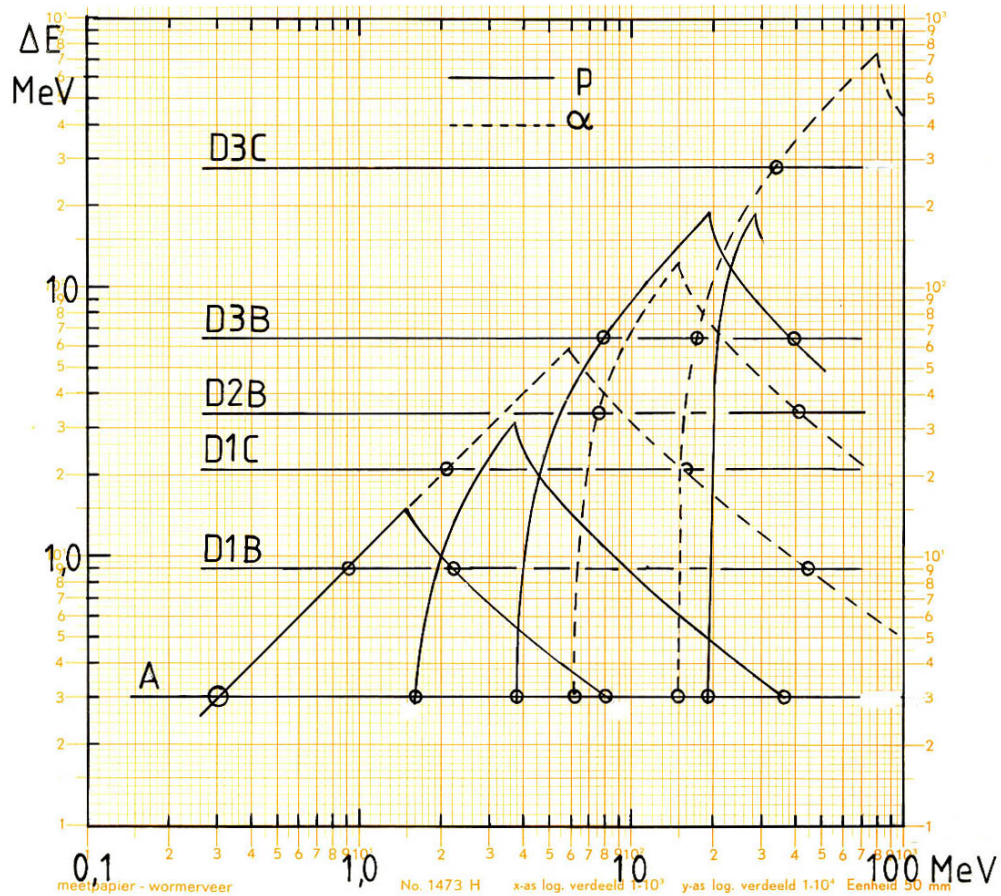


Fig. 2.1 Nominal discriminator threshold levels for detectors D1, D2 and D3, together with the energy loss characteristics for protons and alpha particles.

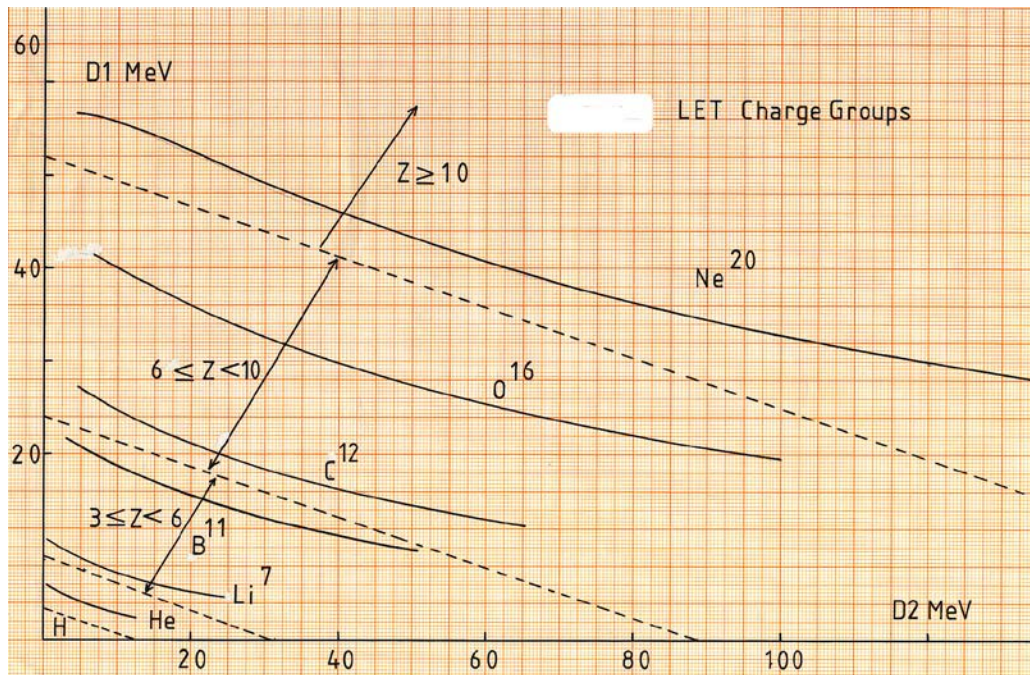


Fig. 2.2 Particle Identifier discriminator boundaries defining the charge groups in the D1-D2 range (particles stopping in detector D2).

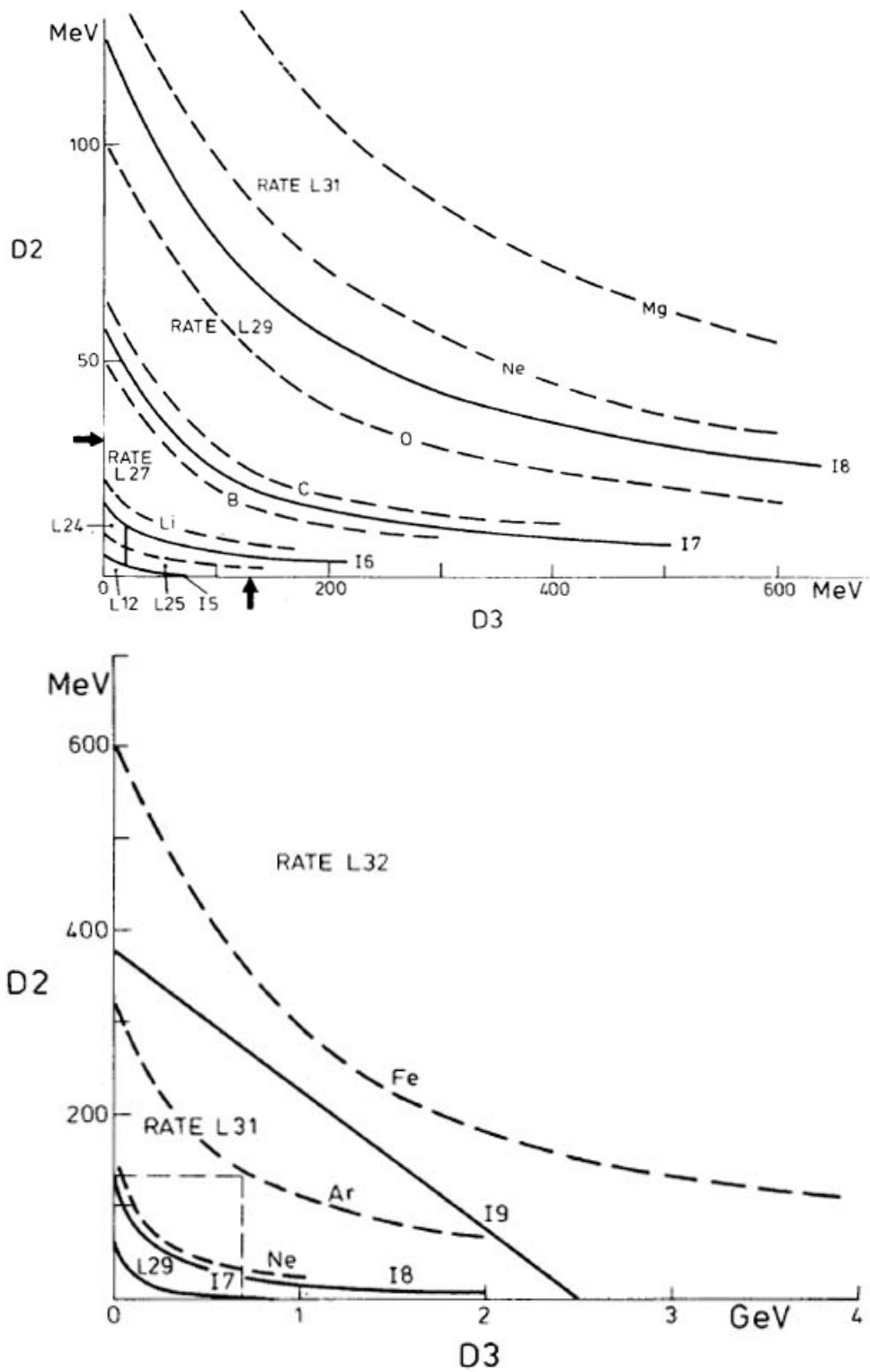


Fig. 2.3 Particle Identifier discriminator boundaries defining charge groups in the D2-D3 range (particles stopping in detector D3).

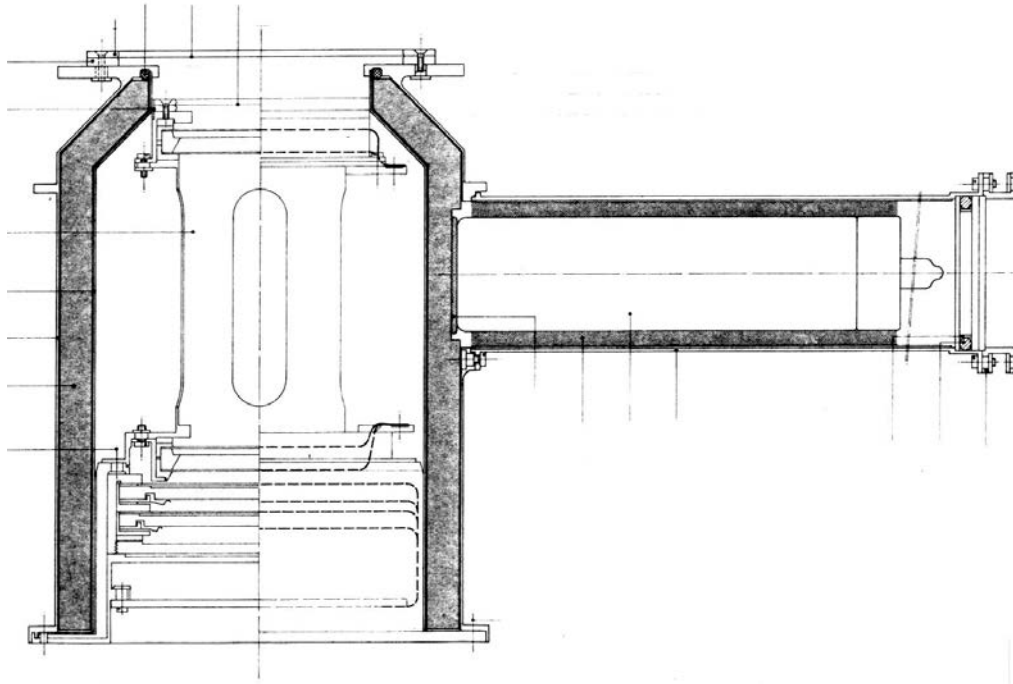
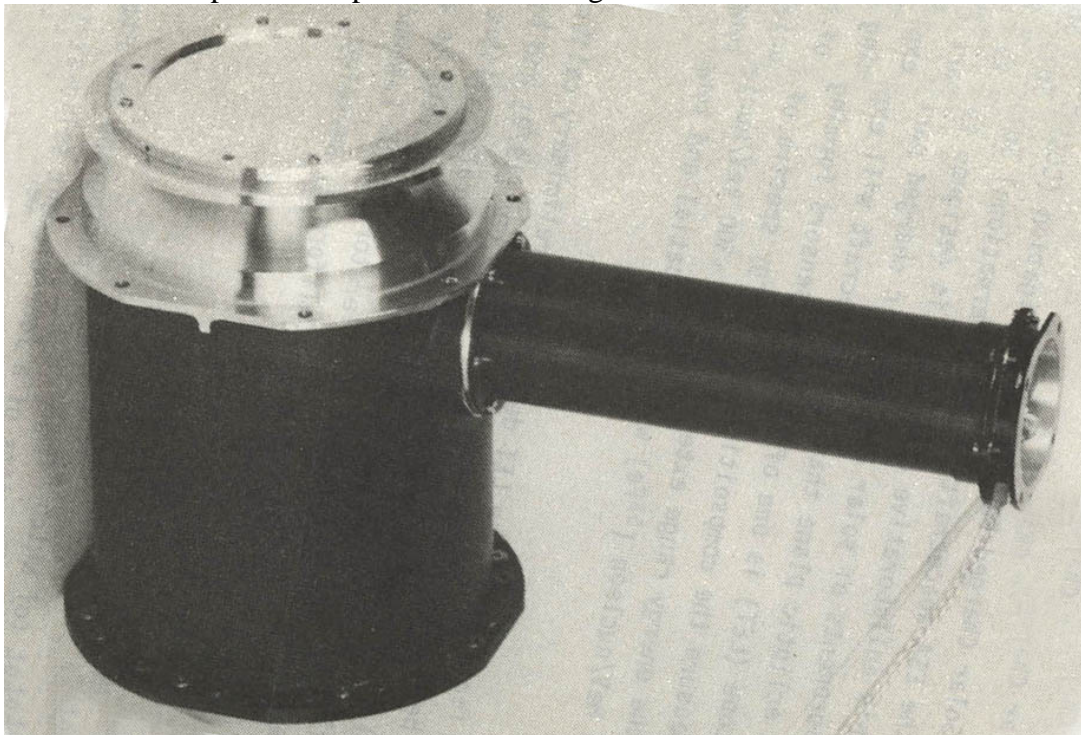


Fig. 3.1 LET telescope: mechanical configuration, showing the internal structure and the photomultiplier tube mounting.



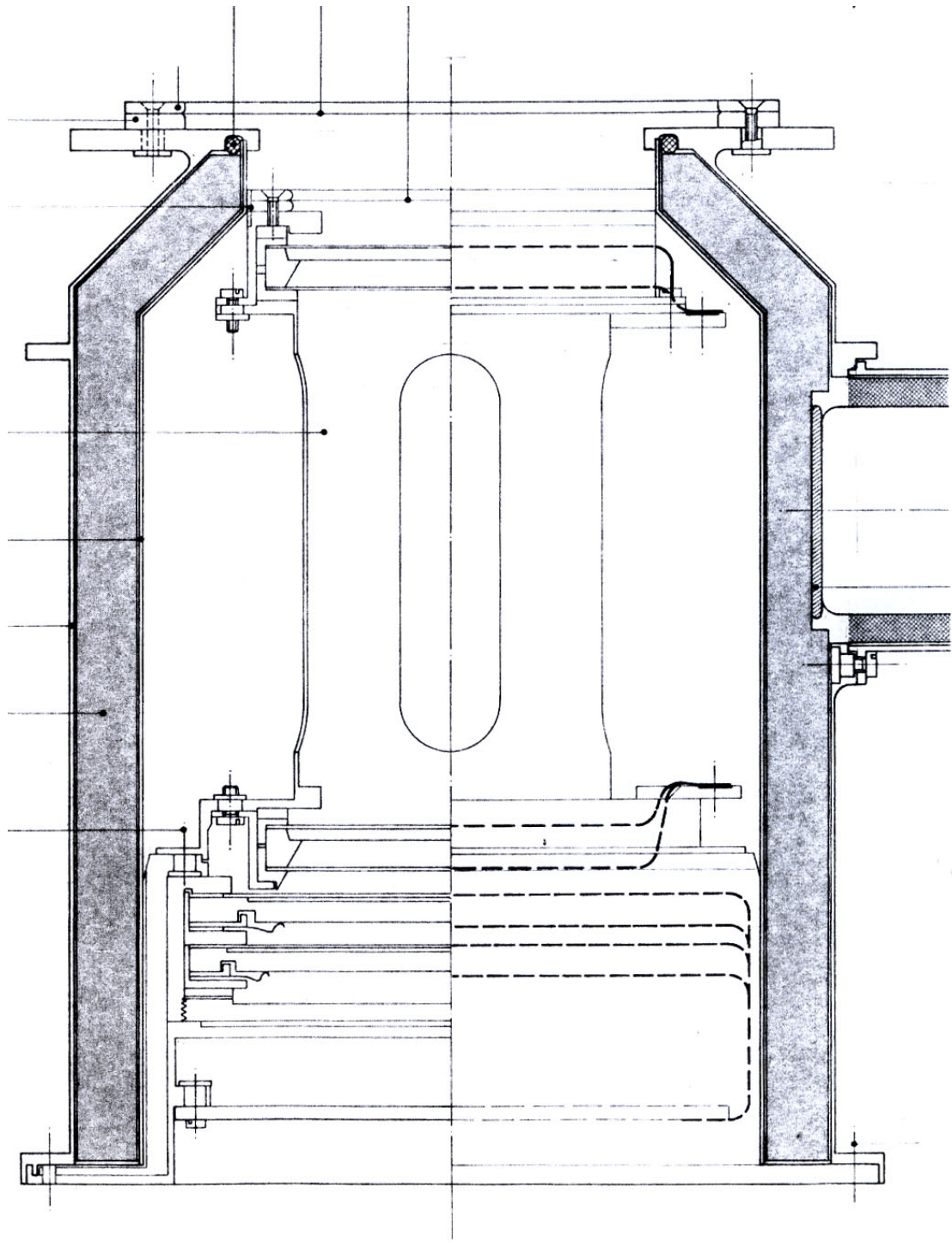


Fig. 3.2 LET telescope: internal structure in detail.

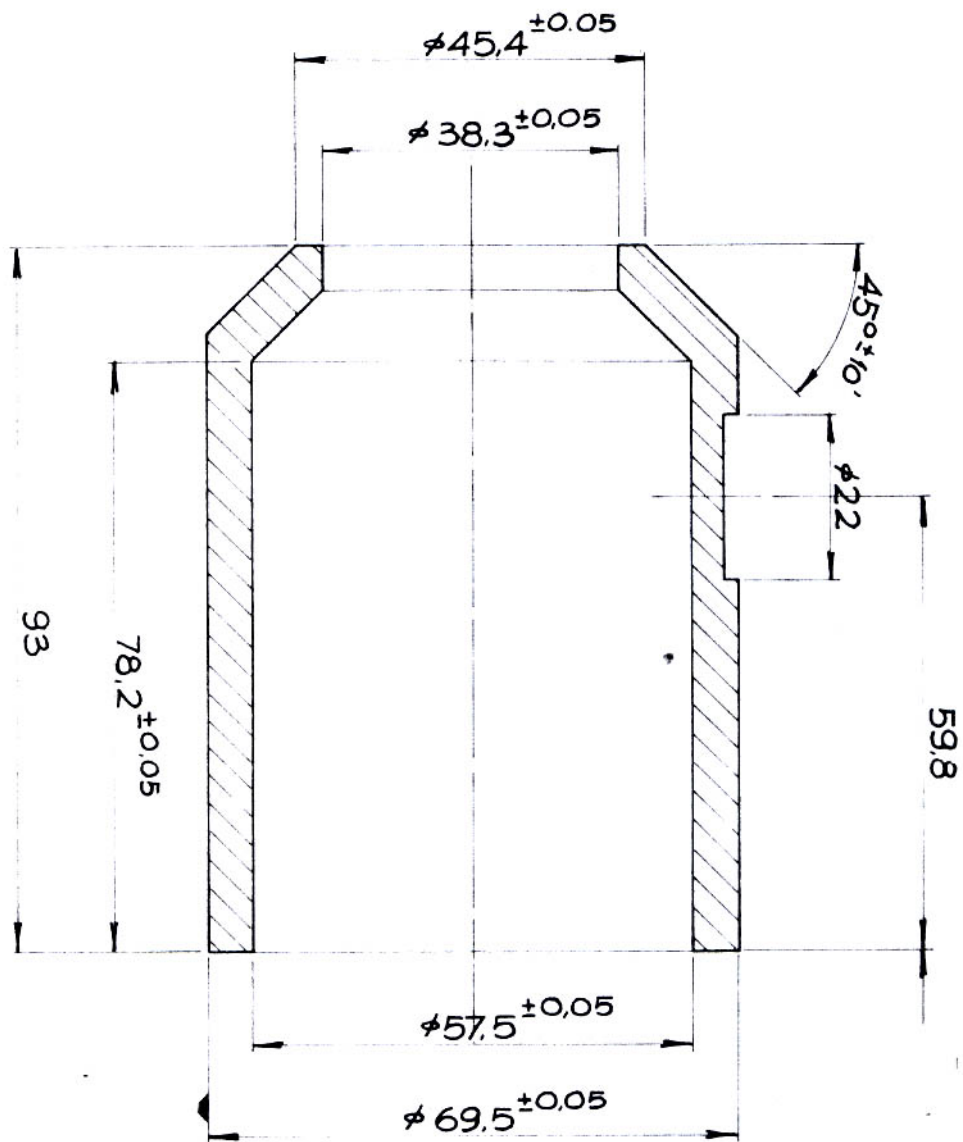


Fig. 3.3 LET sensor: cross-section of the plastic scintillator anti-coincidence shield, including key dimensions in mm.



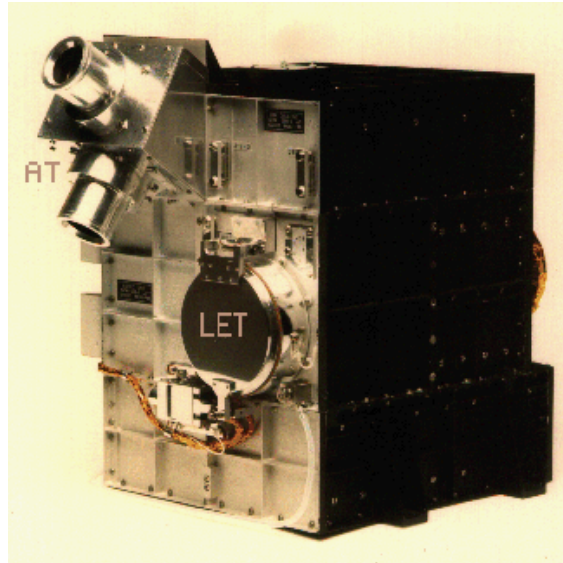


Fig. 3.5 SIM-1 package, with the Anisotropy Telescopes (top), Low Energy Telescope (middle) and Data Processing Unit (bottom).

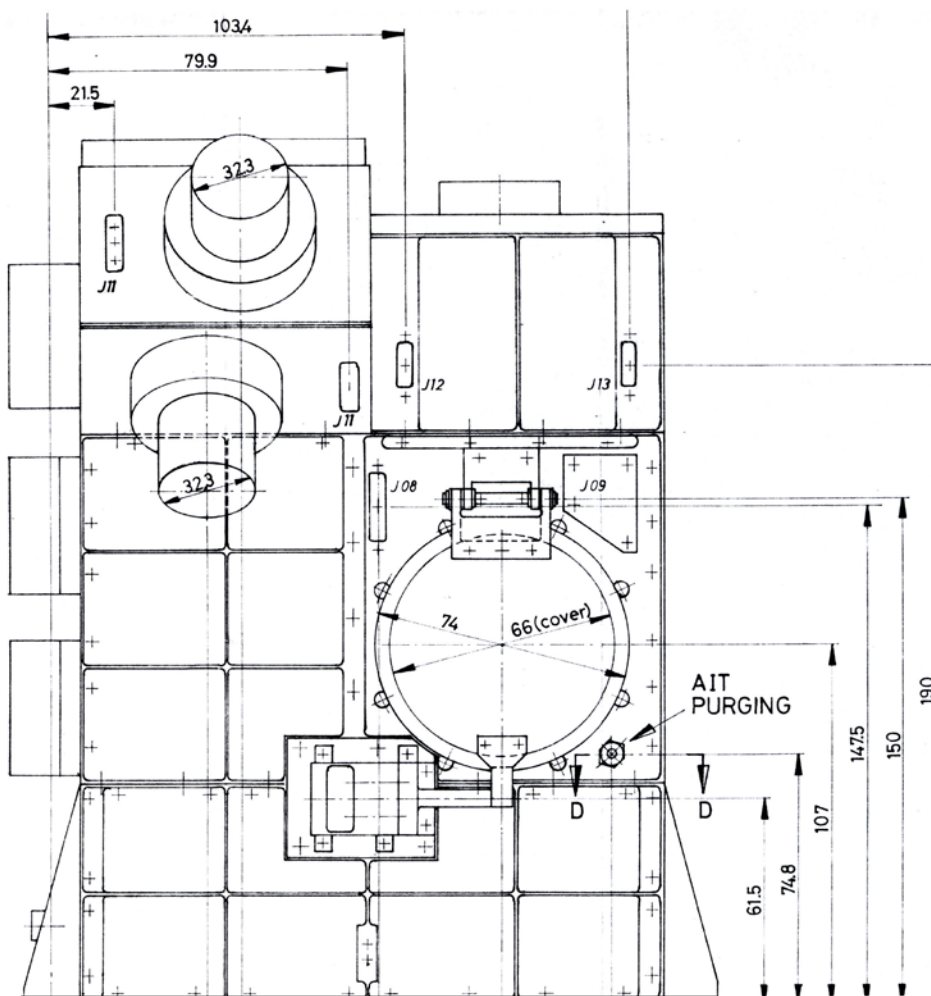


Fig. 3.6a Front view of SIM-1 package with LET in the centre (dimensions in mm).

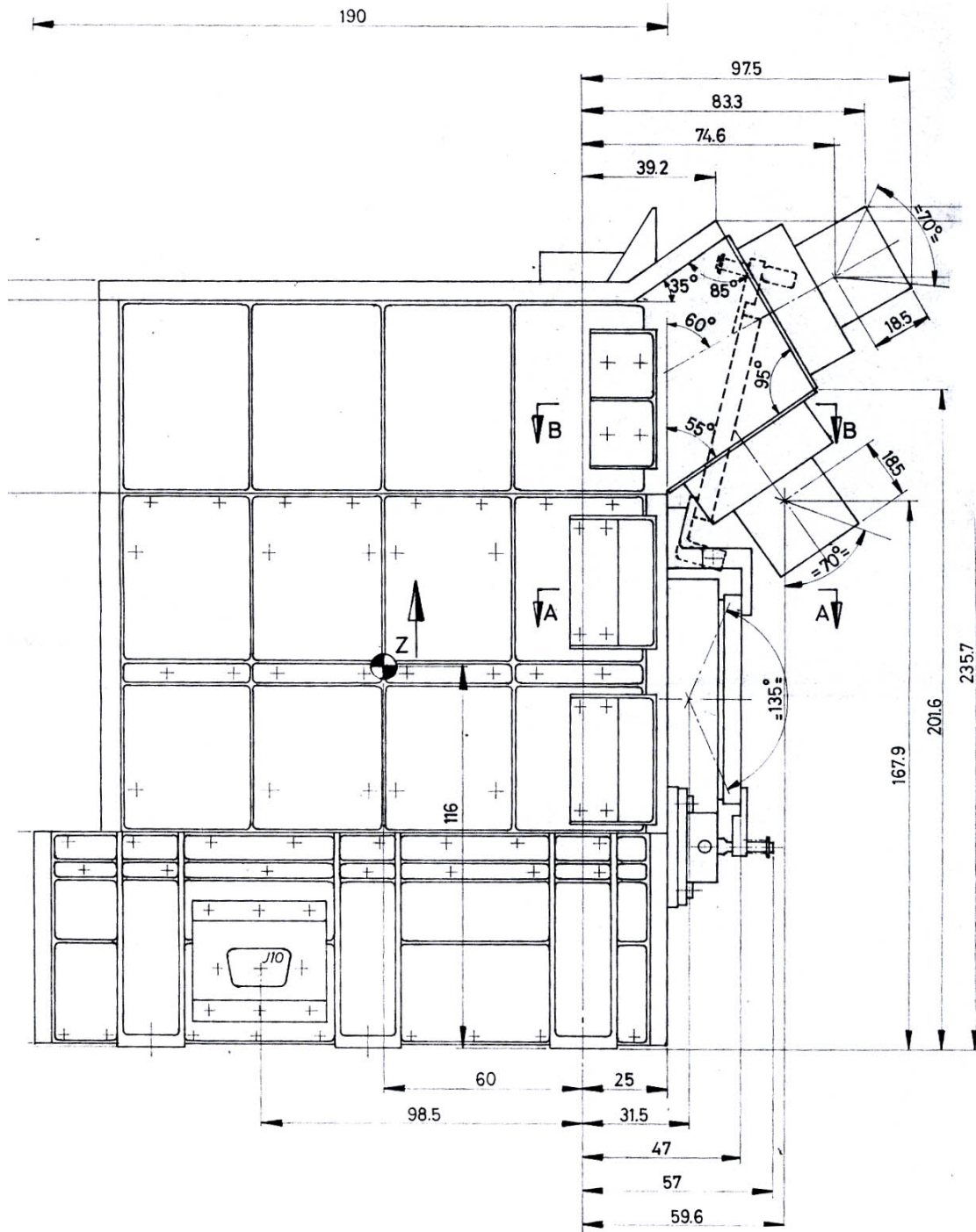


Fig. 3.6b Side view of SIM-1 package with LET in the centre (dimensions in mm).

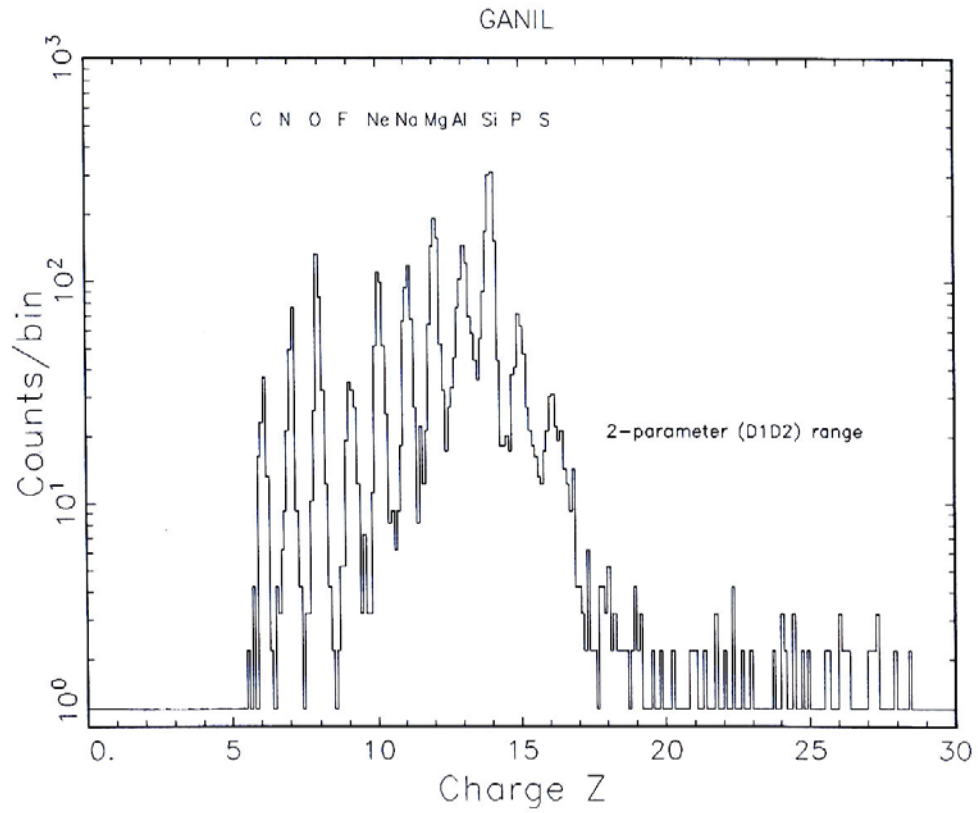


Fig. 5.1 D1-D2 response measured at the GANIL accelerator in Nov 1988.

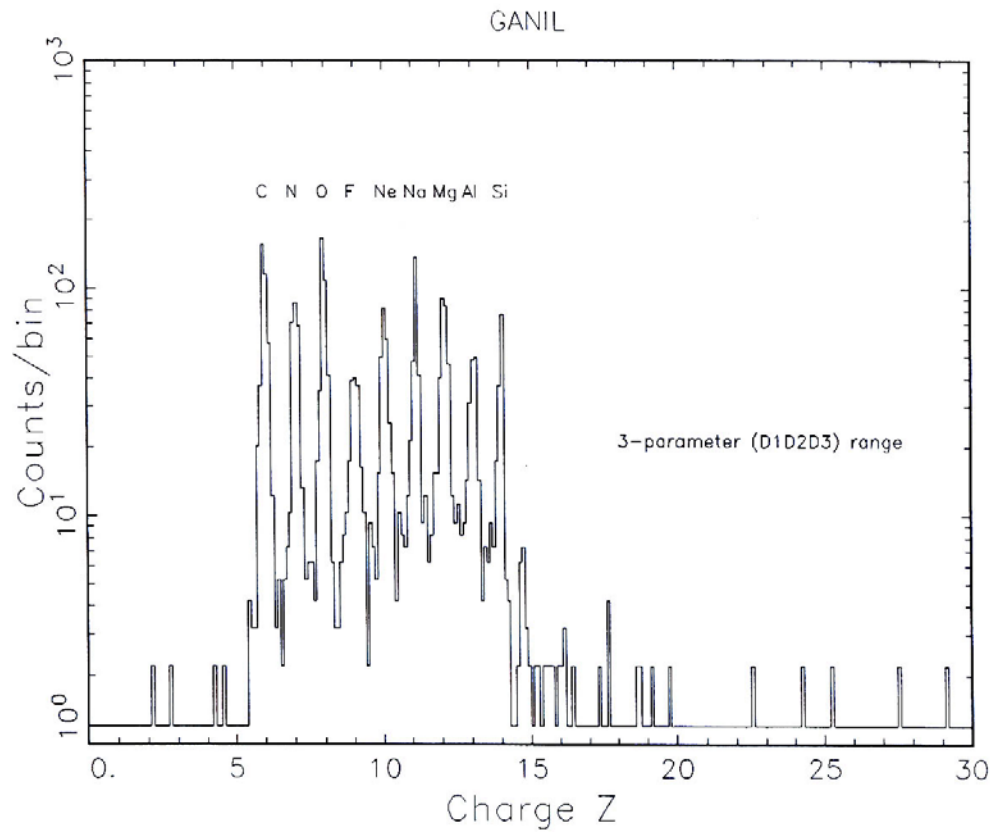


Fig. 5.2 D1-D2-D3 response measured at the GANIL accelerator in Nov 1988.

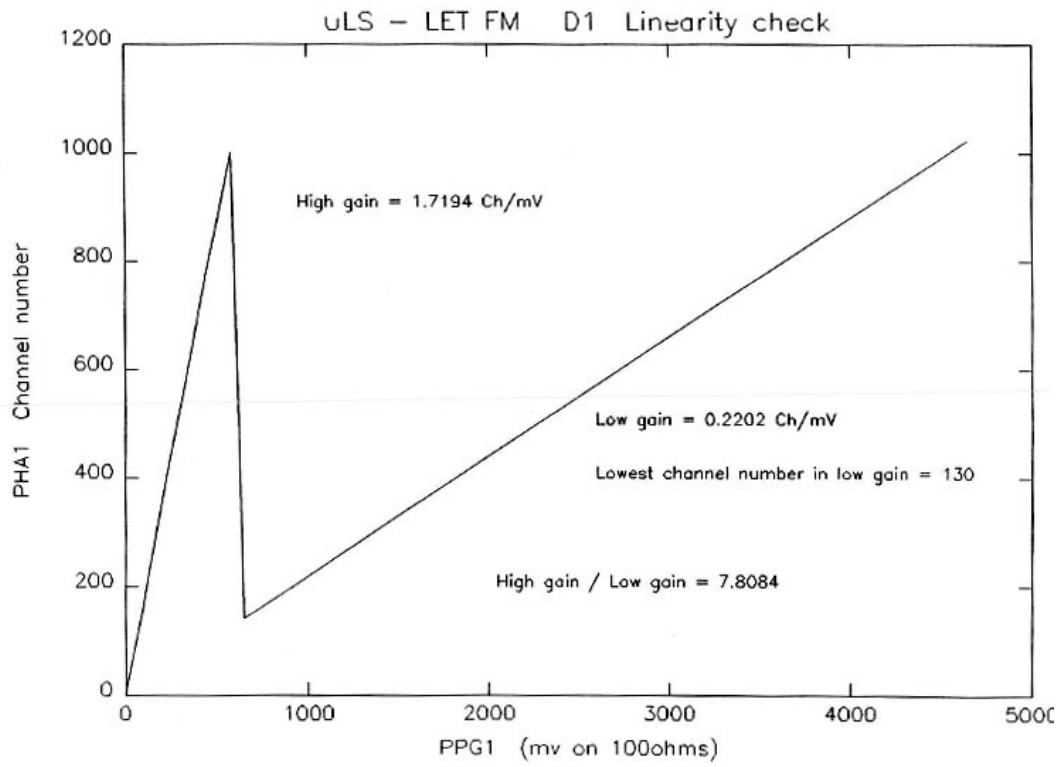


Fig. 5.3 LET detector D1 linearity check.

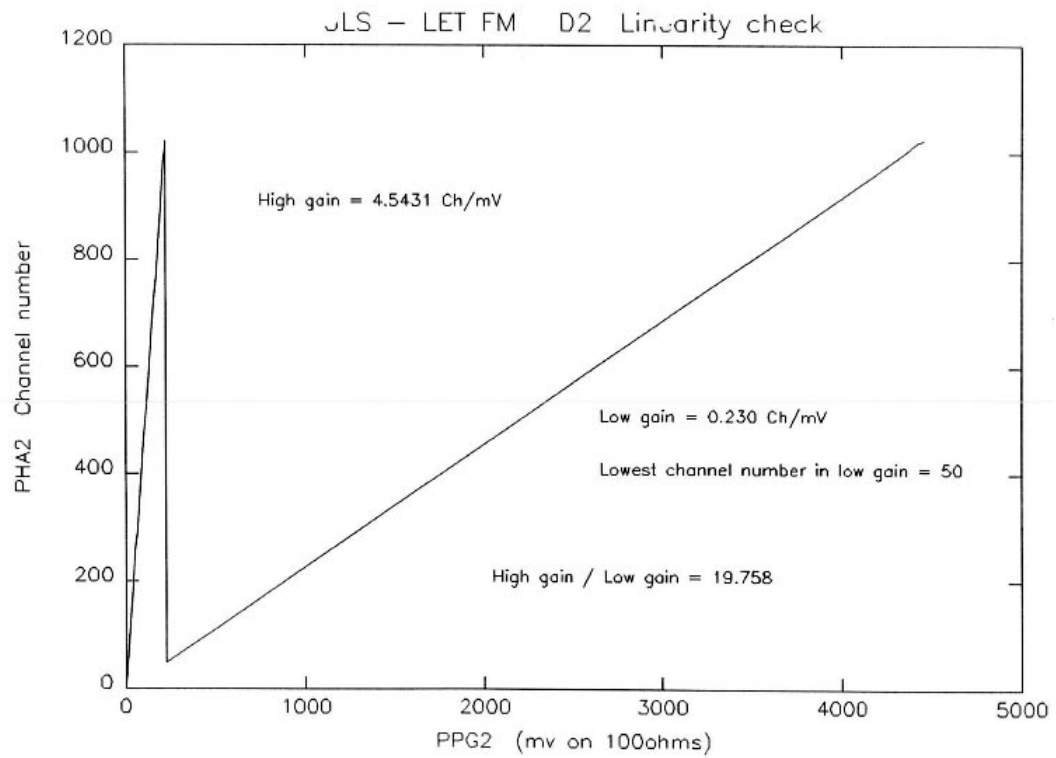


Fig. 5.4 LET detector D2 linearity check.

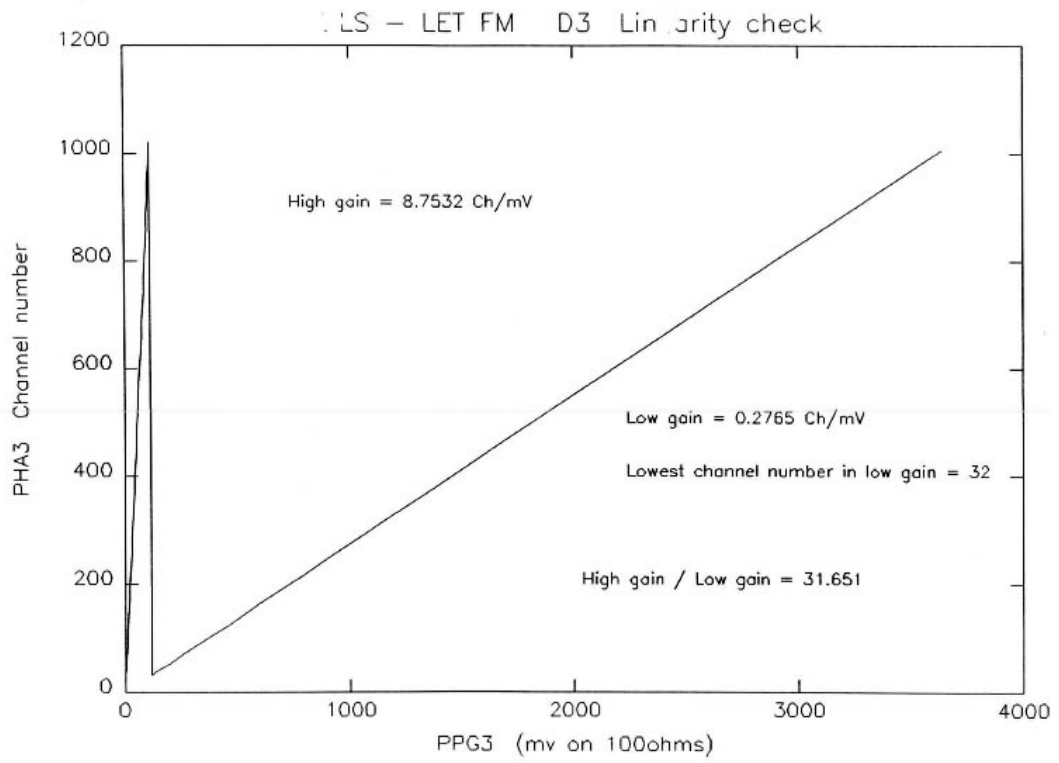


Fig. 5.5 LET detector D3 linearity check.

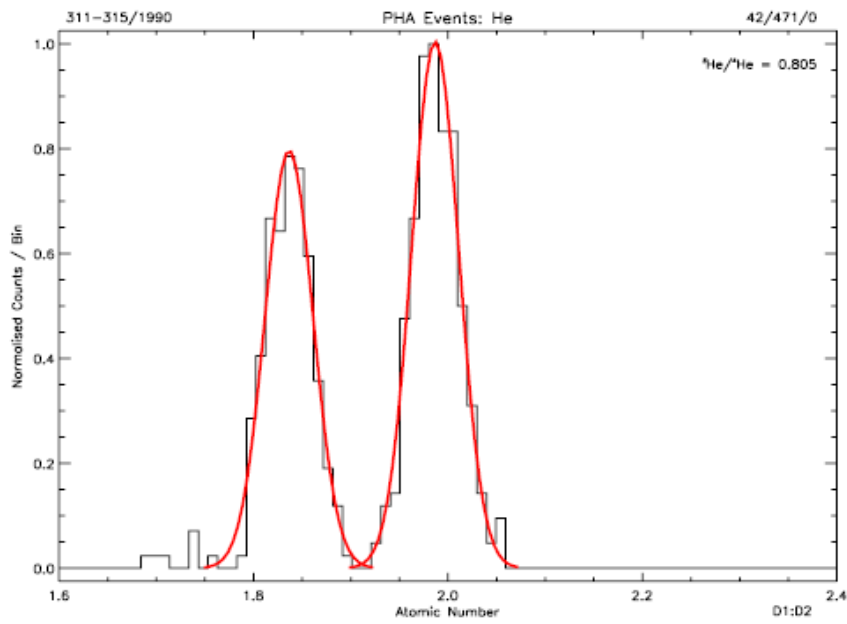
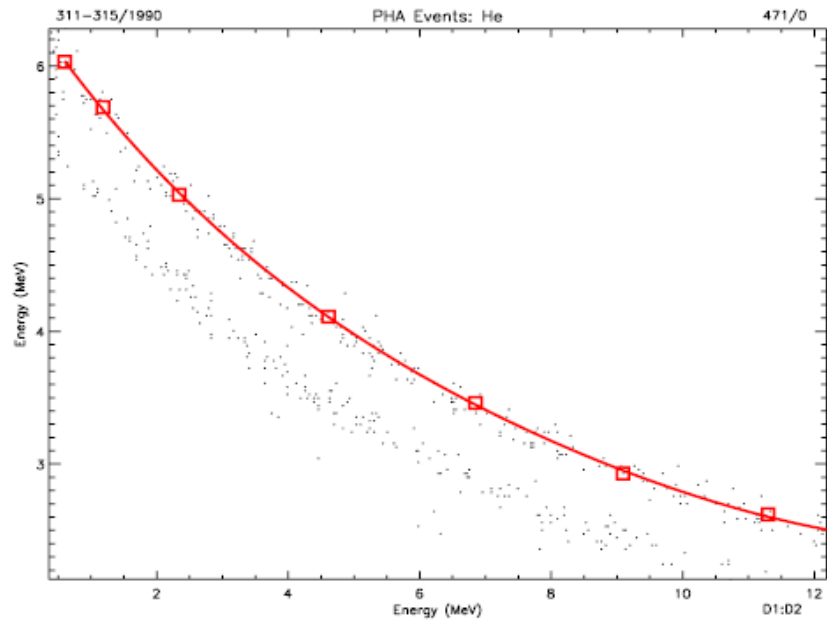


Fig. 6.1a Event “tracks” for Helium ions derived from flight data in the D1-D2 range, together with the reference track for  ${}^4\text{He}$  used in the PHA analysis routines (upper panel), and the corresponding charge histogram (lower panel). Separation of the isotopes  ${}^3\text{He}$  and  ${}^4\text{He}$  is clearly seen.

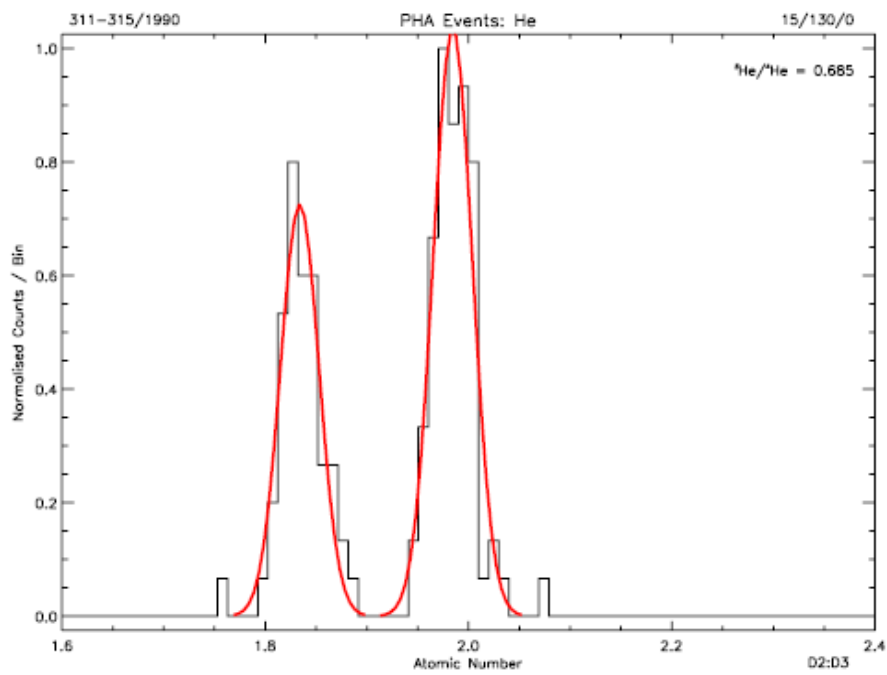
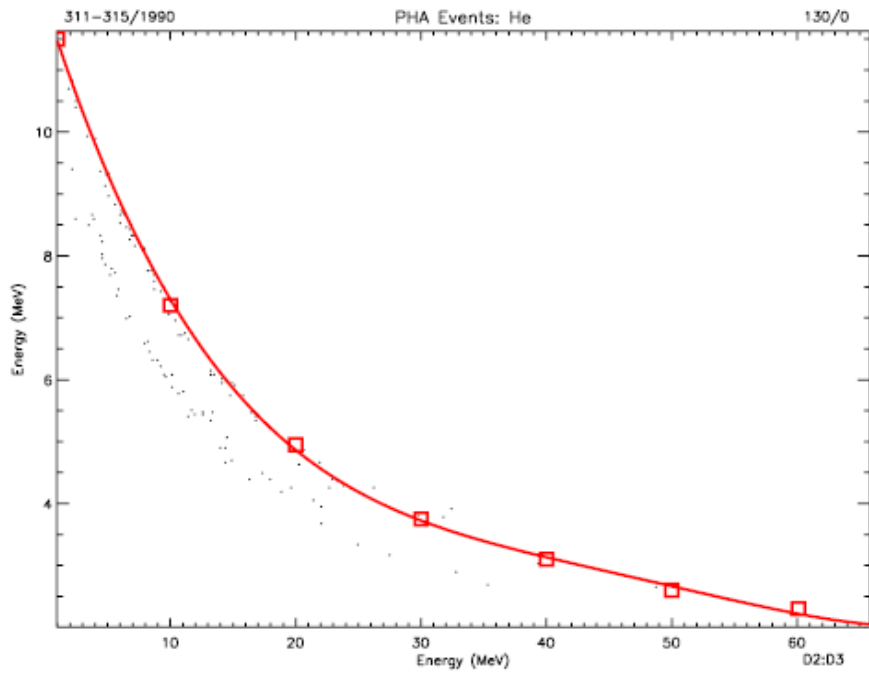


Fig. 6.1b As for Fig. 6.1a, but for the D2-D3 range.

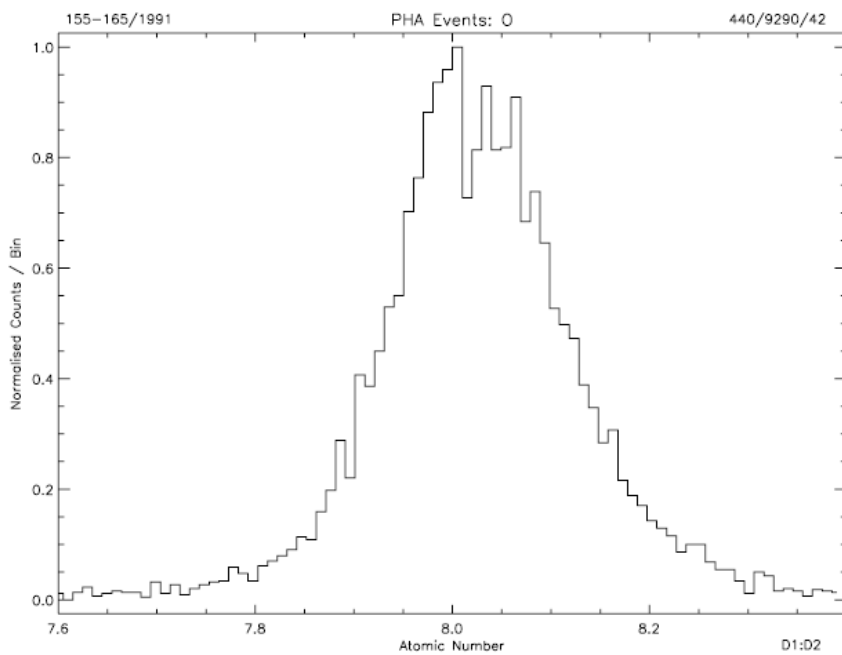
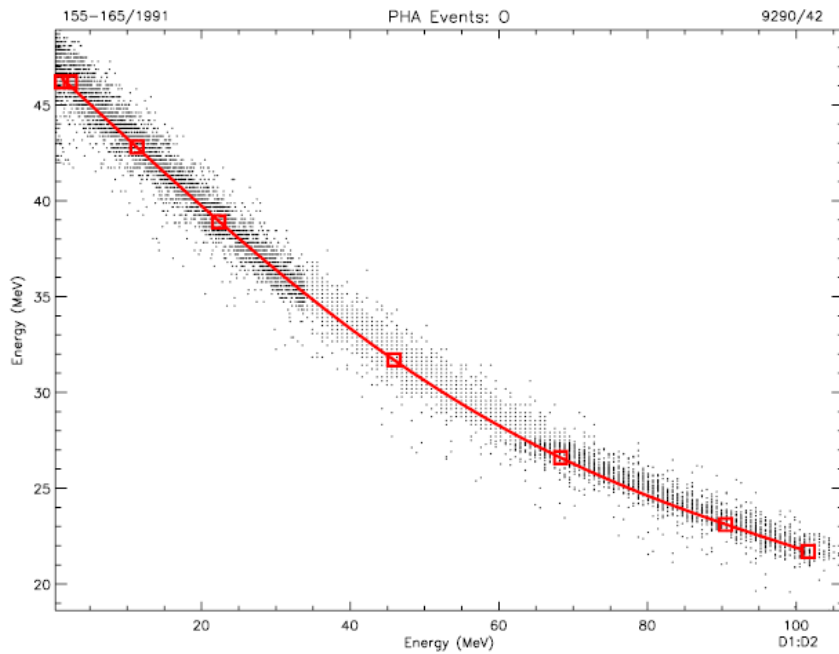


Fig. 6.2a Event “tracks” for Oxygen ions derived from flight data in the D1-D2 range, together with the reference track used in the PHA analysis routines (upper panel), and the corresponding charge histogram (lower panel).

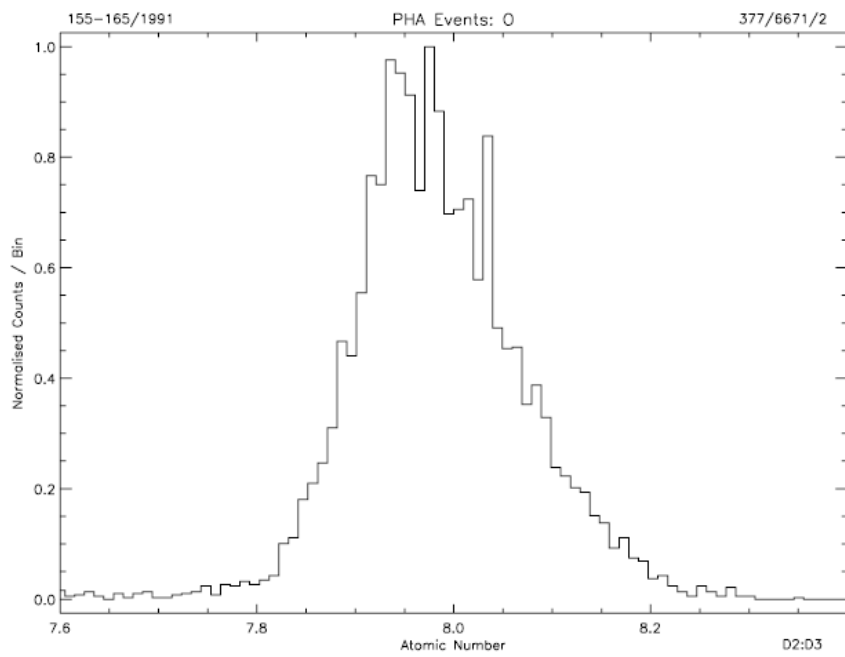
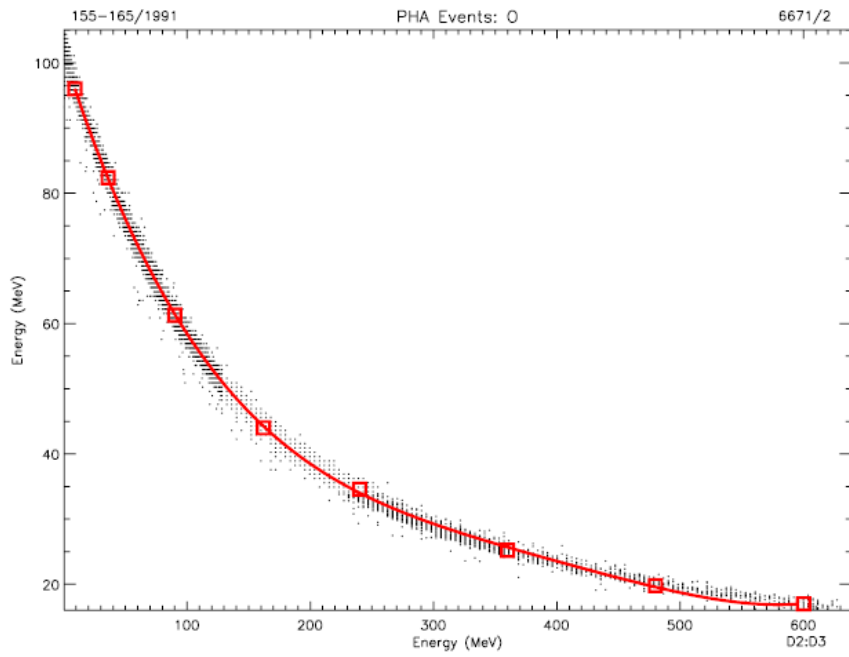


Fig. 6.2b As for Fig. 6.2a, but for the D2-D3 range.

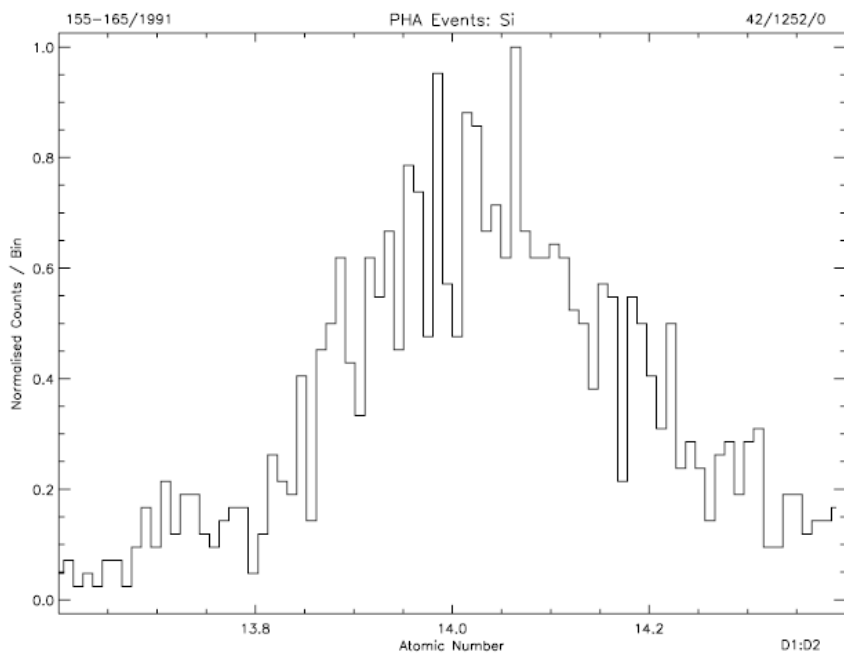
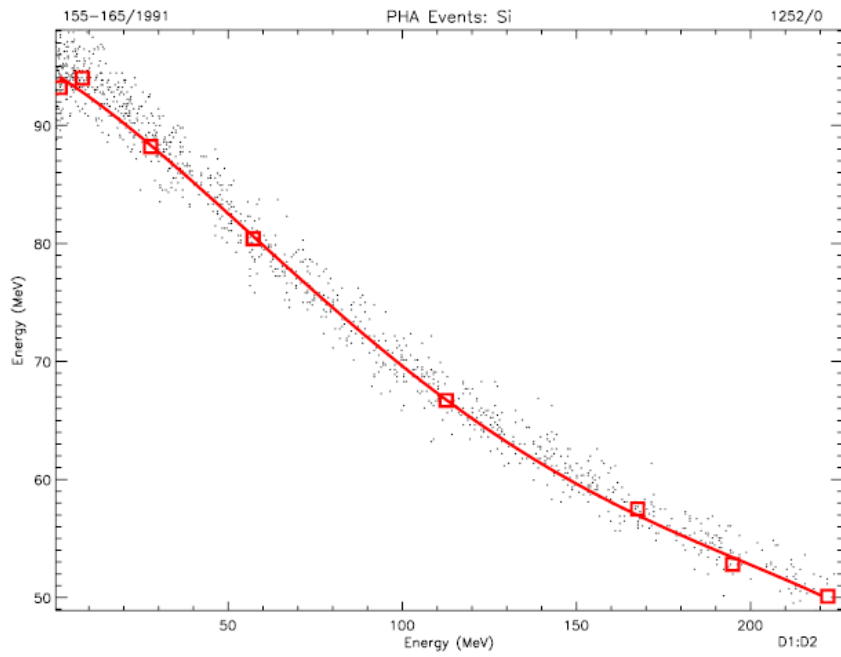


Fig. 6.3a Event “tracks” for Silicon ions derived from flight data in the D1-D2 range, together with the reference track used in the PHA analysis routines (upper panel), and the corresponding charge histogram (lower panel).

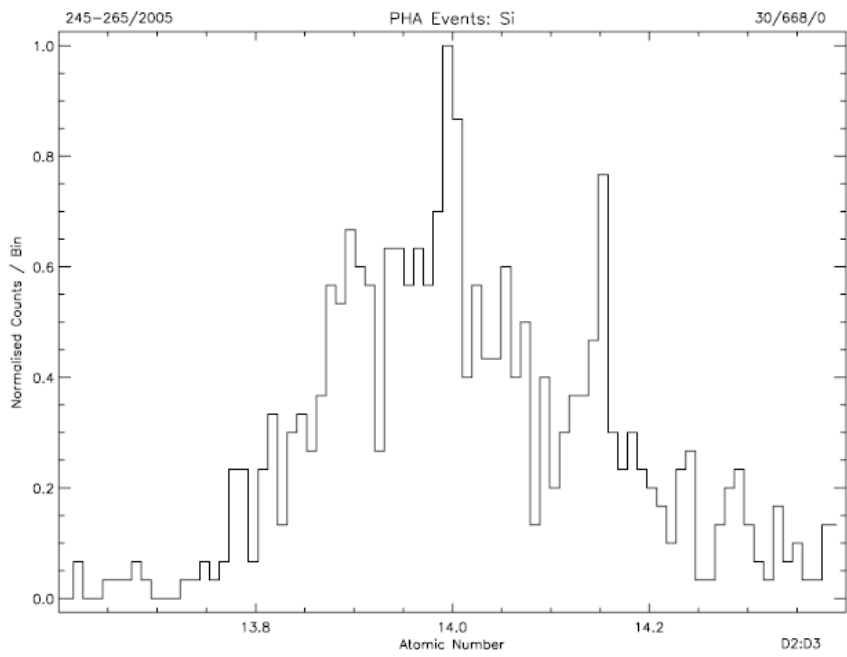
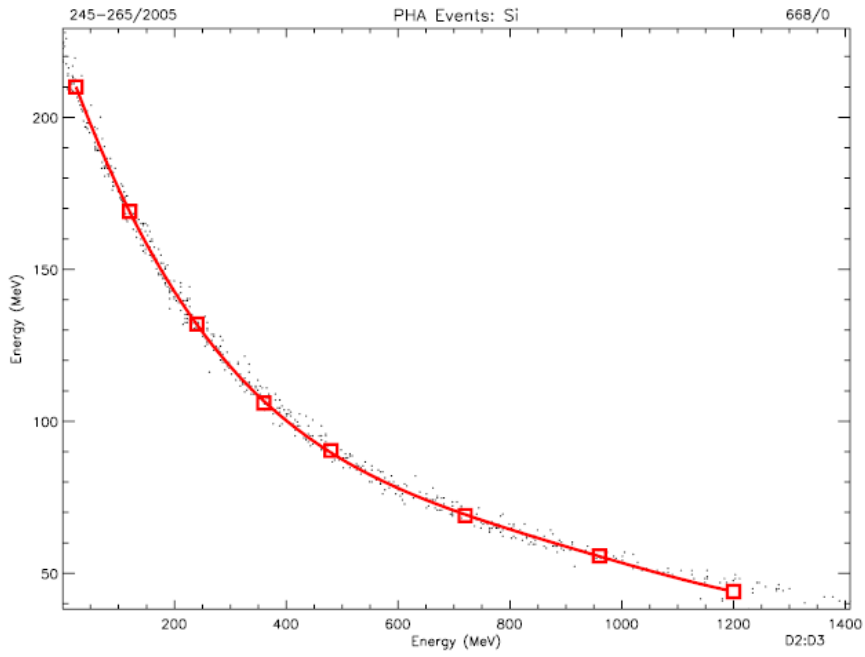


Fig. 6.3b As for Fig. 6.3a, but for the D2-D3 range.

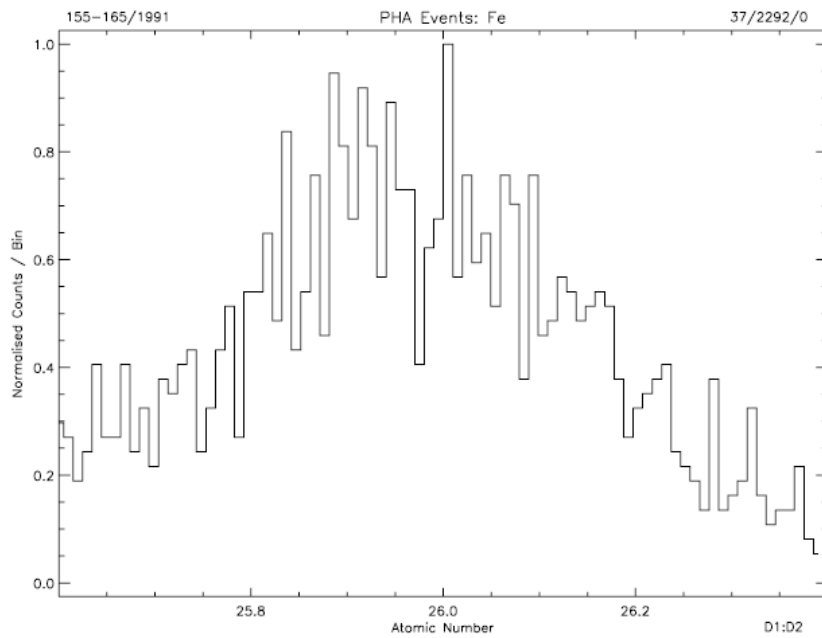
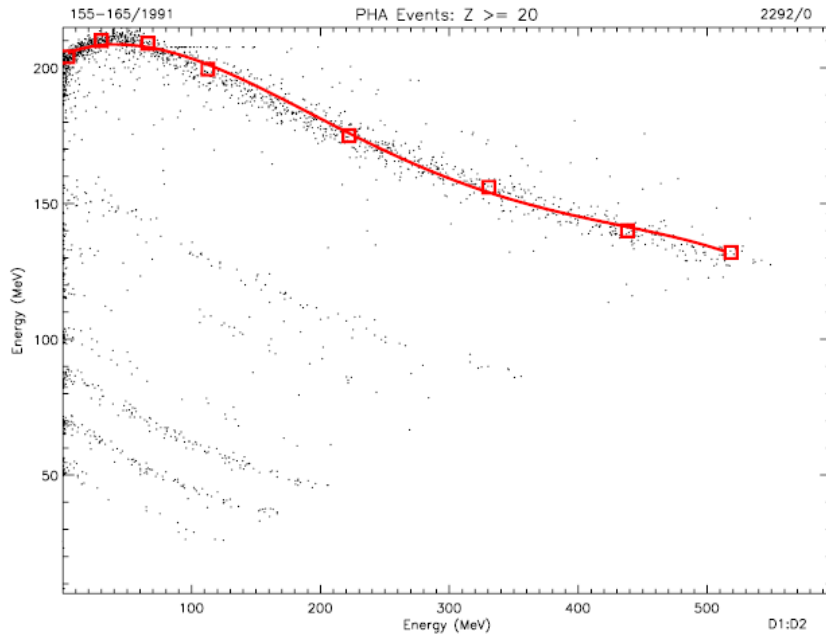


Fig. 6.4a Event “tracks” for Iron ions derived from flight data in the D1-D2 range, together with the reference track used in the PHA analysis routines (upper panel), and the corresponding charge histogram (lower panel).

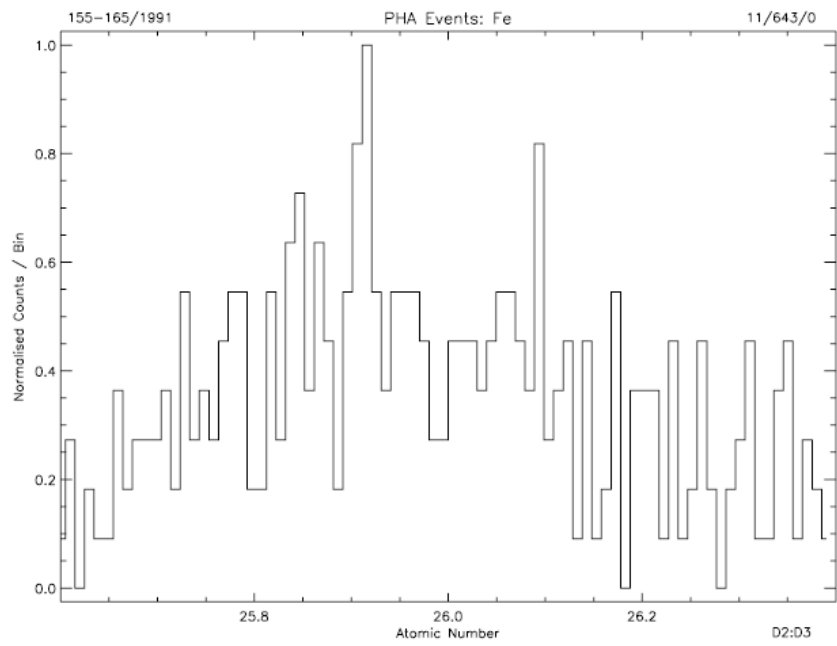
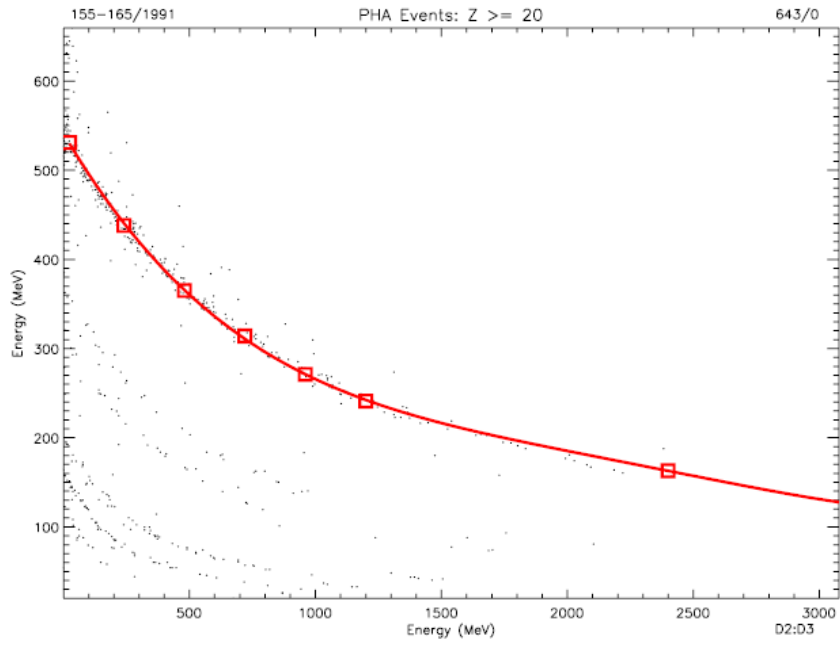


Fig. 6.4b As for Fig. 6.4a, but for the D2-D3 range.

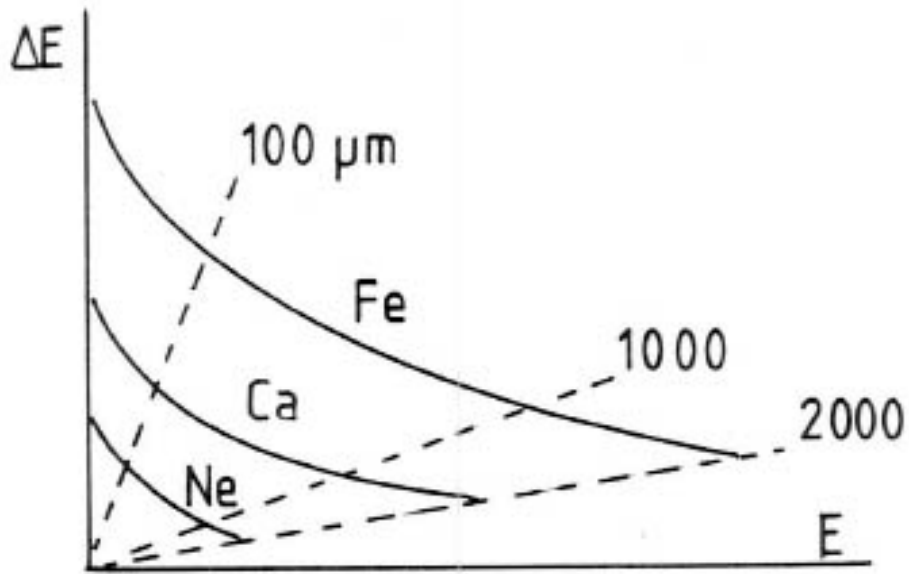


Fig. 6.5 Constant range lines plotted on a typical  $dE$  vs. residual  $E$  diagram.

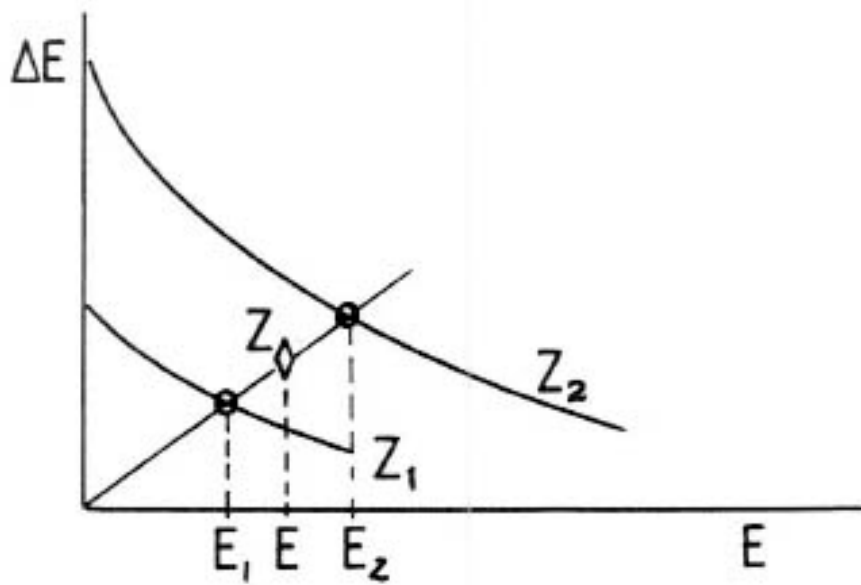


Fig. 6.6 Illustration of the LET charge interpolation algorithm using the reference tracks for  $Z_1$  and  $Z_2$  and the constant range approximation.

### LET Counting Rate Linearity

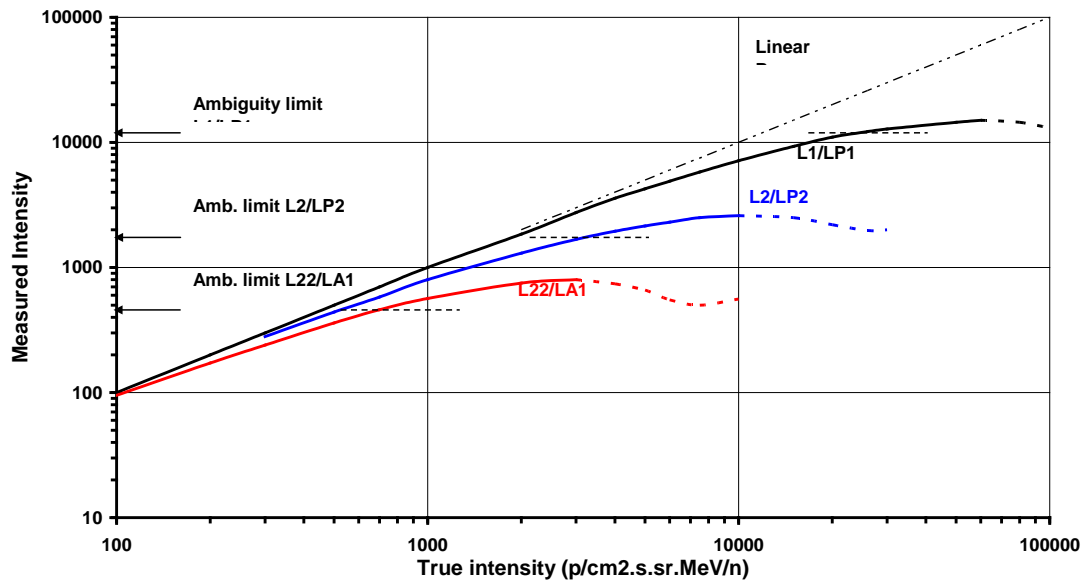


Fig. 7.1 LET counting rate linearity curves for channels L1, L2 and L22.

## ***Appendices***

- Marsden, R.G., J. Henrion, The prototype low-energy telescope system for the international solar polar COSPIN experiment, Report ESA STR-202, 1979.
- Kamermans, R., J. Henrion, R.G. Marsden, T.R. Sanderson, K.-P. Wenzel, Element and Isotope Separation for a Heavy Ion Cosmic Ray Telescope with Large Geometrical Factor, Nucl. Instr. and Meth., 171, 87, 1980.
- LeBorgne, J.F., J. Henrion, R.G. Marsden, T.R. Sanderson, K.-P. Wenzel, Accelerator calibration of the Low Energy Telescope of the International Solar Polar Mission COSPIN Experiment, Report ESA STM-224, 1981.
- Marsden, R.G., J. Henrion, T.R. Sanderson, K.-P. Wenzel, N. de Bray, H.P. Blok, Calibration of a Space-Borne Charged Particle Telescope Using Protons in the Energy Range 0.4 To 20 MeV, Nucl. Instr. and Meth., 221, 619, 1984.
- Marsden, R.G. et al., The Phobos Low Energy Telescope Charged Particle Experiment, Nucl. Instr. and Meth., 290, 211, 1990.
- Marsden, R.G., LET Calibration Document, 1990.
- Henrion, J., LET Response to high fluxes, Technical Report, 1992.

ESA STR-202  
January 1979

# **The prototype low-energy telescope system for the international solar polar COSPIN experiment**

R.G. Marsden & J. Henrion  
European Space Research & Technology Centre  
Noordwijk, The Netherlands

**european space agency / agence spatiale européenne**  
8-10, rue Mario-Nikis, 75738 PARIS 15, France

Published by ESA Scientific and Technical  
Publications Branch, ESTEC, Noordwijk,  
The Netherlands.

Printed in the Netherlands by ESTEC  
Reproduction Services.

790064

Copyright © 1979 by European Space Agency.

## TABLE OF CONTENTS

1. INTRODUCTION	1
2. DESCRIPTION OF THE LOW-ENERGY TELESCOPE	3
3. PRINCIPLE OF LET OPERATION	9
4. INSTRUMENT RESOLUTION	13
5. PRELIMINARY ACCELERATOR CALIBRATIONS	17
6. LET RESPONSE SIMULATIONS	21
7. CONCLUSION	27
ACKNOWLEDGEMENTS	28
REFERENCES	29
APPENDIX: RANGE-ENERGY DATA	31

## LIST OF FIGURES

Figure 1a.	Schematic of the low-energy telescope detector system.	4
Figure 1b.	LET anticoincidence shield and prototype detector telescope housing.	5
Figure 2.	Simplified diagram of LET electronics.	6
Figure 3.	Ideal LET response curves for events stopping in D3.	10
Figure 4.	Thickness profile of standard $30 \mu\text{m}$ $6 \text{ cm}^2$ surface-barrier detector.	18
Figure 5.	Simulated LET proton-counting rate channel response for an input spectrum $dJ/dE \propto E^{-1.0}$ .	22
Figure 6.	Matrix of simulated LET pulse-height data for $2 \leq Z \leq 14$ events stopping in D3.	24
Figure 7.	Matrix of simulated LET pulse height data for $Z = 2$ events stopping in D3, with D2 and D3 in high-gain mode.	25
Figure 8.	Mass histogram for helium computed from the data presented in Figure 7.	26

THE PROTOTYPE LOW ENERGY TELESCOPE SYSTEM FOR THE  
INTERNATIONAL SOLAR POLAR COSPIN EXPERIMENT

ABSTRACT

*This report describes the design and prototype evaluation of the Low Energy Telescope (LET) charged particle detector system included in the Cosmic Ray and Solar Charged Particle Investigations (COSPIN) collaborative experiment to be flown on the European spacecraft of the joint ESA/NASA International Solar Polar Mission. The principal features of the LET design are discussed, and the results of preliminary calibrations and response simulations are presented.*

1. INTRODUCTION

The Cosmic Ray and Solar Charged Particle Investigation (COSPIN) collaborative experiment to be flown on the European spacecraft of the joint ESA/NASA International Solar-Polar Mission is designed to provide comprehensive measurements of solar and galactic charged particles in the essentially unexplored regions of the heliosphere out of the plane of the ecliptic and over the solar poles. In order to accommodate the wide range of nuclear species, energies and fluxes which are likely to be encountered, the COSPIN experiment comprises four independent detection systems, each optimised to provide high-resolution measurements within a specific range of parameters. The system described in this note, the Low

Energy Telescope (LET), is designed and will be built by the Space Science Department to measure the composition and energy spectra of nuclei of hydrogen through iron in the energy range 300 keV/nucleon ( $H^1$ ) to greater than 75 MeV/nucleon ( $Fe^{56}$ ) with high spatial and temporal resolution. The results of these measurements will be used together with the data from the three complementary COSPIN detector systems to study the as-yet largely unsolved problems of solar particle propagation in 3 dimensions, the structure of the heliosphere and related interplanetary phenomena, and the modulation and possible sources of the galactic cosmic rays.

Since the final weight of the scientific payload is critical in determining the maximum heliographic latitude which the two solar polar spacecraft can achieve, a major constraint on the design of the COSPIN systems is the weight available. In addition, the nature of the mission is such that an experiment lifetime of at least four years is essential if the unique trajectory is to be fully exploited. These criteria, together with the ability to survive the harsh radiation environment encountered during the Jupiter swing-by phase, form the (severe) boundary conditions within which the scientific objectives of the LET detector system must be met.

## 2. DESCRIPTION OF THE LOW-ENERGY TELESCOPE

The LET uses four silicon solid state detectors of the surface barrier and lithium-drifted type, together with a plastic scintillator-photomultiplier combination as charged particle detection elements. These detector elements are shown in section in Figure 1a. D1 and D2 are surface barrier devices of equal active area ( $6.0 \text{ cm}^2$ ) having nominal thicknesses of 30 and 100 microns respectively, while D3 and D4 are 2000 micron-thick lithium-drifted devices of 10.0 and  $12.5 \text{ cm}^2$  active area respectively. Such devices, in particular D1, represent state-of-the-art in manufacture of charged-particle detectors of this type. Together with D4, the plastic scintillator guard counter D5 forms the anticoincidence shield for the main elements of the telescope. Figure 1b shows typical solid state and scintillator detector elements used for the preliminary laboratory and accelerator studies, together with the prototype solid state detector telescope housing with the D1 device in position. It should be noted that the base plate of this prototype housing was designed to interface with the laboratory calibration chamber platform, and as such is not representative of the envisaged flight hardware configuration.

The signals from D1, D2 and D3 are fed via charge-sensitive preamplifiers and pulse-shaping voltage amplifiers to a series of threshold discriminators

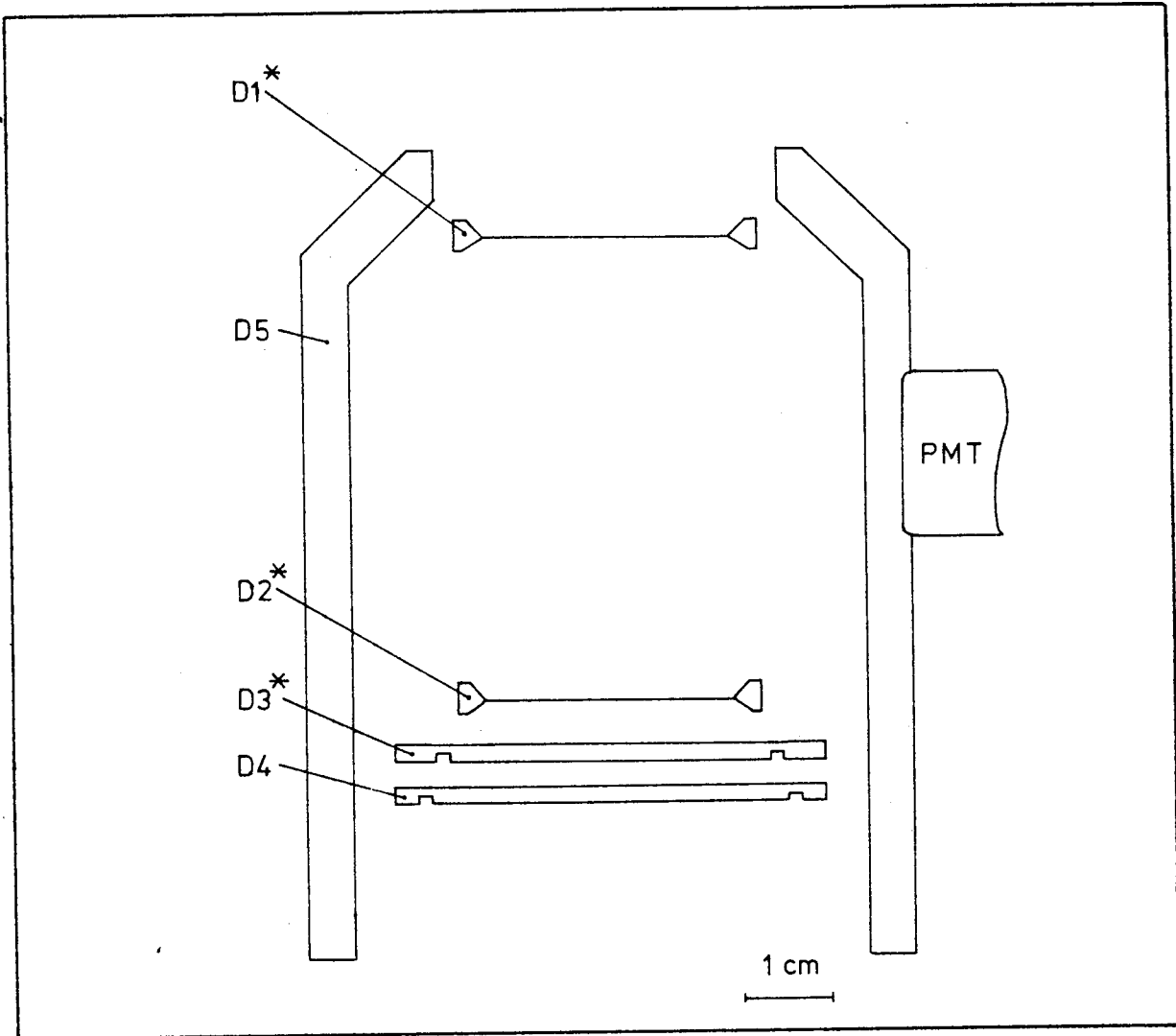
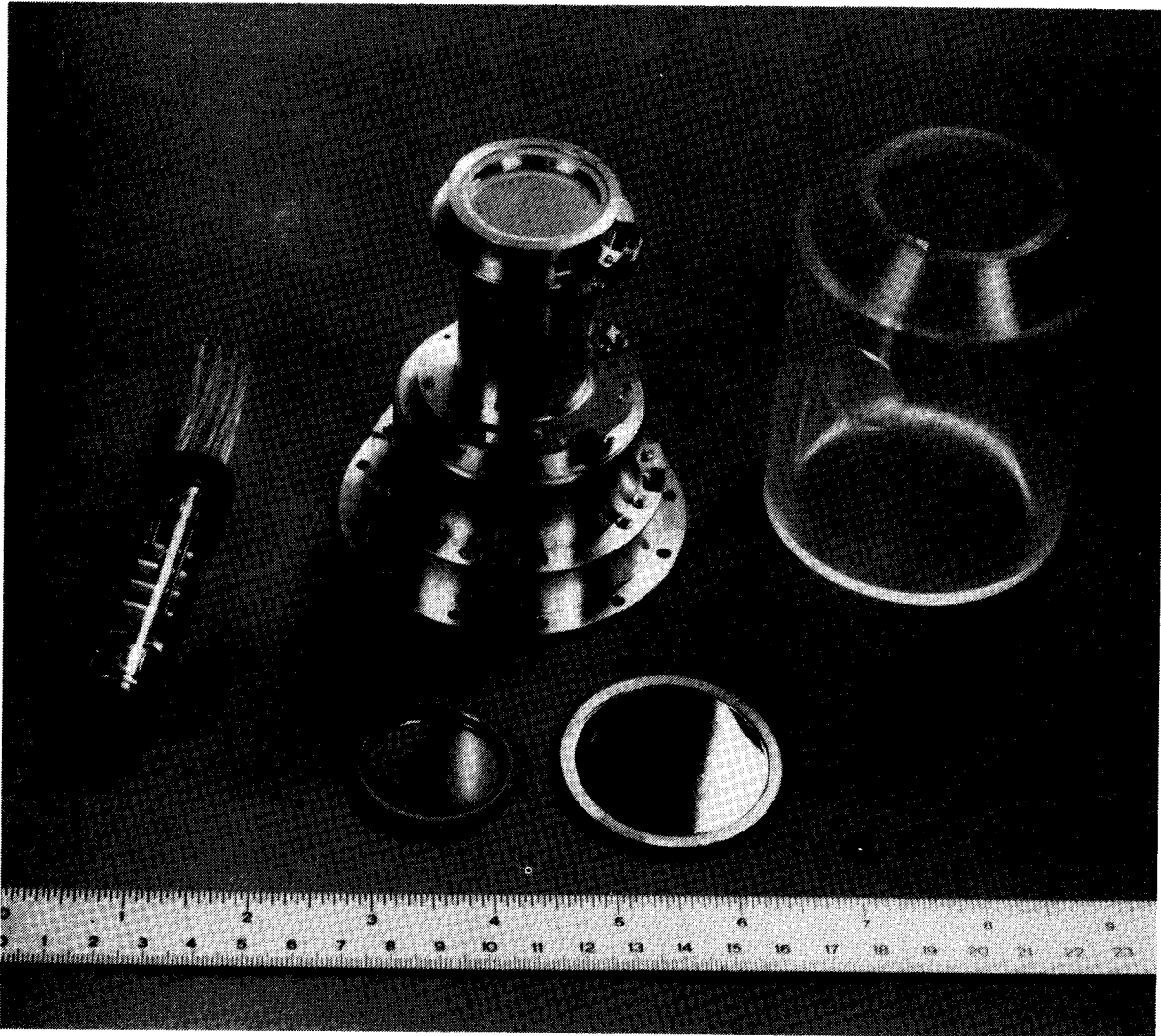


Figure 1a. Schematic of the low-energy telescope detector system.  $D_n^*$  indicates a pulse-height-analysed detector.

for counting rate information, and to the Particle Identifier System (described in detail in the next section) for species rate data, priority information and for sampling by 1024 (D1) and 2048 (D2 and D3) channel pulse height analysers (PHAs). In order to accommodate the large ( $\sim 10^4$ ) dynamic range in pulse amplitude from D1, D2 and D3 necessary for adequate resolution of protons through iron nuclei, dual gain voltage amplifiers are used. The gain selection is made in analogue switches controlled by fast amplifiers and discriminators.



*Figure 1b. Low-energy-telescope anticoincidence shield and prototype detector telescope housing, with typical surface-barrier and lithium-drifted solid-state detectors (D2- and D3-type).*

The constraints of radiation resistance and low weight placed upon the COSPIN experiment by the characteristics of the mission have to a large extent dictated the philosophy concerning the construction of the LET analogue and digital electronics. The logic functions are performed by radiation-hardened CMOS integrated circuits, thick-film substrate technology being employed to provide a very high degree of packing density and reliability. The linear circuitry utilises predominantly hybrid and monolithic microcircuits (radiation hardened) with some discrete components,

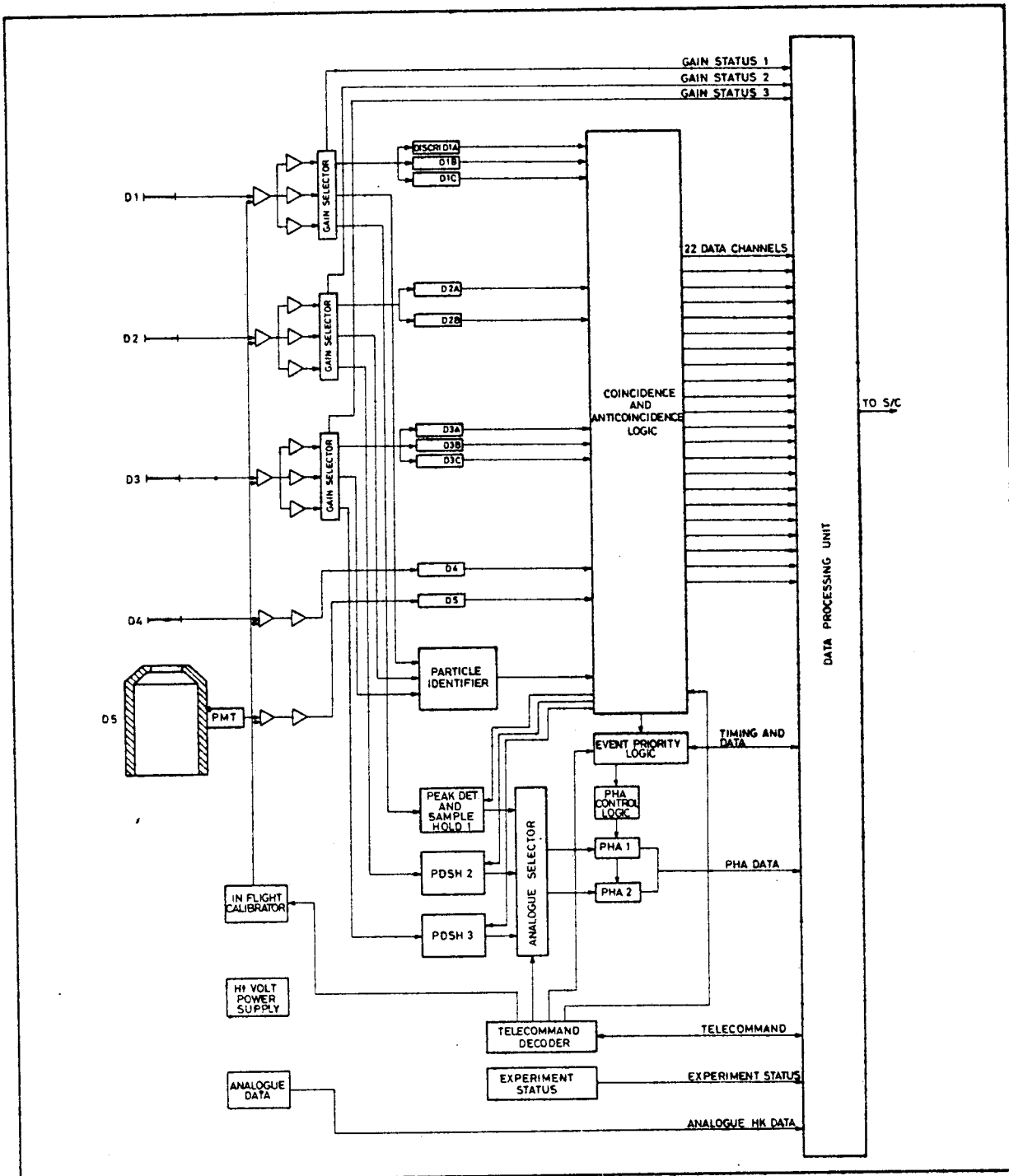


Figure 2. Simplified diagram of LET electronics.

spot shielded where necessary. This type of construction leads to a package having minimum weight for a system of high complexity. A schematic of the LET analogue and digital electronics is shown in Figure 2.

Data from the LET are telemetered in the form of spin-averaged counting rate information for proton, alpha and heavy-ion energy channels, together with pulse-height information on a sampled event-by-event basis for  $Z \geq 2$  events. In order to facilitate the study of the spatial distribution of the particle flux, the counts in two of the proton channels are also accumulated in eight consecutive equatorial sectors of  $45^\circ$ , the telescope axis being perpendicular to the spacecraft spin axis.

BLANK PAGE

### 3. PRINCIPLE OF LET OPERATION

The LET utilises the well-known technique of measuring the energy loss in one or more thin absorbers together with the total incident particle energy to distinguish among the various nuclei of which the charged particle flux consists. This method relies on the fact that the range at a given energy per nucleon of charged particles in matter is, to a first approximation, proportional to the mass of the particle divided by the square of its charge. If the energy lost in a thin absorber is plotted as a function of the residual energy deposited in a second absorber for particles stopping in that absorber, events belonging to a given nuclear species will lie on a unique "track" in such a plot. In Figure 3, the loci of some typical LET tracks are plotted in the D2 versus D3 plane, for events incident parallel to the telescope axis. In reality, events will show some scatter about these ideal lines, owing to the finite resolution of the instrument. This will be discussed in the next section. Provided this scatter is not too large, however, the tracks corresponding to individual species can be identified in such a matrix of D1 versus D2 or D2 versus D3 pulse-height data and thus enable relative abundances and energy spectra to be determined. In order to provide separate counting-rate information for different groups of nuclear species, the LET has an on-board Particle Identi-

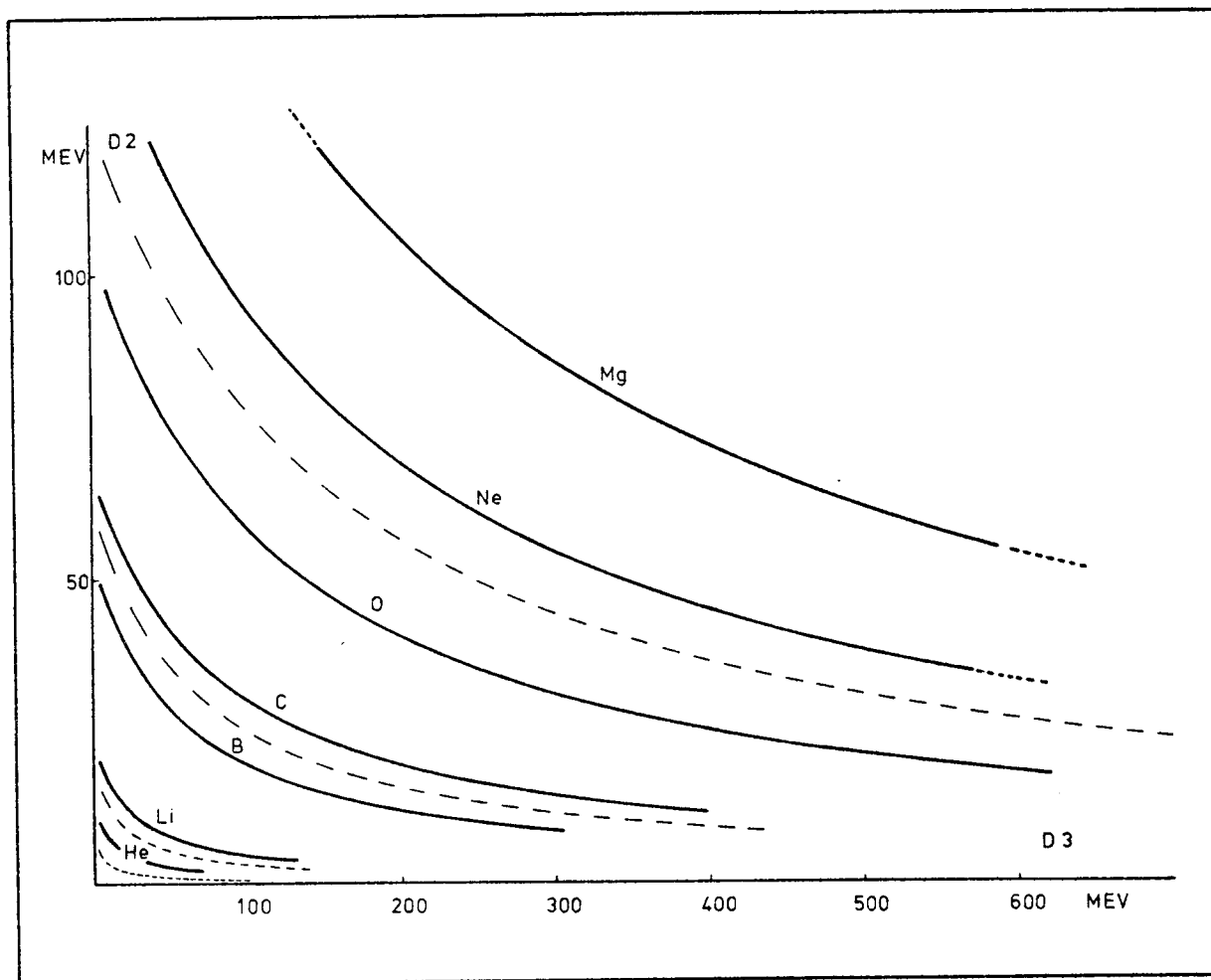


Figure 3. Ideal LET response curves (D2 vs. D3) for events stopping in D3. Dashed lines represent nominal particle identifier system charge-discrimination boundaries.

fier System, which employs a unique set of analogue function generators and discriminators to divide the response into different regions of charge and mass. The nuclide tracks in matrices of the type described above can be fitted empirically by a function

$$\Delta E \cdot (E_{\text{Residual}} + a) = b$$

where  $\Delta E$  is the energy lost in the thin detector(s),  $E_{\text{Residual}}$  is the residual energy for stopping particles, and  $a$  and  $b$  are constants for a given species track. It is clear that boundaries having the same functional form can be used to efficiently divide the " $\Delta E$  versus

residual E" matrix into regions of different mass and charge. Examples of such boundaries are shown in Figure 3 as dashed lines. The LET Particle Identifier System generates, for each valid event stopping in D3, four analogue functions of the type

$$F_i = S2 * (S3 + a_i) \quad i = 1, 2, 3, 4$$

where S2 and S3 are the analogue signals from D2 and D3 respectively, and  $a_i$  is a constant. These values are then applied to a series of threshold discriminators corresponding to different values of the constant b to determine to which region of the D2 vs. D3 matrix the analysed event belongs. These regions correspond to the charge groups  $Z = 1$ ,  $Z = 2$ ,  $3 \leq Z < 6$ ,  $6 \leq Z < 10$  and  $Z \geq 10$ . Additional analogue functions having the form

$$G_i = S1 + C_i S2 \quad i = 1, 2, 3, 4$$

and

$$G_i = S2 + C_i S3 \quad i = 5$$

are used to identify the corresponding charge groups for valid events stopping in D2 ( $i = 1$  to 4) and  $Z > 20$  events stopping in D3 ( $i = 5$ ).

Each of the above charge groups has an associated counting-rate register which is incremented each time a valid event within that group is observed. In addition, the signals for all  $Z \geq 2$  events which stop in either D2 or D3 and do not trigger the anticoincidence elements are pulse-height analysed and stored in a temporary buffer in the LET Event Priority System. In order to maximise the collection efficiency of the rarer species in the incident flux, the LET transmits the highest priority event occurring within each telemetry cycle according to a set of predetermined event-priority levels. Each priority assignment is maintained for a number of

telemetry cycles and then replaced on a rotational basis by a different sequence. Such a Priority System is necessary, because the limitation in available telemetry allows LET PHA data to be transmitted at a maximum rate of only  $\sim 1$  event per second.

The combined operation of the Particle Identifier System and the Event Priority System ensures that no single event type dominates the PHA data sampling during high-counting-rate conditions, whilst at the same time maintaining counting-rate information for all valid events. The complete table of LET priority assignments is to be stored in a single ROM.

#### 4. INSTRUMENT RESOLUTION

The ability to identify the different nuclides incident on the instrument is clearly dependent on the degree of particle track separation apparent in the data matrices. This track separation is a function of the spread in energy loss for a given particle of a given incident energy traversing one or both of the thin D1 and D2 detectors, and it is possible to identify several independent contributions to the spread. Namely,

- 1) Pathlength variations in the thin detector(s) due to the finite opening angle of the telescope system.
- 2) Pathlength variations in the thin detector(s) due to variations in the thickness of these detectors across their active areas.
- 3) Fluctuations in energy loss due to the statistical nature of the processes involved.
- 4) Electronic noise introduced into the system.

While, during the design of the LET, attempts were made to minimise the first two contributions to spread just listed, it was necessary to bear in mind at all stages the requirements imposed by the scientific aims of the experiment. On the one hand, the LET must possess sufficient charge and mass resolution to perform charge identification of species from hydrogen up to and including the iron group nuclei from as low an energy

as possible, while also being able to identify separately the isotopes of helium  $^3\text{He}$  and  $^4\text{He}$ . On the other hand, owing to the nature of the spacecraft's trajectory after it leaves the plane of the ecliptic, the sampling time within a given band of heliographic latitude is relatively short (of the order of 30 days). Since the particle flux in these regions can be expected to be low, the collecting power of the LET must be maximised. This, in turn, implies as large a geometrical factor as possible. These two requirements - high mass resolution and large geometrical factor - are fundamentally conflicting in two areas. Firstly, a large geometrical factor implies a large opening angle, which in turn causes large variations in path length through the telescope. Secondly, given the current state of the art, thin solid-state detectors having large areas suffer from an intrinsic variation of thickness across their active area, which is due to the etching process involved in their manufacture. In the case of the LET, this latter problem is most acute for D1, where, even when strict selection criteria are applied to finished flight-quality detectors, it is difficult to achieve a uniformity better than ca.  $\pm 6\%$  for a nominal  $30\ \mu\text{m}$  thick device of  $600\ \text{mm}^2$  active area. In addition to limiting the intrinsic mass resolution for events stopping in D2 (so-called 2-D or 2-parameter events), this thickness variation problem also affects the 3-D resolution, since the energy lost in *both* thin detectors is compared to provide a self-consistency check for events stopping in D3. The final LET specifications are the result of a careful trade-off between these two conflicting requirements.

The third source of resolution degradation listed above is largely a physical limitation and represents the maximum achievable resolution for an ideal telescope in which all other contributions are negligible. The effects are largest for energy losses that are small compared with the

total incident energy and result in the well-known Landau broadening of the energy-loss distribution towards higher energy losses. For the greater part of the LET response, this effect is not expected to be serious. The contribution of electronic noise to the energy resolution, and hence to the mass resolution, is governed to some extent by the extremely large dynamic range needed from the LET analogue electronics and also by the intrinsic electronic noise of the solid-state devices themselves. This imposes a threshold of  $\gtrsim 300$  keV on the D1 and D2 detector signals, but does not represent a contribution to the mass-resolution degradation of the same magnitude as that of the path-length variations.

BLANK PAGE

## 5. PRELIMINARY ACCELERATOR CALIBRATIONS

As was discussed in the previous section, the thickness uniformity of the thin surface-barrier solid-state devices to be used as the D1 and D2 detecting elements of the LET plays an essential role in determining the resolution of the telescope. With this in mind, a preliminary mapping of two "off-the-shelf" 30- $\mu\text{m}$ , 6- $\text{cm}^2$  devices using carbon-12 accelerator beams of 42 and 54 MeV was performed with the cyclotron at the University of Louvain-la-Neuve, Belgium, during April 1977. The technique used was to study the variation in energy loss (for a penetrating beam of carbon-12 particles incident normal to the detector surface) measured at different points on the detector surface. Using standard range energy curves<sup>†</sup>, these variations in energy loss were converted to equivalent variations in detector thickness. Since the mapped devices were in no way preselected from the point of view of uniformity, the measurements were intended primarily to provide a realistic guideline against which more stringent flight-quality device specifications could be made. An example of a measured uniformity profile is shown in Figure 4, where the inferred detector thickness is plotted for several positions along a diameter. Also shown is a scale giving the actual measured

---

<sup>†</sup>see Appendix.

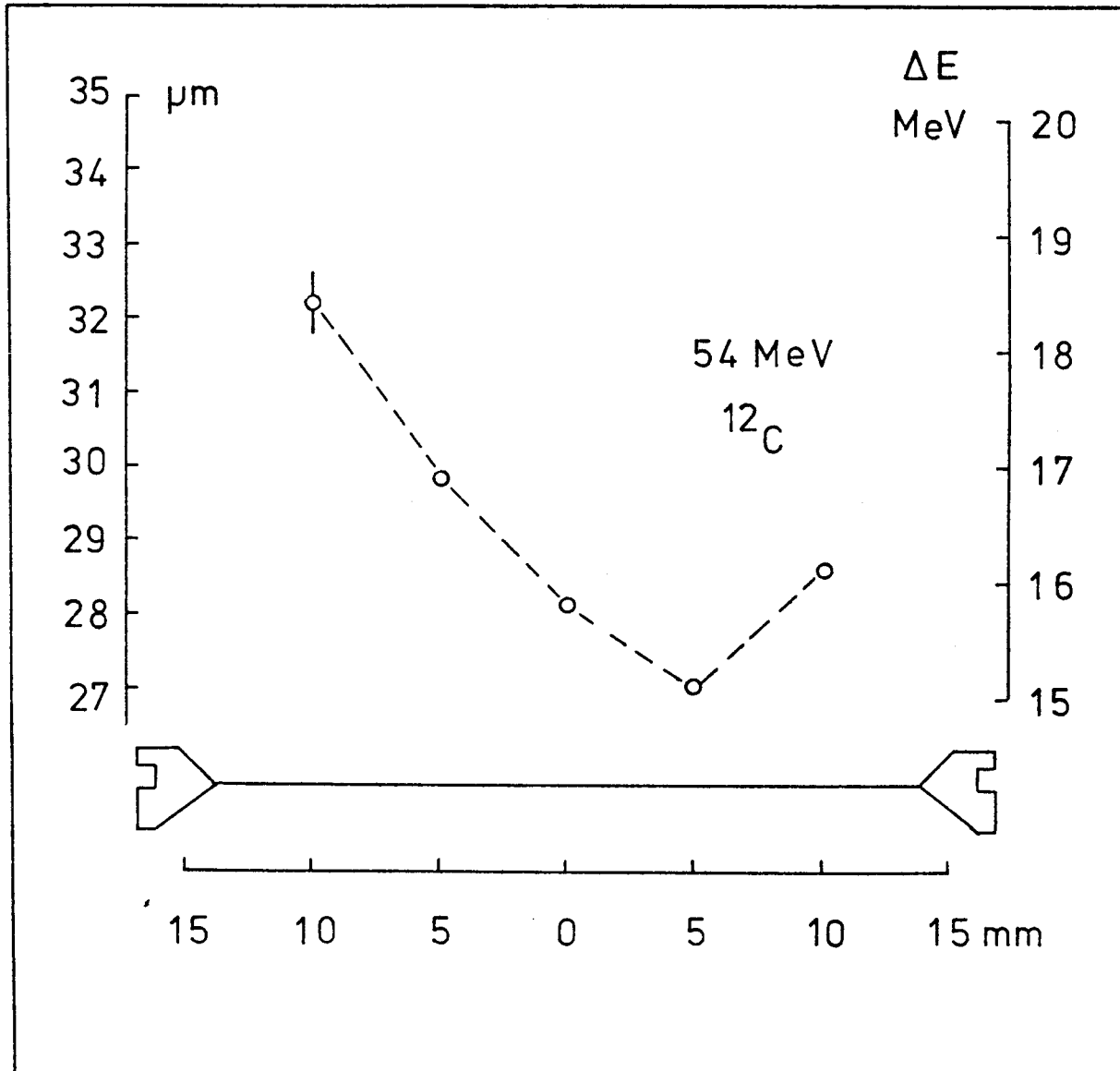


Figure 4. Thickness profile of standard  $30 \mu\text{m}$   $6 \text{ cm}^2$  surface-barrier detector as measured with a 54 MeV carbon-12 accelerator beam

energy loss at each point in MeV. As can be seen, this profile shows a range of thicknesses from  $\sim 27$  to 33 microns, an unacceptably large spread for use as a flight-quality LET DI element. The second device showed somewhat better uniformity, but was still below an acceptable flight standard. On the basis of these measurements taken together with the experiment design aims, a maximum allowable variation of  $\pm 1.75$  microns

in thickness has been established for the flight detector specifications concerning D1 and D2.

In addition to providing a measurement of the relative uniformity of the thin D1 elements, the carbon-12 accelerator runs are useful in establishing a reference point for the energy-loss calculations needed to predict the response of the instrument to other heavy ions. However, since such extrapolations rely to a large extent on calculated range-energy data which are known to contain rather large uncertainties, further accelerator calibrations using the complete telescope will be needed to determine the detailed response of the instrument.

BLANK PAGE

## 6. LET RESPONSE SIMULATIONS

In order to gain an insight at an early stage in the LET design into which parameters most sensitively affect the telescope performance, a series of computer-based calculations was carried out to simulate the response of the LET detector elements to directional and isotropic fluxes of charged particles. The basis for such calculations was the evaluation of the energy lost by an incident ion in a series of absorbers representing both the active telescope elements as well as the mechanical structure, followed by the application of appropriate logic conditions to the resulting "signals".

Events were selected by a Monte Carlo method in which ion energy and arrival direction were chosen at random from given distributions, together with the point of impact upon the absorber configuration. In order to simplify the geometry, all absorbers were required to be annular or disk-like in form. The initial trajectory information enabled the pathlengths in all intersected absorbers to be calculated and, hence, via standard range-energy tables, the energy lost in each such absorber to be found. In a typical run, some 5000 - 10 000 events were analysed. The signals from the active detecting elements D1 through D5 were analysed for coincidence conditions and threshold discriminator

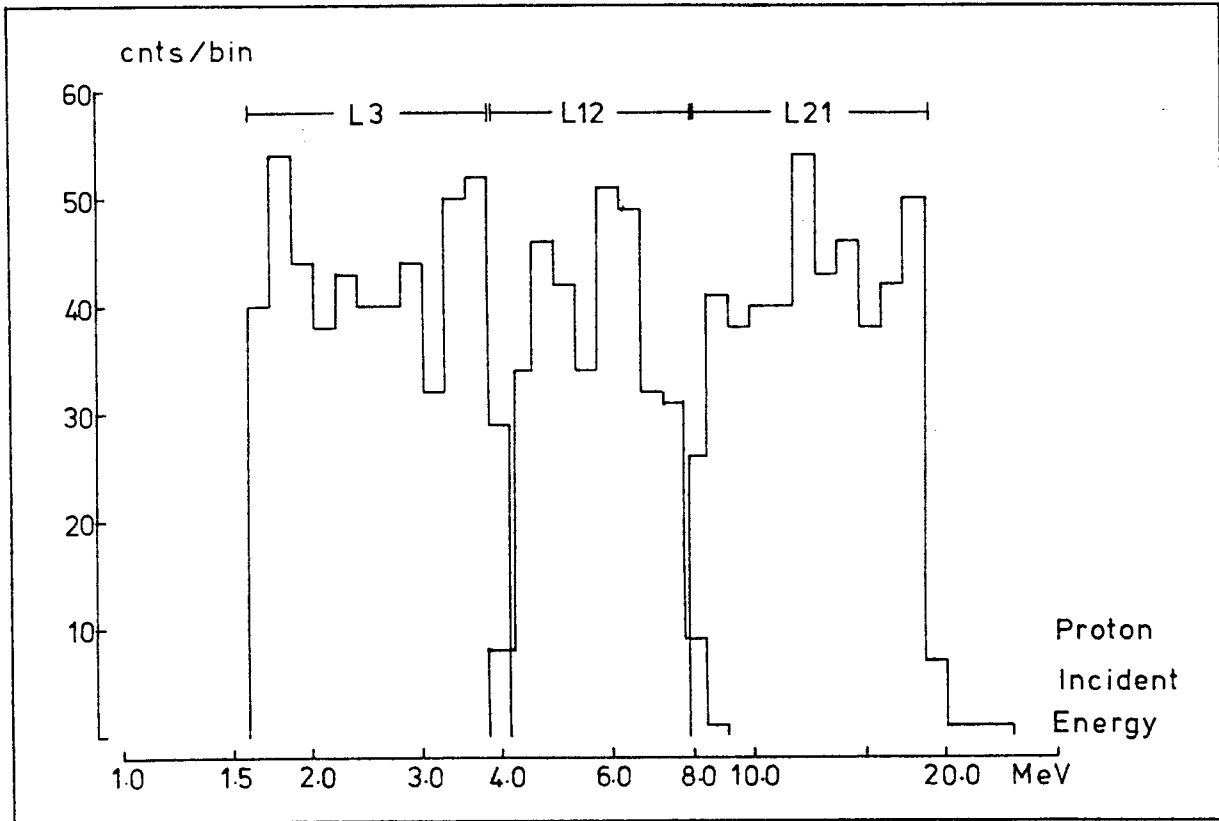


Figure 5. Simulated LET proton counting rate channel response for an input spectrum  $dJ/dE \propto E^{-1.0}$ . The nominal energy bandwidths are also indicated.

firing in the same manner as is effected by the experiment electronics, in addition to possible pulse-height information analysis for D1, D2 or D3. Since the energy pass-bands of the LET counting rate channels are defined on the basis of a given combination of coincidence and discriminator logic, Monte Carlo runs of the type described above are extremely useful when attempts are made to evaluate the extent to which a given rate channel having a certain nominal energy bandwidth is likely to be contaminated by higher- (or lower-) energy events. This particularly true in the case of protons, for which no pulse-height information is anticipated in the prototype LET design. Results of calculations performed for several of the LET proton channels are shown in Figure 5, together with the nominal

channel widths. As can be seen, the expected contamination in these cases is rather small, indicating "clean" channels.

Monte Carlo runs using heavy ions (helium through iron) have been used to investigate the expected resolution of the LET PHA data. For these runs, the effects of thickness variations in the solid state detectors and statistical variations in the energy loss were also taken into account. From each run a data set of  $\sim 12\,000$  events was compiled, including up to 13 different species with specified relative abundances and energy spectra, from which subsets could be made on the basis of, for example, the number of detectors triggered. A display of a typical data set is given in Figure 6, where a D2 versus D3 matrix of helium through argon events is shown together with the appropriate Particle Identifier System discriminator boundaries. At each location in the matrix is printed, according to a coding system, the number of events possessing that pair of pulse heights. The species tracks are clearly visible in this example, since the relative abundances of the rarer particles have been artificially increased over their expected levels for purposes of illustration.

Figure 7 shows a similar matrix, this time displaying helium-3 and helium-4 data with an input ratio  ${}^3\text{He}/{}^4\text{He}$  of 0.1. In so-called " ${}^3\text{He}$ -rich" solar flare events<sup>1,2,3)</sup> this ratio can take values ranging from 0.2 to greater than  $\sim 5$ ; the value of 0.1 thus represents a worst-case situation. So that the predicted mass resolution for helium could be investigated, the matrix data were summed along the particle tracks in intervals of 0.1 mass units (amu). The resulting mass histogram is shown in Figure 8. As can be seen, both mass peaks are clearly visible. The helium-4 distribution has a FWHM

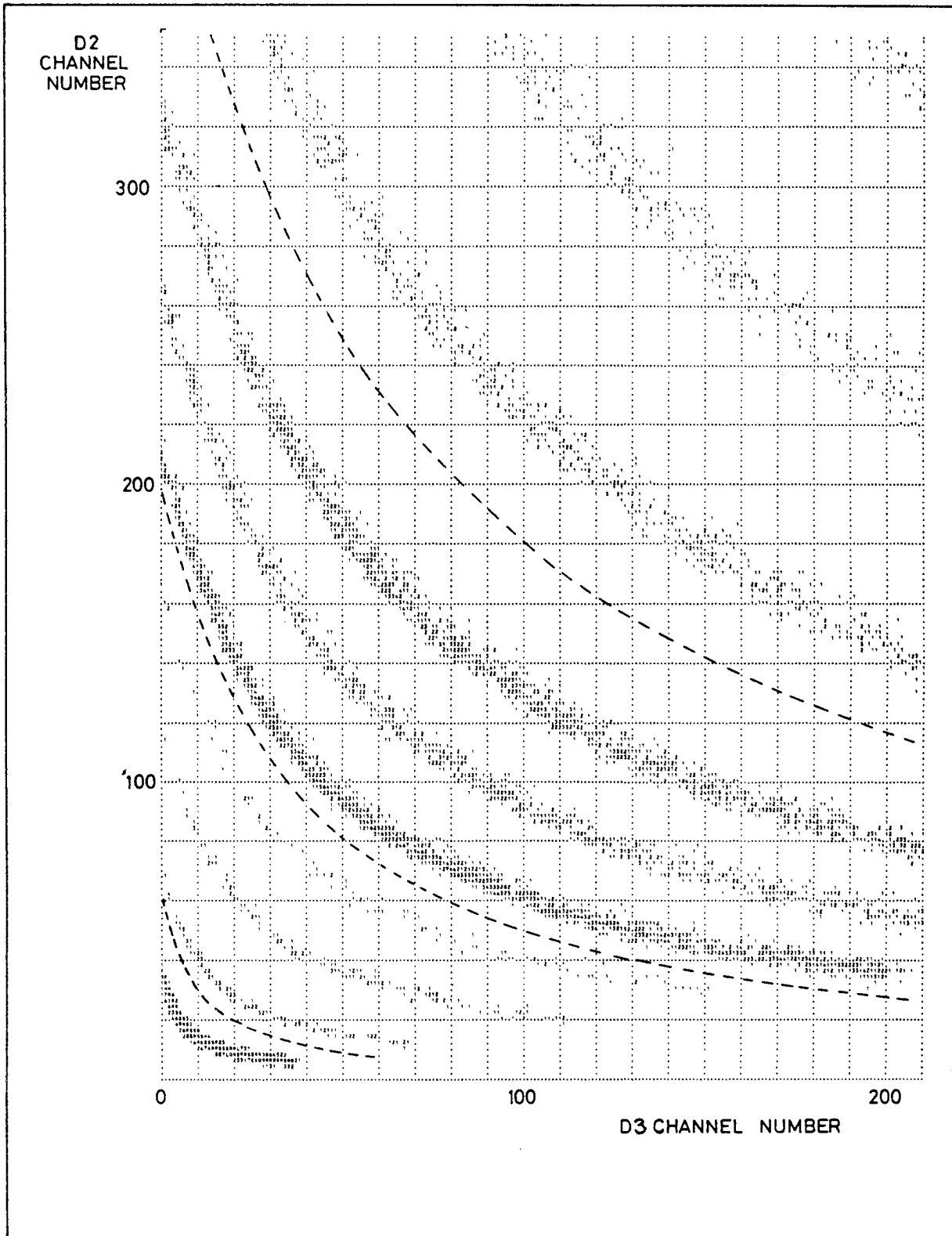


Figure 6. Matrix of simulated LET pulse-height data for  $2 < Z < 14$  events stopping in D3. Dashed lines represent nominal particle identifier system charge-discrimination boundaries.

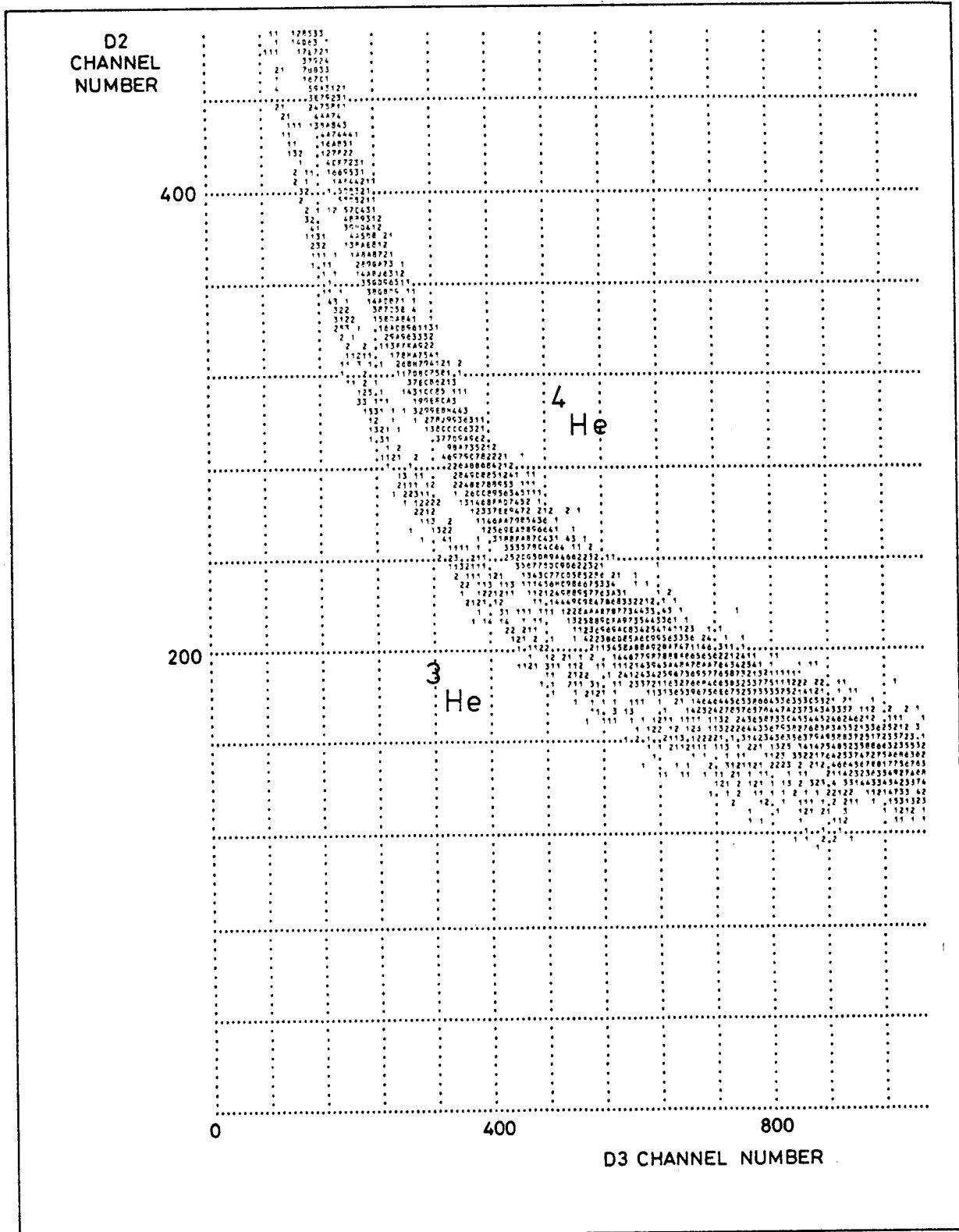


Figure 7. Matrix of simulated LET pulse height data for Z = 2 events stopping in D3, with D2 and D3 in high-gain mode.

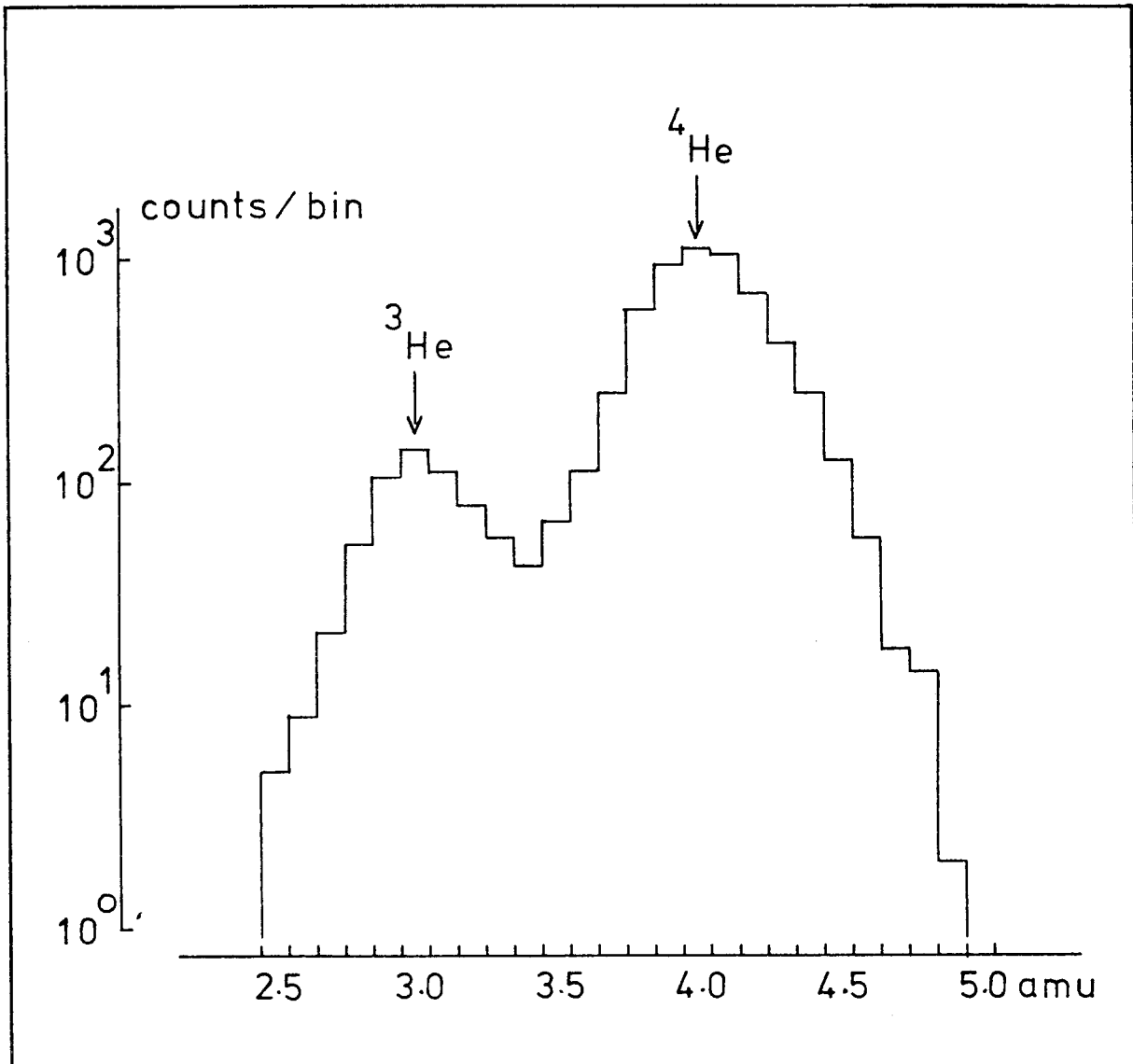


Figure 8. Mass histogram for helium computed from the data presented in Figure 7.

of  $\sim 0.5$  amu ( $\sigma \sim 0.22$  amu), giving a peak separation of  $\sim 4.5 \sigma$  in the energy range considered (4 to 14 MeV/nucleon for  $^4\text{He}$ ). It should be noted that no background event generation was included in the simulation program, so the results shown here are to a certain degree best case. Nonetheless, they do confirm that the detector parameters chosen in the LET design (e.g. thickness-uniformity limits etc.) are compatible with the instrument resolution dictated by the scientific aims of the experiment.

## 7. CONCLUSION

The aim of the Low Energy Telescope system, as stated in the introduction to this report, is to measure - with high spatial and temporal resolution - the composition and energy spectra of nuclei of hydrogen through iron in the energy range 300 keV/nucleon for protons to greater than 75 MeV/nucleon for iron-group nuclei. Moreover, these measurements are to be made with an instrument of low weight and high reliability, especially with respect to its resistance to radiation. The design evaluation and simulations described here have shown that the proposed LET system can achieve these aims.

Further calibrations using the prototype instrument with beams of accelerated nuclei are planned, in order to provide a complete picture of the telescope response, and these measurements should confirm the results of the computer-simulated response studies, while at the same time providing an input to improve their accuracy. In this way, the LET design can be optimised to provide an instrument possessing the capabilities that will enable it to operate effectively in the variety of (essentially unknown) conditions it will encounter during the International Solar Polar Mission.

## ACKNOWLEDGEMENTS

The authors wish to thank the other members of the Cosmic Ray Division at ESTEC for their valuable input at various stages during the definition of the LET experiment, in particular Dr. K.-P. Wenzel for his constant encouragement and support. Dr. R.B. McKibben of IASR, Enrico Fermi Institute of the University of Chicago, is thanked for several very useful discussions and for providing one of the Monte Carlo computer programs. Richard G. Marsden was supported by an ESA Research Fellowship during the course of this work.

## REFERENCES

1. Garrard T L Stone E C & Vogt R E, The isotopes of H and He in solar cosmic rays. *Proc of a symposium on high energy phenomena on the Sun held at Goddard Space Flight Center, Greenbelt, Maryland, USA, September 28-30, 1972*. Ramaty R & Stone R G (Eds), NASA SP-342, 341-354 (1973).
2. Anglin J D, The relative abundances and energy spectra of solar-flare-accelerated deuterium, tritium and helium-3. *Ap J* 198 733 (1975).
3. Anglin J D, Dietrich W F & Simpson J A, Super enrichments of Fe-group nuclei in solar flares and their association with large  $^3\text{He}$  enrichments. *Proc of the 15th International Conf on Cosmic Rays, Budapest*, 5 43 (1977).
4. Barkas W H & Berger M J, Tables of energy losses and ranges of heavy charged particles. *Studies in penetration of charged particles in matter*, NAS-NRC Publication No. 1133, Nuclear Science Series (1964).
5. Northcliffe L C & Schilling R F, Range and stopping-power tables for heavy ions. *Nuclear Data Tables* 7(A), Nos. 3 & 4 (1970).
6. Greiner D E, A versatile, high-resolution particle identifier - Theory. *Nucl. Instrum. and Methods* 103 291-308 (1972).
7. Janni J F, *Calculations of energy loss, range, path length, straggling, multiple scattering and the probability of inelastic nuclear collisions for 0.1- to 1000-MeV protons*. Air Force Weapons Laboratory Technical Report AFWL-TR-65-150 (unpublished) (1966).

Approved for publication on 16th November 1978

BLANK PAGE

A P P E N D I X

## RANGE-ENERGY DATA

In order to compute an accurate representation of the response of a given solid-state-detector telescope configuration to charged-particle radiation, it is first necessary to produce a realistic set of range-energy curves for energetic nuclei in silicon, and any other materials used in the construction of the telescope. Since there are no experimental data covering the required dynamic range in mass and energy (1 - 60 amu;  $< 0.01 - 1000$  MeV/nucleon) encountered in cosmic-ray experiments, it becomes necessary to rely on semi-empirical extrapolations of the available data. Detailed tabulations based on this technique have been given by Barkas and Berger<sup>4)</sup> and Northcliffe and Schilling<sup>5)</sup>, and it is the latter which are normally used in calculations of detector response. These particular tables have disadvantages, however, in that they extend in energy only to 12 MeV/nucleon, and that no direct tabulation is given for silicon (aluminium being the nearest stopping medium given). The range-energy data used predominantly in the LET simulations are the result of computations based upon the treatment of Greiner<sup>6)</sup> which takes as its starting point the proton energy-loss calculations of Janni<sup>7)</sup> which agree rather well with experimental determinations. Corrections are applied to these proton data to include effects important when heavy ions

are considered. Of these effects, the most important are charge neutralisation by electron capture and nuclear stopping. Since heavy nuclei of the energies of interest here do not pass through an absorbing medium fully stripped of electrons, the nuclear charge  $Z$  must be replaced by a velocity-dependent effective charge, which is less than  $Z$  at low velocities. The so-called nuclear stopping correction is due to the fact that a small fraction of the incident particle energy is lost to the absorbing medium without causing ionisation, and as such is not measured by a solid-state detector.

Applying these corrections leads to an expression for  $dE/dx$ , the energy lost by a given ion per unit pathlength in a given medium for energies from 0.01 MeV/nucleon up to 1000 MeV/nucleon tabulated at energy intervals sufficiently small to allow linear interpolation. Clearly, such empirically deduced tables may show systematic differences from the available experimental data, especially at very low energies. Nevertheless, they do form a self-consistent data set from which useful calculations can be made, the results of which can be re-normalised to experimentally determined charged particle telescope response data if necessary.

ESA STM-224  
December 1981

# **Accelerator calibration of the Low Energy Telescope of the International Solar Polar Mission COSPIN Experiment**

J.F. Le Borgne, J. Henrion, R.G. Marsden,  
T.R. Sanderson & K.-P. Wenzel  
European Space Research & Technology Centre  
Noordwijk, The Netherlands

**european space agency / agence spatiale européenne**  
8-10, rue Mario-Nikis, 75738 PARIS CEDEX 15, France

ESA Scientific and Technical Memoranda are informal documents reporting on scientific or technical work carried out by the Agency or on its behalf. The opinions expressed and the conclusions reached carry the approval of the Head of Department concerned, but do not necessarily reflect the policy of the Agency.

This document was approved for publication on 17th November 1981. It has been edited by W.R. Burke, is published by ESA Scientific and Technical Publications Branch and has been printed in The Netherlands by ESTEC Reproduction Services.

Job No.: 820123

ISSN 0379 - 4075

Price code: C1

Copyright © 1982 by European Space Agency

## ABSTRACT

*In this paper, the results of heavy-ion calibration measurements performed with the Low Energy Telescope of the International Solar Polar Mission's COSPIN experiment are presented. It is shown that the instrument is capable of resolving adjacent elements at least up to argon, with a separation of better than seven standard deviations in the energy range 5 to 50 MeV/n.*

## ACKNOWLEDGEMENTS

The authors gratefully acknowledge the invaluable assistance of many members of the Space Science Department of ESA and the supporting Divisions at ESTEC during the development and construction of the LET. We should also like to thank Dr H Crawford, Dr F Lothrop and their colleagues at the Lawrence Berkeley Laboratory for their help and hospitality during the calibration runs. One of the authors (J F Le Borgne) was supported by an ESA Research Fellowship during the course of this work. The Low Energy Telescope is part of the Cosmic Ray and Solar Charged Particle Investigations experiment for the International Solar Polar Mission, for which Professor J A Simpson is Principal Investigator.

CONTENTS

1	INTRODUCTION	1
2	THE LOW-ENERGY TELESCOPE	1
3	CALIBRATION	6
4	EXPERIMENTAL RESULTS	11
5	CONCLUSION	20
	REFERENCES	21

# ACCELERATOR CALIBRATION OF THE LOW-ENERGY TELESCOPE OF THE INTERNATIONAL SOLAR POLAR MISSION COSPIN EXPERIMENT

## 1 INTRODUCTION

The Cosmic Ray and Solar Charged Particle investigation (COSPIN) forms part of the payload of the ESA spacecraft in the International Solar Polar Mission (ISPM). This collaborative experiment is designed to provide comprehensive measurements of solar and galactic charged particles in the region out of the ecliptic plane that the spacecraft will explore. The Low Energy Telescope (LET) is one of the five sensors forming COSPIN. It is designed to measure the composition and energy spectra of hydrogen to iron nuclei in the energy range extending from  $\sim 300$  keV/nucleon ( $^1\text{H}$ ) to greater than 75 MeV/nucleon ( $^{56}\text{Fe}$ ) with high spatial and temporal resolution.

The principal features of the LET design and preliminary calibration results have been reported by Marsden and Henrion (1979) and by Kamermans et al. (1980). This paper reports further accelerator calibration data obtained during exposure of the LET engineering unit (EU) to argon and neon beams at the BEVALAC-BEVATRON accelerator of the Lawrence Berkeley Laboratory (LBL) at the University of California, Berkeley.

## 2 THE LOW ENERGY TELESCOPE (LET)

The instrument (of which Figure 1a is a photograph and Figure 1b a schematic representation) consists of a four-element solid-state detector telescope (D1-D4), surrounded by a cylindrical plastic scintillator anti-coincidence shield (D5). The telescope aperture is covered by two thin foils, an inner titanium foil 2  $\mu\text{m}$  thick and an outer Kapton foil 7  $\mu\text{m}$  thick. D1 and D2 are surface barrier devices of equal active area (6.0  $\text{cm}^2$ ) having nominal thicknesses of 30 and 100  $\mu\text{m}$  respectively, while D3 and D4 are 2 000  $\mu\text{m}$  thick lithium-drifted devices of 10.0 and 12.5  $\text{cm}^2$  active area respectively. D4 forms part of the anticoincidence shield.

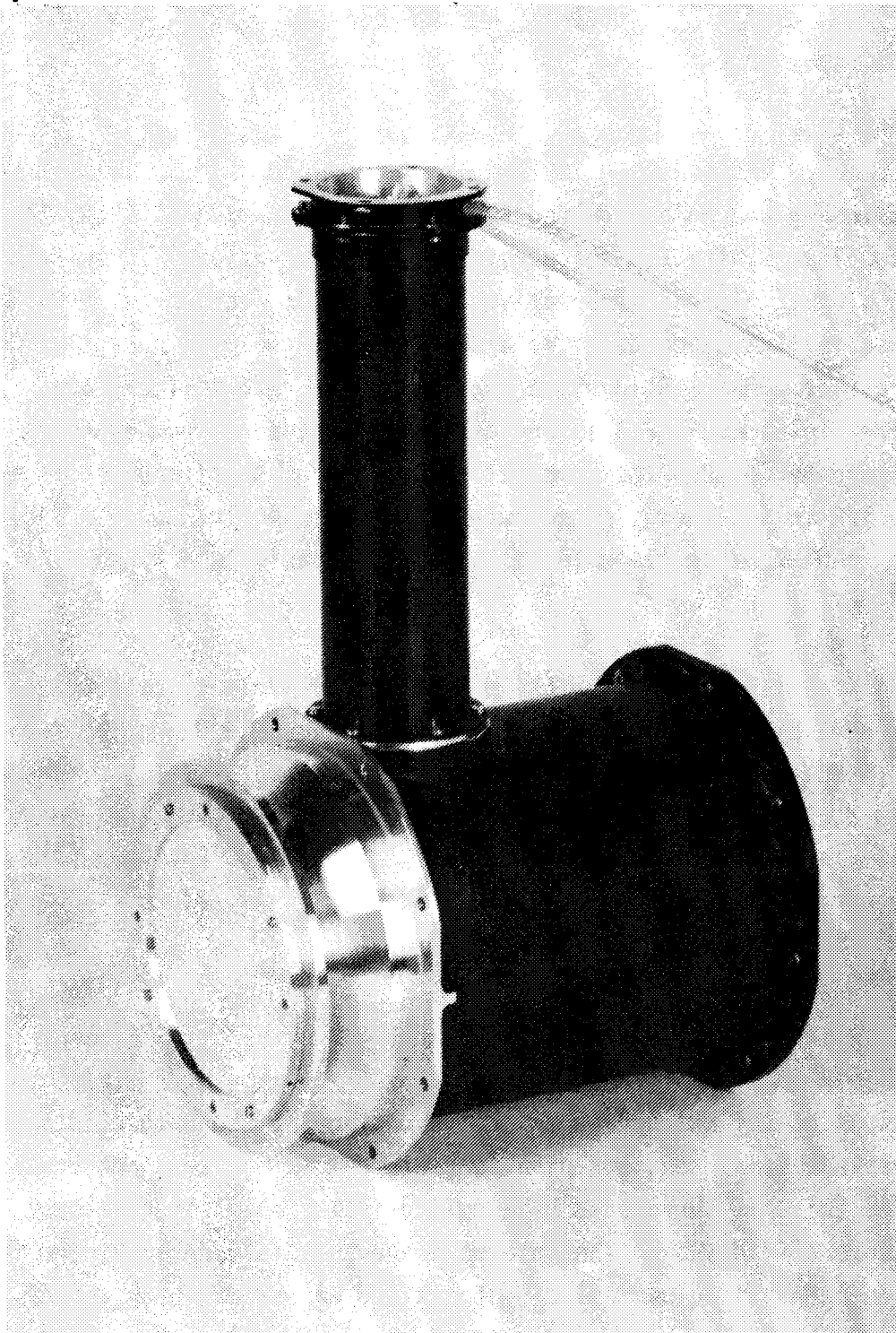


Figure 1a Photograph of the LET

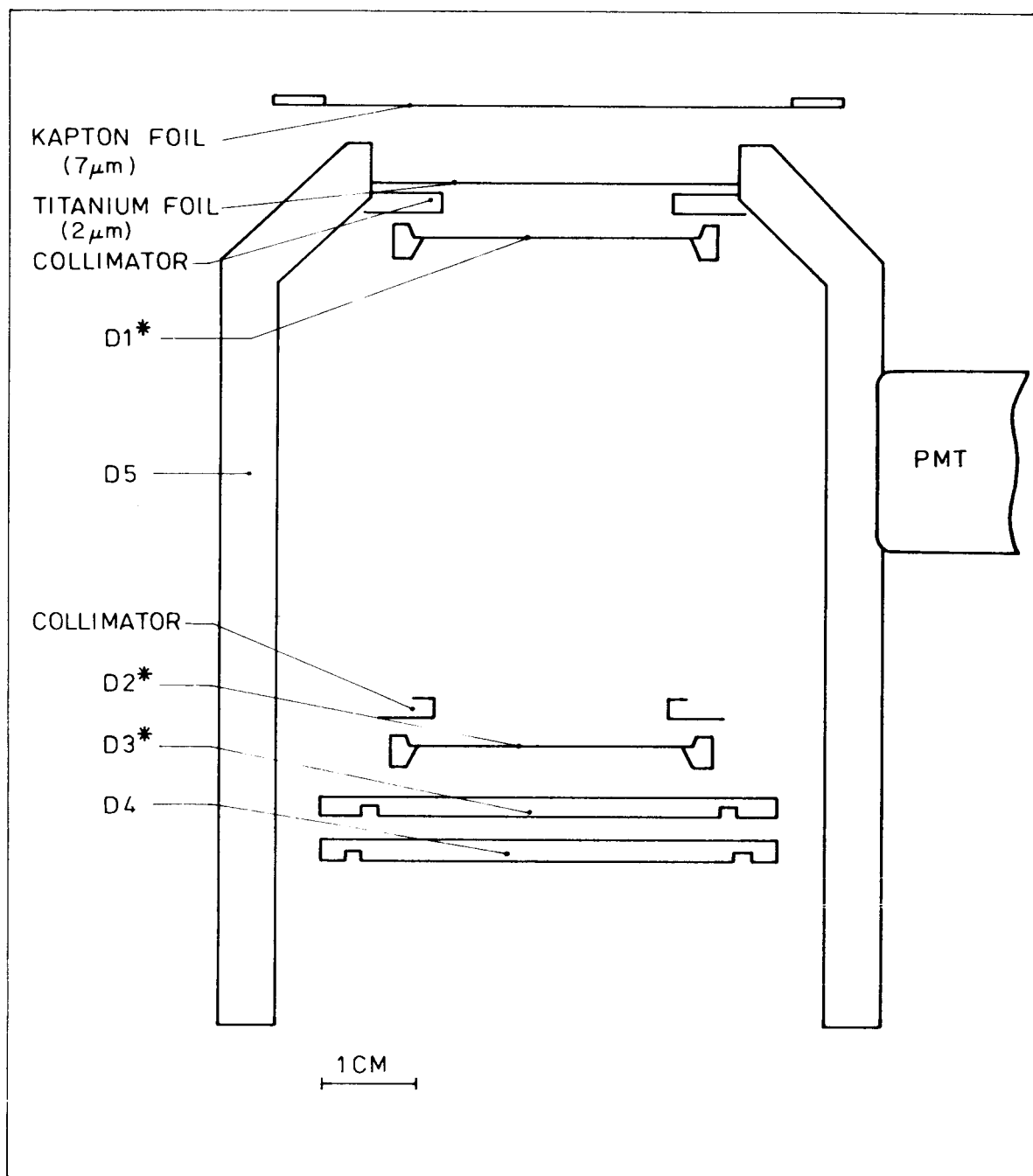


Figure 1b Schematic representation of the LET ( $D_m^*$  indicates a detector that is pulse-height analysed).

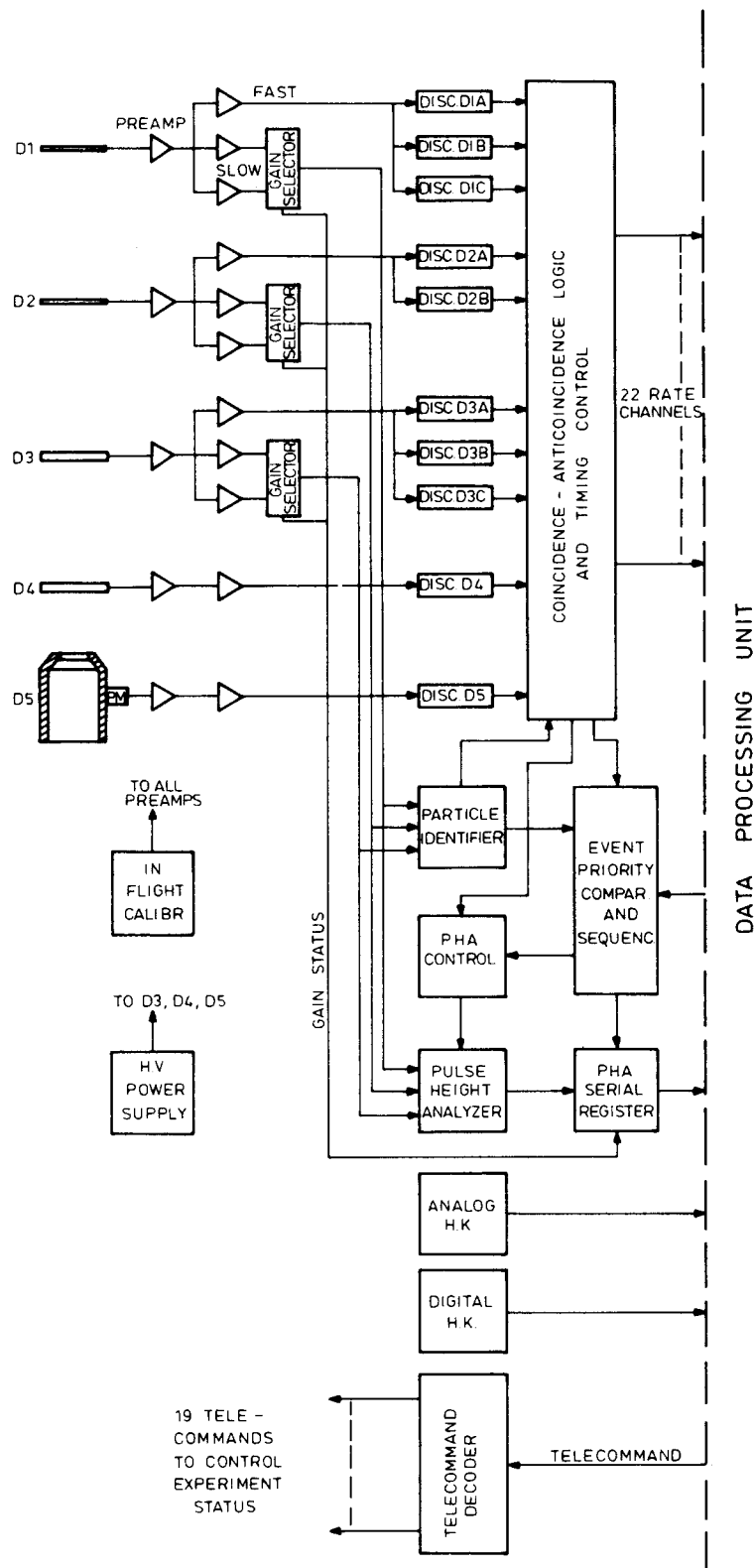


Figure 2 Block diagram of the LET electronics

A block diagram of the LET electronics is shown in Figure 2. The signals from D1, D2 and D3 are fed into individual amplifier chains consisting of a charge-sensitive preamplifier followed by a parallel combination of three pulse-shaping voltage amplifiers (PSAs). In order to accommodate the large dynamic range required, one low- and one high-gain PSA have been used, selected via an analogue switch controlled by a third (fast) PSA in conjunction with a discriminator. The selected outputs are fed into a common 10-bit (1024 channel) analogue-to-digital converter, which provides pulse-height information. The fast PSAs are followed by a number of threshold discriminators, the outputs of which are used in the coincidence logic to define a series of counting-rate channels. In addition, the outputs of the slower PSAs are fed into a Particle Identifier System to provide both event-priority and counting-rate information, as described below.

For particle identification, the LET utilises the proven technique of measuring the energy loss in one or more thin detectors, together with the total incident particle energy. If the energy lost in a thin detector is plotted as a function of the residual energy deposited in a second detector in which particles are stopped, events belonging to a given nuclear species will lie on a unique "track". The tracks corresponding to individual species can be identified in a plot of D1 vs D2 or D2 vs D3 pulse-height data. This enables relative abundances and energy spectra to be determined. The on-board Particle Identifier System makes it possible to obtain the counting rate of groups of nuclear species. The Identifier has a set of analogue function generators and discriminators to divide the response into different regions of charge.

The analogue functions are defined as follows:

$$\begin{aligned} G_i (S1,S2) &= S1 + C_i S2 & i &= 1,2,3,4 \\ G_i (S2,S3) &= S2 + C_i S3 & i &= 9 \\ F_i (S2,S3) &= S2 (S3 + C_i) & i &= 5,6,7,8 \end{aligned}$$

where S1, S2 and S3 are the analogue signals from detectors D1, D2 and D3 respectively, and  $C_i$  are constants. For each valid event stopping in D2 or D3 the values of the appropriate analogue functions are compared with associated discriminator thresholds  $\lambda_i$  ( $i = 1$  to 9) in order to define a series of logic parameters  $I_i$  ( $i = 1$  to 9) as follows:

$$I_i \equiv \begin{cases} G_i > \lambda_i & i = 1,2,3,4 \\ F_i > \lambda_i & i = 5,6,7,8 \\ G_i > \lambda_i & i = 9 \end{cases}$$

$$\bar{I}_i \equiv \begin{cases} G_i \leq \lambda_i & i = 1,2,3,4 \\ F_i \leq \lambda_i & i = 5,6,7,8 \\ G_i \leq \lambda_i & i = 9 \end{cases}$$

The values of the constant  $C_i$  and the thresholds  $\lambda_i$  expressed in energy units are given in Table I. On the respective D1 vs D2 or D2 vs D3 diagrams, where D1, D2 and D3 are now the energies deposited in detectors D1, D2 and D3 in MeV, the loci of points satisfying the equalities

$$D1 = \lambda_i + C_i D2 \quad i = 1,2,3,4$$

$$D2 = \frac{\lambda_i}{(D3 + C_i)} \quad i = 5,6,7,8$$

$$D3 = \lambda_i - C_i D3 \quad i = 9$$

define the boundaries separating groups of elements (charge groups). Figure 3 shows the positions of these boundaries plotted together with the predicted particle tracks. The tracks are calculated for nominal detector thickness using standard range-energy calculations as described in Marsden and Henrion (1979).

Each of the charge groups has an associated counting rate register which is incremented each time a valid event within that group is observed. These rate channels are listed in Table II together with the corresponding groups.

### 3 CALIBRATION

The calibration of the Engineering Unit (EU) of the Low Energy Telescope was performed at the Lawrence Berkeley Laboratory (LBL) Bevalac accelerator using beams of neon and argon nuclei of energy 250 MeV/n and

250 MeV/n

Table I. LET Particle Identifier analogue functions and threshold discriminator levels.

Identifier Logic Parameter I	Analogue Function	Discriminator Level $\lambda$	
I1	$S1 + 0.27 S2$	3.3 MeV	} D1 - D2
I2	$S1 + 0.27 S2$	8.5 MeV	
I3	$S1 + 0.27 S2$	24.0 MeV	
I4	$S1 + 0.27 S2$	52.0 MeV	
I5	$S2 * (S3 + 7)$	53 MeV <sup>2</sup>	} D2 - D3
I6	$S2 * (S3 + 18)$	355 MeV <sup>2</sup>	
I7	$S2 * (S3 + 67)$	4187 MeV <sup>2</sup>	
I8	$S2 * (S3 + 161)$	20342 MeV <sup>2</sup>	
I9	$S2 + 0.15 S3$	375 MeV	

Table II. LET Counting Rate channels and Charge Group definitions.

Rate Channel	Logical function	Species selected
L3	$\overline{I1}$	protons 1.7 - 3.8 MeV
L12	$\overline{I5}$	protons 3.8 - 8.0 MeV
L23	$I1 \overline{I2}$	He 1.9 - 3.7 MeV/n
L24	$I5 \overline{I6}$	He 3.7 - 8.4 MeV/n
L25	$I5 \overline{I6}$	He 8.4 - 19 MeV/n
L26	$I2 \overline{I3}$	Li,Be,B 1.7 - 4.9 MeV/n
L27	$I6 \overline{I7}$	Li,Be,B 4.9 - 26 MeV/n
L28	$I3 \overline{I4}$	C,N,O 2.4 - 7.0 MeV/n
L29	$I7 \overline{I8}$	C,N,O 7.0 - 38 MeV/n
L30	I4	Z > 10 2.8 - 9.0 MeV/n
L31	$I8 \overline{I9}$	$10 < Z < 20$ 9.0 - 51 MeV/n
L32	I9	Z > 20 12 - 75 MeV/n

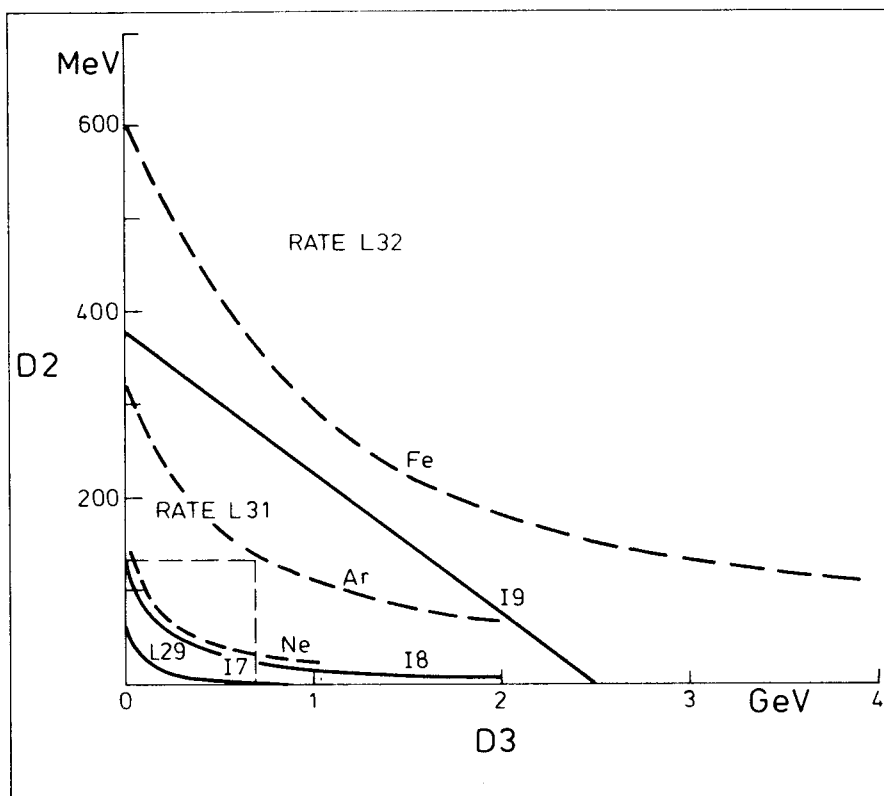


Figure 3a Theoretical LET response curves (D2 vs D3) for particles stopping in D3 (dashed lines). Solid lines represent nominal Particle Identifier boundaries. Rate channel numbers corresponding to the respective charge groups are indicated. This figure shows the full dynamic range.

284 MeV/n, respectively. The aim of these calibration runs was twofold:

- (1) to set the thresholds of the Particle Identifier discriminators described in Section 2;
- (2) to test the full dynamic range of the instrument.

Before the LBL calibration, the Particle Identifier thresholds were set on the basis of system sensitivities determined by means of  $^{241}\text{Am}$   $\alpha$  sources. The LBL runs were used initially to refine these settings and to measure accurately the relative positions of the nuclide tracks and the Particle Identifier loci. To this end, copper and polyethylene absorbers were placed in the beam path, in order to fragment the primary nuclei, thereby producing species of lower nuclear charge, while at the same time reducing the particle energies to between about 5 and 50 MeV/n. This made it

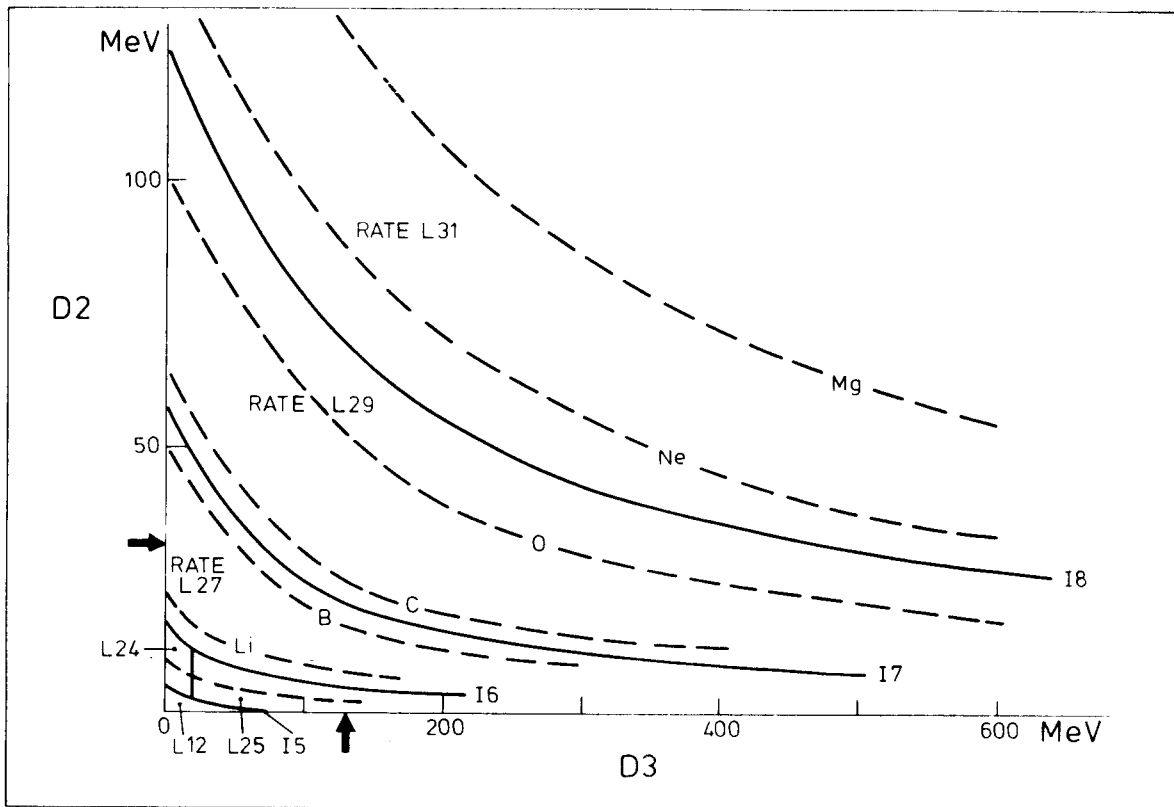


Figure 3b This is an enlargement of the lower left-hand part of Figure 3a. The arrows show the level at which gain switching occurs.

possible to obtain data points for tracks corresponding to nuclides other than the primary species. After adjustments to the discriminator thresholds, the instrument was exposed to the beam again, in order to verify the settings. The results presented in this paper were obtained during these latter exposures.

In 1979, a scientific development model of the LET, which used standard laboratory electronics, was exposed to neon beams of 7.4 MeV/n and 20.1 MeV/n at the Hahn Meitner Institut (HMI) in Berlin (Kamermans et al. 1980). Because of the limited maximum energy available at the facility, it was not possible to exercise the full dynamic range of the instrument during this experiment. It was therefore the intention to calibrate the EU LET at the Bevalac using iron nuclei to provide energy losses of up to 4 GeV in D3. Owing to technical difficulties with the LBL facility, however, only beams of neon and argon were available. Nevertheless, it was

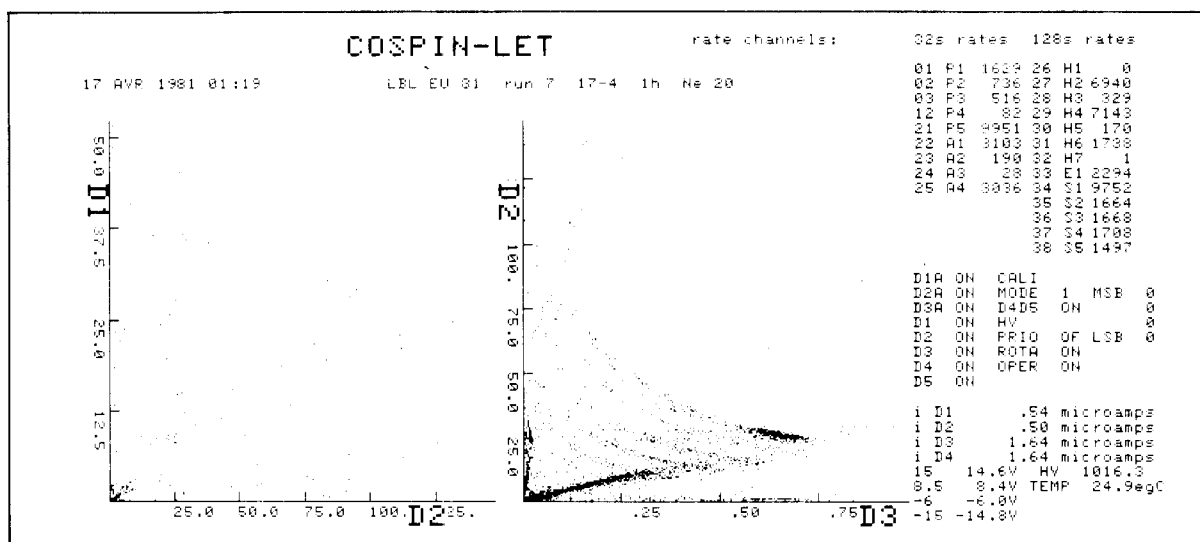


Figure 4 Example of the on-line data display.

still possible to stimulate the LET over approximately three quarters of the full dynamic range.

For the calibration runs described here, the Beam 40 spectrometer facility of the LBL Bevalac was used. Experiment instruments employing this facility are placed in air, the beam leaving the vacuum section of the spectrometer via a thin window. This arrangement has the advantage of allowing easy access to the instruments at any time when the beam is off. In the case of the LET, however, operation in air had a serious disadvantage, since particles with energies corresponding to the lower range of the instrument lost a noticeable part of their energy in the air gap between detectors D1 and D2. For details of this effect, refer to Section 4.

The data-acquisition system was placed 50 m from the room in which the LET was situated. This distance necessitated the communication of data through cables terminated by line drivers and receivers. The acquisition system included a HP 21 MX computer interfaced to the LET to allow real-time acquisition. The software had been designed to give an on-line display of the data together with their record on magnetic tape. The terminal screen displayed on-line the diagrams of energy loss in D1 vs. energy loss in D2 and energy loss in D2 vs energy loss in D3, the counting

rates of each Particle Identifier channel, the status of telecommands and of multiplexed monitor signals. An example of such a display is shown in Figure 4.

#### 4 EXPERIMENTAL RESULTS

Energy loss versus residual energy diagrams for the raw neon and argon beam data are shown in Figures 5 and 6, respectively. In these figures, data from the high-gain amplifiers are scaled to fit with low-gain data by dividing the channel numbers by the known gain ratio. The energy scales shown are approximate, since no precise energy calibration of the individual detectors has been possible. This is due to the fact that, although the initial beam energy was known to better than 0.5%, the use of the absorbers in the beam path prevented an accurate determination of the energy of particles reaching our instrument. Consequently, the energy assignment used in this paper is based on an extrapolation of 5 MeV  $\alpha$ -source calibrations.

The raw data plots shown in Figures 5 and 6 contain several spurious background features, these being largely the result of the high primary beam intensity which had to be used in order to obtain a sufficient yield of secondary particles. Since the particle beam produced by the Bevalac is pulsed, the sensor was exposed instantaneously to very high input rates of primary nuclei. Furthermore, the internal timing of the EU was not optimised at the time of the LBL calibration, and the combination of these two effects was responsible for the extraneous background. The internal timing in the instrument has since been improved, and no problems of this nature are expected in flight. Moreover, such a pulsed input is not characteristic of the charged particle fluxes in space.

An example of the spurious features discussed above can be seen in Figure 5, where incorrect operation of the high/low gain mode selection

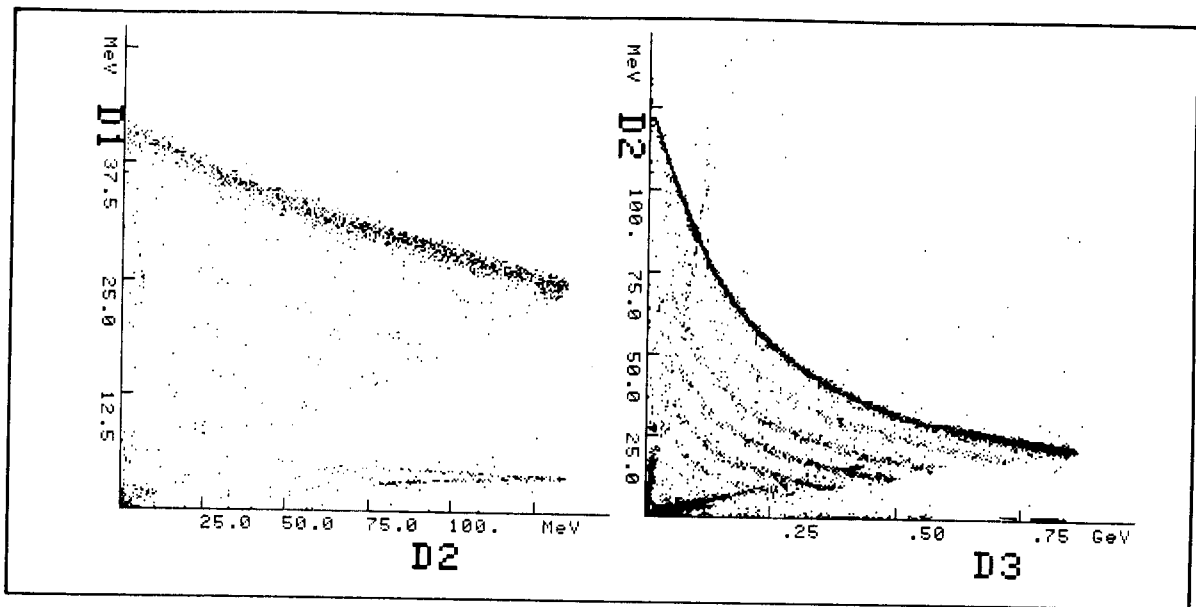


Figure 5 Energy-loss diagrams for the neon-beam data. In the D2 vs D3 diagram, the species from boron to neon are visible. As explained in the text, background counts are the result of the high beam intensities used.

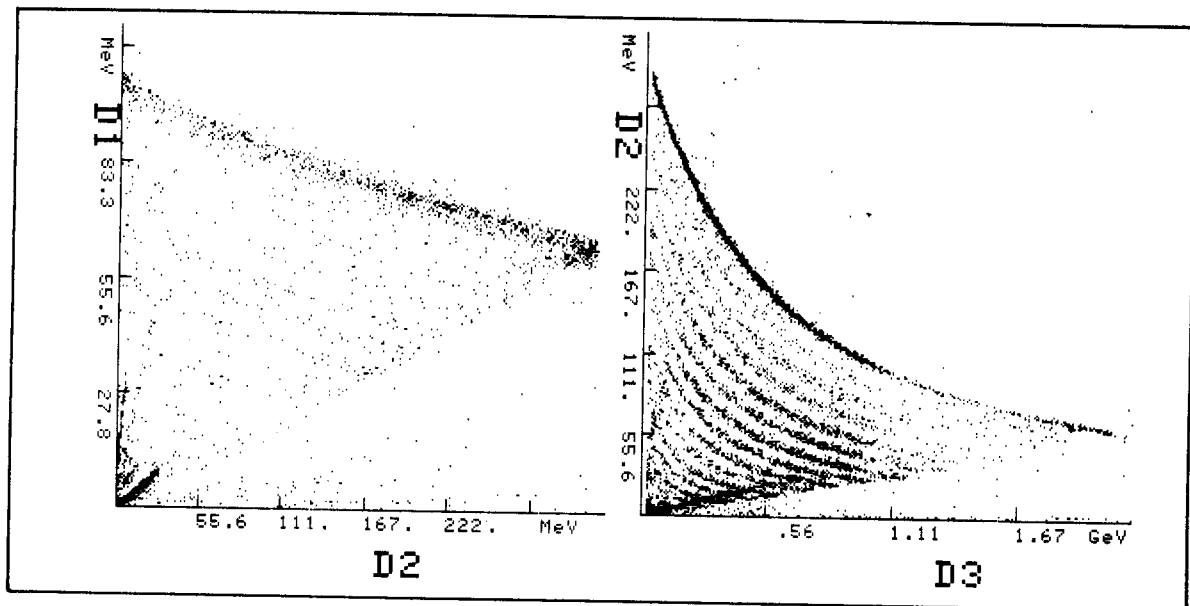


Figure 6 As Figure 5, but for the argon-beam data. Species from boron to argon are visible.

gave rise to additional tracks seen in the D1 vs D2 plot at values of D1 around 5 MeV for D2 between ca. 75 and 125 MeV, and in the D2 vs D3 plot at values of D3 around 100 MeV for D2 between ca. 50 and 100 MeV. Also to be seen in the data plots are traces extending from the nominal track end points back towards the origin. These points are apparently due to the fact that the anticoincidence circuitry associated with D4 occasionally failed to respond to particles which penetrated D3. This effect cannot be clearly attributed to the high-count-rate/internal-timing problem and needs further investigation during future accelerator runs. Another anomaly which has been identified, not related to the above problems, is the appearance of crosstalk between D3 and D4, for signals in D3 greater than ca. 1 GeV. This resulted in the loss of good events during the argon runs, since many particles stopping in D3 were treated as though they had penetrated. The reduction in the number of data points due to this problem is clearly seen in Figure 6. The origin of the crosstalk is currently being investigated by means of laboratory tests using an LED to stimulate the detector concerned.

The verification of the values of the Particle Identifier parameters for the D1 - D2 range of the instrument has been carried out using data from the HMI exposure (see Section 3). Figure 7 shows D1 vs D2 plots of these data, which were obtained with the LET sensor in vacuum. As stated earlier, the D1 - D2 data obtained at LBL had to be corrected for the energy loss in the 53 mm air gap between D1 and D2; the energy loss in the 5 mm gap between D2 and D3 was negligible. For this correction, the energy deposited in D2 without air between the detectors D1 and D2 has been calculated as follows. If  $E_2$  is the actual energy deposited in D2, then the range of a given particle in air emerging from D1 is given by

$$X = R_{\text{air}}(E_2) + 53 \text{ mm}$$

where  $R_{\text{air}}(E)$  is the range of a particle of energy  $E$  in air, determined in our case from range-energy tables for nitrogen (Northcliffe and Schilling, 1970). If  $\Delta E_a$  is the energy lost in the air gap between D1 and D2, then

$$X = R_{\text{air}}(E_2 + \Delta E_a) = R_{\text{air}}(E_2')$$

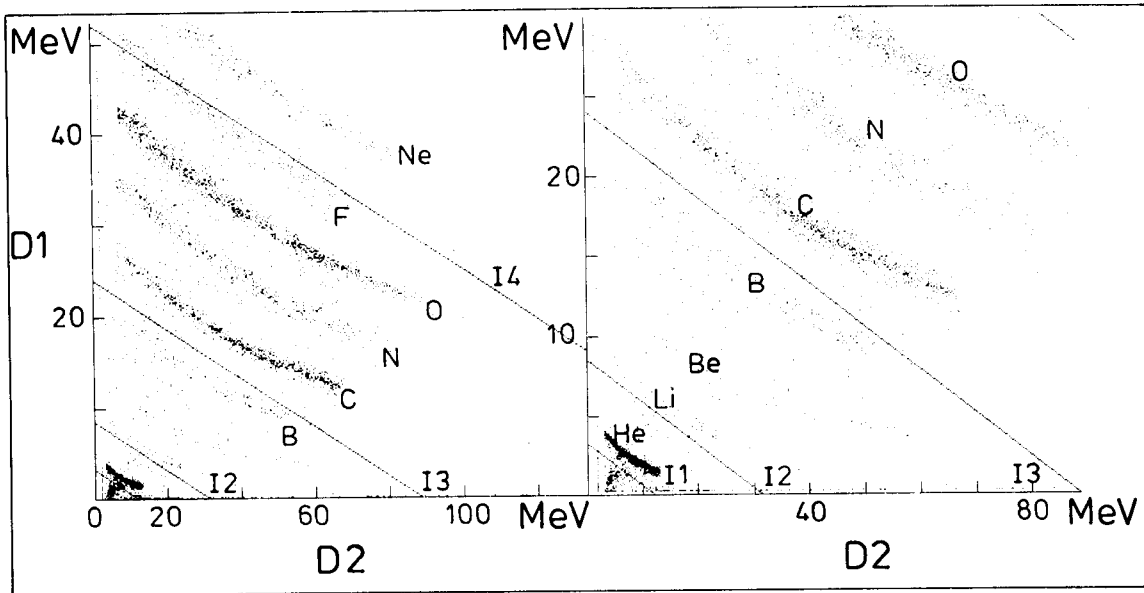


Figure 7 HMI calibration results after normalisation to the LBL data. Also shown are the D1 - D2 Particle Identifier loci.

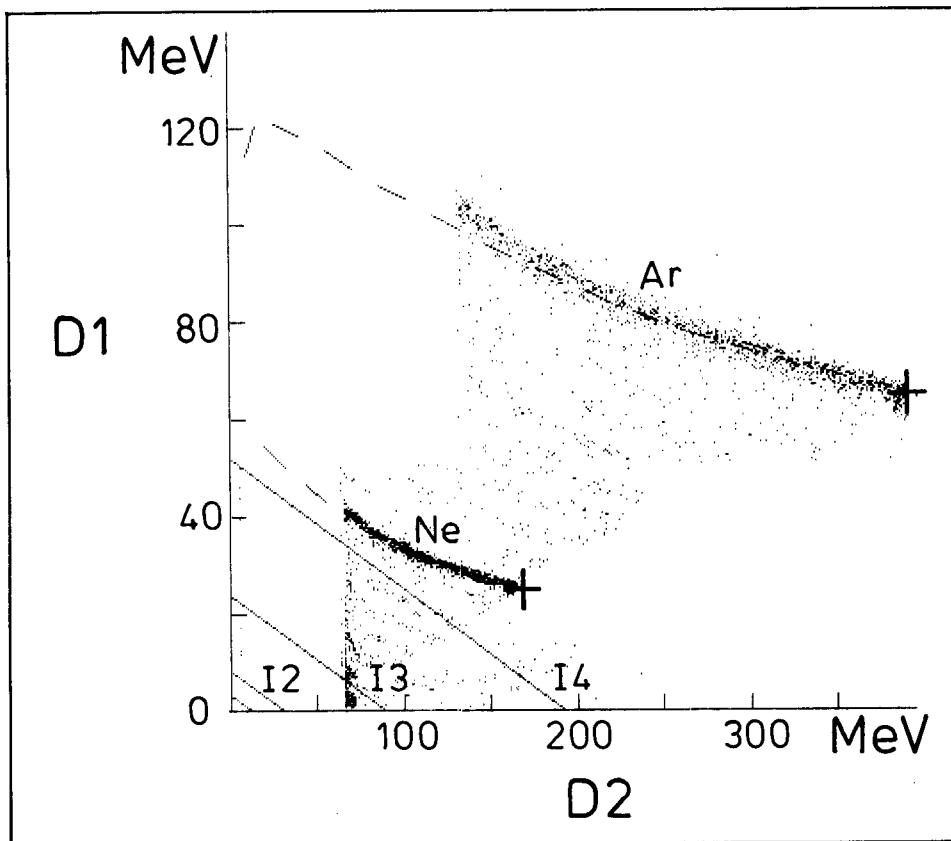


Figure 8 D1 vs D2 energy-loss diagram for the LBL data after correction for absorption in air. Only neon and argon particle tracks are visible. The dashed lines are theoretical tracks calculated from range-energy tables. Crosses represent the theoretical end points for each track.

where  $E_2'$  is the energy which would have been deposited in D2 in vacuum.  $E_2'$  has been obtained from the same range-energy tables, and plotted against the energy lost in D1.

The data have been split into two parts according to the measured pulse height in the first detector. Particles losing less than 50 MeV in D1 have been treated as neon nuclei, whereas losses of 50 MeV or greater have been attributed to argon nuclei. The corrected LBL data are shown in Figure 8. Owing to the low production rate of secondary particles in the Beam 40 spectrometer experiment, only the tracks for neon and argon events are readily identifiable. The absence of data points at low energies is a result of nuclei which have stopped in the air layer. Also shown in Figure 8 are the calculated positions of the neon and argon tracks. These curves, derived from the range-energy table for silicon, agree quite well with the data points with the exception of a slight deviation at low energies. Theoretical track end points, also calculated with the aid of range-energy tables for silicon and nitrogen, are given in Table III. These end-point values, indicated by crosses in Figure 8, are consistent with our measurements.

Table III. Theoretical neon and argon track end points for particles just penetrating D2.

Species	D1 (MeV)	D2 (MeV)
Ne	24.3	168.5
Ar	64.9	387.6

From the corrected D1 vs D2 data we have been able to set the value of the Particle Identifier discriminator corresponding to the Logic parameter I4. Since insufficient LBL experiment data points were obtained in the low-energy regions for particles other than Ne and Ar, the primary neon track has been used to normalise the HMI data set to that obtained in the current experiment. From these normalised data, the discriminator settings corresponding to logic parameters I1 to I3 have been determined. The associated Particle Identifier boundary lines are shown in Figures 7 and 8.

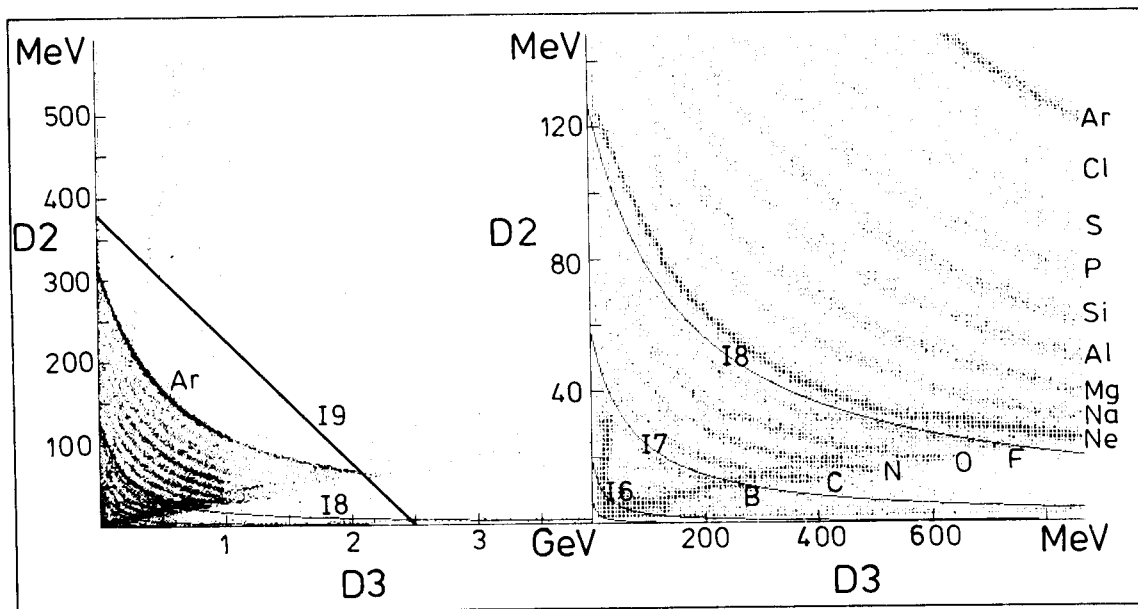


Figure 9 D2 vs D3 energy-loss diagrams for the LBL data, showing the loci of the Particle Identifier thresholds.

Owing to limitations in the available beam energy for the HMI experiment, it was not possible to use HMI data to set any of the discriminator thresholds for the high-energy D2 - D3 range of the Particle Identifier. As stated in Section 3, this was one of the aims of the LBL experiment. Since the production of secondary particles in the copper absorber used to reduce the primary beam energy increases with increasing beam energy, the data of Figures 5 and 6 corresponding to events stopping in the relatively thick D3 detector show a higher abundance of non-primary species than in the low-energy D1 - D2 case. As a result, the tracks for all elements from boron up to and including the primary beam species are easily identified. With the help of these data we have been able to set the discriminator thresholds corresponding to I7 (separating the Li-Be-B group from the C-N-O group), I8 (separating C-N-O from Ne and heavier) and I9 (Fe-group identification). Figure 9 shows the D2 vs D3 pulse height data together with the Identifier boundaries derived internally from these discriminator settings. It should be noted that the data did not allow us to fix the thresholds for the identification parameters I5 (proton-He separation) and I6 (separating He from the Li-Be-B group) directly, since the background in the  $Z = 1,2$  region

obscured any genuine hydrogen or helium events. These thresholds have therefore been provisionally determined by computing the expected positions of the  $Z = 1$  and  $Z = 2$  tracks and normalising these to the measured tracks corresponding to particles of higher nuclear charge. In order to investigate the elemental resolution of the LET we have used our D2 vs D3 data as input to an algorithm described by Seamster et al. (1977) and Kamermans et al. (1980). In an iterative calculation, an identification parameter having the form

$$PI \sim (\frac{1}{2}AZ^2)^{1/3}$$

for a particle of mass  $A$  and charge  $Z$  is derived, and plotted in histogram form.

As can be seen,  $PI$  is effectively the particle charge. Figures 10 and 11 show particle identification spectra computed from the neon and argon beam data, respectively. As a measure of the telescope resolution, values of the FWHM of the neon and argon peaks have been obtained, and are given in Table IV. These results imply a separation from adjacent charge peaks for neon and argon of 10 and 7 standard deviations, respectively.

Table IV. Charge-resolution parameters derived from the LBL D2 vs D3 pulse height data.

Element	FWHM	$\sigma_Z$
Ne	0.23	0.10
Ar	0.32	0.14

It should be noted that the  $PI$  algorithm gave good results only for the light and medium nuclides ( $A < 25$ ). When calculated with the data from heavier species, the value of the parameter, normally constant for a given nuclide, increased with decreasing energy. This tended to cause a broadening of these histogram peaks. It should also be noted that the values given in Table IV do not include the effects of path-length differences due to the finite opening angle of the LET; the effects of detector thickness variations are, however, included.

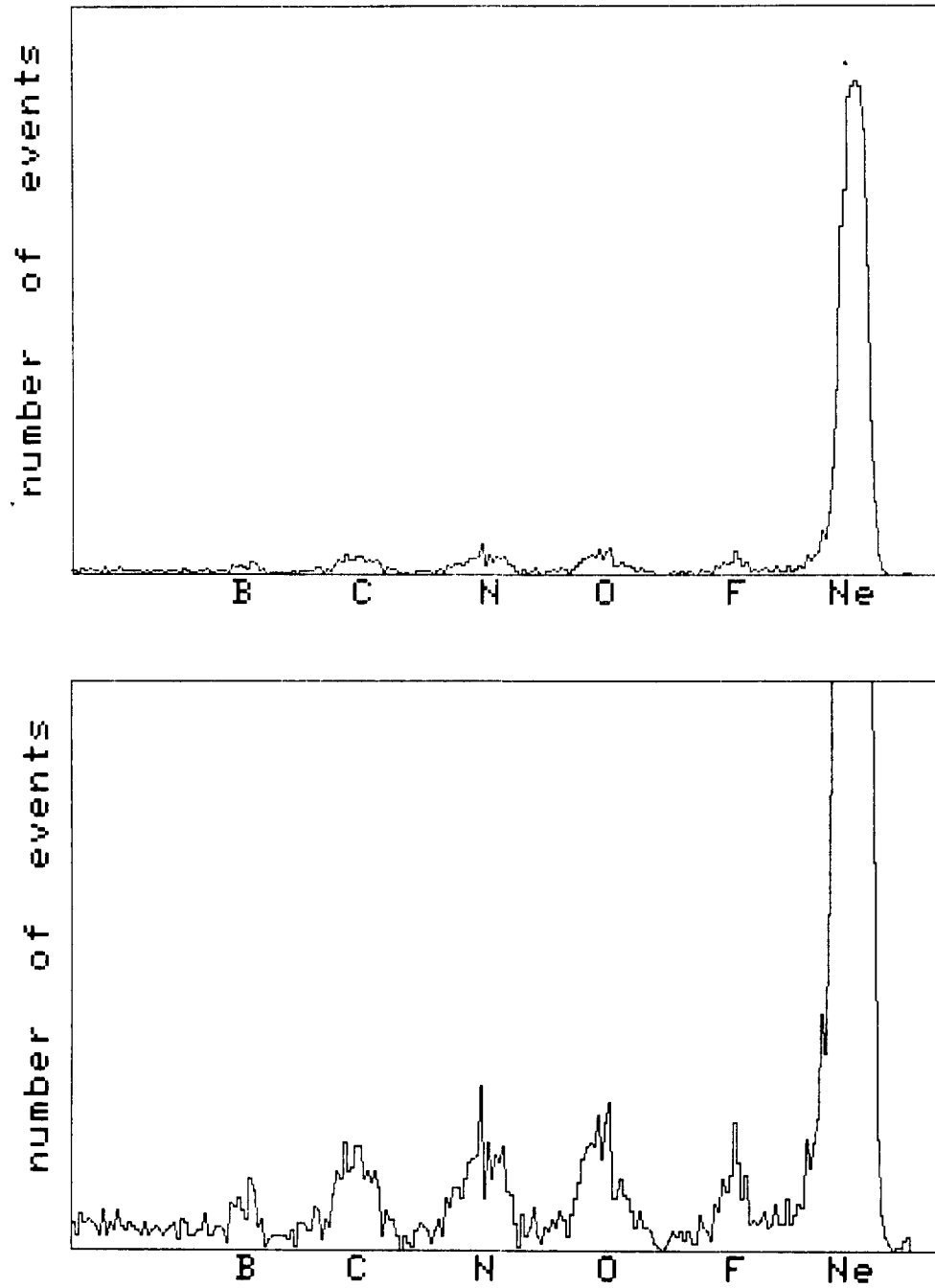


Figure 10 Charge histogram for LBL neon data (particles stopping in D3).

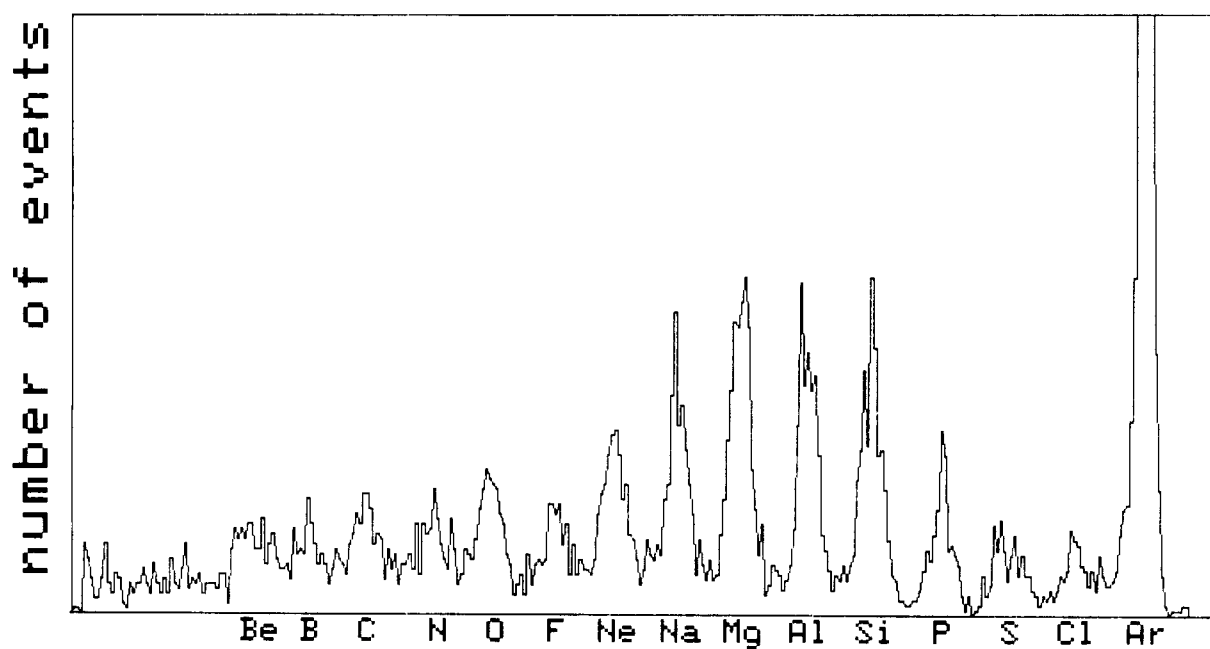
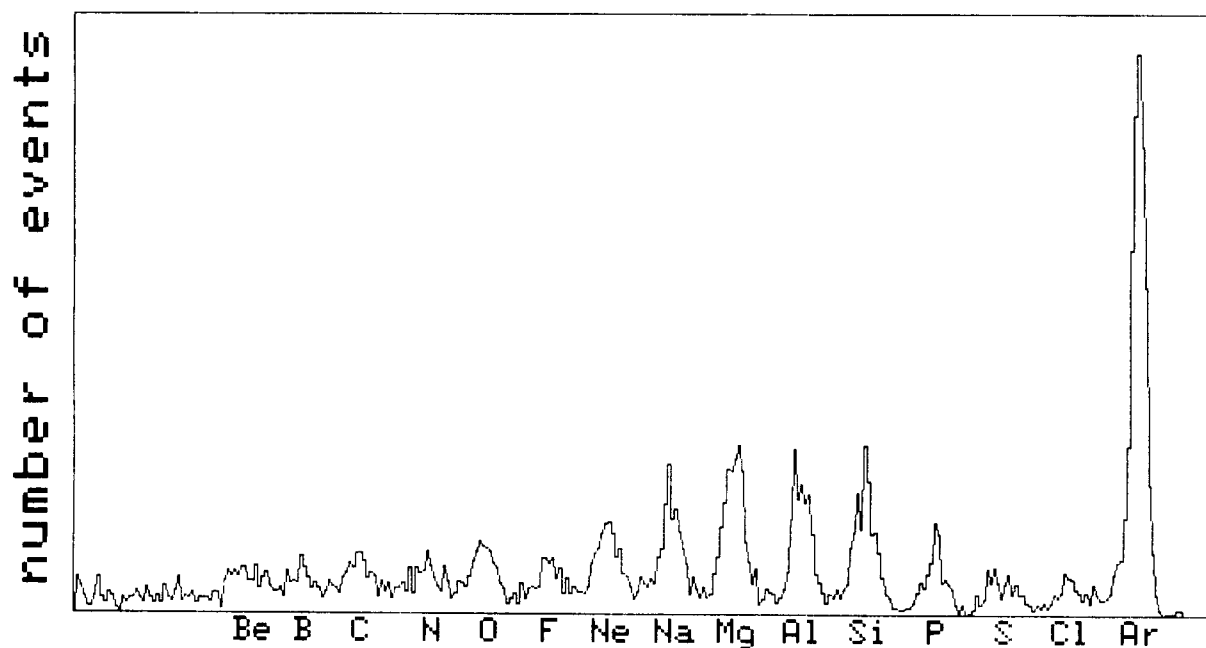


Figure 11 Charge histogram for LBL argon data (particles stopping in D3).

## 5 CONCLUSION

In this paper, we report measurements made with the COSPIN Low Energy Telescope Engineering Unit at the Lawrence Berkeley Laboratory Bevalac facility. The instrument was exposed to beams of 250 MeV/nucleon neon and 284 MeV/nucleon argon. The results of this accelerator experiment have been used to determine the optimum settings of the LET Particle Identifier discriminators for the high-energy response region. Data from previous calibration were normalised to the LBL data, enabling equivalent discriminator settings to be optimised for the low-energy region. Thresholds used to separate protons from helium could not be set directly. The experiment has demonstrated that the Engineering Unit telescope is capable of separating adjacent elements in the range ca. 5 to 50 MeV/n at least up to argon, and in the case of the latter, with a resolution of better than seven standard deviations.

Off-line analysis of the calibration data has revealed some cross talk between the anticoincidence detector D4 and the residual-energy detector D3. This problem is currently under investigation. Further investigations are also needed to determine the cause of the particle track tail-back observed in the D2-D3 data. It is planned to expose the LET Flight Unit to heavy-ion beams at the Bevalac in 1982, in particular to  $^{56}\text{Fe}$  nuclei, since these were not available at the time of the EU calibration. It is also the intention to attempt a direct energy calibration of the Flight Unit with the aid of a facility that produces ion-beam energies lower than is possible at the Bevalac.

## REFERENCES

- Kamermans, R, Henrion, J Marsden, R G, Sanderson, T R and Wenzel, K-P,  
NIM 171, 87 (1980).
- Marsden, R G and Henrion, J, ESA STR-202 (1979).
- Northcliffe, L C and Schilling, R F, Nuclear Data Tables 7, (A), Nos. 3  
and 4 (1970).
- Seamster, A G, Green, R E L and Korteling, R G, NIM 145, 583 (1977).

**ELEMENT AND ISOTOPE SEPARATION FOR A HEAVY ION COSMIC RAY TELESCOPE WITH LARGE GEOMETRICAL FACTOR**

R. KAMERMANS, J. HENRION, R.G. MARSDEN \*, T.R. SANDERSON and K.-P. WENZEL

*Cosmic Ray Division, Space Science Department of ESA, European Space Research and Technology Centre, Noordwijk, The Netherlands*

Received 25 October 1979

The charge and mass response of a space-borne solid state cosmic ray detection system for heavy ions is discussed. Its large geometrical factor causes pathlength variations due to the large opening angle of the telescope, and to the thickness non-uniformity of the thin large area detectors. Accelerator experiments with 147 MeV and 402 MeV  $^{20}\text{Ne}$  beams have been performed and the effect of the pathlength variations in addition to the intrinsic energy-straggling distribution on the heavy ion identification is presented.

**1. Introduction**

Telescopes consisting of several solid state detectors are widely used for the identification of heavy ions. Particle identification is obtained by measuring the energy-loss in the different detectors. In the many cases where contributions due to electronic noise, thickness non-uniformity and window effects play a minor role, the particle identification is determined by the intrinsic spread in the energy-loss distribution. For heavy ions in the region where the energy-loss in a detector is comparable with the total energy, the energy spread is not only of statistical nature but also depends on the change of the average rate of energy-loss during the slowing down process. Calculations of the energy-loss distribution in this region have been performed by Tschalär [1], in good agreement with the experimental results for light ions ( $Z \leq 2$ ). Discrepancies found for heavier ions are partly removed if atomic corrections due to the electron binding energies are included [2]. However experimental information in this area is still rather scarce and mainly limited to energies below  $1 \text{ MeV n}^{-1}$ .

The detection system whose response is described in this paper is a development model of the Low Energy Telescope [3] which will be flown as part of the Cosmic Ray and Solar Charged Particle Investiga-

tions (COSPIN) on the European spacecraft of the joint ESA/NASA International Solar Polar Mission [4]. The telescope is designed to separate elements up to Fe and isotopes up to He, using the  $\Delta E$ - $E$  method, in an energy range from 1.7 MeV (H) up to 4 GeV (Fe) with high spatial and temporal resolution. The telescope consists of four Si solid state detectors of which the last is used as an anticoincidence detector. The required large geometrical factor conflicts with a high mass resolution due to pathlength variations in the  $\Delta E$  detectors caused by the large opening angle and by the thickness non-uniformity of the large area detectors. The stringent limitation on the mass of the payload, which affects the maximum heliographic latitude that can be reached in this mission, excludes the use of position sensitive detectors to correct for these effects. However the recently observed  $^3\text{He}$  rich flares [5] lead to the requirement of isotope separation for the He group. Moreover abundances of individual Be isotopes are of great interest in cosmic ray studies. For example the long half-life of  $^{10}\text{Be}$  has been used to deduce the age of cosmic rays from the  $^{10}\text{Be}/\text{Be}$  ratio [6] and also the yield of the pure electron-capture isotope  $^7\text{Be}$  gives information on the solar modulation process [7].

The accelerator experiments described in this paper have been performed in order to investigate the element and isotope response for a wide range of masses that can be achieved with this instrument. A description of the cosmic ray heavy ion telescope is

\* Now at: Space Division, Fokker VFW BV, Schiphol Oost, P.O. Box 7600, The Netherlands.

presented in section 2. The experimental techniques and data handling are described in section 3. In section 4 the experimental results are shown and the element and mass separations that can be obtained are discussed.

## 2. Cosmic ray heavy ion telescope

The telescope, a cross section of which is shown in fig. 1, consists of four Si solid state detectors (D1–D4), surrounded by a plastic scintillator–photomultiplier combination (D5). D4 and D5 form the anti-coincidence shielding for background rejection in space and will not be considered here. D1 is a 6 cm<sup>2</sup> surface barrier detector with a thickness of 30 μm and a resistivity of 450 Ω cm. Its window thicknesses are 40 μg cm<sup>-2</sup> (Au) and 80 μg cm<sup>-2</sup> (Al). D2 is a 6 cm<sup>2</sup> surface barrier detector with a thickness of 100 μm and a resistivity of 1.8 kΩ cm. Its window thicknesses are 40 μg cm<sup>-2</sup> both for the Au and the Al layer. Both detectors are operated at a bias voltage of about 1 V μm<sup>-1</sup>, which is twice as high as the depletion voltage, in order to reduce the plasma recombination effect. These devices, especially D1, represent the state-of-the-art in the manufacture of solid state detectors of this type. D3 is a 2 mm thick Li drifted Si detector with an active area of 10 cm<sup>2</sup> and an entrance window dead layer of 0.5 μm Li. The geometrical factor of this telescope is 1.1 cm<sup>2</sup> sr.

In contrast to nuclear physics experiments where

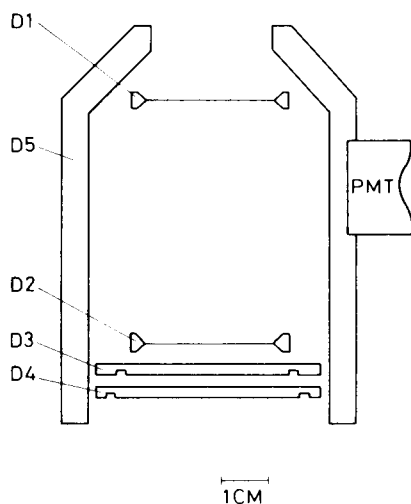


Fig. 1. Schematic cross section of the Low Energy Telescope with D1 = 30 μm, D2 = 100 μm, D3 = D4 = 2 mm and D5 = anti-coincidence shielding with photomultiplier tube (PMT).

normally the direction of the incoming flux is well defined and the mass separation is mainly determined by the shape of the energy-loss distribution, the situation for heavy ion cosmic ray detection is quite different. The limited sampling times during the passage of the spacecraft over the solar poles and the expected particle fluxes require a large geometrical factor, which has two important implications for the mass separation that can be obtained. First the large opening angle of 55° causes pathlength variations and secondly thin large area detectors suffer from an intrinsic thickness variation due to the etching process involved. The effect of these variations on the element and isotope response of this detection system will be discussed in section 4.

## 3. Experimental techniques and data handling

A development model of the telescope has been exposed to the <sup>20</sup>Ne beam at the VICKSI-accelerator of the Hahn-Meitner Institut in Berlin. The incident energies of 147 MeV and 402 MeV were determined from the NMR-frequency of the momentum analysing system and were known with an accuracy of better than 1%. In these experiments particles resulting from nuclear scattering in thin foils have been used. The advantage of this procedure is that time consuming tuning of the accelerator is avoided, and information concerning system performance is obtained for a wide range of energies and elements in a relatively short time.

Self-supporting targets of <sup>197</sup>Au (200 μg cm<sup>-2</sup> and 6 mg cm<sup>-2</sup>) and <sup>12</sup>C (52 μg cm<sup>-2</sup>) were bombarded and the emerging particles were detected in the telescope which was placed at a distance of 20 cm from the target position, with an angular acceptance of 0.6°. Elastic scattering from <sup>197</sup>Au detected at an angle of 15° with respect to the beam axis results in outgoing <sup>20</sup>Ne energies of 146 MeV and 398 MeV respectively. The 6 mg cm<sup>-2</sup> <sup>197</sup>Au foil had to be used in the 402 MeV <sup>20</sup>Ne beam due to the low beam current ( $i_e < 3$  nA). These measurements give detailed information on the straggling effect in the ΔE detectors and on the energy resolution of the whole system. Reaction products resulting from <sup>20</sup>Ne + <sup>12</sup>C collisions measured at somewhat larger scattering angles have a wide range in mass and energy and consequently yield information about the isotope and charge separation within a large dynamic range.

Apart from the charge-sensitive preamplifiers

designed for space flight, standard electronics was used. For each coincidence the energy losses in the three detectors D1, D2 and D3 were written as a 3-fold event on magnetic tape for subsequent "software" particle identification. The energy calibration for each detector chain was obtained with  $\alpha$ -particles from  $^{241}\text{Am}$  in conjunction with precision pulse generators. In this way the gains of the three separate detector chains could be matched in the off-line analyses. By the same method the linearity of the overall system was checked.

#### 4. Experimental results and discussion

The measured energy-loss distribution in D1 of 146 MeV  $^{20}\text{Ne}$  is shown as the histogram in fig. 2. The FWHM of this distribution is 630 keV corresponding to 2.0%. Measurements and calculations of the straggling distribution for heavy ions, including binding energy effects, have been presented by Avdeichikov [2]. In their calculations they found that the energy-loss distribution was rather constant for detector thicknesses between 10  $\mu\text{m}$  and 40  $\mu\text{m}$  and for energy-loss ratios between 0.2 and 0.8. For  $^{20}\text{Ne}$  the calculated FWHM = 1.9% which is in good agreement with our experimental results. The somewhat higher value measured by the authors of ref. [2] is therefore more probably due to their total energy resolution and detector non-uniformity than to the

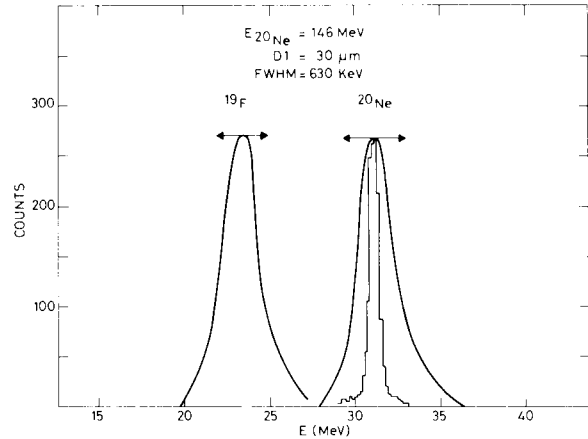


Fig. 2. Energy-loss distribution for D1/D2 coincidences. ( $E_{20\text{Ne}} = 146$  MeV). Corrections due to pathlength variations are shown by the solid lines. The arrows estimate the thickness non-uniformity effect.

contribution of charge exchange processes.

As was discussed in section 2 the pathlength variations, caused by the opening angle of  $55^\circ$  and the thickness variation of the thin detectors, will strongly affect the element and mass separation that can be obtained with this telescope. The effect of the pathlength variations due to the opening angle can be calculated by the reasonable assumption of an isotropic incident flux. The relative contribution to the count rate as function of the incidence angle for an isotropic flux is shown in fig. 3 [8]. Folding our experi-

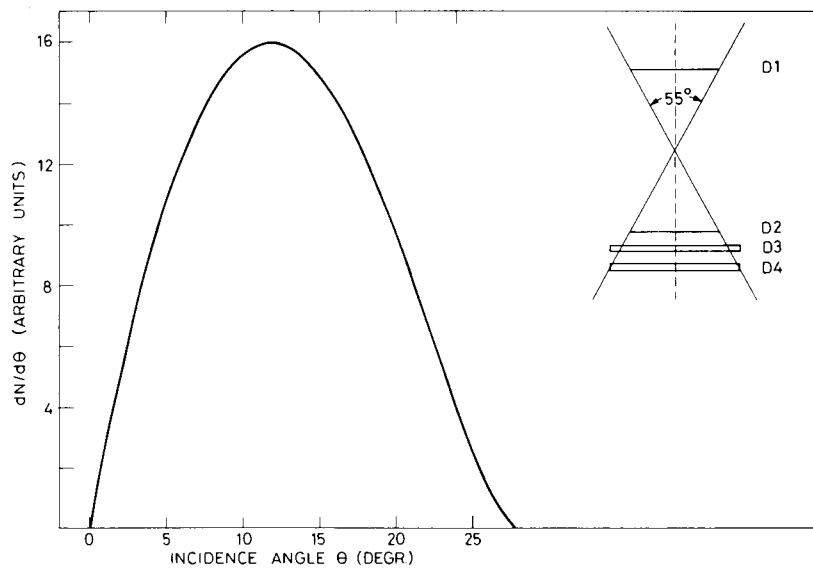


Fig. 3. The relative contribution of the count rate as function of the angle of incidence assuming an isotropic incident flux.

mental distribution with the angular response given in fig. 3 yields the solid curve in fig. 2 which represents the energy-loss distribution in D1 from an isotropic flux of  $^{20}\text{Ne}$  nuclei. To demonstrate the element separation also the distribution for  $^{19}\text{F}$  is shown. The same shape of the distribution is assumed for both elements. Due to the low statistics in our experiment for  $^{19}\text{F}$  at the same incident energy as  $^{20}\text{Ne}$  the position of the  $^{19}\text{F}$  peak relative to the  $^{20}\text{Ne}$  peak was obtained from stopping-power calculations for  $^{19}\text{F}$  in Silicon [3]. The stopping-power calculations are based upon the treatment of Greiner [9], which takes as its starting point the proton energy-loss tables of Janni [10]. In these calculations corrections for nuclear stopping and charge neutralization have been taken into account. For energies below  $12\text{ MeV n}^{-1}$  the stopping-power was compared with the tabulated values given by Northcliffe and Schilling [11] and was found to agree within 4%. The calculated energy-loss differences for F and Ne are consistent with our experimental results.

The flight-quality detectors are being strictly selected to have thickness uniformity of better than  $\pm 1.75\ \mu\text{m}$  for both the D1 and D2 detectors. A conservative estimate of this non-uniformity effect, assuming uncorrelated thickness variations across the detector area will result in a peak broadening as indicated by the arrows in fig. 2.

The experimental energy-loss distribution in D2 =  $100\ \mu\text{m}$  of  $398\text{ MeV }^{20}\text{Ne}$  (elastically scattered  $402\text{ MeV }^{20}\text{Ne}$  from  $^{197}\text{Au}$ ) is shown as the histogram in fig. 4. The solid lines and the arrows were obtained as

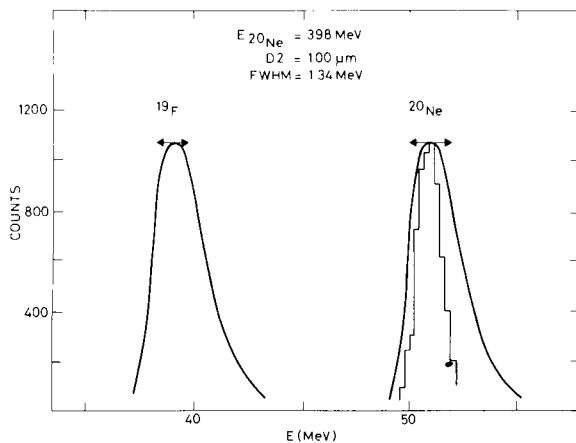


Fig. 4. Energy-loss distribution for D2/D3 coincidences ( $E_{20\text{Ne}} = 398\text{ MeV}$ ). Corrections for pathlength variations are shown by the solid lines. The arrows estimate the thickness non-uniformity effect.

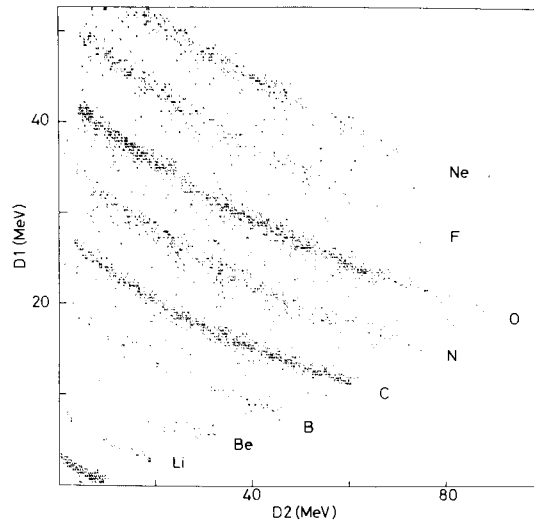


Fig. 5. D1 versus D2 energy-loss matrix from the  $^{20}\text{Ne} + ^{12}\text{C}$  reaction ( $E_{20\text{Ne}} = 147\text{ MeV}$ ). Characters used in this matrix are a non-linear representation of the raw data.

described above for fig. 2. From figs. 2 and 4 it is clear that even if the pathlength variation effects are included element separation in this mass region can be obtained.

The interaction of heavy ions with Si solid state detectors is more complex than for light ions resulting in a total energy resolution for a heavy ion which is quite different from the one for light ions. Both for  $146\text{ MeV}$  and  $398\text{ MeV }^{20}\text{Ne}$  the total energy resolution is 0.3%. For example the total energy resolution for  $E_{20\text{Ne}} = 146\text{ MeV}$  is  $470\text{ keV}$ . Main contributions to the energy resolution are the energy dispersion due to nuclear collisions, calculated to be  $350\text{ keV}$  [12,13] the effect of kinematical broadening of  $170\text{ keV}$  and the energy spread due to recombination of the ionization plasma. In our experiment this latter effect is about  $250\text{ keV}$  in agreement with the values quoted in ref. [13].

As an example of the overall performance of the telescope the results from the  $^{20}\text{Ne} + ^{12}\text{C}$  reaction ( $E_{20\text{Ne}} = 147\text{ MeV}$ ) are shown in fig. 5 for D1/D2 coincidences. It must be pointed out that in such reactions more than one isotope per element can be produced. This experiment has been performed with a small acceptance angle and consequently does not include the pathlength variation effects, however the data show the performance of the system for the different masses over the whole D1/D2 energy range. A particle identification spectrum was obtained from these data using an algorithm described by Seamster

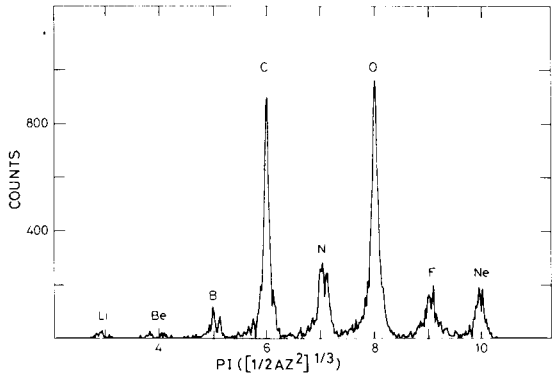


Fig. 6. Particle identification distribution from the  $^{20}\text{Ne} + ^{12}\text{C}$  reaction ( $E_{20\text{Ne}} = 147 \text{ MeV}$ ).

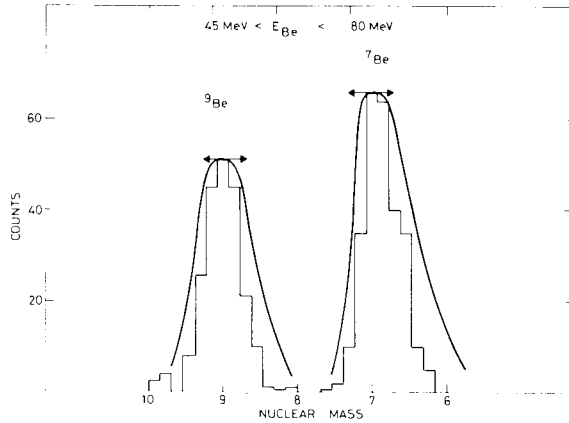


Fig. 8. Be mass distribution for  $45 \text{ MeV} < E_{\text{Be}} < 80 \text{ MeV}$ .

et al. [14] For each event, in an iterative procedure, a particle identification parameter  $PI = (\frac{1}{2}MZ^2)^{1/3}$  was calculated by integrating the Bragg curves using the Bethe–Bloch equation. Fig. 6 gives the particle identification distribution which clearly shows the heavy element separation for the whole energy range.

As was mentioned in the introduction the observation of  $^3\text{He}$  rich flares [5] requires mass separation for the He group. Direct experimental evidence for  $^3\text{He}/^4\text{He}$  isotope separation is hard to obtain due to the much higher  $^4\text{He}$  yield in the type of nuclear reactions described above. In order to evaluate the isotope separation we have therefore followed the same procedure as for the Ne, F charge separation described above. In the left hand part of fig. 7 is shown the D2 energy-loss distribution for  $E_{\alpha} = 34$

MeV. The data was obtained by only selecting from the continuous  $\alpha$ -spectrum those events with  $E_{\alpha} = (34.0 \pm 0.1) \text{ MeV}$ . On the right hand side of fig. 7 the D1 straggling distribution from a  $^{212}\text{Po}$  source ( $E_{\alpha} = 8.785 \text{ MeV}$ ) is given. Both energy-loss distributions have a fwhm of 7% ( $\sim 250 \text{ keV}$ ) in agreement with the results of ref. [2]. With this fwhm, which is larger than for  $^{20}\text{Ne}$ , the relative contribution of the path-length variations to the mass resolution will be smaller. Moreover the thickness non-uniformity effect for D2 (left hand side) is only 1.8% compared with 6% for D1 (right hand side). Comparison with the calculated distributions in fig. 6 shows that isotope separation between  $^3\text{He}$  and  $^4\text{He}$  is possible both for D1/D2 and D2/D3 coincidences.

Information on the isotope separation for Be,

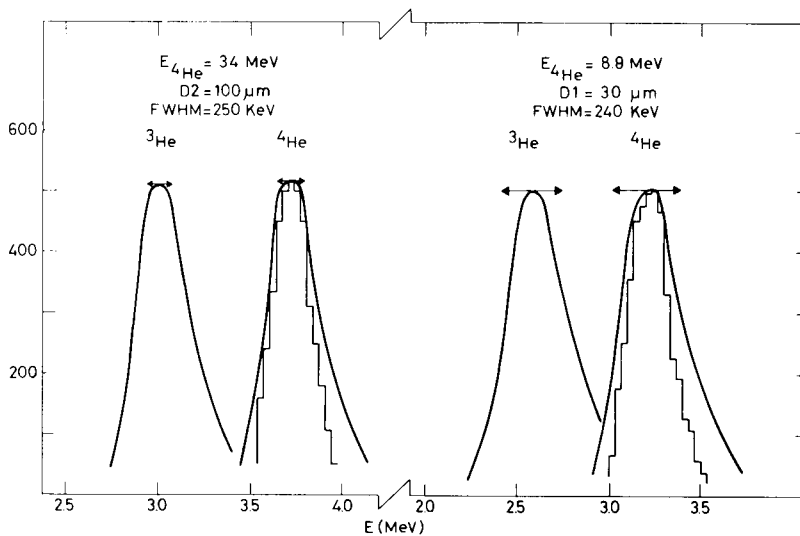


Fig. 7.  $^3\text{He}/^4\text{He}$  isotope separation both for D1/D2 and D2/D3 coincidences.

which is important for the understanding of the solar modulation process [7] and the age of cosmic rays [6], has also been extracted from the measurements. In our experiments the Be yield is too low to analyse the data at fixed energies, as in the  $^4\text{He}$  case. However in a D2 versus D3 pulse height display the  $^7\text{Be}$ – $^9\text{Be}$  energy separation is almost constant. Therefore we have summed the data with  $45 \text{ MeV} < E_{\text{Be}} < 80 \text{ MeV}$  along the particle tracks and the result is presented in fig. 8. As in figs. 2, 4 and 7 the solid lines indicate the effect of the opening angle whereas the arrows represent the thickness non-uniformity effect. The separation of Be isotopes, although dependent on the relative abundances, seems to be quite feasible.

## 5. Conclusions

In this paper we discussed the response to heavy ions of a three-detector telescope for cosmic ray studies. The detection system will be flown on the International Solar Polar Mission, where a large geometrical factor and a low mass are required. Accelerator experiments with  $^{20}\text{Ne}$  beams of 147 MeV and 402 MeV have been performed, yielding experimental straggling distributions which are well described by the calculations of Tschalär [1], if corrections due to the electron binding energy are included [2]. In addition to the intrinsic energy-loss distribution, effects of the pathlength variation in the thin large area detectors caused by the large opening angle and the non-uniformity of the detector thicknesses have been presented. It is shown that isotope separation for light nuclei such as He (and probably for Be isotopes) and good charge separation for elements demonstrated up to Ne and expected up to Fe, can be achieved. Further experiments using high energy Fe beams will be performed in the near future.

We would like to thank Drs. W. v. Oertzen, W. Bohne and B. Lehr for their help and hospitality during the experiments at the Hahn-Meitner Institut in Berlin. Two of the authors (RK and RGM) were supported by ESA Research Fellowships during the course of this work. The Low-Energy Telescope is part of the Cosmic Ray and Solar Charged Particle Investigation developed by several scientific institutes with Prof. J.A. Simpson of the University of Chicago as Principal Investigator.

## References

- [1] C. Tschalär, Nucl. Instr. and Meth. 61 (1968) 141; Nucl. Instr. and Meth. 64 (1968) 237.
- [2] V.V. Avdeichikov, E.A. Ganza and O.V. Lozhkin, Nucl. Instr. and Meth. 131 (1975) 61.
- [3] R.G. Marsden and J. Henrion, Report ESA STR-202 (1979) (unpublished).
- [4] K.-P. Wenzel, Phil. Trans. Roy. Soc. (1979) in press.
- [5] J.D. Anglin, W.P. Dietrich and J.A. Simpson, Proc. 15th Int. Conf. on Cosmic rays 5 (1977) p. 43.
- [6] M. Garcia-Munoz, G.M. Mason and J.A. Simpson, Astrophys. J. 201 (1975) 141.
- [7] G. Raisbeck, C. Perron, J. Toussaint and F. Yion, Proc. 13th Int. Conf. on Cosmic rays 1 (1973) 534.
- [8] T.R. Sanderson and D.E. Page, Nucl. Instr. and Meth. 104 (1972) 493.
- [9] D.E. Greiner, Nucl. Instr. and Meth. 103 (1972) 291.
- [10] J.F. Janni, Report AFWL-TR-65-150 (1966) (unpublished).
- [11] L.C. Northcliffe and R.F. Schilling, Nucl. Data Tables 7 (1970) 34.
- [12] E.L. Haines and A.B. Whitehead, Rev. Sci. Instr. 37 (1966) 190.
- [13] J.B.A. England, Proc. 18th Summer School in Physics. St. Andrews 1977 (D. Reidel, Dordrecht, The Netherlands).
- [14] A.G. Seamster, R.E.L. Green and R.G. Korteling, Nucl. Instr. and Meth. 145 (1977) 583.

## CALIBRATION OF A SPACE-BORNE CHARGED PARTICLE TELESCOPE USING PROTONS IN THE ENERGY RANGE 0.4 TO 20 MeV

R.G. MARSDEN, J. HENRION, T.R. SANDERSON and K.-P. WENZEL

*Space Science Department of ESA, ESTEC, Noordwijk, The Netherlands*

N. DE BRAY and H.P. BLOK

*Natuurkundig Laboratorium, Vrije Universiteit, Amsterdam, The Netherlands*

Received 8 November 1983

Detailed measurements of the response to protons in the energy range 0.4 to 20 MeV of a charged particle telescope to be flown on the International Solar Polar deep-space Mission (ISPM) have been carried out using the cyclotron facility of the Free University, Amsterdam. The purpose of the measurements was two-fold; firstly to accurately calibrate the energy bandwidths of the instrument measurement channels, and secondly to study the effect of two thin foils (0.98 mg/cm<sup>2</sup> aluminised Kapton required for thermal control of the instrument when on the spacecraft, 0.91 mg/cm<sup>2</sup> titanium needed for electrical screening) which cover the telescope aperture. The particle beam used for the measurements was derived from the population of inelastically-scattered protons produced by the interaction of the primary cyclotron beam with a scattering target. The energy of the protons arriving at the telescope was selected by means of a magnetic spectrograph. This procedure enabled changes in incident energy to be made easily and with high precision. Details of the measurement technique are given, together with examples of the telescope response data.

### 1. Introduction

The accurate determination of the response of charged particle telescopes for space applications to all types of incident particles is essential if the full scientific potential of the data returned is to be exploited. This is particularly true in the case of an instrument to be flown on a unique, exploratory mission like the International Solar Polar Mission (ISPM) [1,2], which will for the first, and probably the only time, make in situ measurements of the charged particle populations and plasma environment away from the plane of the ecliptic. In this paper, we discuss measurements performed using the Engineering Model of the Low Energy Telescope (LET) of the Cosmic Ray and Solar Charged Particle Investigation (COSPIN) experiment [3] which will be launched into deep space on board the ISPM spacecraft in May 1986. The LET, which is described in more detail in sect. 2 of this paper, is designed to measure the energy spectra and elemental composition of cosmic rays in the energy range from  $\sim 1$  MeV(<sup>1</sup>H) to 75 MeV/n (<sup>56</sup>Fe), its charge resolution extending up to  $Z = 26$ . The instrument, in addition to returning data on heavy ions, also includes 5 counting rate channels devoted to protons. These channels, which have energy windows defined by a combination of particle range

and energy threshold triggering requirements, provide data from which energy spectra and absolute fluxes can be derived. The proton measurements described in this paper were performed with a view to accurately determining the boundaries of the energy windows for all five channels, with particular emphasis on the lower threshold of the lowest energy channel.

In order to perform such calibration measurements in an efficient way, it is desirable to have a beam of protons for which the energy is known to high precision, but whose energy can be continuously, and easily varied throughout the range of interest. Since the LET responds to protons having energies between  $\sim 1$  and 20 MeV, it would in principle be possible to use the primary beam from a cyclotron to provide particles at specific energies. Such a method has the disadvantage, however, of requiring time-consuming accelerator tuning for each change in energy, as well as providing intensities which are in general too high. It was therefore decided to extract the particles needed for the calibration measurements from the population of inelastically-scattered protons produced by the interaction of the primary cyclotron beam with a scattering target, using a magnetic spectrograph. This technique had the advantage that the protons entering the detector telescope had a well-defined, yet continuously variable en-

ergy, at a beam intensity which could be safely handled by the instrument.

In the following sections we firstly describe the main features of the LET, and then discuss in detail the experimental configuration. Finally, we present examples of the data obtained, and compare these with the results of theoretical calculations based on standard energy-loss tabulations [4,5].

## 2. The low energy telescope

The Low Energy Telescope (LET) sensor shown in schematic form in fig. 1 consists of a four-element solid-state detector telescope (D1–D4), surrounded by a cylindrical plastic scintillator anti-coincidence shield (D5). D1 and D2 are surface barrier devices of equal active area ( $6.0 \text{ cm}^2$ ) having average thicknesses of 31.1 and  $104 \mu\text{m}$  respectively, while D3 and D4 are 2 mm thick lithium-drifted devices of 10.0 and  $12.5 \text{ cm}^2$  active area, respectively. The useful areas of the D1 and D2 detectors are limited to  $4.4 \text{ cm}^2$  by two mechanical collimators, in order to reduce edge effects. The instrument operates in the double  $dE/dX$  vs  $E$  mode, with D4 forming part of the anti-coincidence shield. The telescope aperture is covered by two thin foils, an inner titanium foil of  $0.91 \text{ mg/cm}^2$  and an outer aluminised Kapton foil of  $0.98 \text{ mg/cm}^2$ . The titanium foil acts as an electrical screen for D1, since this detector is operated with its aluminium contact facing outwards in

order to reduce radiation damage; the outer Kapton foil is included in order to meet the thermal requirements of the instrument when integrated into the ISPM spacecraft.

The signal from each of the detectors is fed via a separate amplifier chain to a set of threshold discriminators, the outputs of which are combined in the coincidence logic circuitry in order to define a series of counting-rate channels. The values of the appropriate discriminator thresholds, together with the logic equations used to define the five LET proton channels, are given in table 1. As can be seen, each detector has a nominal lower triggering level of 300 keV. Also shown in the table are the nominal energy windows corresponding to each channel, calculated on the basis of standard energy-loss tabulations [4,5].

As a result of the additional absorbing material introduced into the telescope field-of-view by the thin foils, the lowest incident particle energy to which the instrument responds no longer corresponds to the triggering threshold D1A (300 keV), but to some higher value, as indicated by the nominal energy response for channel LP1 (0.9–1.2 MeV). This effect will also be present, although to a lesser extent, in the other, higher-energy, channels. Since the calculation of absolute fluxes in space requires a precise knowledge of the energy response of the LET detector system, it is clearly important to determine the effect of the foils on this response experimentally.

## 3. Experimental techniques

The Philips variable energy AVF cyclotron of the Free University, Amsterdam, is capable of accelerating the following particles: protons, deuterons, alpha particles and  $^3\text{He}$  ions to maximum energies of 30, 16, 32 and 45 MeV, respectively. The beam can be brought to several experimental areas by means of a bending magnet. In the present experiment, protons travelled along a high-resolution beamline, including slits and an analysing magnet, to a scattering chamber and magnetic spectrograph, shown schematically in fig.2. The energy spread and angular dispersion in the beam are reduced by the slits and magnet at the expense of the beam current.

The magnetic spectrograph is of the split-pole type described by Spencer and Enge [7]. It has good focusing characteristics as a result of two extra magnet edges, which give almost perfect focusing in the horizontal direction and near-focusing in the vertical direction. In its normal mode of operation, the spectrograph is used to measure reaction products from nuclear reactions arising from the interaction of beam particles with target nuclei. Such reaction products are detected in a detector chamber by means of a number of one-dimen-

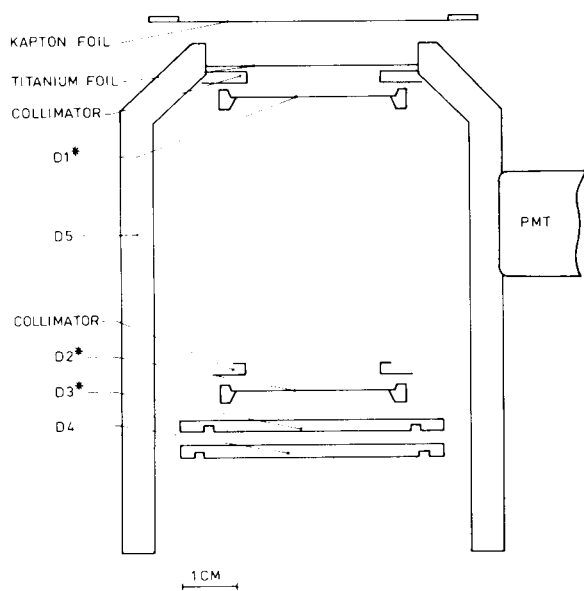


Fig. 1. Schematic representation of the COSPIN Low Energy Telescope.  $D_m^*$  indicates a detector that is pulse-height analysed.

Table 1

LET discriminator threshold values and proton counting-rate channel logic equations. The logic parameters I1 and I5 are derived from the LET Particle Identifier circuit [6].

Disc.	Nominal threshold [MeV]	Disc.	Nominal threshold [MeV]	Disc.	Nominal threshold [MeV]
D1A	0.30	D2A	0.30	D3A	0.30
D1B	0.90	D2B	3.40	D3B	6.50
D1C	2.10			D3C	16.0

Channel	Logic equation	Nominal energy response [MeV]
LP1	D1A $\overline{D1B}$ $\overline{D2A}$ $\overline{D4}$ $\overline{D5}$	0.9–1.2
LP2	D1B $\overline{D1C}$ $\overline{D2A}$ $\overline{D4}$ $\overline{D5}$	1.2–3.0
LP3	D1A D2A $\overline{D3A}$ $\overline{D4}$ $\overline{D5}$ I1	1.8–3.8
LP4	D1A D2A D3A $\overline{D2B}$ $\overline{D3B}$ $\overline{D4}$ $\overline{D5}$ I5	3.8–8.0
LP5	$\overline{D1A}$ D2A D3B $\overline{D4}$ $\overline{D5}$ I5	8.0–19

sional position-sensitive solid state detectors (PSD) [8,9]. The angle between the incoming beam and the detected reaction products can be varied continuously between  $-90^\circ$  and  $+160^\circ$ .

In order to satisfy the LET requirement for a beam of particles for which the energy was known to high precision, but whose energy could be continuously and easily varied throughout a given range, the following procedure was adopted. The LET was mounted on an adjustable baseplate inside the detector chamber of the spectrograph (i in fig. 2), thereby simplifying the mechanical and electrical interfaces. This arrangement also enabled the LET axis to be aligned with the incoming beam. A collimator of 5 mm diameter, incorporating two broom magnets to deflect secondary electrons, was placed in front of the LET aperture, with carbon shield-

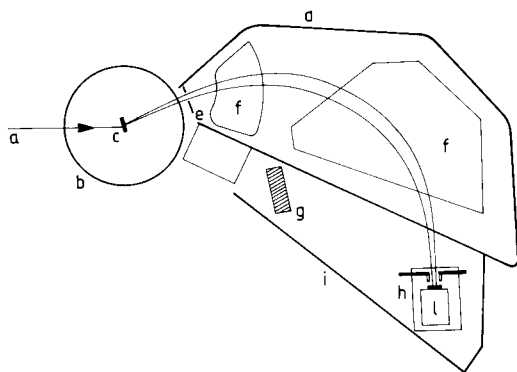


Fig. 2. Schematic representation of the magnetic spectrograph used to perform the LET calibration, showing (a) the incoming proton beam, (b) the scattering chamber, (c) the target, (d) the magnet chamber, (e) the entrance slit, (f) the magnet pole-pieces, (g) paraffin blocks, (h) the LET mounting platform and collimator, (i) the detector chamber and (l) the LET package.

ing extending from both sides of the collimator plate in order to reduce the production of neutrons by particles not passing through the collimator aperture. As further protection from neutrons, paraffin blocks were placed in the detector chamber between the scattering chamber and the LET.

A beam of 25 MeV protons was allowed to impinge on a thick target placed in the scattering chamber (b in fig. 2). The reaction products leaving this target com-

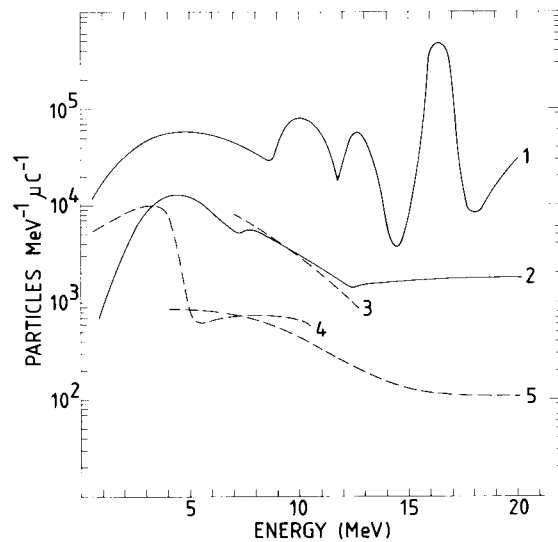


Fig. 3. Yield curves for secondary particles produced by scattering 25 MeV protons on thick carbon and nickel targets, as measured in the detector chamber at the location of the LET using standard spectrograph detectors: (1) protons from carbon target; (2) protons from nickel target; (3)  $\alpha$  particles from carbon target; (4) deuterons from carbon target; (5)  $\alpha$  particles from nickel target.

prised elastically- and inelastically-scattered protons, as well as protons, deuterons and alpha particles resulting from the break-up of the target nuclei. For the purpose of the measurements described here, the entrance aperture of the spectrograph was oriented at  $15^\circ$  with respect to the incoming beam direction in order to maximise the secondary yield, at the same time avoiding unwanted scattering from a Faraday cup used to monitor the beam current. The measured energy distribution of the particles so produced is shown in fig. 3 for carbon and nickel targets of thickness 200 and 25 mg/cm<sup>2</sup>, respectively. As can be seen, there is a considerable difference in yield between the carbon and nickel targets. The peaks in the proton distribution from the carbon are due to the excitation of the inelastic levels, smeared out due to the target thickness. In nickel there are so many inelastic peaks that these are seen as a continuum. The slower fall-off in proton yield with decreasing energy below 5 MeV for carbon as compared with nickel is thought to be due to the lower Coulomb barrier of carbon. The peak in the deuteron spectrum from carbon below 5 MeV is due to the (p,d) reaction on <sup>12</sup>C, which has a Q-value of  $-16.5$  MeV. The few counts seen above 5 MeV must be due to the (p,d) reaction on <sup>13</sup>C. Because of the requirement to measure the LET proton response down to  $\sim 500$  keV, it was decided to use a 1 mm (200 mg/cm<sup>2</sup>) carbon target for the measurements described in this paper, owing to its higher yield over the energy range of interest as compared with nickel.

By varying the magnetic field in the spectrograph, the momentum, and thereby the energy, of the particles passing through the collimator and impinging on the LET could be varied. The advantage of this procedure is that it was possible to expose the LET to protons having energies within the desired range by simple adjustment of the spectrograph magnetic field, without having to perform a time-consuming retuning of the cyclotron. The above is also true for the secondary deuterons and alpha particles, within the constraints implied by the yield curves of fig. 3. It was necessary, however, to perform a separate calibration of the energy of the particles vs the magnetic field, since the location of the LET inside the detector chamber was different from that of the PSDs normally used in measurements with the spectrograph. For the purpose of these energy calibration measurements, the LET was replaced by a PSD and a thin ( $\sim 50$   $\mu$ g/cm<sup>2</sup>) carbon target was used. The energy of the incoming beam was determined to an accuracy of 0.1% by means of the analysing magnet. By determining the magnetic field strength at which the peaks due to elastic and inelastic scattering from <sup>12</sup>C were seen in the PSD, an energy calibration could be made, since particle momentum and magnetic field are linearly proportional for a fixed location in the detector chamber. The internal consistency of this calibration, which is also correct for the other particle species pre-

sent, was better than 0.1% in momentum, giving an uncertainty in energy of less than 0.2%.

The main contribution to the spread in energy of the particles arriving at the LET was from the finite width of the collimator aperture. This spread can be calculated from the known dispersion of the spectrograph, and was found to be approximately 0.5%. The angular spread in the beam at the location of the LET can be calculated as follows: the opening angle of the spectrograph in the vertical and horizontal directions is  $1.75^\circ$  and  $0.62^\circ$ , respectively; the known magnification factors of 0.33 and 3.0 then give a spread of  $0.58^\circ$  in the vertical and  $1.86^\circ$  in the horizontal direction.

In the following section we present some examples of LET data obtained using the above procedure.

#### 4. Experimental results

In order to achieve the experimental objectives described in sect. 1, two types of beam exposures were employed as follows. Firstly, proton beams having constant, well-defined energies (so-called spot energies) were used to determine the triggering thresholds of the five different LET proton energy channels. Secondly, the characteristic tracks for protons, deuterons and alpha particles in the D1 vs D2 and D2 vs D3 pulse height matrices (see sect. 4.2.) were populated by sweeping the beam energy slowly and continuously over the available range. Subsets of these two types of exposures included runs with the outer aluminised Kapton foils removed, and runs for which the LET was positioned with its axis at an angle of  $35^\circ$  with respect to the incident particle direction. A summary of the different beam exposures is given in table 2.

The single-foil measurements were made in order to estimate the relative energy degradation caused by each of the foils, since it is planned for thermal control reasons to cover the aperture of other sensors in the COSPIN experiment package with Kapton foil of the same thickness. The off-axis runs were performed in connection with the response of the two lowest energy channels; as can be seen from table 1, these channels respond to particles which trigger only the front detector D1. The relative contribution to the telescope geometrical factor (and hence count rate) as a function of incidence angle for such events is shown in fig. 4, assuming an isotropic incident flux. The peak in the response curve is around  $35^\circ$ , and so a number of measurements were performed with the LET axis rotated accordingly, in order to determine the low-energy cut-off in this configuration. In addition, because the single-detector channels also respond to high-energy particles which penetrate D1 and then are stopped in the internal telescope structure without triggering the anticoincidence shield D5, data were taken at energies up to 10

Table 2  
Summary of LET calibration exposures.

Incidence angle [degrees] (with respect to telescope axis)	Foil	Energy range covered [MeV]	Exposure type	
	F1 – 0.98 mg/cm <sup>2</sup> Kapton F2 – 0.91 mg/cm <sup>2</sup> titanium		Spot energies	Energy sweep
0	F1 + F2	0.8–20	×	×
	F2	0.4–20	×	×
35	F1 + F2	0.9–10	×	

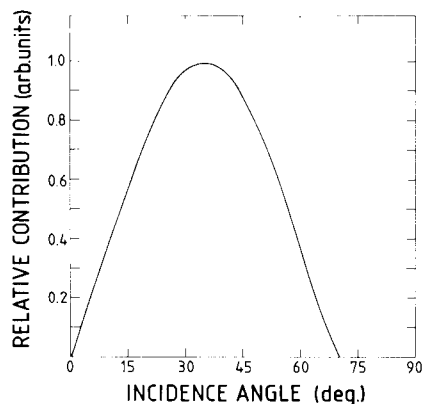


Fig. 4. Normalised relative contribution to the telescope geometrical factor as a function of incidence angle ( $dG/d\theta$ ) for channels LP1 and LP2, assuming an isotropic incident particle flux.

MeV in order to evaluate the background contribution of such events.

4.1. Energy channel threshold determination

Figs. 5 and 6 show examples of LET pulse-height distributions corresponding to beams of protons with

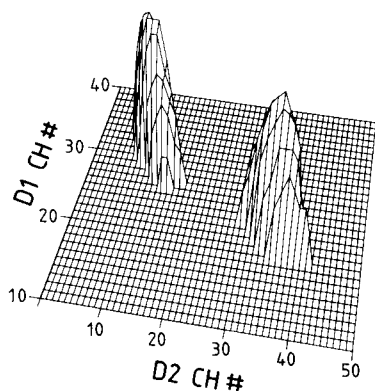


Fig. 5. D1 vs D2 pulse-height distributions plotted on a logarithmic scale for protons of 2.0 and 2.5 MeV incident energy stopping in detector D2.

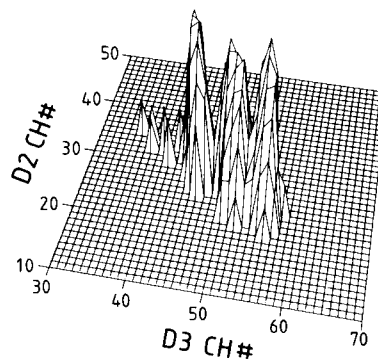


Fig. 6. D2 vs D3 pulse-height distribution plotted on a logarithmic scale for protons of 7.5, 8.0 and 8.5 MeV incident energy stopping in detector D3.

well-defined ( $< 0.5\%$  spread) energies entering the instrument and stopping in D2 and D3, respectively. Despite broadening caused by straggling in the two foils and one or both thin silicon detectors, it was still possible to determine the triggering thresholds of the respective energy channels to better than 1% using such beams. This can be shown as follows. Assuming the distributions of deposited energy to be approximately Gaussian, the uncertainty in the incident energy for which the counting rate in two adjacent channels is

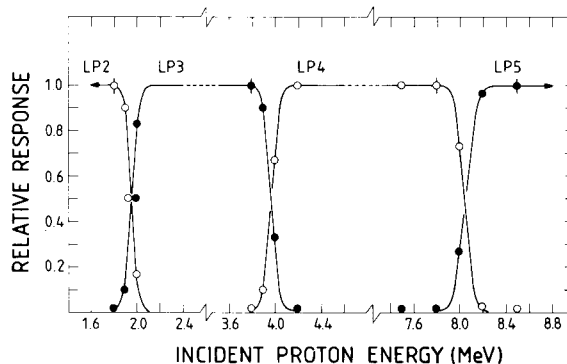


Fig. 7. Relative response of channels LP2, LP3, LP4 and LP5 as a function of incident proton energy.

equal is given by

$$\delta E \leq (2\pi)^{1/2} \sigma_E \delta r,$$

where  $\delta r$  is the measured uncertainty in the adjacent channel counting-rate ratios and  $\sigma_E$  is the standard deviation of the appropriate pulse-height distribution. From the data,  $\delta r \sim 0.06$  ( $2\sigma$ ) and  $\sigma_E$  has a value between  $\sim 85$  and  $120$  keV. This gives  $\delta E \leq 20$  keV for all channels, so that  $\delta E/E \leq 0.01$ .

For each pair of adjacent energy channels, measurements were made of the counting rates at a number of incident energies distributed around the nominal threshold between the two channels. Fig. 7 shows a plot of the relative response of the channels LP2, LP3, LP4 and LP5 as a function of incident proton energy derived from these data. The clean separation between the channels is evident. The threshold determination in the case of the lowest energy channel LP1 was complicated by the change in incident flux as a function of energy described in sect. 3. Taking the yield curves of fig. 3 for protons on carbon gives the following relationship

$$Y(E) \sim E^{+1.0},$$

where  $Y(E)$  is the yield in particles  $\text{MeV}^{-1} \mu\text{C}^{-1}$  for protons of incident energy  $E$  MeV. Integrating this expression gives the number of particles per second,  $N(E)$ , where

$$N(E) \sim E^{+2.0}.$$

Relative response curves based on counting rates normalised in this way are shown in fig. 8 for both  $0^\circ$  and  $35^\circ$  orientations of the telescope axis.

Thresholds for all five proton channels are summarised in table 3. Also given in the table are the nominal thresholds derived from range-energy computations. The agreement between measured and computed values is in general good. The measured threshold for LP1 at the 50% response level is somewhat higher

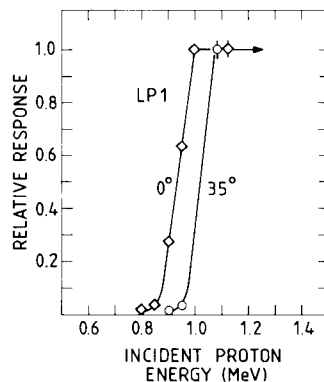


Fig. 8. Relative response of channel LP1 as a function of incident proton energy for particles incident at  $0^\circ$  and  $35^\circ$  with respect to the LET axis.

Table 3  
LET energy channel thresholds.

Channel	Threshold [MeV]	
	Measured	Calculated
LP1	0.93( $0^\circ$ ) 1.02( $35^\circ$ )	0.85( $0^\circ$ ) 0.95( $35^\circ$ )
LP1/LP2	1.30	1.2
LP2/LP3	1.95	1.8
LP3/LP4	3.95	3.8
LP4/LP5	8.05	8.0
LP5	$\sim 19$ (upper)	19

than the calculated value, but the latter assumed a D1A discriminator level of 300 keV and analysis of the D1 vs D2 pulse-height data (see sect. 4.2) indicates a value closer to 450 keV for the instrument tested. Presented in fig. 9 are the results of proton energy-loss calculations based on the data of Northcliffe and Schilling [4] and Littmark and Ziegler [5] for the two thin foils. The residual energy is plotted as a function of incident energy for particles penetrating a 2 micron ( $0.91 \text{ mg cm}^{-2}$ ) titanium foil (curve (a)), a 7 micron ( $0.98 \text{ mg cm}^{-2}$ ) Kapton foil (curve (b)), and the combination of the two (curve (c)). Also shown in fig. 9 is the nominal position of the D1A low-level discriminator, together with the inferred level D1A'. As can be seen, the measured LP1 response data are consistent with this latter value.

Data from the runs performed without the outer

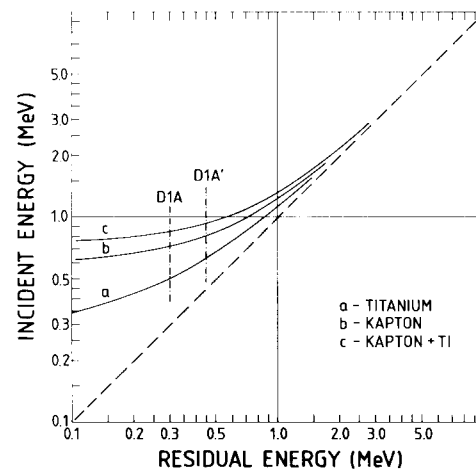


Fig. 9. Theoretical energy-loss curves for protons penetrating a  $0.91 \text{ mg/cm}^2$  titanium foil (curve (a)), a  $0.98 \text{ mg/cm}^2$  aluminised Kapton foil (curve (b)) and the combination of the two foils (curve (c)), based on range-energy tabulations by Northcliffe and Schilling [4] and Littmark and Ziegler [5]. Also shown are the normal (D1A) and inferred (D1A') positions of the low-level discriminator of detector D1.

Kapton foil have been compared with the predicted threshold values given by curve (a) of fig. 9. Again these data are consistent with the inferred D1A' level of 450 keV, corresponding to an incident proton energy threshold of  $\sim 600$  keV at the 50% response level. It should be noted, however, that this value has an associated uncertainty of  $\sim 50$  keV owing to the lower incident flux.

#### 4.2. Pulse-height data

In addition to signal processing via threshold discriminators and coincidence logic, the outputs from the D1, D2 and D3 detectors are pulse-height analysed by means of a common 10-bit (1024 channel) analogue-to-digital converter, permitting particle identification using the  $dE/dx$  vs  $E$  technique. Because of the large dynamic range needed to measure heavy ions up to iron, dual-gain pulse-shaping amplifiers are used, giving full-scale ranges for D1, D2 and D3 of 32, 32 and 128 MeV and 210, 640 and 4096 MeV in high- and low-gain modes, respectively. Figs. 10 and 11 are pulse-height matrices for events stopping in D2 and D3 respectively, both in high-gain mode. The characteristic tracks for protons, deuterons and  $\alpha$  particles, obtained by sweeping through the range of incident particle energies are clearly seen, although the effect of reduced production efficiency for  $\alpha$  particles at higher energies ( $\geq 12$  MeV) is evident in both matrices.

The proton track in the D1 vs D2 matrix shows evidence of a low-energy cut-off for D1 at  $\sim 450$  keV, 50% higher than the nominal 300 keV threshold for the D1A discriminator. This effect is also seen in the LP1 counting rate channel, as described in section 4.1. With the discriminator set at its nominal value, all protons stopping in D2 will give a signal in D1 which is above the threshold.

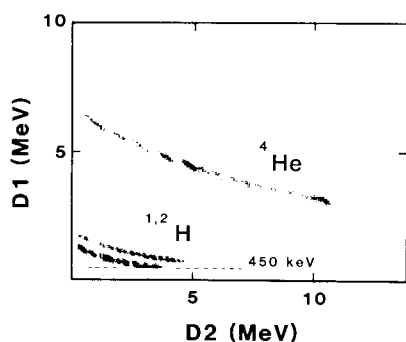


Fig. 10. D1 vs D2 pulse-height matrix (high-gain mode), showing the characteristic tracks for protons, deuterons and alpha particles. The proton track shows evidence of a cut-off caused by an increase in the detector D1 low-level discriminator (D1A) from 300 to circa 450 keV.

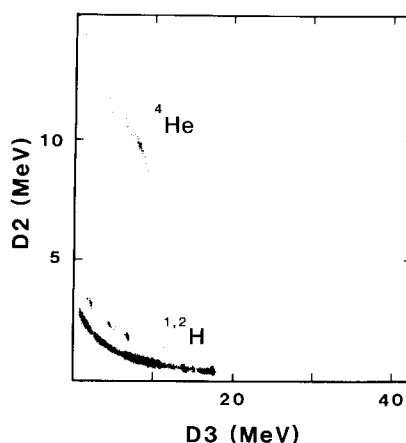


Fig. 11. D2 vs D3 pulse-height matrix (high-gain mode), showing the characteristic tracks for protons and deuterons. Owing to the reduced yield above  $\sim 12$  MeV, the alpha particle track is not clearly evident.

The measured particle track positions will be used in combination with data obtained from heavy ion calibrations at the Lawrence Berkeley Laboratory Bevatron, in order to define the reference levels required for the LET Particle Identifier circuit [6].

#### 5. Conclusions

In this paper we have described the calibration of a cosmic ray detector telescope using protons in the energy range 0.4 to 20 MeV. The use of a magnetic spectrograph to extract particles of well-defined energies from a continuum of elastically- and inelastically-scattered protons and reaction products has been shown to be a successful and efficient technique, enabling an accurate determination of the thresholds and bandwidths of the low energy telescope proton channels. The measurements performed have demonstrated the clean separation between these channels, confirming the ability of the instrument to measure accurately proton energy spectra in space. The low-energy cut-off introduced by aluminised Kapton and titanium foils covering the telescope aperture was found to be consistent with calculations based on range-energy tabulations by Northcliffe and Schilling [4] and Littmark and Ziegler [5]. It is planned to perform similar calibrations of the LET Flight and Flight Spare models in early 1984.

COSPIN is an international collaborative experiment with Prof. J.A. Simpson as Principal Investigator.

**References**

- [1] K.-P. Wenzel, R.G. Marsden and E.J. Smith, in: The international solar polar mission – its scientific investigations, ESA SP-1050 (1983).
- [2] R.G. Marsden and K.-P. Wenzel, in: The solar system and its exploration, ESA SP-164 (1981).
- [3] J.A. Simpson, D. Anglin, A. Balogh, M. Bercovitch, J.M. Bouman, B. Budzinski, R. Burrows, R. Carvell, J. Firth, M. Garcia-Munoz, J. Henrion, R.J. Hynds, B. Ivers, R.M. Jacquet, C. Julliot, H. Kunow, J.E. Lamport, G.A. Lentz, R.G. Marsden, R.B. McKibben, R. Müller-Mellin, M.A. Perkins, A. Raviart, E. Roche, T.R. Sanderson, R.J. Scheper, K.H. Stellmaschek, L. Treguer, M. Trischberger, A.J. Tuzolino and K.-P. Wenzel, in: The international solar polar mission – its scientific investigations, ESA SP-1050 (1983).
- [4] L.C. Northcliffe and R.F. Schilling, Nucl. Data Tables 7 (1970) 34.
- [5] U. Littmark and J.F. Ziegler, Handbook of range distributions for energetic ions in all elements (vol. 6 of the stopping and ranges of ions in matter) (Pergamon Press, New York, 1979).
- [6] J.F. LeBorgne, J. Henrion, R.G. Marsden, T.R. Sanderson and K.P. Wenzel, Report ESA STM-224 (1981).
- [7] J.E. Spencer and H.A. Enge, Nucl. Instr. and Meth. 49 (1967) 181.
- [8] H.P. Block, thesis, Vrije Universiteit, Amsterdam (1972).
- [9] E. Laegsgaard, Nucl. Instr. and Meth. 162 (1979) 93.

## THE PHOBOS LOW ENERGY TELESCOPE CHARGED PARTICLE EXPERIMENT

R.G. MARSDEN<sup>1)</sup>, V.V. AFONIN<sup>2)</sup>, A. BALAZS<sup>4)</sup>, G. ERDÖS<sup>4)</sup>, J.P.G. HENRION<sup>1)</sup>,  
A.K. RICHTER<sup>3)</sup>, P. RUSZNYAK<sup>4)</sup>, A. SOMOGYI<sup>4)</sup>, S. SZALAI<sup>4)</sup>, A. VARGA<sup>4)</sup>,  
L. VARHALMI<sup>4)</sup>, K.-P. WENZEL<sup>1)</sup> and M. WITTE<sup>3)</sup>

<sup>1)</sup> Space Science Department of ESA, ESTEC, Noordwijk, The Netherlands

<sup>2)</sup> Space Research Institute, Moscow, USSR

<sup>3)</sup> Max-Planck-Institut für Aeronomie, Lindau, FRG

<sup>4)</sup> Central Research Institute for Physics, Budapest, Hungary

Received 25 May 1989

The Low Energy Telescope (LET) experiment on board the Phobos 1 and 2 spacecraft measures the flux, energy spectra and elemental composition of solar energetic particles and cosmic ray nuclei from hydrogen up to iron in the energy range  $\sim 1$  to  $\sim 75$  MeV/n. The LET sensor system comprises a double  $dE/dX$  vs  $E$  solid-state detector telescope surrounded by a cylindrical plastic scintillator anticoincidence shield, and the instrument is equipped with a comprehensive particle identifier and event priority system that enables rare nuclei to be analysed in preference to the more common species. Isotope separation for light nuclei such as He is also achieved. The sensor is mounted on a rotating platform to enable coarse anisotropy measurements of low energy protons to be made.

### 1. Introduction

Measurements of solar energetic particles and low energy cosmic rays made by instruments on board the two Soviet Phobos spacecraft contribute to the study of the propagation and acceleration of charged particles on the Sun and in interplanetary space during the rising phase of solar cycle 22. This period is of particular interest since it coincides with the transition between the steady, recurrent solar wind flow patterns characteristic of solar minimum, and the transient flows, often related to energetic flare events on the Sun, encountered at solar maximum. The instrument described in this paper, the Low Energy Telescope (LET), is part of the ESTER experiment package on board Phobos [1] that has been designed to make measurements of the solar wind, the suprathermal and energetic particle populations, and low energy cosmic rays.

Specifically, the LET experiment measures the flux, energy spectra and elemental composition of solar energetic particles and low energy cosmic ray nuclei from hydrogen up to iron. The instrument covers an energy range from  $\sim 1$  to  $\sim 75$  MeV/n, using a double  $dE/dX$  vs  $E$  solid-state detector telescope surrounded by a cylindrical plastic scintillator anticoincidence shield. A comprehensive particle identifier and event priority system enables rare nuclei to be analysed in preference to the more common species, and isotope separation for

light nuclei such as He is also achieved. The sensor is mounted on a rotating platform to enable coarse directional measurements of low energy protons to be made.

The paper is organized as follows. In section 2 we describe the LET experiment hardware, including a brief discussion of the thermal design. Section 3 deals with the performance of the LET in flight, illustrated by an example of data obtained during the cruise phase. Concluding remarks are contained in section 4.

### 2. Instrumentation

The LET experiment hardware, which is identical on both Phobos spacecraft, comprises three elements: the LET sensor unit itself; a rotating platform on which the sensor is mounted in order to permit coarse directional information to be obtained on the 3-axis stabilised spacecraft; the LET Interface Unit (LIU). A block diagram of the complete LET instrument is shown in fig. 1. All three components are attached to a common mounting frame that also accommodates the ESTER SLED experiment [2]. The LET flight instrument, shown in the photograph of fig. 2, weighs 6 kg (excluding mounting frame and thermal hardware) and has an average power consumption of 2.5 W. The electrical interface to the spacecraft is provided by the ESTER Data Processing Unit (DPU-B) [1].

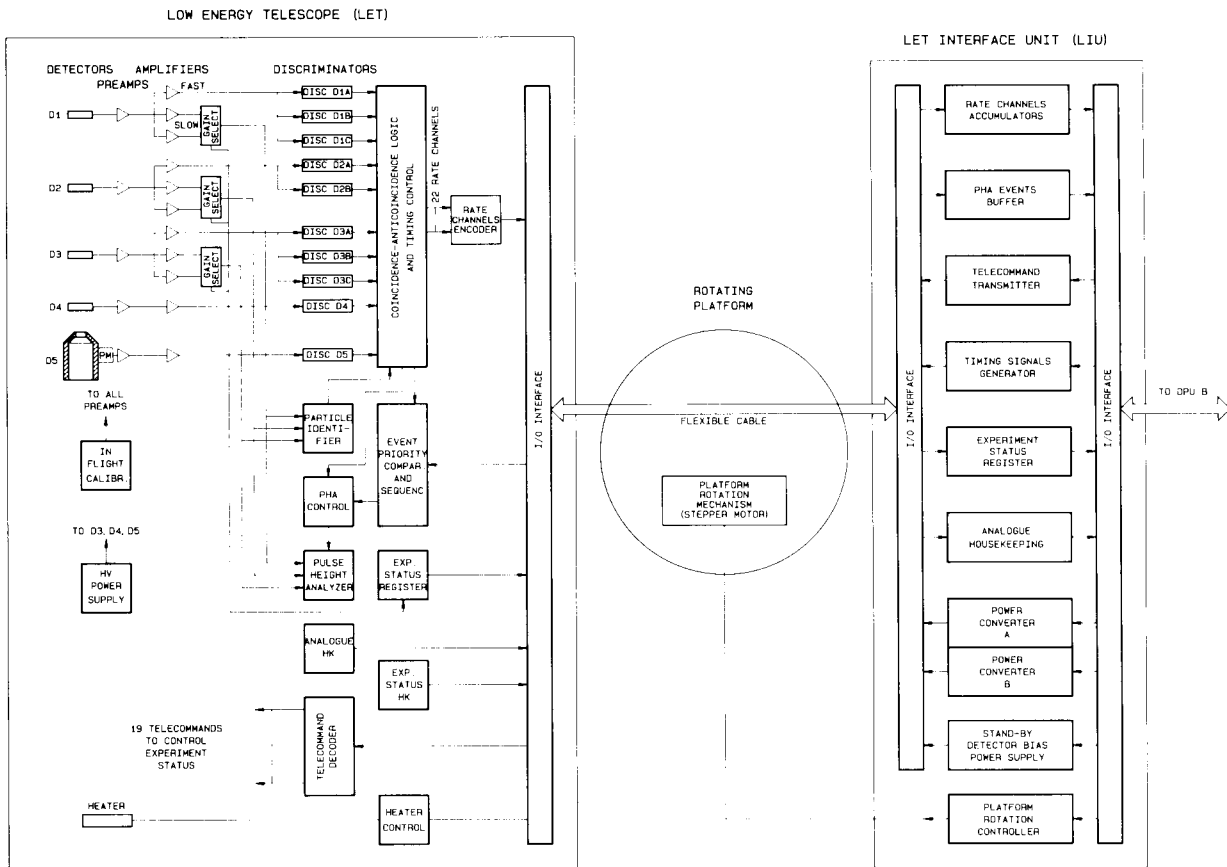


Fig. 1. Block diagram of the LET experiment, including the LET sensor, the rotating platform and the LET interface unit.

2.1. LET sensor

The LET sensor consists of a four-element solid-state detector telescope surrounded by a cylindrical plastic scintillator anticoincidence shield, together with its associated analog electronics. The telescope is shown in schematic form in fig. 3. Detectors D1 and D2 are large-area (6 cm<sup>2</sup>) surface barrier devices having nominal thicknesses of 30 μm (D1) and 100 μm (D2), while D3 and D4 are 2000 μm thick Li-drifted devices of 10.0 and 12.5 cm<sup>2</sup> active area, respectively. D4 forms part of the anticoincidence shield. Relevant physical parameters for the detectors used in the flight sensors are given in table 1. The aperture of the telescope is covered by two thin foils, an inner Ti foil (2 μm) and an outer Kapton foil (8 μm), included for electrical screening and thermal control purposes, respectively. The telescope geometrical factor, defined by two circular collimators mounted in front of D1 and D2 in order to reduce unwanted edge effects, has a value of 0.58 cm<sup>2</sup>sr for the coincidence channels. Low resolution single-detector (D1 only) measurements of protons and alpha

particles are also made. In this case, the geometrical factor is ~ 4 cm<sup>2</sup>sr.

The signals from detectors D1, D2 and D3 are fed into individual amplifier chains consisting of a charge-sensitive preamplifier followed by a parallel combination of three pulse-shaping voltage amplifiers (PSAs). To accommodate the large dynamic range required, separate low- and high-gain PSAs have been used, selected via an analog switch controlled by the third (fast) PSA in conjunction with a discriminator. The selected outputs are fed into a common 10-bit (1024-channel) ADC that provides pulse height information. The fast PSAs are followed by a number of threshold discriminators, the outputs of which are used in the coincidence logic to define a series of counting rate channels.

In addition, the outputs of the slower PSAs are fed into a Particle Identifier (PI) circuit that provides both counting rate and event priority information. The LET PI circuit makes it possible to obtain the counting rates corresponding to groups of nuclear species, and comprises a set of analog function generators and dis-

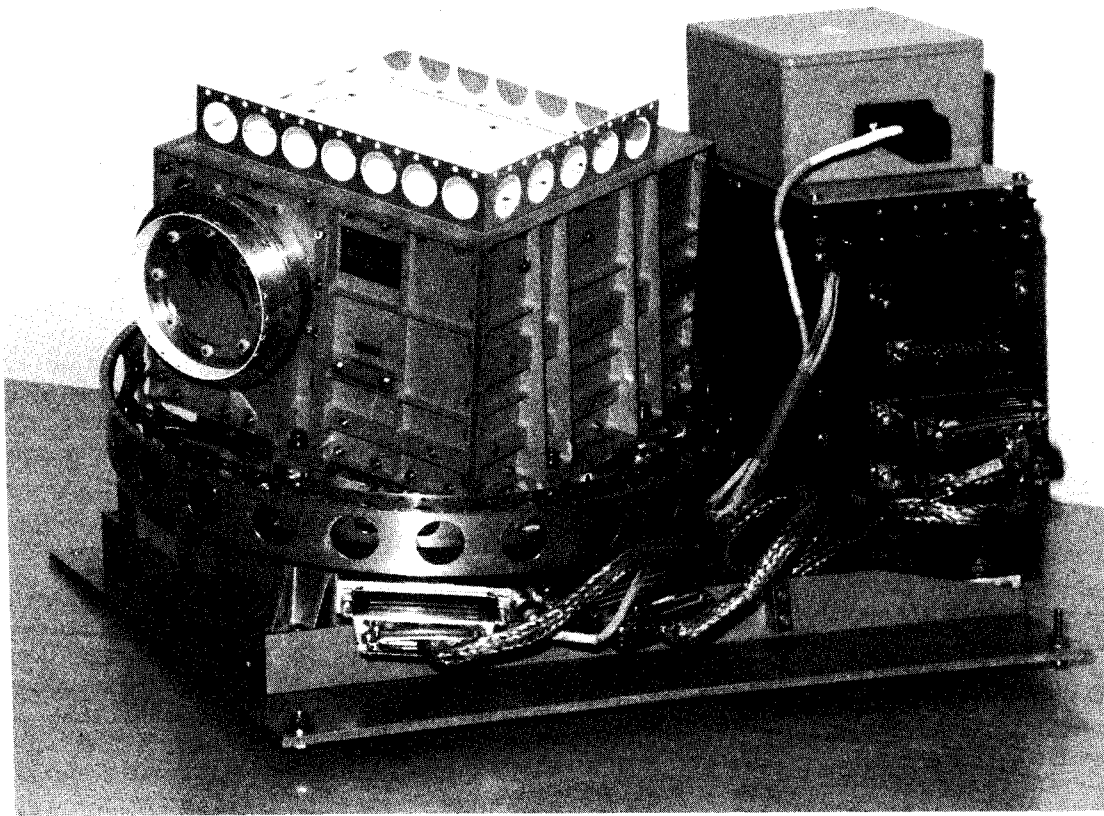


Fig. 2. The LET experiment configuration, showing the LET sensor unit, rotating platform and LIU, mounted on the common ESTER mounting frame.

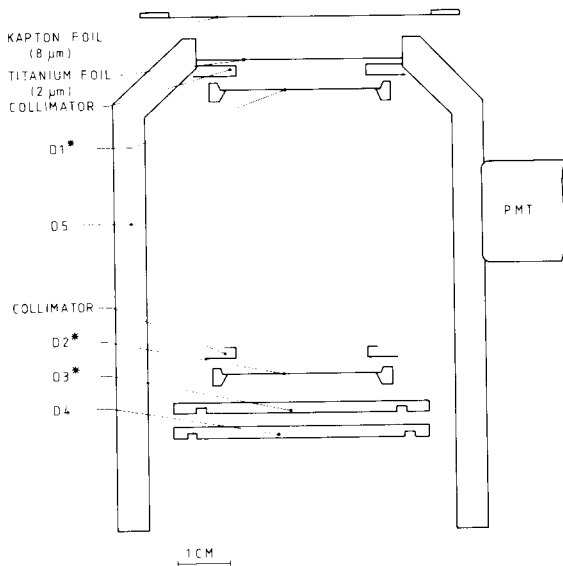


Fig. 3. Schematic representation of the LET detector telescope:  $Dm^*$  denotes a pulse height analysed detector.

criminators that divide the instrument response into regions of different nuclear charge. The actual analog functions used are of two types, namely

$$E1 + b_i E2 = a_i, \tag{1}$$

and

$$E2(b_i + E3) = a_i, \tag{2}$$

where  $E1$ ,  $E2$  and  $E3$  are the energies deposited in detectors  $D1$ ,  $D2$  and  $D3$ , respectively, and  $a_i$ ,  $b_i$  are constants. For particles stopping in  $D2$ , the loci of points satisfying eq. (1) for given pairs of  $(a_i, b_i)$  values define boundaries on the  $\Delta E (\equiv E1)$  vs residual  $E (\equiv E2)$  diagram that separate the tracks corresponding to different elements or groups of elements into so-called "charge groups". The charge groups defined for the  $D1$ - $D2$  range are: protons; ( $^3\text{He}$ ,  $^4\text{He}$ ); (Li, Be, B); (C, N, O);  $Z \geq 10$  nuclei. In a similar way, charge group boundaries for particles stopping in  $D3$  are defined by eq. (2) with suitable pairs of  $(a_i, b_i)$  values. A different functional form is required in this case because of the

Table 1  
Phobos LET detector summary

Detector	Type <sup>a)</sup>	Thickness		Area [cm <sup>2</sup> ]
		[μm]	[mg/cm <sup>2</sup> ]	
Phobos-1				
D1	SSB (Ortec)	27.6	6.43	6.0
D2	SSB (Ortec)	95.2	22.18	6.0
D3	Si(Li)(LBL)	2038	474.8	10.0
D4	Si(Li)(LBL)	2000	466	12.5
Phobos-2				
D1	SSB (Ortec)	28.7	6.69	6.0
D2	SSB (Ortec)	103.8	24.19	6.0
D3	Si(Li)(LBL)	2031	473.2	10.0
D4	Si(Li)(LBL)	2000	466	12.5

<sup>a)</sup> SSB – silicon surface barrier.

pronounced curvature of the  $\Delta E$  vs residual  $E$  tracks resulting from the large thickness of D3 relative to D2. The same charge groups as before are defined for the D1–D2–D3 range, with the addition of a high  $Z$ -group corresponding to  $Z \geq 20$ . The boundaries corresponding to the (C, N, O) charge group are illustrated schematically in figs. 4 and 5 for the D1–D2 and D1–D2–D3 ranges, respectively.

Each of the charge groups has an associated counting rate register which is incremented each time a valid event within the group is observed. Accumulation intervals are 236 s for the proton and alpha particle rate channels and 1180 s for the heavy ion rate channels. In addition to providing counting rate information, the PI output is used to generate a 4-bit event code that controls the Event Priority System. The latter is included in order to maximise the LET PHA data-collection efficiency for the rarer nuclear species in the cosmic ray flux. Such a system is needed because the LET telemetry allocation (2.4 bits per s) limits the number of PHA events that can be transmitted to 2 per minute. Each pulse-height-analysed event is assigned a 4-bit

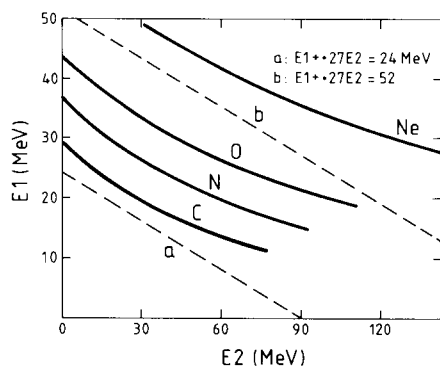


Fig. 4. LET particle identifier boundaries (dashed lines) plotted for (C, N, O) groups events stopping in D2.

priority value on the basis of its event code via predefined sequences stored in a ROM. Only the pulse heights corresponding to the highest-priority event occurring within every 30 s sampling period are transferred to the telemetry stream. The sequence of priority assignments for all event codes is changed periodically in order to prevent biasing effects. In addition to pulse height data and proton, alpha and heavy ion rates, the 360-byte LET data frame contains digital status information and analog housekeeping values, as well as counting rate data for the individual detectors. Housekeeping information includes instrument voltages, the detector leakage currents and temperature values for the detector telescope and electronics. A summary of the LET digital data channels is given in table 2.

Also included in the instrument is an In-Flight Calibrator (IFC) circuit that checks, on command, the electrical characteristics of the instrument by delivering a sequence of pulses having well-defined amplitudes to all amplifier inputs.

## 2.2. Rotating platform

In order to measure the directional characteristics of the particle fluxes, the LET sensor is mounted on a rotating platform. The full rotation range of the platform (175°) is adjusted so that in the extreme positions, the sensor axis is oriented close to the average direction of the interplanetary magnetic field. This range is divided into steps of 44°, data accumulation occurring for a fixed period of 236 s at each of the five positions. In normal operation, the platform makes a complete +60° (with respect to the spacecraft  $X$ -axis) → -115° → +60° scan cycle in 40 min, corresponding to two telemetry periods. The scan plane of the platform is tilted with respect to the ecliptic by 12° in order to avoid obscuring the LET field-of-view by other payload elements.

The main components of the platform unit are a stepper motor and its associated transmission gear that

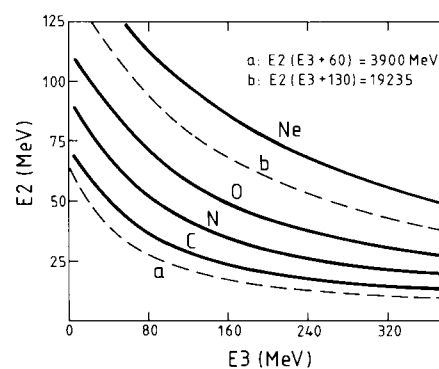


Fig. 5. As for fig. 4, but for particles stopping in D3.

Table 2  
Phobos LET data channel summary

Channel no.	Code	Measurement	Time resolution [s]
1	P1	proton 0.9–1.2 MeV	240
2	P2	1.2–3.0	240
3	P3	1.8–3.8	240
4	P4	3.8–8.0	240
5	P5	9.0–19	240
6	A1	alpha 1.0–5.0 MeV/n	240
7	A2	1.9–4.0	240
8	A3	4.0–9.0	240
9	A4	9.0–19	240
10	H1	Li, Be, B 2.3–5.2	1200
11	H2	5.2–56	1200
12	H3	C, N, O 3.2–7.5	1200
13	H4	7.5–39	1200
14	H5	Z ≥ 10 3.9–9.5	1200
15	H6	9.5–50	1200
16	H7	Z ≥ 20 12.–75	1200
17	E1	e <sup>-</sup> 0.35–1.5 MeV	1200
18	S1	D1 singles	600
19	S2	D2 singles	600
20	S3	D3 singles	600
21	S4	D4 singles	600
22	S5	D5 singles	600
	PHA	pulse heights/flags LET status	30 1200

drives the circular platform which is supported at its rim by two rows of Delrin ball-bearings. Two flexible cables, consisting of two layers of printed copper tracks enclosed in three layers of 50 μm Kapton foil, are wrapped around the axis of the platform and provide the electrical connection between the LET and LIU. A high precision potentiometer delivers accurate (better than 0.5%) measurements of the platform position, and end-switches followed by mechanical stops are incorporated to prevent rotation beyond the +60° or -115° positions.

During flight, the platform, which is controlled by DPU-B via the motor drive circuitry incorporated in the LIU (see below), can be operated in two modes: normal mode and high power mode. In normal mode, the platform moves between each of the five pointing positions in 4 s; in high power mode, a higher (by a factor 4) motor torque is provided, and the travel time between positions is correspondingly longer. This latter mode is included for operation under special conditions (test, platform malfunction, extreme temperatures, etc.). The platform can also be commanded to move directly

to either end position, stopping once it reaches +60°, or starting the normal scan from the -115° position.

### 2.3. LET interface unit (LIU)

The LET Interface Unit, as the name implies, serves as the interface between the LET analog electronics and the ESTER DPU-B (see fig. 1). The unit is physically separate from the LET sensor and, as mentioned above, also houses the motor drive control electronics for the platform. Functionally, the LIU comprises: the LET rate channel and PHA digital data interfaces; the telecommand and status interfaces; the analogue housekeeping interface and the power supply interface. In addition, the LIU provides the timing signals necessary for correct operation of the LET.

### 2.4. LET thermal design

The thermal design is driven by two contradictory boundary conditions, namely (1) temperature extremes of -20° and +50°C are to be expected for equipment mounted on the spacecraft body, and (2) the operating temperature of the solid-state detectors should never exceed +35°C (danger of irreversible damage). These constraints dictate that the LET sensor unit be thermally isolated from the rotating platform and other structural elements. Thermal control is then achieved as follows: the power dissipated inside the LET sensor (~2 W) is radiated to space through a ca. 100 cm<sup>2</sup> white-painted radiator surface on top of the sensor box, while a 0.5 W heater prevents excessive cooling. This thermal design has proven to be very effective in flight, and the detector telescope is maintained at a stable temperature ranging between -5° and +10°C.

## 3. LET performance in flight

The Phobos spacecraft 1 and 2 were successfully launched from the Baikonur Cosmodrome on 7 and 12 July 1988, respectively. Following a period of ca. 12 days to allow for outgassing, the LET experiments were switched on on 19 July, 00:30 UT (Phobos 1) and 25 July, 05:59 UT (Phobos 2). Initial data showed that the LET sensors on both spacecraft were functioning nominally, although the rotating platform on Phobos 1 was apparently unable to move from the -115° launch position. Attempts to free the platform by telecommand were unsuccessful, and the condition persisted up to the end of August 1988, at which time radio contact with Phobos 1 was lost. As an example of the data obtained on Phobos 2 during the cruise phase from Earth to Mars, fig. 6 shows pulse height information plotted in the ΔE vs residual E format for particles stopping in D2. The data cover a 4 d period starting at 00:00 UT on

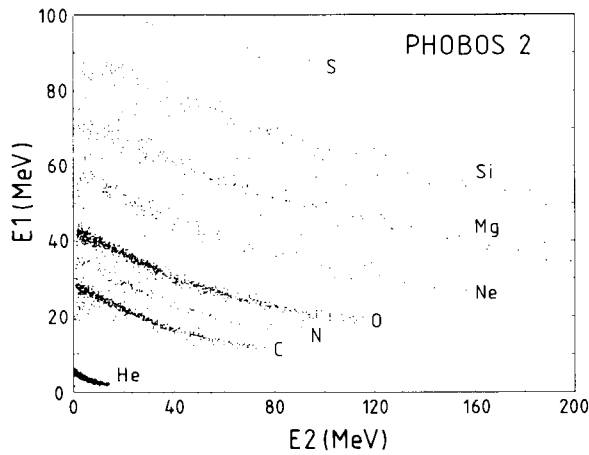


Fig. 6. Flight data from the LET experiment on Phobos 2. Shown is the D1 vs D2 pulse height matrix for the solar flare event of 17–20 December 1988.

17 December 1988, and represent particles of solar origin that have been accelerated during solar flare events and transported out to the location of Phobos 2. The tracks corresponding to the different nuclear species are clearly seen. By normalising the pulse height data to the total number of counts registered in each charge group rate accumulator, the relative abundance and energy spectrum of each individual element may be derived.

In addition to the flight data, a substantial database on the performance of the LET has been accumulated during ground testing. The LET sensors for the Phobos mission are, with the exception of the interface to the DPU, largely identical to the Low Energy Telescope to be flown on the much-delayed Ulysses mission [3]. In particular, the detector telescopes have the same specifications as the Ulysses LET instrument. The latter has already been extensively calibrated at particle accelerator facilities, with exposures to both heavy ion and proton beams [4–6].

#### 4. Conclusions

The performance of the LET instruments on the multidisciplinary Phobos mission has matched that expected from ground calibration and test, and the experiments will make important contributions to our knowledge of the particle populations in interplanetary space during the transition phase between solar minimum and solar maximum. Furthermore, based on the measured performance of the Phobos flight hardware, the LET experiment on the exploratory Ulysses mission to the solar poles is confidently expected to provide high-quality data following its launch in 1990.

#### Acknowledgements

Institutes collaborating on the LET experiments are the Space Science Department of ESA, the Space Research Institute, Moscow, the Central Research Institute for Physics, Budapest, and the Max-Planck-Institut für Aeronomie, Lindau. The authors wish to express their thanks to all those who have contributed to the success of the experiments. In particular, from ESA/SSD, L. Smit, J.M. Bouman, J. Fleur and J. Dalcolmo; from MPAe, U. Strohmeyer, K. Fischer and W. Engelhardt; from CRIP, A Steiner, I.T. Szücs and J. Erő; from IKI, S. Gubsky and V. Semenova.

#### References

- [1] V. Afonin et al., this issue, *Nucl. Instr. and Meth. A290* (1990) 223.
- [2] S. McKenna-Lawlor et al., this issue, *Nucl. Instr. and Meth. A290* (1990) 217.
- [3] K.-P. Wenzel, R.G. Marsden, D.E. Page and E.J. Smith, *Adv. Space Res.* 9 (1989) 425.
- [4] R. Kamermans, J. Henrion, R.G. Marsden, T.R. Sanderson and K.-P. Wenzel, *Nucl. Instr. and Meth.* 171 (1980) 87.
- [5] J.F. LeBorgne, J. Henrion, R.G. Marsden, T.R. Sanderson and K.-P. Wenzel, Report ESA STM-224 (1981).
- [6] R.G. Marsden, J. Henrion, T.R. Sanderson, K.-P. Wenzel, N. de Bray and H.P. Blok, *Nucl. Instr. and Meth.* 221 (1984) 619.

**ULYSSES**

**COSPIN**  
**Low Energy Telescope**

**CALIBRATION DOCUMENT**

R. G. Marsden and J. P. G. Henrion  
Space Science Dept. of ESA, ESTEC, Noordwijk

September 1990

# LET CALIBRATION DOCUMENT

## 1. Scope

The purpose of this document is to provide information on the calibration parameters needed to interpret the raw data from the COSPIN Low Energy Telescope (LET). In addition, we give a brief overview of the LET calibration history, and an outline of the data reduction procedure to be applied to the LET pulse height information. Many of the parameter values given are preliminary, and may be updated when flight data become available.

## 2. Overview

The COSPIN LET solar energetic particle/cosmic ray instrument [1, 2, 3] measures the flux, composition and energy of nuclei from hydrogen up to iron in the energy range  $\sim 1$  to  $\sim 75$  MeV/n. The sensor is a double dE/dX vs. E solid state detector telescope surrounded by a plastic scintillator anticoincidence shield, as shown in schematic form in Figure 1. The characteristics of the various detector elements are summarised in Table 2. In addition to these active elements, the two thin foils covering the entrance aperture form part of the sensor assembly. The inner foil is titanium ( $2 \mu\text{m}$ ), and the outer foil is aluminised Kapton ( $8 \mu\text{m}$ ). Table 1 summarises the digital data output from the LET, which is in the form of counting rates and pulse-height information. In order to optimise the use of the telemetry allocation, the instrument employs a system of onboard particle identification (PI), together with a PHA event priority system (EPS) to provide a balanced sample of pulse-height analysed events.

## 2. LET Calibrations

### 2.1 Accelerator calibrations

Since their manufacture in 1982 (!), the two flight models of the LET have been calibrated at a number of accelerator facilities, as shown in Table 3. The main objective of the heavy ion calibrations has been to trim the different discriminator levels in the PI electronic circuitry against the measured positions of the particle dE/dX vs. E tracks, and to verify the stability of these settings with time. In an ideal world, the LET instruments would have been exposed to all nuclear species within their detection range, and at all measurable energies, i.e. from H (0.9 - 19 MeV) to Fe (3 - 75 MeV/n). In practice, this ideal exposure was satisfactorily approximated using a high-mass primary beam (e.g. Fe or Ar) which was fragmented on a target, together with a variable-thickness absorber to achieve the required spread in energies. The above technique was employed at LBL, Berkeley and GANIL, Caen.

Additional calibration information has been obtained from so-called "spot" measurements, for which unfragmented beams of well-defined energy with minimum spread were used in an attempt to derive a first-order energy calibration, and to study the energy loss characteristics of the aperture foils. Measurements of this type were performed at the Heidelberg MP Tandem.

The energy windows of the five LET proton channels were mapped using the magnetic spectrograph of the Amsterdam Free University cyclotron [4].

## 2.2 Electronic calibrations

In addition to the accelerator calibrations discussed above, the electronic characteristics of the various LET amplifier chains and ADC circuitry have been accurately determined. These calibrations include a measurement of the overall linearity of the combined CSA (charge sensitive amplifier)  $\rightarrow$  PSA (pulse shaping amplifier)  $\rightarrow$  ADC chains, as well as the relative gains of the High- and Low-Gain amplifiers associated with each of the pulse-height analysed detectors. The results are reproduced as Figures 2, 3 and 4. Pulse height-to-energy conversion factors have been determined using high precision programmable pulse generators (PPG) to stimulate the different amplifier chains, in combination with the known sensitivity of the CSAs (i.e. mV per MeV). The ADC channel number-to-MeV conversion factors are listed in Table 4. Note that two values are given for each detector, corresponding to the High- and Low-Gain modes. In order to determine which factor should be applied, the appropriate gain flags (bits 33 – 35 of the PHA word, see Table 5) must be checked as follows: High-Gain mode is indicated by a gain flag value of 0; Low-Gain mode is indicated by a gain flag value of 1.

## 3. LET PHA Data Reduction

COSPIN LET flight data will be processed using the same set of algorithms that have been used to analyse data from the *Phobos* LET [5]. A three-step procedure has been developed in which the first step consists of a charge ( $Z$ ) interpolation algorithm that creates a charge spectrum, or histogram, followed by the second step in which a correction factor is applied to the *measured* total energy of each PHA event to take into account the energy lost in the two aperture foils. Finally, an “energy per nucleon” value is derived using the corrected incident energy and a mass number based on the calculated charge, allowing relative abundances and energy spectra to be computed.

### 3.1 Charge spectra

The conversion factors given in Table 4 have been applied to pulse height data from the GANIL accelerator runs in order to define a set of reference particle “tracks” when the data are plotted in “ $\Delta E$  vs. residual  $E$ ” format. Reference elements are He, O, Si and Fe. Using these so-called “reference tracks” as input to the charge interpolation algorithm as described in Appendix A, the charge spectra shown in Figures 5 and 6 have been derived. The spectrum of Figure 5 corresponds to events stopping in D2 (single  $dE/dX$  vs.  $E$  mode), whereas events stopping in D3 (double  $dE/dX$  vs.  $E$  mode) are presented in Figure 6, to which no background rejection has been applied. Experience with the *Phobos* data confirms that the in-flight resolution is equal to (and often better than) that seen in the accelerator data.

### 3.2 Energy loss in aperture foils

In order to determine the incident energy of heavy ions stopping in the LET, a correction factor has to be applied to take into account the energy loss occurring in the two aperture foils. Range-energy data for the two materials concerned, titanium and Kapton, have been used to construct a look-up table for all species and covering all energies detected by the LET. In the case of Kapton, for which no range-energy data exist, the tabulations of Northcliffe and Schilling [6], hereafter NS70, for polyethylene were used. These were found to be in reasonable agreement with experimental data acquired for carbon ions at the MPK MP Tandem accelerator (energy loss in flight-quality foils measured at three incident energies). NS70 data were also used for titanium. In both cases, extrapolations were made

beyond the maximum energy given in the NS70 tables (12 MeV/n). The resulting look-up table is reproduced here as Table 6. A list of other range-energy tabulations/computations that have been used to define nominal energy ranges etc. is given in Appendix B.

### References

- [1] R. Kamermans, J. Henrion, R.G. Marsden, T.R. Sanderson and K.-P. Wenzel, Nucl. Instr. and Meth., **171**, 87, (1980).
- [2] J.F. LeBorgne, J. Henrion, R.G. Marsden, T.R. Sanderson and K.-P. Wenzel, Report ESA STM-224 (1981).
- [3] J.A. Simpson et al., in: The international solar polar mission - its scientific investigations, ESA SP-1050, 155, (1983).
- [4] R.G. Marsden, J. Henrion, T.R. Sanderson, K.-P. Wenzel, N. de Bray and H.P. Blok, Nucl. Instr. and Meth., **221**, 619, (1984).
- [5] R.G. Marsden et al., Nucl. Instr. and Meth., **290**, 211, (1990).
- [6] L.C. Northcliffe and R.F. Schilling, Nucl. Data Tables, **7**, (1970).

### Figure Captions

- Fig. 1** Schematic representation of the LET detector telescope;  $Dm^*$  denotes a pulse height analysed detector.
- Fig. 2** LET SFM D1 amplifier chain: gain and linearity characteristics.
- Fig. 3** LET SFM D2 amplifier chain: gain and linearity characteristics.
- Fig. 4** LET SFM D3 amplifier chain: gain and linearity characteristics.
- Fig. 5** Charge spectrum corresponding to 2-parameter (D1D2) events constructed using data from GANIL accelerator calibration (LET SFM).
- Fig. 6** Charge spectrum corresponding to 3-parameter (D1D2D3) events constructed using data from GANIL accelerator calibration (LET SFM).

Fig. 1

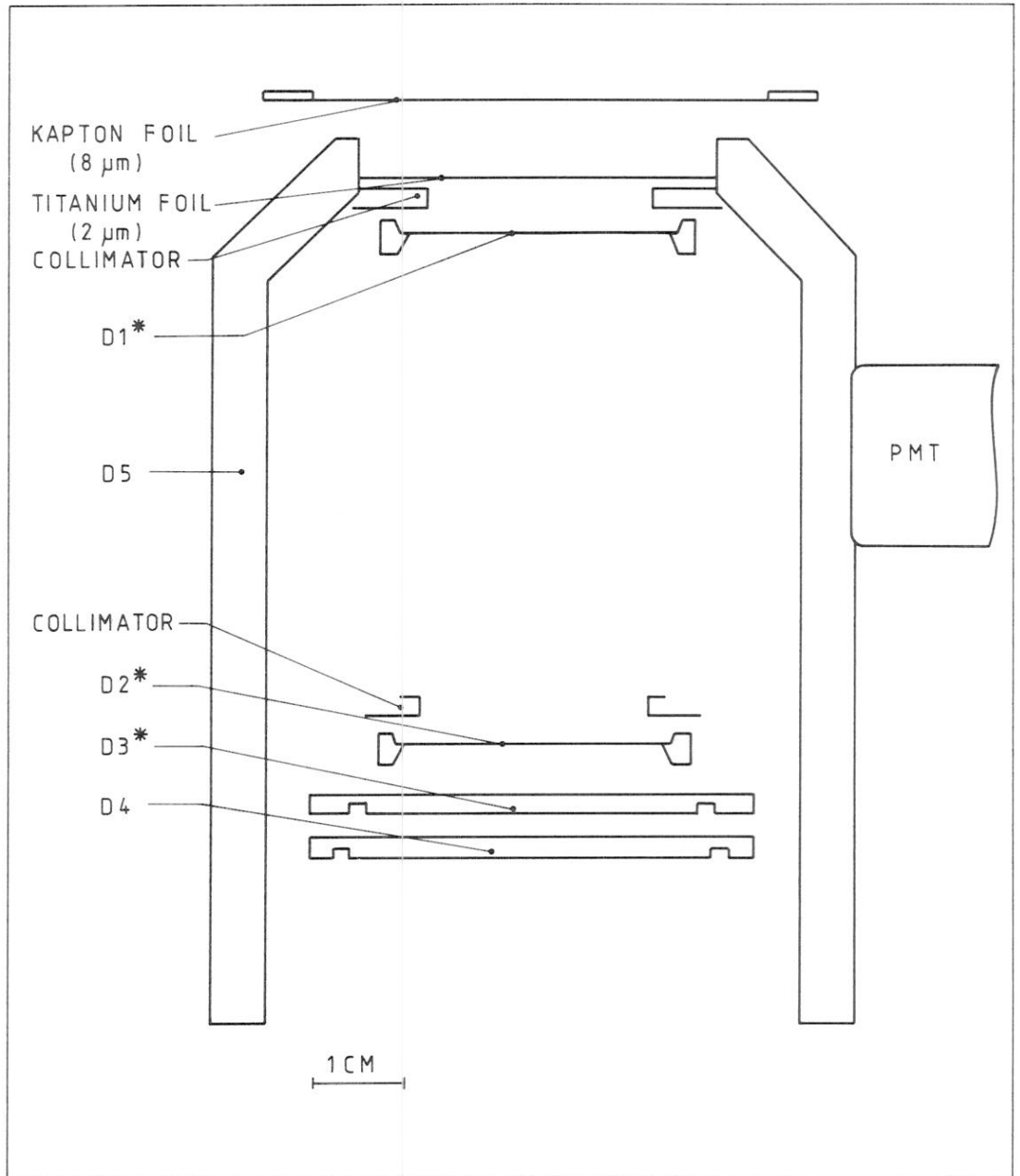


Fig. 2

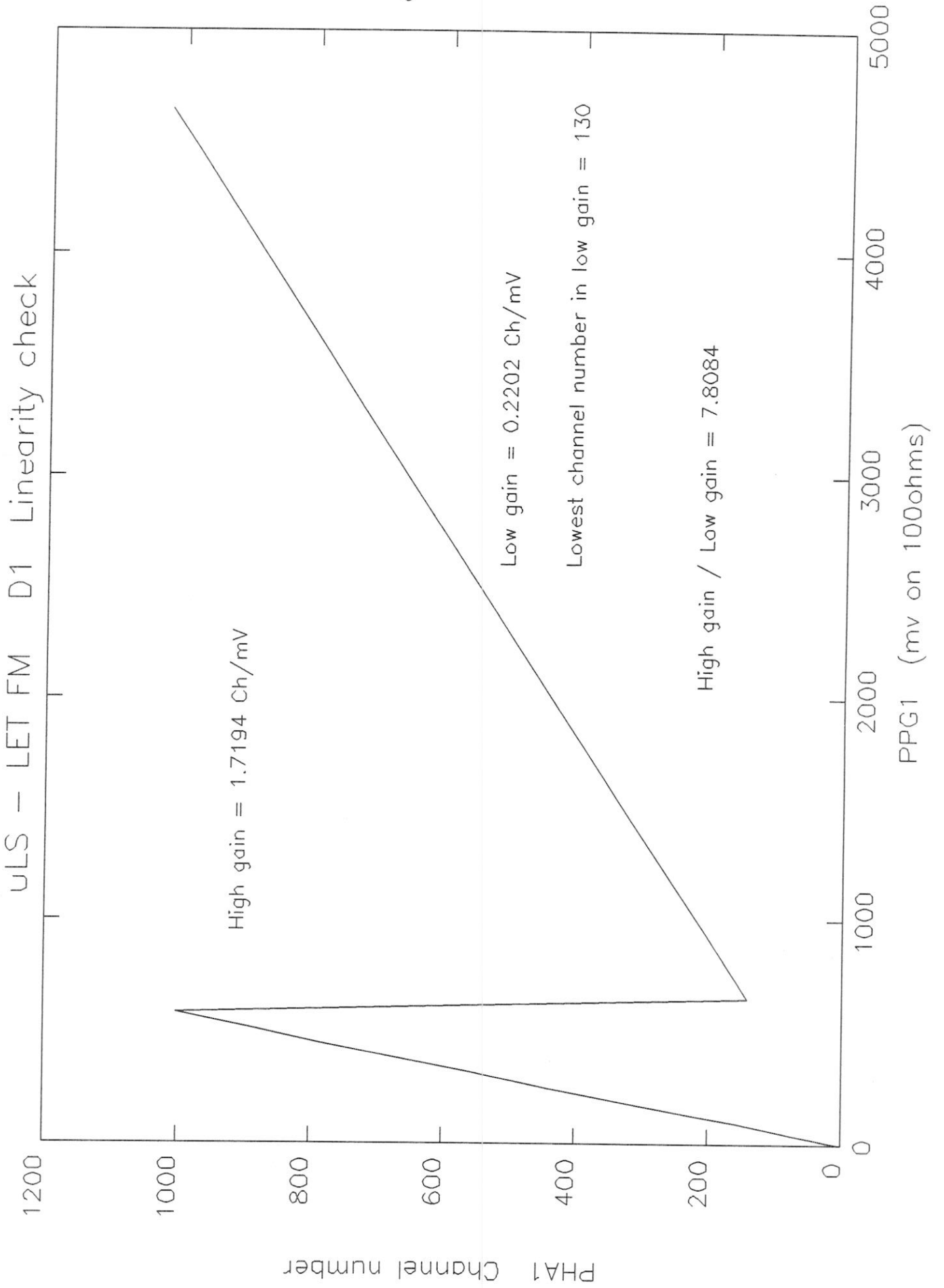


Fig. 3

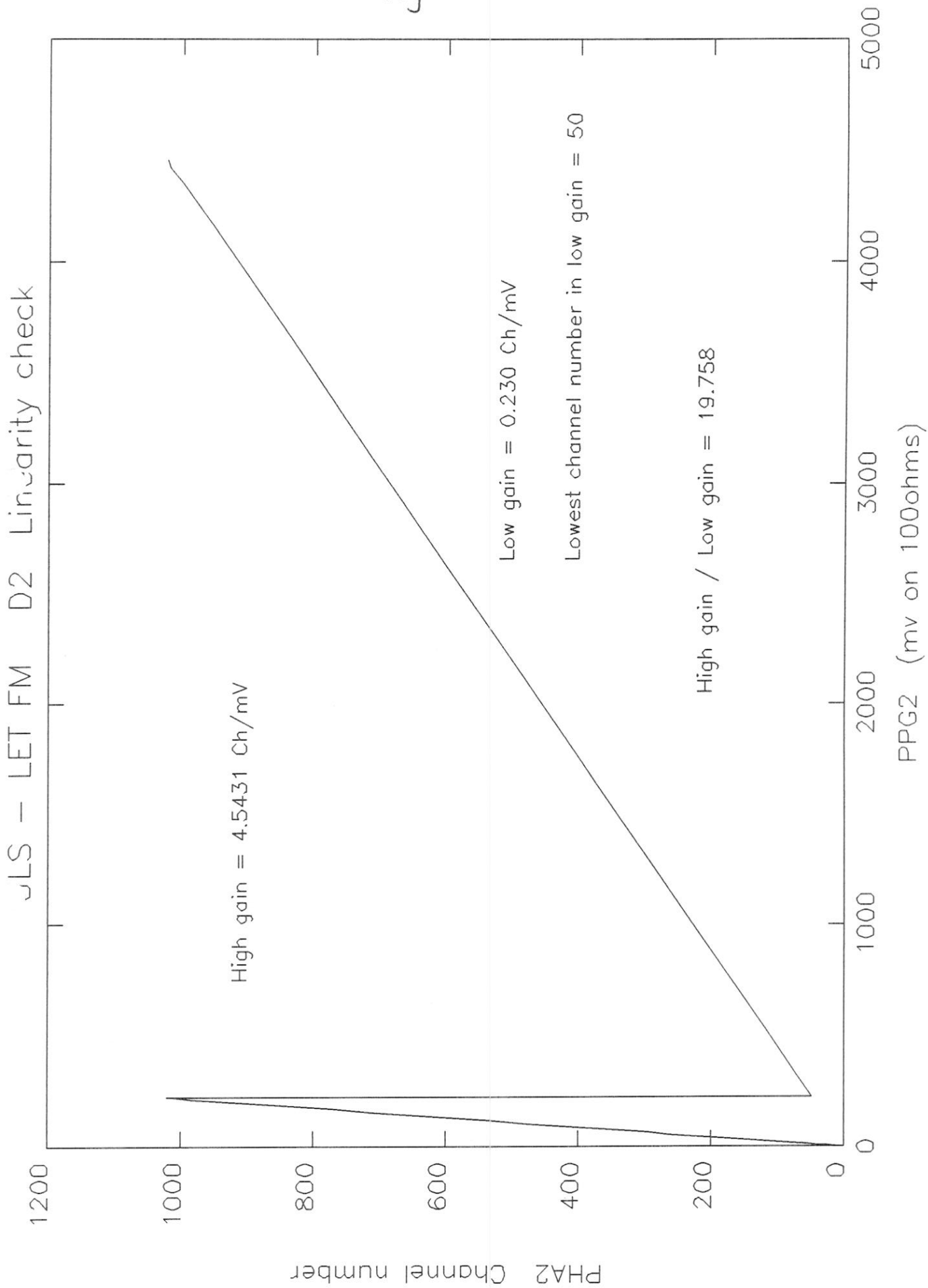


Fig. 4

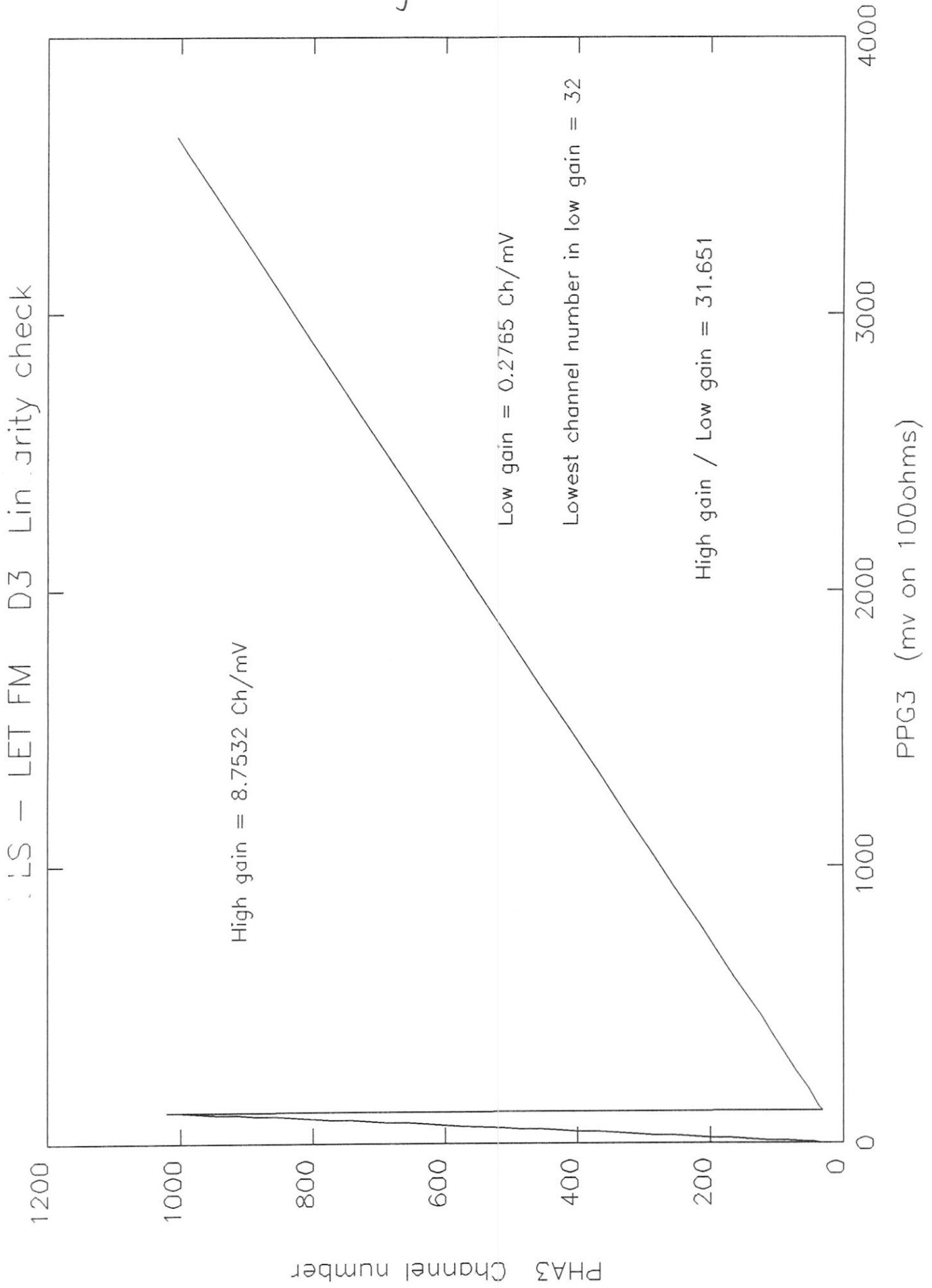


Fig. 5

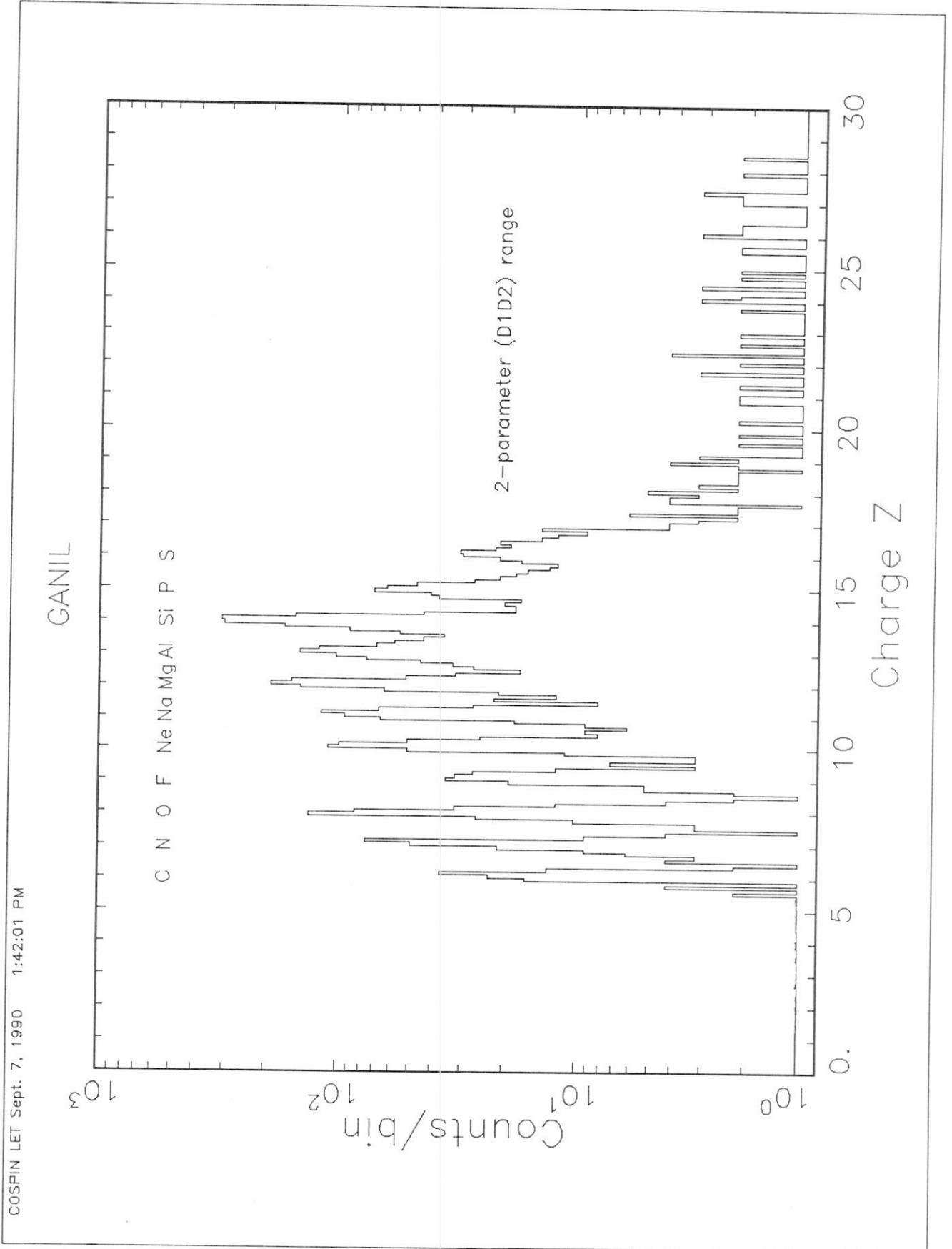


Fig. 6

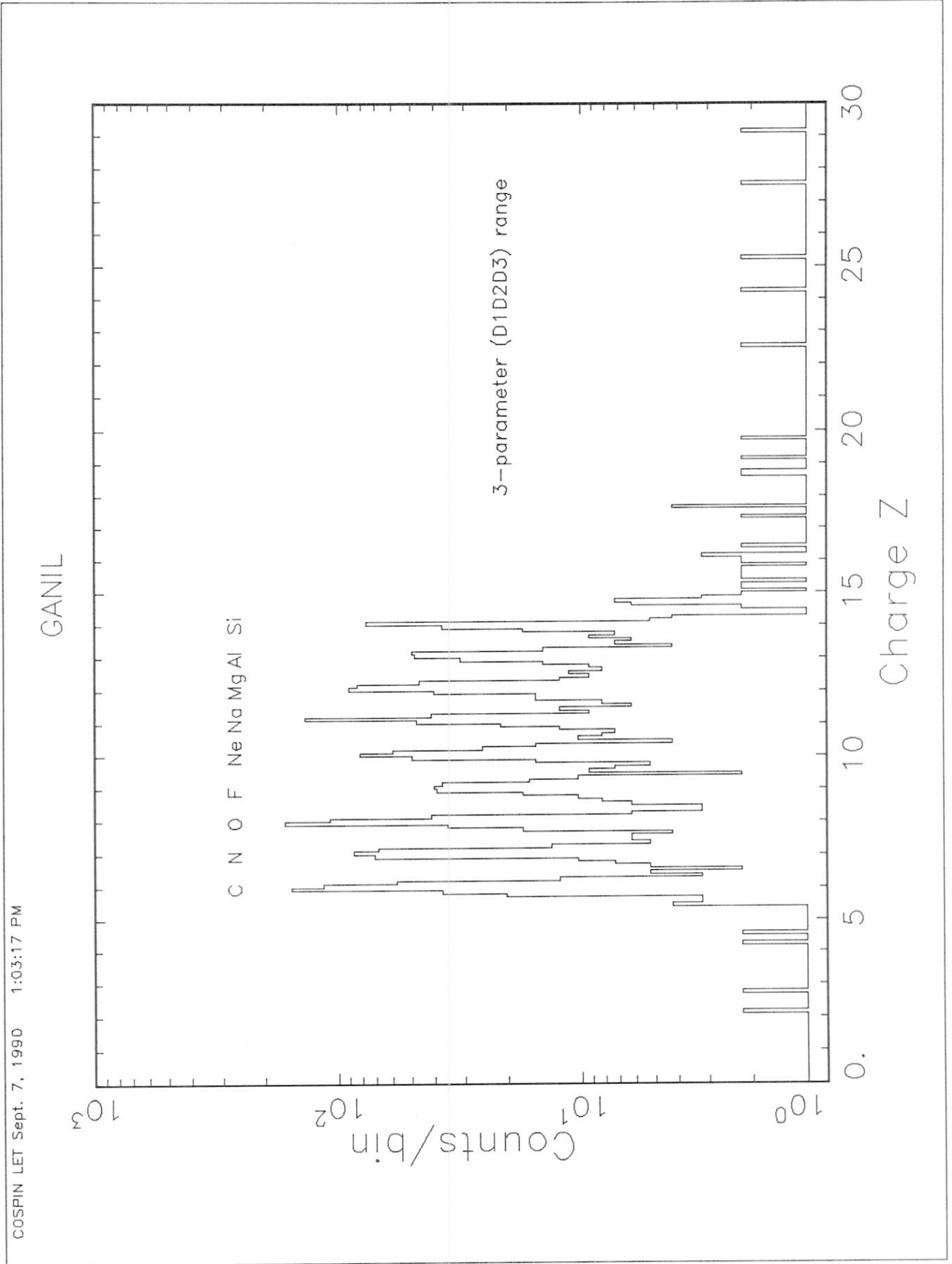


Table 1. LET digital data channels

Channel	Measurement		GF (cm <sup>2</sup> sr)	Time resolu. (sec)	Synchron.
LP1	proton	0.9–1.2 MeV	9.1	32	Format
LP2		1.2–3.0	9.1	32	Format
LP3		1.8–3.8	0.58	32	Format
LP3S*		1.8–3.8	0.58	24/36	Spin
LP4		3.8–8.0	0.58	32	Format
LP4S*		3.8–8.0	0.58	24/36	Spin
LP5		9.0–19	0.58	32	Format
LA1	alpha	1.0–5.0 MeV/n	9.1	32	Format
LA2		1.9–4.0	0.58	32	Format
LA3		4.0–9.0	0.58	32	Format
LA4		9.0–19	0.58	32	Format
LH1	Li,Be,B	2.3–5.2	0.58	128	Format
LH2		5.2–26	0.58	128	Format
LH3	C,N,O	3.2–7.5	0.58	128	Format
LH4		7.5–39	0.58	128	Format
LH5	$z \geq 10$	3.9–9.5	0.58	128	Format
LH6		9.5–50	0.58	128	Format
LH7	$z \geq 20$	12–75	0.58	128	Format
LE1	e <sup>-</sup>	0.35–1.5 MeV	–	128	Format
LS1		D1 singles		128	Format
LS2		D2 singles		128	Format
LS3		D3 singles		128	Format
LS4		D4 singles		128	Format
LS5		D5 singles		128	Format
PHA		pulse heights/flags		1	Format
		LET status		32	Format

\* 8-sector rates

**Table 2.** COSPIN SFM LET detector summary

Detector	Type	Serial no.	Thickness	
			( $\mu\text{m}$ )	( $\text{mg}/\text{cm}^2$ )
D1	Ortec 600-30	22-235B	32.2	7.503
D2	Ortec 600-100	20-663C	95.9	22.345
D3	LBL 1000-2000	4469	2054	478.6
D4	LBL 1250-2000	4506	2000	466.0
D5	RCA C70102E	4F4	–	–

**Table 3.** COSPIN LET accelerator calibration history

Date	Facility <sup>1)</sup>	Beam <sup>2)</sup>
14-23 Apr 1981 <sup>3)</sup>	LBL Bevatron	Ne <sup>20</sup> Ar <sup>40</sup>
28 Jul 1982 - 2 Aug 1982	LBL Bevatron	Si <sup>28</sup> Fe <sup>56</sup>
17-20 May 1983	VU Cyclotron	p, H <sup>2</sup> , He <sup>4</sup>
1-4 Apr 1984	MPK MP Tandem	C <sup>12</sup> Ni <sup>58</sup>
12-20 May 1984	LBL Bevatron	Si <sup>28</sup> Fe <sup>56</sup>
25-26 Oct 1984	VU Cyclotron	p, H <sup>2</sup> , He <sup>4</sup>
20-24 Nov 1988	GANIL	Ar <sup>40</sup>

Notes:

- 1) LBL: Lawrence Berkeley Lab; VU: Amsterdam Free University; MPK: Max-Planck-Institut für Kernphysik, Heidelberg; GANIL: Grand Accélérateur National d'Ions Lourds, Caen.
- 2) Primary beam types (LBL and MPIH: separate runs; VU: all species simultaneously).
- 3) LET Engineering Model

**Table 4.** LET SFM channel number-to-MeV conversion factors

Detector	Conversion (MeV/channel)	
	High-Gain	Low-Gain
D1	0.0322	0.2534
D2	0.0300	0.5932
D3	0.1244	3.9480

**Table 5.** LET PHA data word

Bits (LSB=0)	Content
0 - 9	: detector D1 pulse height
10 - 19	: detector D2 pulse height
20 - 29	: detector D3 pulse height
30 - 32	: status flags
33	: detector D1 gain flag
34	: detector D2 gain flag
35	: detector D3 gain flag
36 - 39	: event code
40 - 42	: sector ID
43	: CAL ON flag

**Table 6.** Energy loss look-up table for LET aperture foils (data are listed on following pages).

Notes:

1. The (Z,A) values refer to the incident ion.
1. All energy values are tabulated in MeV/nucleon.
2.  $E_{instr}$  is the energy per nucleon measured in the LET.
3.  $E_{ext}$  is the incident energy per nucleon corrected for energy losses in the two foils.

ENERGY LOSS CALCULATIONS IN LET FOILS

Z = 1 A= 1

Einstr(MeV/n): 1.00 1.50 2.00 2.50 3.00 3.50 4.00 4.50  
 Ext(MeV/n): 1.44 1.84 2.27 2.73 3.22 3.69 4.16 4.66  
 Einstr(MeV/n): 5.00 5.50 6.00 6.50 7.00 7.50 8.00 8.50  
 Ext(MeV/n): 5.14 5.64 6.12 6.62 7.11 7.61 8.10 8.60  
 Einstr(MeV/n): 9.00 9.50 10.00 10.50 11.00 11.50 12.00 30.00  
 Ext(MeV/n): 9.09 9.59 10.08 10.58 11.08 11.58 12.08 30.04  
 Einstr(MeV/n): 50.00 80.00  
 Ext(MeV/n): 50.02 80.02

Z = 2 A= 4

Einstr(MeV/n): 1.00 1.50 2.00 2.50 3.00 3.50 4.00 4.50  
 Ext(MeV/n): 1.43 1.84 2.27 2.73 3.22 3.69 4.16 4.66  
 Einstr(MeV/n): 5.00 5.50 6.00 6.50 7.00 7.50 8.00 8.50  
 Ext(MeV/n): 5.14 5.64 6.12 6.62 7.11 7.61 8.10 8.60  
 Einstr(MeV/n): 9.00 9.50 10.00 10.50 11.00 11.50 12.00 30.00  
 Ext(MeV/n): 9.09 9.59 10.08 10.58 11.08 11.58 12.08 30.04  
 Einstr(MeV/n): 50.00 80.00  
 Ext(MeV/n): 50.02 80.02

Z = 3 A= 7

Einstr(MeV/n): 1.00 1.50 2.00 2.50 3.00 3.50 4.00 4.50  
 Ext(MeV/n): 1.52 1.92 2.35 2.79 3.27 3.74 4.20 4.70  
 Einstr(MeV/n): 5.00 5.50 6.00 6.50 7.00 7.50 8.00 8.50  
 Ext(MeV/n): 5.17 5.67 6.15 6.65 7.14 7.64 8.12 8.62  
 Einstr(MeV/n): 9.00 9.50 10.00 10.50 11.00 11.50 12.00 30.00  
 Ext(MeV/n): 9.11 9.61 10.10 10.60 11.10 11.60 12.10 30.05  
 Einstr(MeV/n): 50.00 80.00  
 Ext(MeV/n): 50.03 80.02

Z = 4 A= 9

Einstr(MeV/n): 1.00 1.50 2.00 2.50 3.00 3.50 4.00 4.50  
 Ext(MeV/n): 1.65 2.05 2.47 2.90 3.36 3.83 4.28 4.78  
 Einstr(MeV/n): 5.00 5.50 6.00 6.50 7.00 7.50 8.00 8.50  
 Ext(MeV/n): 5.24 5.74 6.21 6.71 7.19 7.69 8.17 8.67  
 Einstr(MeV/n): 9.00 9.50 10.00 10.50 11.00 11.50 12.00 30.00  
 Ext(MeV/n): 9.16 9.66 10.14 10.64 11.13 11.63 12.13 30.06  
 Einstr(MeV/n): 50.00 80.00  
 Ext(MeV/n): 50.04 80.03

Z = 5 A= 11

Einstr(MeV/n): 1.00 1.50 2.00 2.50 3.00 3.50 4.00 4.50  
 Ext(MeV/n): 1.76 2.15 2.57 3.00 3.45 3.92 4.36 4.86  
 Einstr(MeV/n): 5.00 5.50 6.00 6.50 7.00 7.50 8.00 8.50  
 Ext(MeV/n): 5.31 5.81 6.27 6.77 7.24 7.74 8.22 8.72  
 Einstr(MeV/n): 9.00 9.50 10.00 10.50 11.00 11.50 12.00 30.00  
 Ext(MeV/n): 9.20 9.70 10.18 10.68 11.17 11.67 12.17 30.08  
 Einstr(MeV/n): 50.00 80.00  
 Ext(MeV/n): 50.05 80.04

Z = 6 A= 12

Einstr(MeV/n): 1.00 1.50 2.00 2.50 3.00 3.50 4.00 4.50  
 Ext(MeV/n): 1.92 2.30 2.70 3.14 3.57 4.04 4.47 4.97  
 Einstr(MeV/n): 5.00 5.50 6.00 6.50 7.00 7.50 8.00 8.50  
 Ext(MeV/n): 5.40 5.90 6.36 6.86 7.32 7.82 8.29 8.79  
 Einstr(MeV/n): 9.00 9.50 10.00 10.50 11.00 11.50 12.00 30.00  
 Ext(MeV/n): 9.26 9.76 10.24 10.74 11.23 11.73 12.23 30.11  
 Einstr(MeV/n): 50.00 80.00  
 Ext(MeV/n): 50.07 80.05

Z = 7 A= 14

Einstr(MeV/n): 1.00 1.50 2.00 2.50 3.00 3.50 4.00 4.50  
 Ext(MeV/n): 2.01 2.39 2.78 3.22 3.64 4.10 4.53 5.03  
 Einstr(MeV/n): 5.00 5.50 6.00 6.50 7.00 7.50 8.00 8.50  
 Ext(MeV/n): 5.46 5.96 6.41 6.91 7.37 7.87 8.33 8.83  
 Einstr(MeV/n): 9.00 9.50 10.00 10.50 11.00 11.50 12.00 30.00  
 Ext(MeV/n): 9.31 9.81 10.28 10.78 11.26 11.76 12.26 30.12  
 Einstr(MeV/n): 50.00 80.00  
 Ext(MeV/n): 50.08 80.06

Z = 8 A= 16

Einstr(MeV/n): 1.00 1.50 2.00 2.50 3.00 3.50 4.00 4.50  
 Ext(MeV/n): 2.07 2.45 2.85 3.28 3.70 4.16 4.59 5.08  
 Einstr(MeV/n): 5.00 5.50 6.00 6.50 7.00 7.50 8.00 8.50  
 Ext(MeV/n): 5.52 6.01 6.46 6.96 7.41 7.91 8.38 8.88  
 Einstr(MeV/n): 9.00 9.50 10.00 10.50 11.00 11.50 12.00 30.00  
 Ext(MeV/n): 9.35 9.85 10.32 10.82 11.30 11.80 12.30 30.14  
 Einstr(MeV/n): 50.00 80.00  
 Ext(MeV/n): 50.10 80.07

Z = 9 A= 19

Einstr(MeV/n): 1.00 1.50 2.00 2.50 3.00 3.50 4.00 4.50  
 Eext(MeV/n): 2.07 2.46 2.84 3.28 3.74 4.18 4.61 5.10  
 Einstr(MeV/n): 5.00 5.50 6.00 6.50 7.00 7.50 8.00 8.50  
 Eext(MeV/n): 5.54 6.04 6.48 6.98 7.44 7.94 8.40 8.90  
 Einstr(MeV/n): 9.00 9.50 10.00 10.50 11.00 11.50 12.00 30.00  
 Eext(MeV/n): 9.37 9.87 10.34 10.84 11.32 11.82 12.32 30.15  
 Einstr(MeV/n): 50.00 80.00  
 Eext(MeV/n): 50.10 80.07

Z = 10 A= 20

Einstr(MeV/n): 1.00 1.50 2.00 2.50 3.00 3.50 4.00 4.50  
 Eext(MeV/n): 2.15 2.54 2.94 3.37 3.81 4.25 4.69 5.17  
 Einstr(MeV/n): 5.00 5.50 6.00 6.50 7.00 7.50 8.00 8.50  
 Eext(MeV/n): 5.61 6.10 6.55 7.05 7.50 8.00 8.46 8.96  
 Einstr(MeV/n): 9.00 9.50 10.00 10.50 11.00 11.50 12.00 30.00  
 Eext(MeV/n): 9.42 9.92 10.39 10.89 11.37 11.87 12.37 30.16  
 Einstr(MeV/n): 50.00 80.00  
 Eext(MeV/n): 50.12 80.08

Z = 11 A= 23

Einstr(MeV/n): 1.00 1.50 2.00 2.50 3.00 3.50 4.00 4.50  
 Eext(MeV/n): 2.14 2.53 2.93 3.36 3.80 4.25 4.69 5.17  
 Einstr(MeV/n): 5.00 5.50 6.00 6.50 7.00 7.50 8.00 8.50  
 Eext(MeV/n): 5.61 6.10 6.55 7.05 7.50 8.00 8.46 8.96  
 Einstr(MeV/n): 9.00 9.50 10.00 10.50 11.00 11.50 12.00 30.00  
 Eext(MeV/n): 9.43 9.93 10.40 10.90 11.37 11.87 12.37 30.16  
 Einstr(MeV/n): 50.00 80.00  
 Eext(MeV/n): 50.13 80.09

Z = 12 A= 24

Einstr(MeV/n): 1.00 1.50 2.00 2.50 3.00 3.50 4.00 4.50  
 Eext(MeV/n): 2.21 2.61 3.01 3.43 3.88 4.31 4.76 5.23  
 Einstr(MeV/n): 5.00 5.50 6.00 6.50 7.00 7.50 8.00 8.50  
 Eext(MeV/n): 5.68 6.16 6.61 7.10 7.56 8.05 8.51 9.01  
 Einstr(MeV/n): 9.00 9.50 10.00 10.50 11.00 11.50 12.00 30.00  
 Eext(MeV/n): 9.48 9.98 10.44 10.94 11.42 11.92 12.42 30.22  
 Einstr(MeV/n): 50.00 80.00  
 Eext(MeV/n): 50.14 80.10

Z = 13 A= 27

Einstr(MeV/n): 1.00 1.50 2.00 2.50 3.00 3.50 4.00 4.50  
 Eext(MeV/n): 2.20 2.60 3.01 3.44 3.88 4.32 4.76 5.23  
 Einstr(MeV/n): 5.00 5.50 6.00 6.50 7.00 7.50 8.00 8.50  
 Eext(MeV/n): 5.68 6.16 6.62 7.11 7.57 8.06 8.52 9.02  
 Einstr(MeV/n): 9.00 9.50 10.00 10.50 11.00 11.50 12.00 30.00  
 Eext(MeV/n): 9.48 9.98 10.45 10.95 11.43 11.93 12.43 30.22  
 Einstr(MeV/n): 50.00 80.00  
 Eext(MeV/n): 50.14 80.10

Z = 14 A= 28

Einstr(MeV/n): 1.00 1.50 2.00 2.50 3.00 3.50 4.00 4.50  
 Eext(MeV/n): 2.27 2.67 3.08 3.50 3.94 4.38 4.82 5.29  
 Einstr(MeV/n): 5.00 5.50 6.00 6.50 7.00 7.50 8.00 8.50  
 Eext(MeV/n): 5.74 6.21 6.67 7.16 7.61 8.10 8.57 9.06  
 Einstr(MeV/n): 9.00 9.50 10.00 10.50 11.00 11.50 12.00 30.00  
 Eext(MeV/n): 9.53 10.03 10.50 11.00 11.47 11.97 12.47 30.25  
 Einstr(MeV/n): 50.00 80.00  
 Eext(MeV/n): 50.17 80.12

Z = 15 A= 31

Einstr(MeV/n): 1.00 1.50 2.00 2.50 3.00 3.50 4.00 4.50  
 Eext(MeV/n): 2.25 2.66 3.08 3.50 3.94 4.38 4.83 5.29  
 Einstr(MeV/n): 5.00 5.50 6.00 6.50 7.00 7.50 8.00 8.50  
 Eext(MeV/n): 5.74 6.22 6.67 7.16 7.62 8.11 8.57 9.07  
 Einstr(MeV/n): 9.00 9.50 10.00 10.50 11.00 11.50 12.00 30.00  
 Eext(MeV/n): 9.53 10.03 10.50 11.00 11.47 11.97 12.47 30.25  
 Einstr(MeV/n): 50.00 80.00  
 Eext(MeV/n): 50.17 80.12

Z = 16 A= 32

Einstr(MeV/n): 1.00 1.50 2.00 2.50 3.00 3.50 4.00 4.50  
 Eext(MeV/n): 2.31 2.71 3.13 3.55 4.00 4.43 4.88 5.34  
 Einstr(MeV/n): 5.00 5.50 6.00 6.50 7.00 7.50 8.00 8.50  
 Eext(MeV/n): 5.79 6.26 6.72 7.20 7.66 8.15 8.62 9.11  
 Einstr(MeV/n): 9.00 9.50 10.00 10.50 11.00 11.50 12.00 30.00  
 Eext(MeV/n): 9.58 10.07 10.54 11.04 11.51 12.01 12.51 30.28  
 Einstr(MeV/n): 50.00 80.00  
 Eext(MeV/n): 50.19 80.14

Z = 17 A= 35

Einstr(MeV/n):	1.00	1.50	2.00	2.50	3.00	3.50	4.00	4.50
Ext(MeV/n):	2.31	2.71	3.13	3.55	4.00	4.43	4.88	5.34
Einstr(MeV/n):	5.00	5.50	6.00	6.50	7.00	7.50	8.00	8.50
Ext(MeV/n):	5.79	6.26	6.72	7.20	7.66	8.15	8.62	9.11
Einstr(MeV/n):	9.00	9.50	10.00	10.50	11.00	11.50	12.00	30.00
Ext(MeV/n):	9.58	10.07	10.54	11.04	11.51	12.01	12.51	30.28
Einstr(MeV/n):	50.00	80.00						
Ext(MeV/n):	50.19	80.14						

Z = 18 A= 40

Einstr(MeV/n):	1.00	1.50	2.00	2.50	3.00	3.50	4.00	4.50
Ext(MeV/n):	2.31	2.71	3.13	3.55	4.00	4.43	4.88	5.34
Einstr(MeV/n):	5.00	5.50	6.00	6.50	7.00	7.50	8.00	8.50
Ext(MeV/n):	5.79	6.26	6.72	7.20	7.66	8.15	8.62	9.11
Einstr(MeV/n):	9.00	9.50	10.00	10.50	11.00	11.50	12.00	30.00
Ext(MeV/n):	9.58	10.07	10.54	11.04	11.51	12.01	12.51	30.28
Einstr(MeV/n):	50.00	80.00						
Ext(MeV/n):	50.19	80.14						

Z = 19 A= 39

Einstr(MeV/n):	1.00	1.50	2.00	2.50	3.00	3.50	4.00	4.50
Ext(MeV/n):	2.31	2.71	3.13	3.55	4.00	4.43	4.88	5.34
Einstr(MeV/n):	5.00	5.50	6.00	6.50	7.00	7.50	8.00	8.50
Ext(MeV/n):	5.79	6.26	6.72	7.20	7.66	8.15	8.62	9.11
Einstr(MeV/n):	9.00	9.50	10.00	10.50	11.00	11.50	12.00	30.00
Ext(MeV/n):	9.58	10.07	10.54	11.04	11.51	12.01	12.51	30.28
Einstr(MeV/n):	50.00	80.00						
Ext(MeV/n):	50.19	80.14						

Z = 20 A= 40

Einstr(MeV/n):	1.00	1.50	2.00	2.50	3.00	3.50	4.00	4.50
Ext(MeV/n):	2.31	2.71	3.13	3.55	4.00	4.43	4.88	5.34
Einstr(MeV/n):	5.00	5.50	6.00	6.50	7.00	7.50	8.00	8.50
Ext(MeV/n):	5.79	6.26	6.72	7.20	7.66	8.15	8.62	9.11
Einstr(MeV/n):	9.00	9.50	10.00	10.50	11.00	11.50	12.00	30.00
Ext(MeV/n):	9.58	10.07	10.54	11.04	11.51	12.01	12.51	30.28
Einstr(MeV/n):	50.00	80.00						
Ext(MeV/n):	50.24	80.17						

Z = 21 A= 45

Einstr(MeV/n):	1.00	1.50	2.00	2.50	3.00	3.50	4.00	4.50
Ext(MeV/n):	2.30	2.74	3.19	3.63	4.08	4.52	4.99	5.44
Einstr(MeV/n):	5.00	5.50	6.00	6.50	7.00	7.50	8.00	8.50
Ext(MeV/n):	5.90	6.37	6.84	7.32	7.78	8.27	8.74	9.22
Einstr(MeV/n):	9.00	9.50	10.00	10.50	11.00	11.50	12.00	30.00
Ext(MeV/n):	9.70	10.19	10.66	11.15	11.63	12.13	12.63	30.35
Einstr(MeV/n):	50.00	80.00						
Ext(MeV/n):	50.24	80.17						

Z = 22 A= 48

Einstr(MeV/n):	1.00	1.50	2.00	2.50	3.00	3.50	4.00	4.50
Ext(MeV/n):	2.30	2.74	3.19	3.63	4.08	4.52	4.99	5.44
Einstr(MeV/n):	5.00	5.50	6.00	6.50	7.00	7.50	8.00	8.50
Ext(MeV/n):	5.90	6.37	6.84	7.32	7.78	8.27	8.74	9.22
Einstr(MeV/n):	9.00	9.50	10.00	10.50	11.00	11.50	12.00	30.00
Ext(MeV/n):	9.70	10.19	10.66	11.15	11.63	12.13	12.63	30.35
Einstr(MeV/n):	50.00	80.00						
Ext(MeV/n):	50.24	80.17						

Z = 23 A= 51

Einstr(MeV/n):	1.00	1.50	2.00	2.50	3.00	3.50	4.00	4.50
Ext(MeV/n):	2.30	2.74	3.19	3.63	4.08	4.52	4.99	5.44
Einstr(MeV/n):	5.00	5.50	6.00	6.50	7.00	7.50	8.00	8.50
Ext(MeV/n):	5.90	6.37	6.84	7.32	7.78	8.27	8.74	9.22
Einstr(MeV/n):	9.00	9.50	10.00	10.50	11.00	11.50	12.00	30.00
Ext(MeV/n):	9.70	10.19	10.66	11.15	11.63	12.13	12.63	30.35
Einstr(MeV/n):	50.00	80.00						
Ext(MeV/n):	50.24	80.17						

Z = 24 A= 52

Einstr(MeV/n):	1.00	1.50	2.00	2.50	3.00	3.50	4.00	4.50
Ext(MeV/n):	2.30	2.74	3.19	3.63	4.08	4.52	4.99	5.44
Einstr(MeV/n):	5.00	5.50	6.00	6.50	7.00	7.50	8.00	8.50
Ext(MeV/n):	5.90	6.37	6.84	7.32	7.78	8.27	8.74	9.22
Einstr(MeV/n):	9.00	9.50	10.00	10.50	11.00	11.50	12.00	30.00
Ext(MeV/n):	9.70	10.19	10.66	11.15	11.63	12.13	12.63	30.35
Einstr(MeV/n):	50.00	80.00						
Ext(MeV/n):	50.24	80.17						

Z = 25 A= 55

Einstr(MeV/n):	1.00	1.50	2.00	2.50	3.00	3.50	4.00	4.50
Eext(MeV/n):	2.30	2.74	3.19	3.63	4.08	4.52	4.99	5.44
Einstr(MeV/n):	5.00	5.50	6.00	6.50	7.00	7.50	8.00	8.50
Eext(MeV/n):	5.90	6.37	6.84	7.32	7.78	8.27	8.74	9.22
Einstr(MeV/n):	9.00	9.50	10.00	10.50	11.00	11.50	12.00	30.00
Eext(MeV/n):	9.70	10.19	10.66	11.15	11.63	12.13	12.63	30.35
Einstr(MeV/n):	50.00	80.00						
Eext(MeV/n):	50.24	80.17						

Z = 26 A= 56

Einstr(MeV/n):	1.00	1.50	2.00	2.50	3.00	3.50	4.00	4.50
Eext(MeV/n):	2.30	2.74	3.19	3.63	4.08	4.52	4.99	5.44
Einstr(MeV/n):	5.00	5.50	6.00	6.50	7.00	7.50	8.00	8.50
Eext(MeV/n):	5.90	6.37	6.84	7.32	7.78	8.27	8.74	9.22
Einstr(MeV/n):	9.00	9.50	10.00	10.50	11.00	11.50	12.00	30.00
Eext(MeV/n):	9.70	10.19	10.66	11.15	11.63	12.13	12.63	30.40
Einstr(MeV/n):	50.00	80.00						
Eext(MeV/n):	50.28	80.20						

## Appendix A: Charge Interpolation Algorithm

The charge interpolation algorithm used to process LET PHA data is based on a generalized range-energy relation for projectiles of charge  $Z$  and mass  $M$  of the form

$$R (\mu\text{m Si}) = \frac{11.9 E (\text{MeV})^{1.77}}{Z^2 M^{0.77}}$$

so that

$$E (\text{MeV}) = (A \times R)^\beta$$

where

$$A = \frac{Z^2 M^{\frac{1}{\beta}-1}}{11.9}$$

and

$$\beta = \frac{1}{1.77}$$

Consider a 2-detector  $dE/dX$  vs.  $E$  telescope, having detector thicknesses  $t$  and  $T$ , respectively. For projectiles of initial energy  $E_0$  stopping in the second detector with residual energy  $E_{res}$  and corresponding range  $R_{res}$ , the following relations apply:

$$E_0 = A^\beta (t + R_{res})^\beta$$

and

$$E_{res} = A^\beta R_{res}^\beta$$

so that

$$\begin{aligned} \Delta E &= E_0 - E_{res} \\ &= A^\beta \left( (t + R_{res})^\beta - R_{res}^\beta \right) \\ &= E_{res} R_{res}^{-\beta} \left( (t + R_{res})^\beta - R_{res}^\beta \right) \end{aligned}$$

This last equation defines the locus of so-called *track end-points* in the  $\Delta E$  vs.  $E_{res}$  diagram, and (within the constraints of the assumed range-energy relation) represents a straight line (referred to here as the *constant range line*, illustrated in Figure A1).

The separation  $s$  along a given constant range line of the endpoints corresponding to two different nuclear species  $(Z_1, M_1)$  and  $(Z_2, M_2)$  is given by

$$\begin{aligned} s &= \sqrt{(\Delta E_2 - \Delta E_1)^2 + (E_2 - E_1)^2} \\ &= C \left( A_2^\beta - A_1^\beta \right) \end{aligned}$$

where

$$C = \sqrt{B^2 + R_{res}^{2\beta}}$$

and

$$B = (t + R_{res})^\beta - R_{res}^\beta$$

Assuming that  $M \approx 2Z$ , and substituting this in the expression for  $A$  gives

$$s = \alpha R_{res}^{0.565} (Z_2^{1.565} - Z_1^{1.565})$$

where  $\alpha$  is a constant  $\sim 0.33$ . Strictly speaking, this relation will only be valid over the same energy range as the power-law approximation to the generalized range-energy equation (i.e. for incident energies  $\gtrsim 5$  MeV). For the constant range interpolation charge determination method to work optimally, the relative spacing of individual species tracks along given constant range lines must remain constant. For residual ranges  $\lesssim 20\mu\text{m}$  the approximation becomes less good, and slight broadening of the charge peaks can occur. The contribution due to this effect to the overall width of the charge peaks is, however, small.

Assuming now that  $(Z_1, M_1)$  and  $(Z_2, M_2)$  are reference species for which the track positions are known, the charge corresponding to each event can be computed from the relative spacing along the appropriate constant range line as follows:

$$\frac{s_Z(\text{MeV})}{s_{Z_2}(\text{MeV})} = \frac{Z^{1.565} - Z_1^{1.565}}{Z_2^{1.565} - Z_1^{1.565}}$$

but

$$\frac{s_Z}{s_{Z_2}} = \frac{E_{res} - E_{1,res}}{E_{2,res} - E_{1,res}} = r$$

so that

$$Z = \sqrt[1.565]{Z_1^{1.565}(1-r) + rZ_2^{1.565}}$$

This is shown graphically in Figure A2.

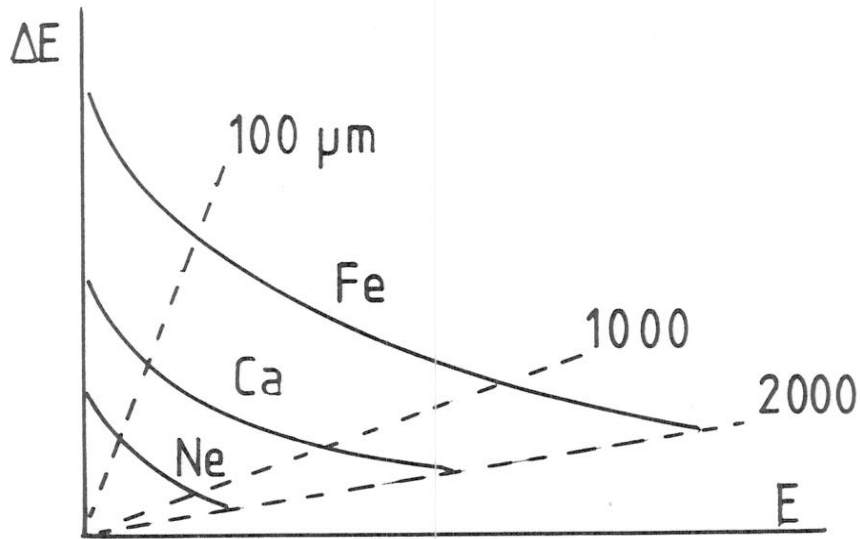


Fig. A1 Constant range lines.

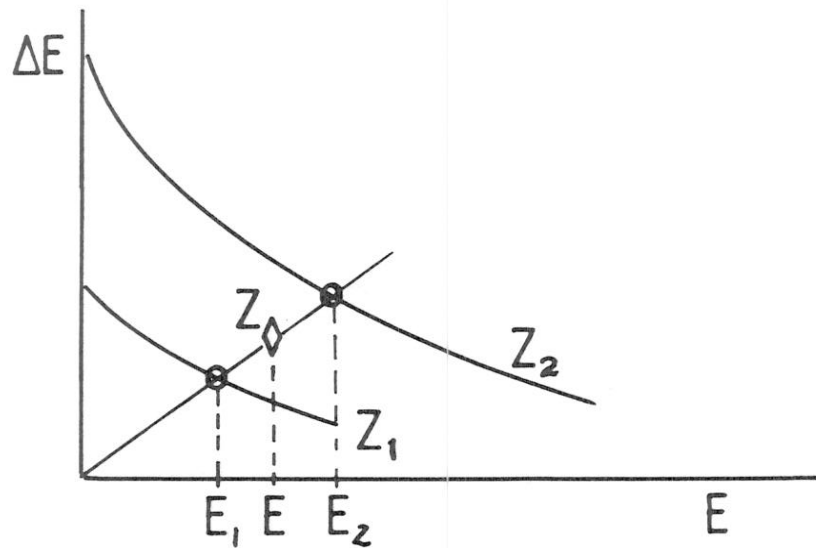


Fig. A2 Charge determination using constant range interpolation.

#### Appendix B: Range-Energy Relations: Tables/Computations/Useful References

The following range-energy tabulations and/or computations have been used during the course of the development of LET hardware and software:

Northcliffe, L.C. and R.F. Schilling, Nucl. Data Tables, **7**, (1970).

Littmark, U. and J.F. Ziegler, Stopping and ranges of ions in matter, **6**, Pergamon Press, New York, (1979).

Janni, J.F., Techn. Rep. AFWL-TR-65-150, USAF, (1966).

Some other useful references:

Butler, G.W., A.M. Poskanzer and D.A. Landis, Nucl. Instr. and Meth., **89**, 189, (1970).

Goulding, F.S., Nucl. Instr. and Meth., **162**, 609, (1979).

Greiner, D.E., Nucl. Instr. and Meth., **103**, 291, (1972).

## LET RESPONSE TO HIGH FLUXES - JCA DATA EVALUATION.

(prepared by J. Henrion - 29 Sept.1992.)

### 1 - LET response to high fluxes.

#### 1.1 - Introduction.

The response of the LET rate channels and the LS1, LS2 and LS3 "singles" channels is affected with at least 3 different effects originating in the electronic circuits

a/ Dead time effect. The detection of one event is affected with a dead-time of approx.18  $\mu$ sec created in the Event Clock. With repetitive events a maximum counting rate of about 55 kHz can be reached. For a higher counting rate the LET output saturates and remains  $5.5 \cdot 10^4$  cps.

With a random distribution of the event occurrences the response saturates for a lower average value, about  $2.8 \cdot 10^4$  cps. This is due to the loss of the events closer to 18  $\mu$ sec in the counts distribution.

Although the dead time is independent of the pulse amplitude (or the energy) it may create a distortion of the energy spectrum calculated from the different energy channels since the most populated part of the particle stream is more affected by the dead time.

b/ Pulse pile-up, When two or more events arrive too close to each other (within a few  $\mu$ sec) they will be detected as a single event of higher amplitude (or energy). This corresponds to a shift of the event energy toward higher values. This effect is important around the energy boundaries of the channels.

c/ Baseline shift, The apparent amplitude of the pulses decreases as the rate increases.

The shift is amplitude and rate dependent.

The effect a/ is predominant and becomes important above 104 cps, Effects b/ and c/ work in opposite directions but do not cancel each other.

The combination of the different effects leads to a response which is depending at the same time on the energy distribution (spectrum) and the population (counting rate) of the incident events. Therefore it is very difficult, if not impossible, to correct the data collected with the instrument deeply into saturation, as it was the case on Day 39, 1992, where the sum of the counts collected in LP1, LP2, LP3, LA1 and LP5) exceeded the saturation level of approx.  $3 \cdot 10^4$  cps.

An attempt to determine the importance of each effect was performed on the LET EM with a series of measurements made by E. Rouat (stagiaire) using random pulse generators to simulate the events. The results are reported in the Annex 1: "Study of the LET counting rate performance".

## 1.2 - Rate channel response to mono-energetic random pulses.

The Table 1 gives the LP1 and LP2 channels response as fractions of the input counts randomly occurring with constant amplitude corresponding approximately to the centre of the energy window. It also gives the fractions of incident LP1 counts recorded in LP2 due to pile-up.

Table 1. LP1 and LP2 response to LP1 events.

In counts (cps)	LP1/input ratio:	LP2/input ratio
1	1	0.0001
150	1	0.0001
500	0.991	0.0002
750	0.989	0.0003
1010	0.979	0.0004
1500	0.97	0.0005
2010	0.962	0.0007
3000	0.945	0.001
5000	0.91	0.0016
7500	0.87	0.0027
10000	0.833	0.0036
15000	0.766	0.0056
20080	0.706	0.0073
25090	0.654	0.0087
30100	0.609	0.01
40050	0.531	0.013
50140	0.468	0.016
60070	0.416	0.019
70100	0.372	0.02
80060	0.336	0.023
100100	0.278	0.025
121000	0.229	0.028
150000	0.185	0.03
175000	0.156	0.031
200700	0.135	0.032
250100	0.106	0.032
300400	0.088	0.031
403000	0.069	0.03
527000	0.053	0.029
756000	0.04	0.029
936000	0.036	0.029

Up to  $10^4$  cps the response stays above 80%.

The pile-up effect (b/) remains low because of the input pulse amplitude is far apart from the channel boundary. The baseline shift effect (c/) is not measured here since the affected events are lost under the D1A threshold.

The results are plotted on Fig.1.

Table 2 gives similar data for the LP1, LP2 and LA1 channels when pulses are centred in the channel LP2.

Table 2. LP1. LP2 and LA1 response to LP2 events.

In counts (cps):	LP1/input ratio	LP2/input ratio	LA1/input ratio
1	0	1	0
150	0	0.99	0.0002
500	0	0.985	0.00029
750	0	0.981	0.00042
1010	0	0.973	0.0007
1500	0.0046	0.963	0.0008
2010	0.01	0.945	0.0012
3000	0.015	0.91	0.0022
5000	0.024	0.871	0.0033
7500	0.034	0.831	0.0045
10000	0.044	0.764	0.007
15000	0.06	0.705	0.0093
20080	0.075	0.652	0.011
25090	0.086	0.605	0.013
30100	0.097	0.527	0.017
40050	0.11	0.463	0.02
50140	0.12	0.41	0.023
60070	0.13	0.366	0.025
70100	0.133	0.327	0.027
80060	0.137	0.267	0.03
100100	0.14	0.218	0.033
121000	0.14	0.17	0.036
150000	0.13	0.139	0.037
175000	0.122	0.115	0.038
200700	0.114	0.084	0.037
250100	0.096	0.067	0.036
300400	0.081	0.052	0.031
403000	0.061	0.044	0.029
527000	0.053	0.032	0.027
756000	0.044	0.029	0.027
936000	0.041		

The LP2 response is very similar to LP1. The baseline shift effect is clearly seen in the LP1/input ratio. It exceeds 10% of the counts above  $3 \cdot 10^4$  cps and reaches 14% at  $10^5$  cps. The pile-up effect does not exceed 3.8%. It should be kept in mind that these numbers correspond to a mono-energetic input signal and would probably be different with a wide distribution of the energies.

The response of the LA1 channel is also very similar to LP1 and LP2.

### 1.3 - Response to a wide energy distribution.

The difficulty to generate a broad energy spectrum together with a random pulse occurrence resides in the lack of suitable instruments. Pulse generators generate either random pulses with constant amplitude (exempt of pile-up effect) or repetitive pulses with adjustable amplitude and fall time which would suffer from the pile-up effect if the repetition frequency is too short for the selected fall time.

This last property was used to simulate random amplitude distribution by means of two pulse generators a (DB2) pulser used as random trigger to a normal "tail pulse" generator (9010). The output amplitude decreased exponentially with the time between two pulses (cfr. E. Rouat report, ch.3). However it was difficult to control separately the average rate and the amplitude distribution because of the relation between these two parameters in the "9010" pulse generator. Moreover the MCA (Tennelec PCA) used to measure the spectrum was also too slow to give an undistorted spectrum from which the input counts to the LET could be measured.

Nevertheless this set-up was used study the response of LP1 to a "solar" type spectrum.

The curve of Fig.2 shows the LP1 response to a "solar" type spectrum.

This response is similar to the response with mono-energetic pulses, perhaps slightly better.

These measurements should be confirmed with faster measuring equipment (faster MCA or fast single channel analyser with counters).

### 1.4 - Rate-channel response vs. pulses in adjacent channel.

Another set of measurement was taken with random counts in LP1 and repetitive counts in LP2 (cfr. E. Rouat report ch.2). The graph of Fig.3 shows the response of LP1 to interference. The LP1 response (Y axis) is the average of 5 different conditions where the input counts (random) in LP1 were comprised between about  $5 \cdot 10^3$  and  $2 \cdot 10^4$  cps. All results were very similar and could be averaged.

The scale gives the normalised values to the LP1 counts without interference (about  $1,3 \cdot 10^4$  cps). The interfering counts (x axis) are

(LS1 - LP1) counts repetitive

The output decreases proportionally to the interference. Additional measurements are needed to establish the mechanism of this interference effect.

### 1.5 - Conclusion,

Dead-time is the principal factor affecting the rate channel response.

Since all the events detected by the LET need about 18  $\mu\text{sec}$  to be recorded in a rate channel the total dead-time depends on the sum of the counting rates in all the channels. This means that, close to the saturation limit of about  $3 \cdot 10^4$  cps, to any increase of the counting rate in one of the channels corresponds a decrease of the counting rate observed in the other channels.

As seen on Fig.1 the response of the instrument, i.e. the sum of the rate channels, which is the same as one specific channel (here the LP1), decreases by 10% at  $5 \cdot 10^3$  cps, by 20% at  $1.3 \cdot 10^4$  cps by 50% at  $3.5 \cdot 10^4$  cps, etc....

How the response of each individual channel is affected depends on the distribution of the counting rates in all the channels.

A "first order" correction to the data might consist of checking first the sum of the counting rates in all the channels, then correcting it for the response losses (curve "LP1" of Fig.1). In a second step the counting rates of the different channels should be individually corrected according to the counting rates observed in the other channels.

This could be further studied when time and suitable measuring instruments are available.

The "second order" correction would take the pile-up and baseline shift effects into consideration.

## 2 - JCA data evaluation.

The analysis of the plots of Days 038, 039 and 040 (1992), shows that when the sum of the counts (cps) in channels LP1, LP2, LP3, LP4 and LA1 approaches the  $1.5$  to  $2 \cdot 10^4$  cps the variations observed in one particular channel is reflected in opposite direction in the other channels.

A first example of this might be in the feature A of day 038 at 15H00 (Fig.4), where LP1 reaches  $2.2 \cdot 10^4$  cps then decreases in steps. A "mirrored" feature can be observed in LP2, at much lower counting rate.

The feature in B might be of the same type.

Feature C (large drop in counting rate between 22 to 23H00) is obviously correct since the "singles" do the same (Fig.5).

The real saturation effect is clearly seen in the part D of the plot (day 039 from OH30 to 4H00) LP1 increases dramatically up to  $1.5 \cdot 10^4$  cps, LP2 and LP3 follow behind. When LP2 passes approx.  $10^4$  cps it produces a decrease in LP1.

In its turn when LP3 passes the  $5$  to  $6 \cdot 10^3$  cps its increase produces a further decrease in LP1 and LP2.

At the same time LA1 is also increasing and peaks at 2H45 at about  $5 \cdot 10^3$  cps (Fig.6) At that time the sum of the counts in the four channels is approximately

$$5 \cdot 10^3 \text{ (LP1)} + 8.5 \cdot 10^3 \text{ (LP2)} + 9 \cdot 10^3 \text{ (LP3)} + 5 \cdot 10^3 \text{ (LA1)} = 2.75 \cdot 10^4 \text{ cps}$$

which is the maximum counts observable in the rate channels.

The flattening of the peak in the LA1 curve between 2 and 4H00 is likely due to the saturation of the channel.

The dip E (day 039 between 5 and 7h00) is also real and is also visible in the "singles".

In F (day 039, 8H00 to 24H00) the 3 lower channels LP1, LP2 and LP3 follow each other rather well, the counts ratios are probably close to reality, here again the counting-rates seem to "mirror" the LP5 curve variations.

The decreases in LP5 around 13H00 and after 17H00 allow the lower LP channels to re-increase to a similar value as in the D period. The likely situation during period F is that the LP1 to 3 channels were probably "stable" at levels similar to the period D but were distorted by the large increase of LP5.

LP1 and LP2 response to LP1 events.

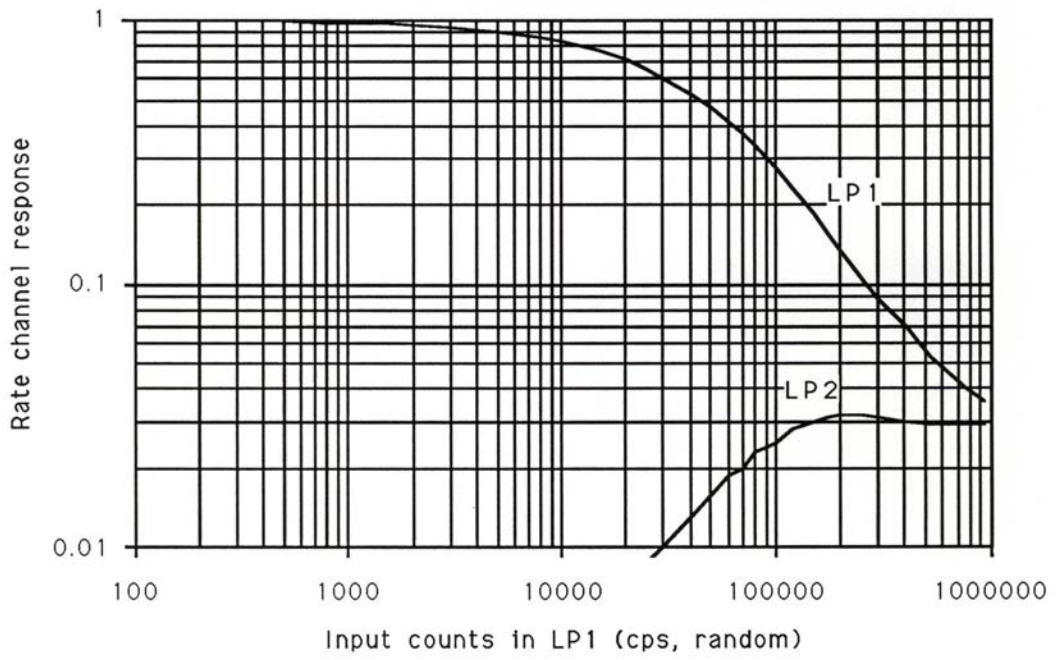


Fig.1 - LP1 and LP2 response to LP1 events.

LP1 RESPONSE TO SOLAR SPECTRUM

20-Jul-92

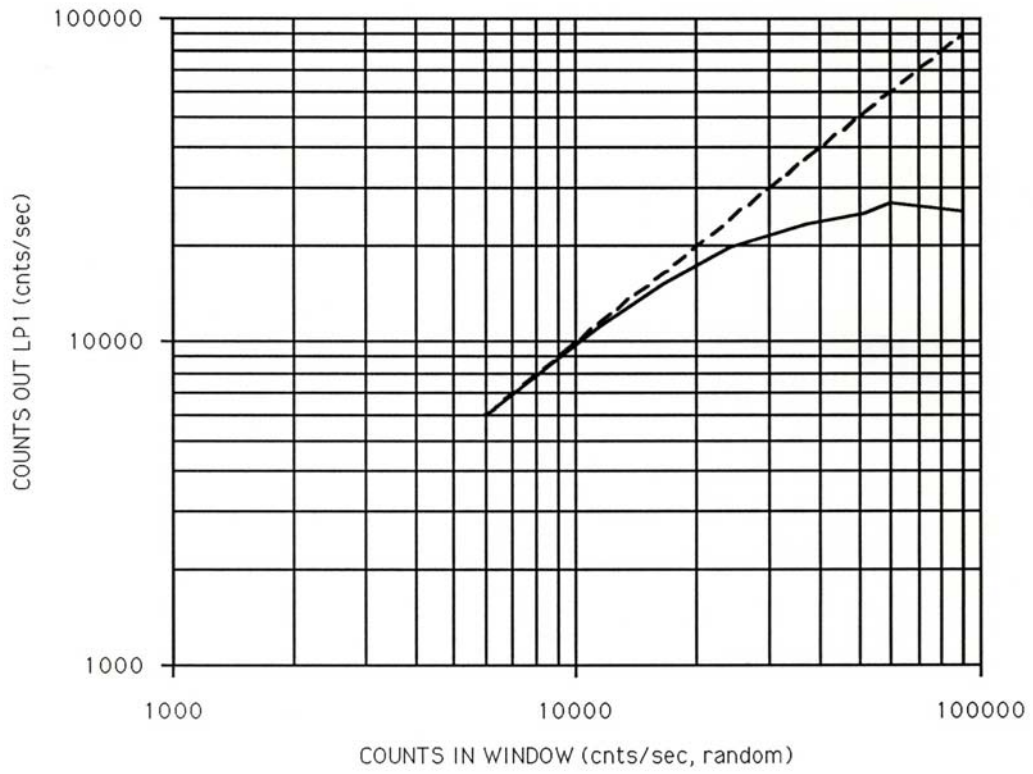


Fig. 2 - LP1 response to a "solar" energy spectrum.

# LP1 RESPONSE TO INTERFERENCE

31-Jul-92

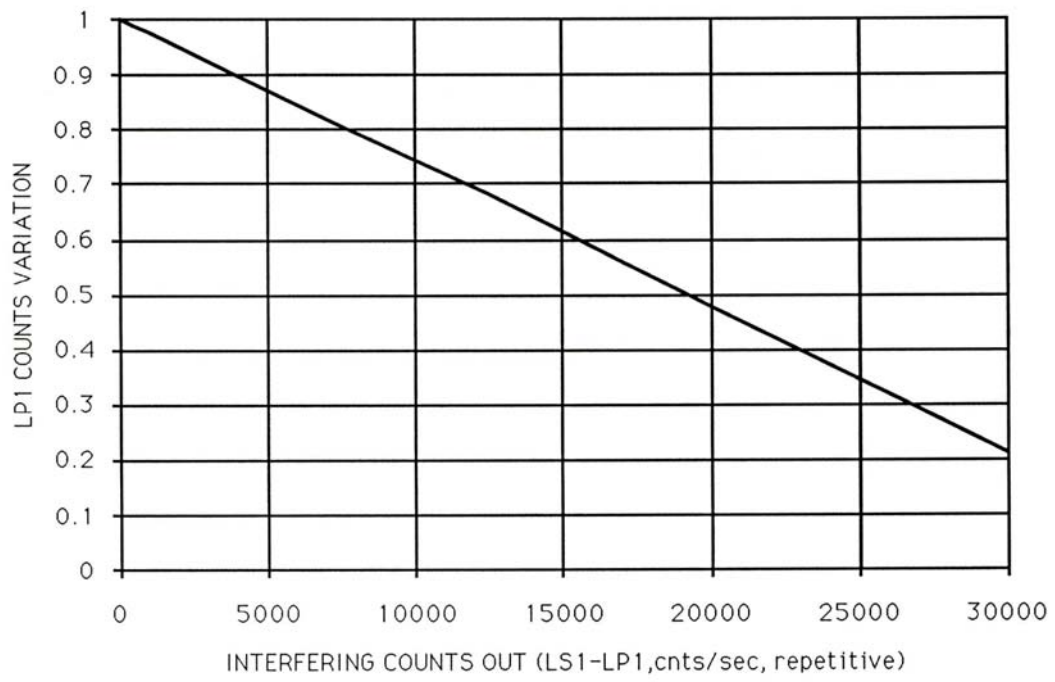


Fig.3 - LP1 response to interference in the D1 channel.